ALMA MATER STUDIORUM

UNIVERSITÀ DI BOLOGNA

Dipartimento di Fisica e Astronomia

DOTTORATO DI RICERCA IN

ASTROFISICA

Ciclo XXXIII

Tesi di Dottorato

The merger-driven evolution of early-type galaxies and the connection with their dark matter halos

Presentata da:
Carlo Cannarozzo

Supervisore:
Prof. Carlo Nipoti

Coordinatore di Dottorato:
Prof. Francesco Rosario Ferraro

Co-supervisore:
Dr. Alessandro Sonnenfeld

Esame finale anno 2021

Settore Concorsuale: 02/C1 – Astronomia, Astrofisica, Fisica della Terra e dei Pianeti
Settore Scientifico Disciplinare: FIS/05 – Astronomia e Astrofisica

Ph.D. thesis

The merger-driven evolution of early-type galaxies and the connection with their dark matter halos

Carlo Cannarozzo

Supervisors
Prof. Carlo Nipoti & Dr. Alessandro Sonnenfeld

November 01, 2017 – December 31, 2020

Ph.D. thesis defence: May 24, 2021

Carlo Cannarozzo

The merger-driven evolution of early-type galaxies
and the connection with their dark matter halos

November 01, 2017 – December 31, 2020
Ph.D. thesis defence: May 24, 2021
Supervisors: Prof. Carlo Nipoti and Dr. Alessandro Sonnenfeld

Alma Mater Studiorum Università di Bologna
Dipartimento di Fisica e Astronomia
Via Piero Gobetti, 93/2
40129, Bologna

Istituto Nazionale di Astrofisica
Osservatorio di Astrofisica e Scienza dello Spazio di Bologna
Via Piero Gobetti, 93/3
40129, Bologna

The project presented in Chapter 4 of this Ph.D. thesis has received funding from the European Union's Horizon 2020 research and innovation programme under the Marie Skłodowska-Curie grant agreement No 777822.

Abstract

Massive early-type galaxies (ETGs) are "red and dead" systems mainly composed by old and metal-rich stellar populations. In a cosmological context, present-day ETGs are believed to be the remnants of a complex stellar mass assembly history marked by several mergers, which are the consequence of the underlying hierarchical assembly of their host dark matter halos.

This Ph.D. thesis deals mainly with the merger-driven evolution of ETGs, studying how scaling relations evolve across cosmic time, how the stellar populations of the progenitors settled into the remnant galaxies, and how the mass of the host dark matter halos can be inferred from other galaxy properties.

In the first part of this thesis, I will present the results of the first systematic study in the literature of the evolution of the scaling relation that links the stellar mass of ETGs to their stellar velocity dispersion. By exploiting a Bayesian hierarchical formalism, I tested different functional forms to investigate how the stellar mass–velocity dispersion relation may vary as a function of redshift, finding evidence for an evolution over the redshift range $0 \lesssim z \lesssim 2.5$.

In the second part, I will illustrate a comparison between observed ETGs from the MaNGA survey and simulated galaxies from the cosmological simulation suite IllustrisTNG. The aim of this project is to provide an interpretative scenario of the stellar mass assembly history of present-day ETGs, comparing the radial distributions of their stellar properties with those of simulated galaxies, in which we can disentangle the role of stars formed *in situ* (i.e. within the main progenitor galaxy) and stars formed *ex situ* (i.e. in other galaxies) and then accreted through mergers.

Finally, in the last part, I will exhibit the preliminary results of a project aimed at inferring the dark matter mass of halos hosting central galaxies of the IllustrisTNG simulation, using Explainable Boosting Machine, a state-of-the-art machine learning implementation of the generalised additive models with pairwise interactions. I will show the strength of this new machine learning method that allows us to provide a prediction for the dark matter halo mass using several galaxy properties, in order to understand which of them are the most relevant to be used in observed galaxies.

Overall, the results presented in this manuscript confirm and extend previous outcomes about ETGs, their merger-driven evolution and the galaxy-halo connection, highlighting also the importance of making contrast between observations and simulations. The projects illustrated in this thesis make use of novel methods of statistics, data analysis and machine learning, which are becoming fundamental during the last years to handle huge amount of data and to face complex astrophysical problems.

To my Family.
To Elenina.
To Matilde.

“Every day I remind myself that my inner and outer life are based on the labors of other men, living and dead, and that I must exert myself in order to give in the same measure as I have received and am still receiving.”

— **Albert Einstein**, *The World As I See It*

— **Vincent Willem van Gogh**, *Starry Night Over the Rhône*

Acknowledgements

The first person I would like to sincerely thank is Prof. Carlo Nipoti. Carlo taught me how to approach a problem, how to think about it, how to overcome it. In simple words, he taught me how to do science. He had an enormous patience in explaining and clarifying concepts to me, leaving his office door always open for me. It has been a pleasure to be part of his research group.

An enormous thanks goes to Dr. Alessandro Sonnenfeld. Together with teaching me how to approach statistically a scientific problem, Ale certainly gave me a lot of suggestions during these years, also concerning my future, being available at any time.

I am really grateful to Carlo and Ale for being careful, supportive, and thoughtful in accompanying me in taking my first steps in astrophysics.

Another sincere thanks goes to Dr. Francesco Calura. During the first year of my Ph.D., I had started to collaborate with Francesco, and he shared with me his knowledge and time. I really hope to pursue our collaboration in the future.

During my time as a Ph.D. student, I have been lucky enough to meet Prof. Alexie Leauthaud. Alexie welcomed me into her research group, making me feel totally part of it. Since the first time we met, I have always appreciated her kindness and her clarity in explaining concepts and ideas to me. Naturally, it has been a great pleasure to be part of Alexie's group, and I would really like to warmly thank Prof. Kevin Bundy, Prof. Benedikt Diemer, Dr. Song Huang, Grecco Oyarzún, Enia Xhakaj, Felipe Ardila, Christopher Bradshaw, and all the others. I will never forget the time spent at the University of California Santa Cruz, such a wonderful place.

I am grateful to Prof. Mariangela Bernardi and Dr. Matthew Auger who gave me their crucial pieces of advice and comments, which remarkably enriched this manuscript and improved the quality of the debated topics.

I wish to acknowledge all the people who have contributed over the years to my works by sharing data and providing valuable insights: in alphabetic order, Dr. Cecilia Bacchini, Dr. Sirio Belli, Dr. Rich Caruana and the Microsoft Research team, Prof. Andrea Cimatti, Prof. Ivana Damjanov, Dr. Giulia Despali, Prof. Sandra Faber, Dr. Carlo Giocoli, Dr. Giuliano Iorio, Dr. Michael Maseda, Dr. Matilde Mingozzi, Dr.

Michele Moresco, Dr. Matteo Nori, Dr. Raffaele Pascale, Dr. Salvatore Quai, Prof. Vicente Rodriguez-Gomez, Prof. Tommaso Treu, and Prof. Dandan Xu.

I have benefited enormously also from the Professors and Researchers of the Department of Physics and Astronomy of the Alma Mater Studiorum University of Bologna and the Astrophysics and Space Science Observatory of Bologna, thanks to whom I have scientifically grown during these years.

My gratitude also goes to the European Union's Horizon 2020 research and innovation program which awarded me the Marie Skłodowska-Curie grant No 777822. This grant allowed me to spend six months of my Ph.D at the University of California Santa Cruz.

Being in Bologna these (almost) ten years has been made unique and unforgettable by a lot of fantastic friends and colleagues I have met. Thank you for every moment, guys!

Last but not least, I would like to conclude with the two most precious and heartfelt thanks to do.

An immense thanks to my Family: Mum and Dad, Marcella and Ivan, and the wonderful Elenina, you have always supported me from the very beginning of this long journey and I know you will always continue to do so. Thanks Zio.

And finally, I would like to thank Matilde from the bottom of my heart. Matilde and I have shared, step by step, everything: the Bachelor's degree, the Master's degree, the Doctorate, a thousand trips and much, much, much more. Thanks to be always by my side.

There are still two very last thanks. Thanks Bologna for essentially being Bologna. Thanks Music for hugging me every day.

Ringraziamenti

...quelli lunghi!

Adesso è l'ora dei ringraziamenti!

La prima persona che vorrei davvero ringraziare è il Prof. Carlo Nipoti. In questi anni, Carlo mi ha insegnato come approcciare un problema, sviluppare le idee ed oltrepassare le varie difficoltà. In poche parole, Carlo mi ha insegnato come fare scienza. Ha avuto un'enorme pazienza con me nello spiegarmi e chiarirmi tutti i possibili dubbi, lasciando la porta del suo ufficio sempre aperta. È stato un grandissimo piacere essere parte integrante del suo gruppo di ricerca.

Naturalmente, un altro enorme grazie va al Dr. Alessandro Sonnenfeld. Ale mi ha insegnato sicuramente come sfruttare la statistica in un problema scientifico, ma soprattutto mi ha dato tanti suggerimenti nel corso di questi anni, anche riguardanti il mio futuro, essendo sempre chiaro e disponibile con me.

Sono davvero grato a Carlo ed Ale per essere stati attenti, di supporto e premurosi durante i miei primi effettivi passi nel mondo dell'astrofisica.

Un altro sincero grazie va al Dr. Francesco Calura. Durante il primo anno del mio dottorato, io e Francesco abbiamo iniziato a collaborare, e ho trovato in lui una persona che ha condiviso con me la sua conoscenza e tutto il tempo necessario. Spero davvero di poter continuare la nostra collaborazione in futuro.

Durante il mio dottorato, ho avuto l'enorme fortuna di conoscere la Prof. Alexie Leauthaud. Alexie mi ha accolto nel suo grupppo di ricerca a Santa Cruz, facendomi sentire da subito parte di esso. Sin dai primi istanti, ho sempre apprezzato la gentilezza e la chiarezza di Alexie nello spiegare concetti ed idee. Essere parte del gruppo di ricerca di Alexie è stato un grandissimo piacere. E con Alexie, vorrei ringraziare il Prof. Kevin Bundy, il Prof. Benedikt Diemer, il Dr. Song Huang, Grecco Oyarzún, Enia Xhakaj, Felipe Ardila, Christopher Bradshaw e tutti gli altri. Non scorderò mai i miei periodi a Santa Cruz, in quel meraviglioso campus immerso tra sequoie e scoiattoli, ed in quella magnifica cittadina che si affaccia sul Pacifico. Natural Bridges e, soprattutto, Seabright State Beach le porterò sempre con me.

Sono grato alla Prof. Mariangela Bernardi ed al Dr. Matthew Auger per avermi fornito preziosi commenti e suggerimenti che hanno significativamente arricchito il contenuto di questa tesi, migliorandone la qualità.

Ci sono tantissime persone che in questi anni, condividendo dati e dandomi saggi consigli, hanno contribuito alla realizzazione dei miei lavori: in ordine alfabetico, la Dr. Cecilia Bacchini, il Dr. Sirio Belli, il Dr. Rich Caruana e tutto il gruppo di Microsoft Research, il Prof. Andrea Cimatti, la Prof. Ivana Damjanov, la Dr. Giulia Despali, la Prof. Sandra Faber, il Dr. Carlo Giocoli, il Dr. Giuliano Iorio, il Dr. Michael Maseda, la Dr. Matilde Mingozzi, il Dr. Michele Moresco, il Dr. Matteo Nori, il Dr. Raffaele Pascale, il Dr. Salvatore Quai, il Prof. Vicente Rodriguez-Gomez, il Prof. Tommaso Treu e la Prof. Dandan Xu.

Un ulteriore grazie va a tutti i Professori e Ricercatori del Dipartimento di Fisica e Astronomia dell'Alma Mater Studiorum Università di Bologna e dell'Osservatorio Astronomico di Bologna (Istituto Nazionale di Astrofisica - Osservatorio di Astrofisica e Scienza dello Spazio Bologna), grazie ai quali sono cresciuto scientificamente durante questi anni.

Ringrazio il programma di ricerca ed innovazione European Union's Horizon 2020 per avermi insignito del premio Marie Skłodowska-Curie grant No 777822. Grazie a questa borsa ho potuto trascorrere un periodo di sei mesi presso la University of California Santa Cruz.

Bologna in questi anni mi ha fatto conoscere fantastici amici e colleghi con i quali ho trascorso momenti unici ed indimenticabili. L'elenco è veramente lungo.

Con i loro *Ma è meglio...*, Giovanni e Francesco sono stati - e sono tuttora - dei carissimi amici fraterni, con i quali condividiamo l'amore per la Musica e che mi hanno incoraggiato in ogni momento.

Poi c'è il buon Fanelli! Tra qualche whisky e sigaro, io e Cristiano siamo da sempre stati "due anziani in un Mondo di giovani". E la cosa ci è sempre piaciuta un sacco.

Seppur lontani fisicamente, io ed Andrea abbiamo da subito condiviso, tra risate, Red Label come fosse acqua, "compà" in forlivese e viaggi in macchina nel Big Sur, ogni singolo passo nel mondo dell'Astrofisica.

Ad un certo punto è entrato un silenzioso Salvestrini. Con Francesco ci siamo ritrovati a condividere l'ufficio e da allora è nata una grandissima amicizia. Poi si è venuto a schiantare Antonio e, tra "gniii" alla finestra e tabacco sparso nel mio ufficio, è nato il trio dei *Disagggiati*.

Io e Fede ci siamo ritrovati tantissimo nella Musica e, con “poetiche" citazioni, ci siamo sempre scambiati brani che allietassero le nostre giornate, facendone scoprire all’altro sempre di nuovi.

Poi c’è Chiaretta con i suoi interminabili vocali. “Scatman (ski-ba-bop-ba-dop-bop)" ed innumerevoli altre idiozie hanno “edulcorato" ogni singolo giorno del nostro marasma nell’Astrofisica.

Imola mi ha accolto in questi anni tra la sua Rocca ed il suo orologio. Ed Imola significa Laura e Frank, ma significa anche Marta e Giammi, Lisa e Davide, Mimmo, Pietro, Bebè, Dami, Anna ed Enrico.

Ci sono poi altre quattro, ormai storiche, amiche che ci sono sin dai primi tempi qui a Bologna: Frà, Cate, Ceci ed Ambra.

Innumerevoli poi sono le accurate disamine *sanremesi* fatte con Ale, Mario, Matte e Silvia.

Ad un certo punto, come un’improvvisa ventata di freschezza, ho trovato in questo percorso quei tre meravigliosi *cinechini* di Viviana, Jacopo e Francesco.

In questo interminabile elenco ci sono anche gli amici di sempre, Valerio, Paolo, Maurizio, Peppe ed Orazio con i quali, sin dal liceo, siamo cresciuti insieme facendo discorsi “da grandi".

Un enorme grazie va a Chiara che da sempre, tra rock ‘n’ roll, blues, swing e chi più ne ha più ne metta, è stata come una seconda sorella per me, sempre pronta a sostenermi.

Il Prof. Fiorino è uno dei primi responsabili (in senso più che buono) del mio aver intrapreso e perseverato lungo questo percorso.

L’elenco di amici e colleghi sarebbe ancora davvero molto lungo e servirebbero almeno altri due tomi per includervi tutti. A tutti voi, un immenso e sincero grazie di tutto!

Infine, rimangono i ringraziamenti più speciali e preziosi tra quelli fatti.

Il primo immenso ringraziamento va alla mia Famiglia: Mamma e Papà, Marcella ed Ivan, e la meravigliosa Elenina mi hanno sempre sostenuto, sin dall’inizio di questo lungo, stancante, accidentato, ma splendido viaggio. Grazie per esserci da sempre e grazie perché continuerete ad esserci. Grazie Zio.

L’ultimo ringraziamento dal profondo del mio cuore va a Mati. Mati ed io abbiamo condiviso, passo dopo passo, tutto di questo percorso: la Triennale, la Magistrale, il

Dottorato. A questo si sono aggiunti i nostri fantastici viaggi insieme e molto, molto, molto altro ancora. Grazie per essere sempre al mio fianco.

Ah! Quasi dimenticavo! Ancora due ringraziamenti speciali.

Grazie mille Bologna per essere semplicemente Bologna. Quella Bologna nel cui centro *"non si perde neanche un bambino*". Quella Bologna che tra Piazza Maggiore, Santo Stefano e via d'Azeglio ti riscalda anche nelle giornate più fredde.

Grazie alla Musica perché ogni giorno mi abbraccia, mi carica, mi consola, mi arricchisce e mi colora.

Grazie!

Contents

1 An overview of early-type galaxies **1**

1.1 The nature of galaxies 1

1.1.1 The integrated light of galaxies 5

1.2 A few useful definitions 6

1.2.1 Mass-to-light ratio 6

1.2.2 Surface brightness profiles 7

1.2.3 Sérsic profiles 7

1.3 The red sequence of ETGs 8

1.4 The stellar population relations of ETGs 9

1.4.1 The colour–magnitude relation 10

1.4.2 The stellar mass–metallicity relation of ETGs 10

1.4.3 Relations involving the velocity dispersion 12

1.5 Selecting ETGs 14

1.6 The scaling relations of ETGs 15

1.6.1 The Faber-Jackson relation 15

1.6.2 The Kormendy relation 16

1.6.3 The Fundamental Plane of ETGs 16

1.6.4 The evolution of the structural and kinematic properties of ETGs 17

1.7 The role of the environment for ETGs 19

1.8 The merger-driven evolution of ETGs 21

1.8.1 The two-phase formation scenario of ETGs 23

1.9 Thesis structure 24

2 The cosmic evolution of the stellar mass–velocity dispersion relation of early-type galaxies **27**

2.1 Introduction 27

2.2 Galaxy sample 30

2.2.1 The fiducial sample 31

2.2.2 The high-redshift and extended samples 43

2.3 Method 46

2.3.1 Bayesian hierarchical formalism 46

2.3.2 The model . . . 47
2.3.3 Sampling the posterior probability distribution functions of the model hyper-parameters . . . 50
2.3.4 Bayesian evidence . . . 51
2.4 Results . . . 52
2.4.1 Fiducial sample ($0 \lesssim z \lesssim 1$) . . . 54
2.4.2 Extended sample ($0 \lesssim z \lesssim 2.5$) . . . 60
2.4.3 Comparing the results for the fiducial and extended samples . 61
2.5 Discussion . . . 62
2.5.1 Potential systematics . . . 62
2.5.2 Comparison with previous works . . . 65
2.5.3 Connection with the size evolution of ETGs . . . 70
2.6 Conclusions . . . 71

3 The role of in-situ and ex-situ star formation in early-type galaxies: MaNGA versus IllustrisTNG 83
3.1 Introduction . . . 83
3.2 Galaxy samples . . . 87
3.2.1 The MaNGA survey . . . 87
3.2.2 IllustrisTNG simulations . . . 90
3.2.3 ETG selection . . . 92
3.2.4 Stellar mass estimates . . . 94
3.3 Methods . . . 97
3.3.1 Radial profiles for MaNGA galaxies . . . 98
3.3.2 Radial profiles for IllustrisTNG galaxies . . . 99
3.3.3 Building stellar mass bins . . . 100
3.3.4 Building median radial profiles with errors . . . 102
3.4 Results . . . 103
3.4.1 Comparing profiles in stellar mass bins . . . 103
3.4.2 Comparing profiles in number-density-based stellar mass bins 110
3.4.3 Central versus satellite galaxies . . . 110
3.4.4 Comparison with recent works in literature exploiting MaNGA data . . . 116
3.5 Conclusions . . . 118

4 Inferring the Dark Matter halo mass in galaxies from other observables with Machine Learning 141
4.1 Introduction . . . 141
4.1.1 The importance of machine learning in astrophysics . . . 142

4.1.2 Linking DM halos to other galactic properties 143
4.2 The Method 145
4.2.1 Generalized additive models & GA^{2}Ms 145
4.2.2 The Explainable Boosting Machine model 147
4.3 An application to the cosmological simulation IllustrisTNG 151
4.3.1 The training and test samples 151
4.3.2 Predicting DM mass at different redshift 162
4.4 Conclusion & Future perspectives 170

5 Conclusions & Future Perspectives **171**

Bibliography **179**

1 An overview of early-type galaxies

> *This fright, this night of the mind must be dispelled not by the rays of the sun, nor day's bright spears, but by the face of nature and her laws.*
>
> **— Titus Lucretius Carus**

In the middle of the XVIII century, Thomas Wright (1711 - 1786) and, soon thereafter, Immanuel Kant (1724 - 1804) suggested that our locus in the Universe, the Milky Way, is a structure with a finite size, whose shape is more or less like a flat disk. Over the centuries, we have learned much more about the Milky Way: this system, totally sustained by gravity, is not composed only by stars, but there are a few other components like gas, dust, black holes and dark matter that work together to sustain this complex scaffolding. We have also learned that the faint "elliptical nebulae" seen in the obscurity of the sky might be something very similar to our galaxy. Kant named these other objects *island universes*.

1.1 The nature of galaxies

Galaxies we observe close to us show a wide variety of shapes and sizes, spanning broad ranges in luminosities and masses. The most evident property that characterises galaxies is their morphology. Indeed, akin to the classifications of animals and plants, it is useful to classify galaxies based on how they look like in the sky. Galaxy shapes result as a combination of their real intrinsic three dimensional shape and their orientation along the line of sight. The first "zoological" classification of galaxies was purposed in 1926 by Edwin Hubble (1889 - 1956) in his paper "*Extragalactic Nebulae*" (Hubble, 1926) and, subsequently, in his book "*The Realm of the Nebuale*" (Hubble, 1936). Understanding the physical processes behind the formation and evolution of the galaxies and their morphology is still one of the crucial aims of extragalactic astrophysics.

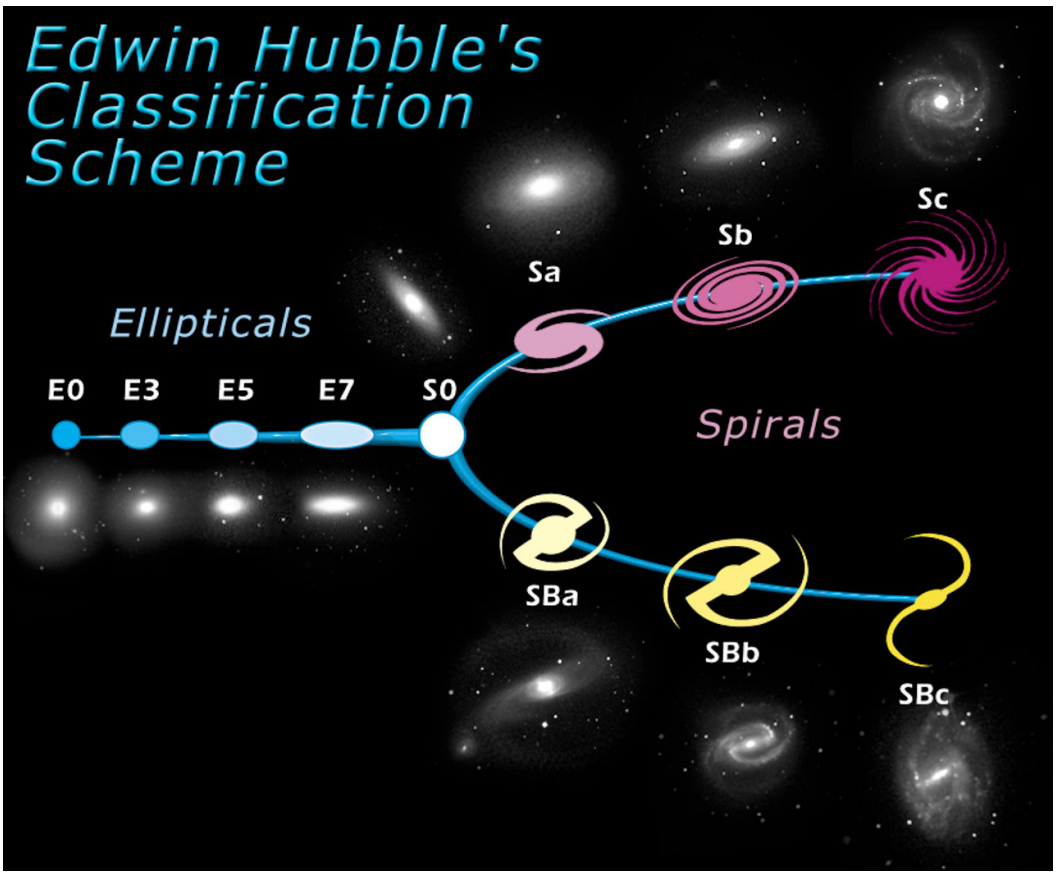

Fig. 1.1: The Hubble tuning-fork sequence diagram. This plot is taken from https://www.spacetelescope.org/images/heic9902o/.

According to their morphologies, galaxies were placed by Hubble upon the classical *tuning fork*, known as the *Hubble Sequence*. In this tuning-fork diagram, galaxies are arranged as shown in Figure 1.1. This morphological scheme divides galaxies in three main classes: *ellipticals* (Es), *spirals* (Ss) and *irregulars* (Irrs). Originally, Hubble interpreted (incorrectly) the tuning fork as an evolutionary diagram for galaxies. Therefore, from the left to the right, we move from *early-type galaxies* towards the *late-type galaxies*. Nowadays, we currently refer to the two main types of galaxies using this "wrong" terminology, but not considering more the Hubble diagram as an evolutionary sequence.

Starting from the left of the Hubble sequence, we find the class of ellipticals. Hubble subdivided these galaxies on the basis of their observed *flattening*, a quantity that is related to the *ellipticity*

$$\epsilon = 1 - \frac{\beta}{\alpha}, \tag{1.1}$$

where α and β are the apparent semi-major and semi-minor axes of an ellipse, respectively. The "E" Hubble type is quoted in units of 10ϵ: elliptical systems, indeed,

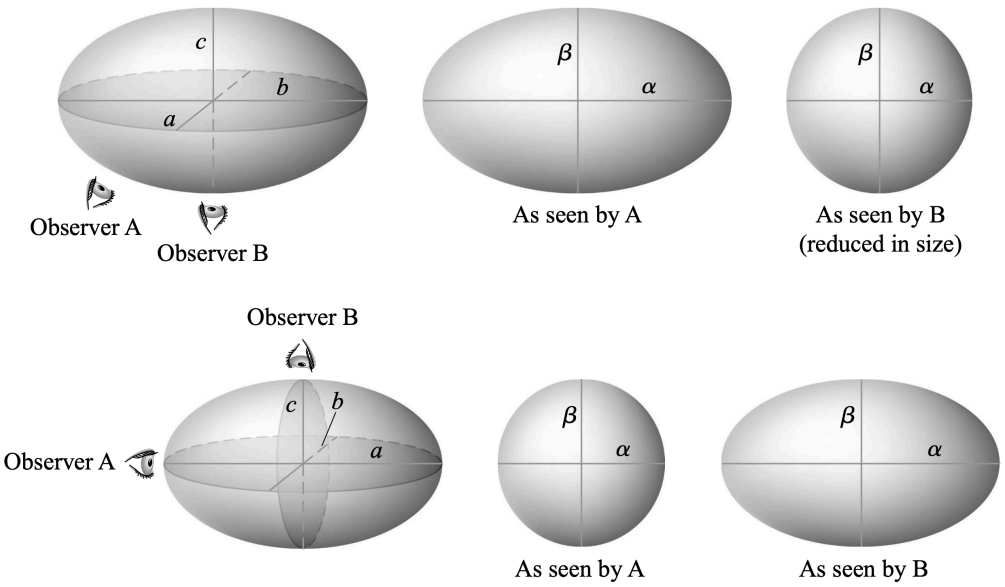

Fig. 1.2: Examples of oblate (top panels) and prolate (bottom panels) spheroids. Top panels: oblate spheroid with $a = b > c$. If $c/a = 0.6$, the apparent shape for observer A corresponds to an E4 galaxy ($\beta/\alpha = 0.6$), while for observer B corresponds to an E0 galaxy ($\beta/\alpha = 1$). Bottom panels: prolate spheroid with $a > b = c$. If $b/a = 0.6$, the apparent shape for observer A corresponds to an E0 galaxy, while for observer B corresponds to an E4 galaxy. This plot is an adapted version of two original plots taken from Carroll & Ostlie (2006).

can vary from a circular distribution of stars in the plane of the sky, E0, to a very flattened distribution, E7. Galaxies with values of ellipticity $\epsilon > 0.7$ have never been observed. Indeed, moving to the right of the Hubble sequence, galaxies start to show a different morphology mainly dominated by a central spheroid, the so-called *bulge*, surrounded by a disc without spiral arms. We stress here that, the apparent ellipticity does not necessarily correspond to the intrinsic ellipticity of Es, since their orientation along the line of sight may affect their observed real morphology. This effect is illustrated in Figure 1.2. In general, an ellipsoid is triaxial with axes $a \geq b \geq c$. Special cases are a sphere ($a = b = c$), an oblate spheroid ($a = b$) and a prolate spheroid ($b = c$).

Moving toward the right part of the Hubble sequence, we find the lenticular systems, S0s, a transitional class of galaxies between ellipticals and spirals. Proceeding further to the right, the spiral sequence forks into two subgroups. The upper prong includes normal spiral galaxies that are characterised by a central bulge and a surrounding disc. Depending on the prominence of the bulge and the importance of the winding of the arms, we subdivide normal spirals into Sa, Sb and Sc. The lower

prong, instead, considers the barred spirals (SBs), which present a bar in the central regions, like a bridge between the bulge and the arms.

Finally, the remaining category of galaxies is composed by irregulars that can be divided into Irr I, which show at least a hint of spiral arms or organised substructures, and Irr II that, instead, are completely disordered systems.

As we will see in this Chapter and in the rest of this manuscript, massive ellipticals (Es) and S0s systems, which we will refer to as early-type galaxies (ETGs) hereafter, are galaxies composed by old and metal-rich stellar populations (both responsible for the red colours of these objects), a quasi-absent star formation activity, characterised by the presence or not of a significant rotation, and that tend to occupy the innermost parts of overdense regions (like galaxy groups and clusters) in the Universe. Instead, spirals (both barred and not) are bluer galaxies, because of their more recent star formation activity, owing to a large amount of cold gas, whose stellar populations span a wide range in age. Moreover, they are more rotationally supported than ETGs, and tend to occupy lower density regions of the Universe.

In 1959, the classical Hubble sequence was extended following the revision by Gérard Henri de Vaucouleurs (1918 - 1995). In addition to elliptical and spiral galaxies, the novel classification included also further subclasses of lenticulars (S0a and S0b), spirals (Sd and Sm), and the irregular galaxies Im (where "m" stands for Magellanic-like objects such as the Small Magellanic Cloud). Moreover, other intermediate types were added along and between the two prongs of the original Hubble fork, that consider galaxies with ring structures (letter "r") or pure spirals (letter "s"), and much more. A detailed description of the revised version of the Hubble sequence can be found, for instance, at the beginning of Chapter 3 of Cimatti, Fraternali, & Nipoti (2019).

The morphological classification of galaxies strongly depends on which wavelength range is used to obtain their images. This difference in morphology, caused by a different wavelength used to observe the same galaxy, is called *morphological K correction*. There are two main reasons for this effect. On the one hand, younger stellar populations, usually located in the spiral arms of galaxies, are characterised by bluer colours and they are better revealed by UV observations; instead, older stars, usually occupying bulges, show redder colours, that are better identified by infrared observations. On the other hand, the presence of dust causes an extinction effect that tends to attenuate bluer colours. However, since ETGs are mainly composed by red stellar populations and almost completely free of dust, they do not strongly suffer the effects of the morphological K correction.

1.1.1 The integrated light of galaxies

For the closest galaxies to the Milky Way, i.e. those at most within a few Mpc, we are able to resolve individual stars. However, the majority of galaxies that we observe can be studied in terms of their integrated light properties. The information about stellar populations in a galaxy are derived from its *spectral energy distribution* (SED), i.e. the energy emitted by a source as a function of wavelength (or frequency).

The evolution of galaxies is a very complex subject to deal with, involving both dynamical and spectral evolution. Analysing the spectral evolution of galaxies allows to understand how the stellar populations change across cosmic time. From a theoretical point of view we know that high-mass stars (e.g., $> 1\,\mathrm{M}_{\odot}$) evolve over timescales shorter than the age of the galaxy where they live. This implies a succession of the type of stars whose emission dominates at different stages, causing a change in the observed spectra. If two similar galaxies have different ages this is reflected on their SEDs which can be interpreted in terms of spectral evolution (e.g., Spinrad, 1977; Wilkinson & Oke, 1978; Spinrad, 1980). For instance, in a single stellar population (SSP) evolving passively, the most massive stars continuously die and their role in dominating the integrated light goes to less massive stars. Galaxies, however, are more complex systems where multiple stellar populations coexist due to both new star formation episodes and accreted stars from other galaxies via mergers, cannibalism, stripping, etc.

In this context, it is interesting to take a look at the behaviour of a SSP and how it evolves during its lifetime. In Figure 1.3, the evolution of a SSP with solar metallicity and assuming a Salpeter (1955) initial mass function is shown, highlighting the relative contribution to the bolometric luminosity of each type of stars. The general behaviour is that the SSP fades as it ages. Specifically, for the first $\approx 20\,\mathrm{Myr}$ the bolometric luminosity is dominated by *main sequence stars*. Subsequently, the role of *asymptotic giant branch stars* grows. In old stellar populations (i.e. $\gtrsim 10\,\mathrm{Gyr}$) half of the total luminosity comes from the *red giant branch stars*. ETG stellar populations are mainly composed by old G-type and K-type giant stars, responsible for the typical red colours (see section 1.3 and section 1.4). However, a blue component in light has been observed in ETGs, not compatible with the expected ageing of stars (e.g., Faber, 1972, 1973; O'Connell, 1980; Trager, 1999). The presence of young and blue stars within ETGs is usually interpreted as recent star formation induced by interactions with other galaxies.

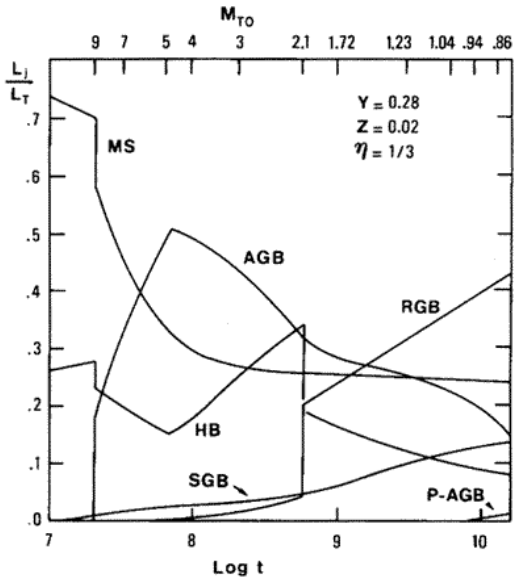

Fig. 1.3: The bolometric luminosity of the different types of stars as a function of time for a solar metallicity population SSP with a Salpeter initial mass function. The types of stars shown are *main sequence* (MS), *horizontal branch* (HB), *subgiant branch* (SGB), *red giant branch* (RGB), *asymptotic giant branch* (AGB), and *post asymptotic giant branch* (P-AGB) stars. The upper x-axis indicates the corresponding main sequence turnoff (TO) mass. This plot is taken from Renzini & Buzzoni (1986, in *Spectral Evolution of Galaxies*, eds. C. Chiosi & A. Renzini, Reidel Publishing).

For a more detailed description about the spectral evolution of galaxies, we refer the reader to Bruzual A. (1983), Renzini & Buzzoni (1986), Binney & Merrifield (1998), and section 8.6 of Cimatti, Fraternali, & Nipoti (2019).

1.2 A few useful definitions

In the following we introduce some concepts that are frequently used through this manuscript.

1.2.1 Mass-to-light ratio

The brightness of an astrophysical object is usually expressed in solar units, and, specifically, it is quantified as the number of the Suns required to reproduce the flux

of that object at its distance (Binney & Merrifield, 1998). If the stellar mass derived for this object is M_*, it is useful to compute the so-called *mass-to-light ratio*

$$\Upsilon_{*,x} = \frac{M_*/\mathrm{M}_\odot}{L_{*,x}/\mathrm{L}_{\odot,x}}, \tag{1.2}$$

where $L_{*,x}$ and $\mathrm{L}_{\odot,x}$ are the luminosity of the source and of the Sun in the waveband x, respectively.

1.2.2 Surface brightness profiles

Establishing which are the limits in size of a galaxy is not straightforward. Galactic systems are extended sources on the sky and their shape can be derived by analysing their *surface brightness profiles*. The curves on the observed image of a galaxy characterised by the same value of surface brightness are called *isophotes*. If the shape of the isophotes is approximately an ellipse, their ellipticity has the same form of Equation 1.1, and the *elliptical raidus* α or, alternatively, the *circularised radius* $R_\mathrm{c} = \sqrt{\alpha\beta}$ can be used to obtain the surface brightness radial profile, i.e. a 1D curve showing how the surface brightness changes as a function of the galactocentric distance. Since galaxies do not have sharp edges, their physical size is often expressed in units of the *isophotal radius*, i.e. the radius of the isophote that includes a given level of surface brightness. It is commonly used as a radius the so-called *effective radius* R_e (or *half-light radius*), i.e. the radius of the isophote including 50% of the total flux of the galaxy.

1.2.3 Sérsic profiles

The surface brightness profile of a galaxy can be modelled with different functional forms. For instance, discs are usually modelled using an exponential decay, while historically bulges of spiral galaxies and ellipticals are fitted by the $r^{1/4}$ law of the de Vaucouleurs profile (de Vaucouleurs, 1948). A generalised version of these models is given by the so-called *Sérsic profile* (Sérsic, 1968):

$$I = I_\mathrm{e}\ \exp\left\{-b(n)\left[\left(\frac{R}{R_\mathrm{e}}\right)^{1/n} - 1\right]\right\}, \tag{1.3}$$

where I_e is the surface brightness at the effective radius, n is the *Sérsic index*, and b is a parameter depending on n that can be approximated by $b(n) = 2n - 1/3 + 4/(405n)$

(Ciotti & Bertin, 1999). Equation 1.3 reduces to the classical de Vaucouleurs profile, when $n = 4$, while assuming $n = 1$ we end up with an exponential distribution.

As deeply discussed in Ciotti & Bertin (1999), as the Sérsic index increases, the surface brightness profiles tends to become steeper at small radii and shallower at large radii. Usually, when fitted by one Sérsic component, ETGs are separated from late-type galaxies (LTGs), by selecting those objects with $n > 2.5$. In many cases, however, since galaxies can be composed by more the one stellar population, a multi-component fit is adopted, by combining two (or more) Sérsic laws.

1.3 The red sequence of ETGs

Galaxies in the Universe can be classified depending on the colours of their stellar populations. Indeed, it is well known that we can identify two galaxy families: blue galaxies, which usually are star-forming and disc-dominated systems, and red galaxies, which, instead, are usually early-type, quiescent and bulge-dominated systems.

In Figure 1.4 three colour–mass diagrams from Schawinski et al. (2014) for a galaxy sample based on photometric and spectroscopic data from the Sloan Digital Sky Survey (SDSS) Data Reease 7 (York et al., 2000; Abazajian et al., 2009) is illustrated. Specifically, this figure shows galaxies with $u - r$ colours already corrected for dust extinction (see section 1.1), adopting the correction at $z = 0.0$ from the NYU-VAGC (Blanton et al., 2005; Blanton & Roweis, 2007; Padmanabhan et al., 2008). The upper-left panel of Figure 1.4 shows the entire sample considered which is separated in ETGs and LTGs in the two plots on the right side. The global arrangement of galaxies in the three colour–mass diagrams reveals the presence of the so-called *colour bimodality*. Indeed, we can easily identify two well-defined regions: the *red sequence* (mainly populated by ETGs) and the *blue cloud* (mainly populated by LTGs). Although both ETGs and LTGs span the entire range of colours, highlighting the contamination of some blue ETGs and red LTGs, the two galaxy populations tend to be separated, showing a transition "bridge" called *green valley*. Moreover, the location of the red sequence in these colour–mass plots suggests that, on average, as already said in section 1.1, the most massive galaxies tend to be ETGs.

From a galaxy-evolution point of view, an important question concerns the origin of the observed bimodality, that is also found at higher redshifts (e.g., Bell et al., 2004; Brammer et al., 2009; Wuyts et al., 2011; Cheung et al., 2012; McIntosh et al., 2014). This origin should be sought in the building-up processes of the red sequence

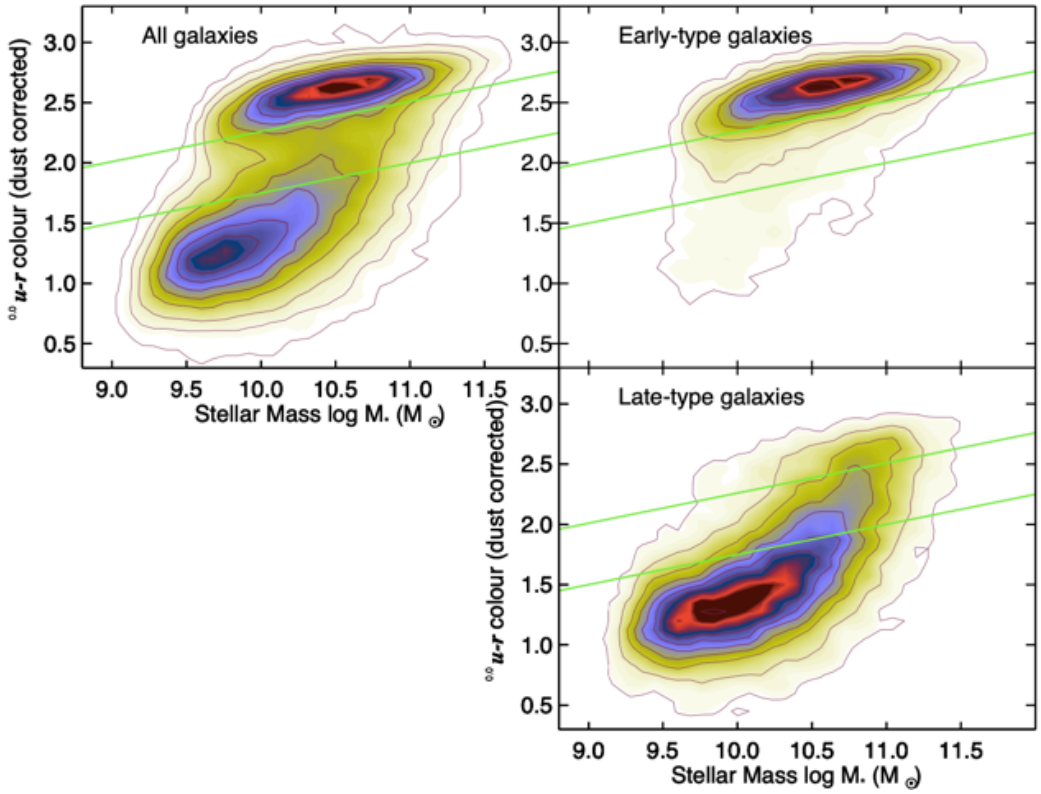

Fig. 1.4: The reddening-corrected $u - r$ colour–mass diagrams for the whole galaxy sample (top-left panel), and for the ETGs (top-right panel) and LTGs (bottom-right panel), respectively of the SDSS DR7. The two green lines in the three plots delimit the green valley. This plot is taken from Schawinski et al. (2014).

itself. Several processes can be responsible for the movement of the galaxies in the colour–mass plane, such as mergers, quenching of star formation in galaxies, etc (e.g., Faber et al., 2007; Pozzetti et al., 2010).

1.4 The stellar population relations of ETGs

The star formation history of ETGs is influenced by all the evolutionary processes occurred during their cosmic evolution. As described in the previous section, ETG colours tend to be redder with respect to those of star forming galaxies because of a combination of factors. Indeed, as a consequence of the lack of cold gas, the stars that populate ETGs are old and metal rich, and, since the *quasi* absence of dust, the observed red colours of ETGs are basically coinciding with their intrinsic red colours.

1.4.1 The colour–magnitude relation

In 1992, by observing galaxies within the Virgo and Coma galaxy clusters, it was discovered that ETGs obey the *colour–magnitude relation* (Bower, Lucey, & Ellis, 1992). This tight correlation involves the $U - V$ rest-frame colour and the absolute magnitude of ETGs. An important property of this relation is its scatter. In particular, if ETGs actually are the result of a passive evolution, this scatter can give us information about the redshift of their formation. From the observed colour scatter, Bower, Lucey, & Ellis (1992) stated that ETGs in clusters are mainly composed by very old stellar populations, whose bulk of formation dates back to $z \gtrsim 2$. A correlation is also found between colour and stellar velocity dispersion σ, consistent with the fact that σ correlates with luminosity (see section 1.6).

As we already said, the presence of red stellar populations in a galaxy cannot be sufficient to provide a satisfying explanation for the evolution of ETGs and the already mentioned relations, because of the presence of the so-called *age-metallicity degeneracy*: indeed, red colours can be caused by old and/or metal-rich stars. This degeneracy can be circumvented by extending the analysis to other and more stringent properties of stars looking at ETG spectra. Some features within spectra of ETGs like the shape of the stellar continuum, the presence of absorption lines or the D4000 break show peculiarities typical of old stellar populations, that can be derived by adopting two specific methods: the *full spectral fitting* technique adopting stellar population synthesis models and the exploitation of *Lick indices* (or other estimators) for deriving the equivalent widths of specific absorption lines. Both techniques can give us consistent results and help in breaking the age-metallicity degeneracy (for a more detailed explanation we refer the reader to Cimatti, Fraternali, & Nipoti 2019). Anyway, regardless of the method adopted, on the average, the stellar populations composing ETGs in the present-day Universe are both old and metal-rich.

1.4.2 The stellar mass–metallicity relation of ETGs

Metallicity of stars is found to correlate with the stellar mass, giving rise to the so-called *mass–metallicity relation*[1]. The stellar mass–metallicity relation was discovered in present-day ETGs combining the analysis of their spectra and colour–magnitude diagrams (McClure & van den Bergh 1968; Sandage 1972; Mould, Kristian, & Da Costa 1983, Buonanno et al. 1985). The first interpretation of the existence of

[1] We underline that also the gas-phase metallicity of galaxies shows a correlation with the stellar mass. In this manuscript, however, when we will refer to metallicity in general, we consider only the stellar metallicity.

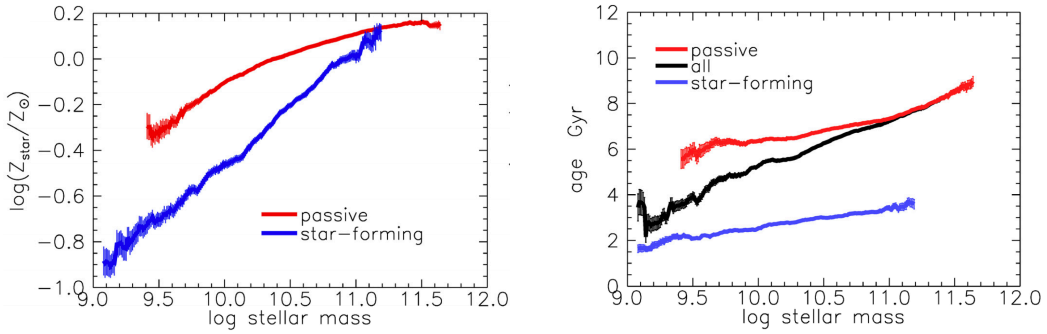

Fig. 1.5: Stellar mass–metallicity relation (left panel) and stellar mass–age relation (right panel) for $z \simeq 0.05$ SDSS quiescent (red curves) and star forming (blue curves) galaxies. These plots are adapted from Peng, Maiolino, & Cochrane (2015).

the stellar mass–metallicity relation was in terms of the chemical pollution due to supernova winds from low-mass galaxies: a part of the expelled material from these small systems is captured and retained by galaxies with higher masses, which mix and dilute their global metal content (Tinsley, 1974, 1978; Mould, 1984). Recently, by exploiting information from optical spectra, relevant studies have been conducted in particular using SDSS galaxies to obtain the stellar mass–metallicity relation for both star forming and passive galaxies (e.g., Trager et al., 2000; Kuntschner et al., 2001; Gallazzi et al., 2005; Thomas et al., 2005; Gallazzi et al., 2006, 2008; Thomas et al., 2010; Conroy et al., 2014; González Delgado et al., 2015; Zahid et al., 2017; Zhang et al., 2018).

Disentangling the role of star forming and quiescent galaxies, Peng, Maiolino, & Cochrane (2015) studied in detail the stellar mass–metallicity and also the *mass-age* relations for a sample of SDSS galaxies (see Figure 1.5). The authors found evidence that environment-related processes such as the so-called *strangulation* (e.g., Larson et al., 1980; Balogh et al., 2000; Kereš et al., 2005) in galaxy may be responsible for the existence of these relations. Indeed, strangulation stops the gas accretion onto galaxies, causing a passive evolution of the systems, which evolve like *closed boxes* (Tinsley, 1968; Searle & Sargent, 1972). When the gas reservoir is consumed, there is no more star formation activity.

For a more detailed presentation of the stellar mass–metallicity relation, we refer the reader to the review by Maiolino & Mannucci (2019).

1.4.3 Relations involving the velocity dispersion

Of course, in light of the relations presented so far, the direct consequence is the presence of other scaling relations involving evolutionary and dynamical properties of ETGs, that allow to reconstruct their star formation history. We will briefly summarise these scaling relations below.

Metallicity–velocity dispersion relation

The $[Z/H]-\sigma$ relation is an empirical correlation between the galaxy velocity dispersion and stellar metallicity (e.g., Greggio, 1997; Thomas et al., 2005, 2010). This relation suggests that massive ETGs, and so systems with high velocity dispersion, tend to be metal rich, even supersolar. The presence of such relation is somewhat related to the fact that the deep potential wells of ETGs are able to retain material expelled through galactic winds, that enrich globally their interstellar medium.

α-element abundance–velocity dispersion relation

Similarly to the $[Z/H]-\sigma$ relation, the $[\alpha/\mathrm{Fe}]-\sigma$ relation contains information on the star formation history in ETGs, since α elements[2] are optimal indicators of the star formation timescale. Indeed, the presence of α elements in galaxies is mainly due to the explosions of Type II supernovae, and longer timescales imply a lower values of $[\alpha/\mathrm{Fe}]$, because, in the meanwhile, explosions by Type Ia supernovae – main responsible for the presence of iron (and the other peak elements) in galaxies – dilute the α-element content. The deep potential wells of ETGs ensure that these galaxies have a large amount of α elements (e.g., Worthey et al., 1992; Greggio, 1997; Jørgensen, 1999; Kuntschner, 2000).

Age–velocity dispersion relation

The age of stellar populations is found to correlate with stellar velocity dispersion in ETGs. As we already seen, massive ETGs tend to be populated by old stars ($\gtrsim 5\,\mathrm{Gyr}$) even reaching at $z \approx 0$ ages comparable with the age of the Universe. This relation shows a large scatter (e.g., Proctor & Sansom 2002, Thomas et al. 2005, 2010).

[2] α elements, such as C, O, Ne, Mg, Si, etc, are chemical elements synthesised in stars as a consequence of fusion processes involving helium.

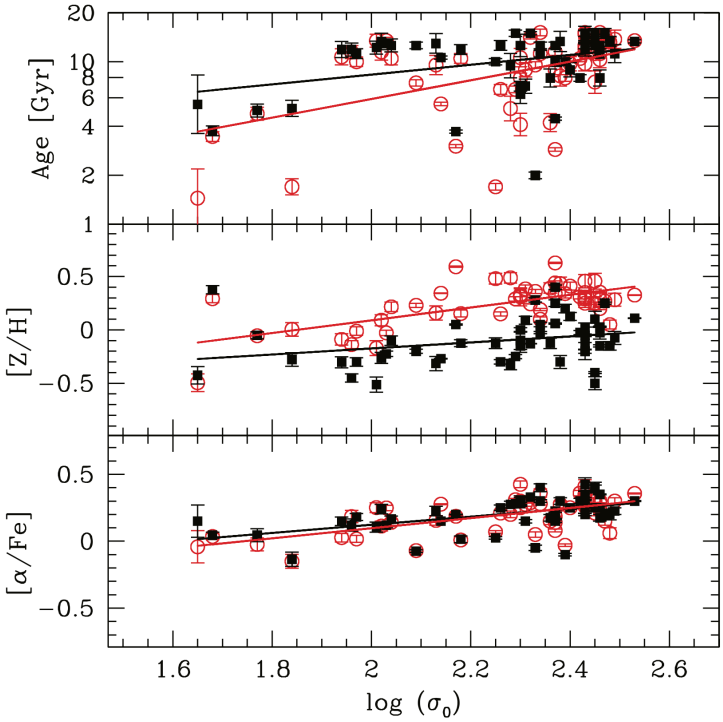

Fig. 1.6: The age$-\sigma$ (top panel), $[Z/\mathrm{H}]-\sigma$ (middle panel), and $[\alpha/\mathrm{Fe}]-\sigma$ (bottom panel) relations are shown. Open red dots and black squares represent central values and mean stellar values of stellar population parameters of the sample considered by Spolaor et al. (2010). The red and black lines are the weighted least-squares linear fits. This plot is taken from Spolaor et al. (2010).

In Figure 1.6 the age$-\sigma$, $[Z/H]-\sigma$ and $[\alpha/\mathrm{Fe}]-\sigma$ relations described above from Spolaor et al. (2010) are displayed.

The relations presented in this section involve integrated properties of ETGs. Spatially-resolved stellar properties can give us a more detailed view on the variations of these properties within galaxies. For instance, by analysing a sample of ETGs and spiral galaxies from the MaNGA survey (Bundy et al., 2015), Li et al. (2018) studied how stellar age, metallicity and stellar mass-to-light ratio are distributed in galaxies, confirming that these properties tend to increase for increasing local σ. In particular, they found that the stellar age and, especially, the stellar metallicity gradients strongly depend on stellar velocity dispersion, that peaks at around $100\,\mathrm{km\,s^{-1}}$, corresponding approximately to a stellar mass of $\log(M_*/\mathrm{M}_\odot) \approx 10.5$, i.e. the critical mass where the break in the stellar mass–size relation occurs (Cappellari, 2016). The fact that these gradients tend to become flatter as the velocity dispersion increases can be interpreted in terms of the rising role of mergers, which redistribute the stellar metallicity in these high-velocity-dispersion systems.

1.5 Selecting ETGs

Massive ETGs are spheroidal or elliptical systems (E/S0) composed by red, old and metal-rich stellar populations, and with an almost negligible activity in forming new stars, which makes these galaxies essentially passive. However, their identification in galaxy surveys is not always trivial.

In their work, Moresco et al. (2013) deeply analysed the nature of ETGs, shedding light on similarities and differences of various selection criteria adopted to identify ETGs. In the following we briefly summarise the analysis made by Moresco et al. (2013) for different samples of galaxies out to $z \simeq 1$ extracted from the zCOSMOS-20k survey (Lilly et al., 2009). Leaving out from this summary all the details of each selection method presented, the authors discuss pros and cons of six different criteria:

- "*morphological*" *ETGs*, i.e. a morphological selection that combines the information from a principal component analysis of five structural diagnostics and a single-Sérsic fit of the surface brightness;
- "*red-sequence*" *galaxies*, i.e. a criterion based on the $(U-B)$ colour–stellar mass relation;
- "*red UVJ*" *galaxies*, i.e. a selection made on the UVJ colour–colour diagram;
- "*red SED*" *galaxies*, i.e. a criterion based on fitting photometric data with templates of photometric galaxy types;
- "*quiescent*" *galaxies*, i.e. a selection based on the values of specific star formation rate of galaxies;
- "*red & passive*" *ETGs*, i.e. a criterion based on a combination of morphological, photometric and optical spectroscopic information.

Though each galaxy sample selected with one of the previous methods displays a percentage of contamination due to the presence of blue/star-forming/non-passive galaxies, among these six approaches, the "red & passive" method performs best, identifying galaxies by fitting their spectral energy distributions (SEDs) with E/S0 templates, keeping only objects with weak or negligible emission lines using EW([O II]) or EW(Hα), requiring a spheroidal morphology and observed $(K-24\mu m)$ colours of $z \approx 0$ E/S0 objects. However this approach is very demanding, because it requires a large number of data, often hard to be retrieved, in particular for galaxies at high redshift.

In this thesis we consider various methods to select ETGs. Indeed, since galaxies in the projects presented are taken from different surveys, the same quantities used for the selection of ETGs are often not available for different catalogues. In particular, in Chapter 2 we will make use of a sample of galaxies, which we will refer to as the *fiducial sample*, identified by combining a selection in EW([O II]) with a morphological visual inspection, while the so-called *high-redshift sample* is composed by galaxies presented in other works selected in UVJ colours or in morphology. Concerning the fiducial sample, we will show also the results of our analysis adding a further selection based on UVJ colours.

In Chapter 3, we will select both observed and simulated ETGs adopting two different selection criteria: a method based on a cut in $g-r$ colours, and a method based on the locus of galaxies in the SFR–stellar mass plane.

Finally, in Chapter 4 we will focus our analysis on central galaxies (and not specifically on ETGs). However, as we will see in section 1.7, massive central galaxies tend to be ETGs.

1.6 The scaling relations of ETGs

In section 1.4 we have briefly described relations for some stellar population properties of ETGs. In the following we will introduce scaling relations involving structural and kinematic properties.

1.6.1 The Faber-Jackson relation

In the late 70's, the first empirical relation found for ETGs was the *Faber-Jackson relation* (Faber & Jackson, 1976). This relation links the central velocity dispersion to the magnitude M_B, or equivalently, to the luminosity so that

$$L \propto \sigma_0^{\beta}, \tag{1.4}$$

where $\beta \approx 4$. Although this relation, historically, was set as a single power-law, subsequent evidence for a more complex behaviour was found (e.g., Hyde & Bernardi, 2009b). In fact, while low-luminosity ETGs tend to be better reproduced by $\beta \approx 3$, the high-luminosity tail show a steeper correlation, with $\beta \approx 5$. The Faber-Jackson relation, as well as the Tully-Fisher relation (Tully & Fisher, 1977)

for spirals – where the circular velocity takes the role of the velocity dispersion –, show a correlation between a kinematic property of galaxies and luminosity. Such correlations are not necessarily satisfied by a stationary stellar systems and thus contains precious information on the galaxy formation and evolution processes.

1.6.2 The Kormendy relation

Just one year after the discovery of the Faber-Jackson relation, another empirical law, the *Kormendy relation*, connecting the effective radii $R_{\rm e}$ of ETGs to their surface brightness at that radius, $I_{\rm e}$, was found (Kormendy, 1977). The Kormendy relation can be formulated also in terms of the effective surface brightness $\bar{I}_{\rm e} = L/(2\pi R_{\rm e}^2)$, which is the average surface brightness within $R_{\rm e}$. Converting $\bar{I}_{\rm e}$ into luminosity, we obtain

$$L \propto R_{\rm e}^{\alpha}, \tag{1.5}$$

with $0.6 \lesssim \alpha \lesssim 0.7$ (for instance in the r band).

The Kormendy relation indicates that within the effective radius, very luminous galaxies have lower surface brightness than low-luminosity galaxies, implying a lower average stellar density for the more luminous systems.

1.6.3 The Fundamental Plane of ETGs

Soon after the discovery of the Faber-Jackson and the Kormendy relations, both laws were found to be just two projections of a plane in parameter space where ETGs lie: the *Fundamental Plane* (Djorgovski & Davis, 1987; Dressler et al., 1987). In the 3D parameter space $(\log R_{\rm e};\ \log \sigma_0; \log \bar{I}_{\rm e})$, the Fundamental Plane can be expressed as

$$\log R_{\rm e} \equiv \alpha \log \sigma_0 + \beta \log \bar{I}_{\rm e} + const, \tag{1.6}$$

where generally $1 \lesssim \alpha \lesssim 1.4$ and $-0.9 \lesssim \beta \lesssim -0.75$, depending on the photometric band adopted for observations. A 3D visualisation of the Fundamental Plane for the near-infrared sample of ETGs in the 6-degree Field Galaxy Survey (6dFGS; Jones et al., 2004, 2005, 2009) is displayed in Figure 1.7.

The Fundamental Plane shows a smaller intrinsic scatter (around $15\%\, R_{\rm e}$) with respect to its projections, the Faber-Jackson and the Kormendy relations. It must

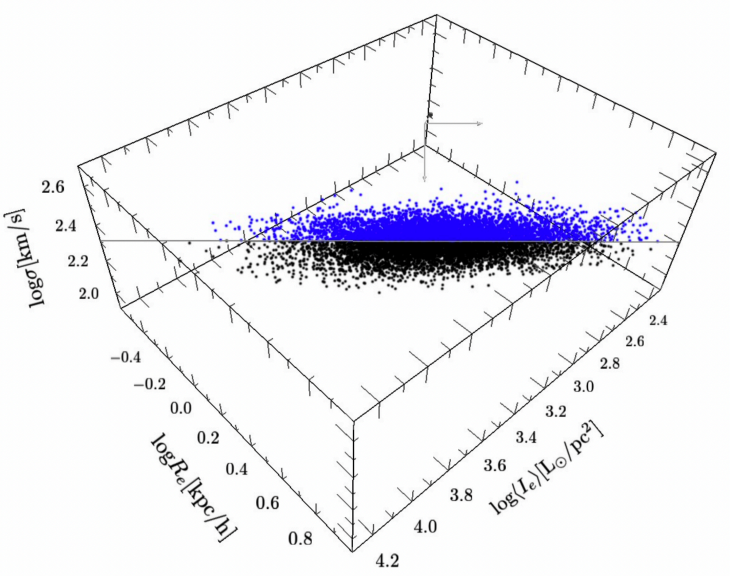

Fig. 1.7: The Fundamental Plane of galaxies from the 6dFGS. Blue and black dots trace galaxies above and below the best-fitting plane, respectively. This plot is taken from Magoulas et al. (2012).

be underlined that ETGs sharing the same position in the edge-on view of the Fundamental Plane, do not necessarily have the same positions on the Faber-Jackson and the Kormendy projections.

The location of an ETG in the space $(R_{\rm e}; \sigma_0; \bar{I}_{\rm e})$ depends on various properties, such as stellar density distribution, stellar velocity distribution, stellar M_*/L and relative distributions of dark and luminous matter. The properties of the observed Fundamental Plane are usually interpreted so that ETGs with higher luminosities have higher mass-to-light ratios and also a higher fraction of dark matter. These differences lead to variations of properties like metallicity and age, as we have seen in section 1.4.

A more detailed description of the Fundamental Plane is provided in Binney & Merrifield (1998), Binney & Tremaine (2008), and Cimatti, Fraternali, & Nipoti (2019).

1.6.4 The evolution of the structural and kinematic properties of ETGs

With the advent of newest technologies and surveys that observe galaxies at higher redshifts, it is possible to extend the analysis of scaling relations looking for evidence

for their evolution. Indeed going towards high redshift, the effective radius of ETGs of given stellar mass is found to reduce, on average, even by a factor of around $2-3$, implying that galaxies today tend to be less compact than galaxies of similar stellar mass at high redshift (e.g., Trujillo et al. 2006; van der Wel et al. 2008; Cimatti, Nipoti, & Cassata 2012). In the last decades the stellar mass–size relation of galaxies at different redshift has been largely studied (e.g. Ferguson et al., 2004; van der Wel et al., 2014; Damjanov et al., 2019). In Figure 1.8, the stellar mass–size relation studied by van der Wel et al. (2014) for the 3D-HST+CANDELS composite-sample of galaxies in six redshift bins for both ETGs and LTGs is shown.

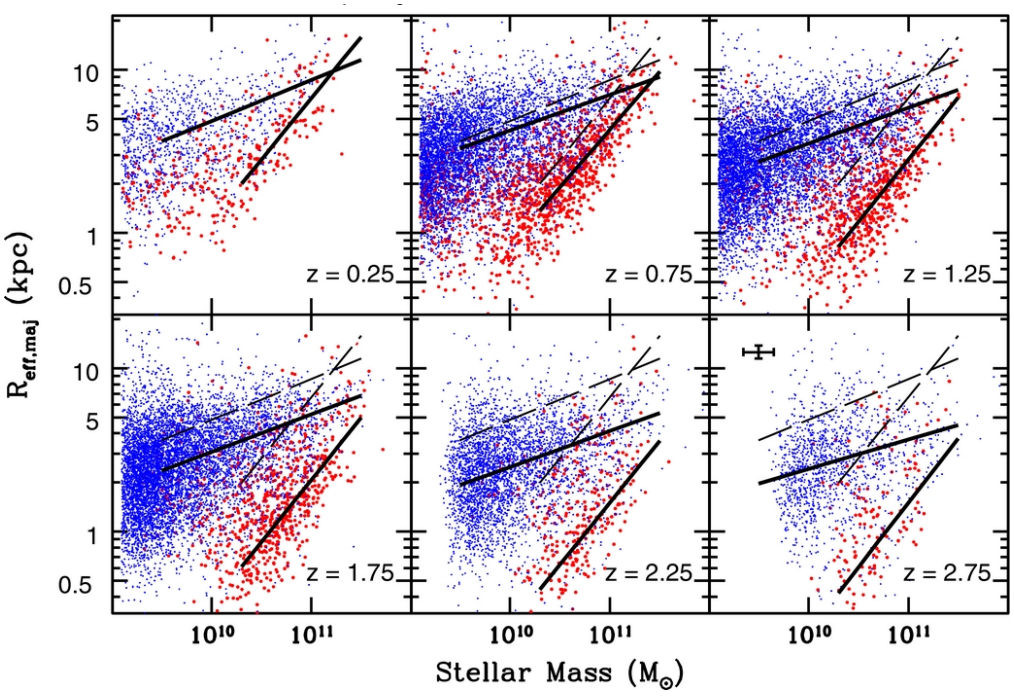

Fig. 1.8: The stellar mass–size relation in six redshift bins for ETGs (red dots) and LTGs (blue dots) from the 3D-HST+CANDELS composite-sample. This plot is taken from van der Wel et al. (2014).

As clearly visible, for both galaxy populations, at fixed stellar mass, galaxies at $z \approx 0$ are more extended than those at $z \approx 3$.

Analogously, the velocity dispersion of ETGs of given stellar mass is found to evolve with redshift (e.g., Cenarro & Trujillo 2009, van de Sande et al. 2011; Oser et al. 2012). In Figure 1.9, a plot from Oser et al. (2012) showing the evolution of the velocity dispersion as a function of redshift is reported. It is clear that, at a given stellar mass (in this plot, $\approx 10^{11}\,M_\odot$), the velocity dispersions of ETGs systematically decrease going towards $z = 0$.

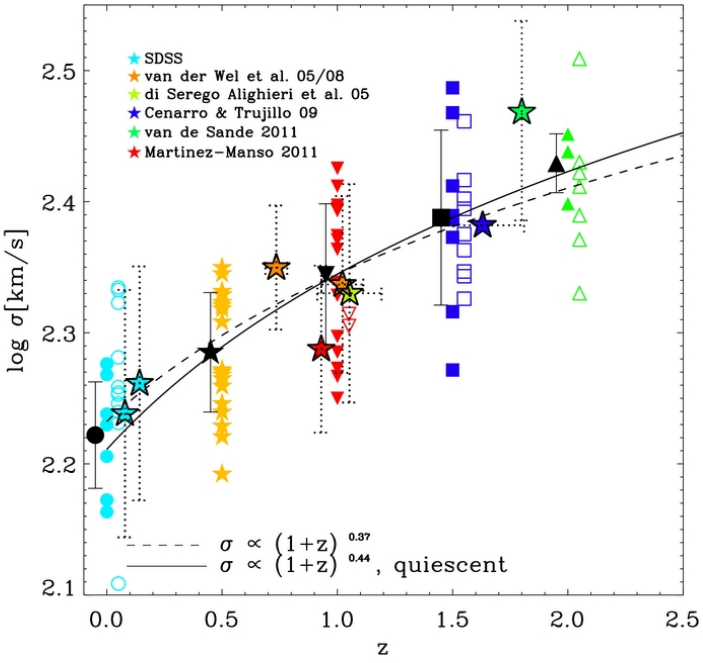

Fig. 1.9: The central projected velocity dispersion as a function of redshift for observed and simulated galaxies with $M_* \approx 10^{11}\,\mathrm{M}_\odot$ from Oser et al. (2012). Solid symbols trace star-forming galaxies, while empty symbols represent quiescent galaxies. The black curves show the result of a power-law fit for all (dashed curve) and the quiescent (solid curve) galaxies, respectively. Adapted from Oser et al. (2012).

However, unlike the estimates of galaxy sizes, measuring velocity dispersion is very demanding and requires high-resolution spectroscopic observations. Hence, it is more difficult to study the evolution of scaling relations that involve velocity dispersion as the stellar mass–velocity dispersion relation or the stellar mass Fundamental plane. In Chapter 2, we will present our state-of-the-art study of the evolution of the $M_*{-}\sigma_0$ relation for ETGs from the present-day Universe out to $z \approx 2.5$, making use of different galaxy samples in the literature.

1.7 The role of the environment for ETGs

One of the most relevant factors to be taken into account when considering galaxies and their evolution is the environment. Depending on the properties of the regions of the Universe where galaxies are located, the interaction with other galaxies as well as with the surrounding medium can alter dramatically the evolution of individual objects.

Defining which is the environment of a galaxy basically means understanding how other galaxies are located with respect to that galaxy. In this sense, we can identify three types of environment for galaxies:

- *Field galaxies* are isolated objects almost alone, sometimes in cosmic voids, that are rarely surrounded by smaller satellites;

- *Galaxy Groups* consist of aggregations of few tens of galaxies ($\lesssim 50$ members) with size of around $1\,\mathrm{Mpc}$, velocity dispersion $\lesssim 500\,\mathrm{km\,s^{-1}}$, and virial mass[3] at most of $10^{14}\,\mathrm{M_\odot}$;

- *Galaxies Clusters* are systems larger than Groups, even containing up to around 1000 galaxies, with size $\gtrsim 1\,\mathrm{Mpc}$, virial masses $\gtrsim 10^{14}\,\mathrm{M_\odot}$ and velocity dispersions of $\approx 10^{3}\,\mathrm{km\,s^{-1}}$.

One of the most relevant environmental effects is the so-called *morphology–density relation* (Dressler, 1980). This relation is an observationally determined connection between the environment in which galaxies are found (specifically, the density of the environment, i.e. the number of galaxies per unit volume) and the Hubble morphological type (see section 1.1). In Figure 1.10, the morphology–density relation found by Dressler (1980) for more than 6000 galaxies in 55 clusters is illustrated.

As found by Dressler (1980), this study revealed that the fraction of ETGs is higher in denser environments. In particular, the percentage of ETGs can reach even $80{-}90\,\%$ in the densest galaxy clusters, while spirals and irregulars dominate in the field. Since ETGs populate the red sequence in the colour–mass plane (section 1.3), densest environments are mainly dominated by red galaxies (see Balogh et al., 2004).

We have seen that the most luminous and massive galaxies tend to be ETGs. In particular, some of the most massive and luminous galaxies in the Universe are those located in the densest environments: they are giant ETGs sitting in the centres of clusters. These galaxies are called *brightest cluster galaxies* (BCGs). BCGs are characterised by luminosities higher than $10^{12}\,\mathrm{L_\odot}$. Their total mass can be as high as $\approx 10^{13}\,\mathrm{M_\odot}$. Naturally, because of their central location in clusters and their properties, BCGs are expected to be the culmination of a hierarchical assembly scenario characterised by several mergers.

[3] The *virial mass* is the integrated mass of a galaxy within a sphere of radius equal to the *virial radius*, i.e. the radius within which the system is virialised.

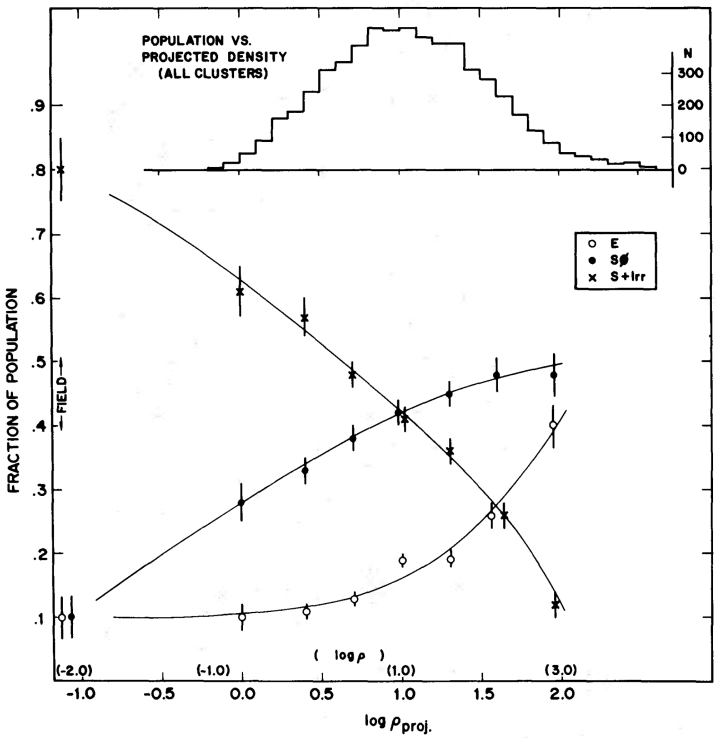

Fig. 1.10: The morphology–density relation for more than 6000 galaxies in 55 clusters. The fraction of galaxies as a function of the projected galaxy density $\rho_{\rm proj}$ (or the 3D density ρ) is shown for ellipticals E (open dots), lenticulars S0 (filled dots), and spiral + irregular (crosses). This plot is taken from Dressler (1980).

1.8 The merger-driven evolution of ETGs

So far, we have seen that massive ETGs are, on average, composed by red, metal-rich and old stellar populations. They are preferentially located in central regions of overdensities like groups and clusters and they obey scaling relations that involve structural, kinematic and stellar population properties. Now, we try to address the question of how they formed and why their properties evolve through cosmic time.

One of the most significant results that astrophysicists reached about galaxy formation and evolution, using both observations and simulations, is that galaxies collide and merge, forming new galaxies whose masses, sizes, shapes and other properties inevitably depend on how these mergers happen. The *galaxy merging* is a process in which two or more galaxies form a new galaxy. There are several aspects to be taken into account when galaxies interact. For instance, if the encounter occurs at high speed, usually called *high-speed encounter* or *fly-by*, the result is just a perturbation. Instead, if two (or more) systems interact with sufficiently low relative speed, they end up forming a single new object.

Mergers can be categorised under different points of view. For instance, by the number of galaxies (usually called *progenitors*) involved in the merger, we can distinguish *binary mergers*, when only two progenitors take part to the merger, or *multiple mergers*, when three or more progenitors are involved. Concerning the relative masses of progenitors, we can distinguish between *minor mergers* and *major mergers*, by defying the *merger mass ratio*

$$\zeta = \frac{M_1}{M_2}, \tag{1.7}$$

where M_1 and M_2 are the mass of the two progenitors, and $M_1 \leq M_2$. In the literature, we commonly refer to merger as minor when $\zeta \lesssim 1/3$, otherwise, we refer to a major merger. Another classification for mergers depends on the presence (or not) of gas in the progenitors. Specifically, we talk about *wet mergers* (or *dissipative mergers*) when at least one of the two progenitors has a relatively high content of gas (usually, blue and star forming galaxies). Instead, two progenitors that are gas-poor systems (so, basically formed by dark matter and stars) produce a *dry merger* (or *dissipationless merger*).

Concerning ETGs, it is commonly believed that they are the results of a building-up process composed by two phases: in a first phase, galaxies at high redshift formed their stars *in situ*, while later, stars formed in other galaxies, i.e. *ex situ*, were accreted onto the main progenitor in a stellar assembly history mainly marked by dry mergers.

When comparing observations with theoretical models, it is useful to estimate the *merger rate* Γ of galaxies, i.e. the number of mergers per unit of time per unit of volume. The merger rate can be estimated from observations as

$$\Gamma = \frac{n_{\rm merger}}{\tau_{\rm merger}}, \tag{1.8}$$

where $n_{\rm merger}$ is the number of mergers per unit of volume and $\tau_{\rm merger}$ is the merging timescale. The value of $n_{\rm merger}$ is inferred from observations by counting objects that show typical signatures of interactions, such as tidal disruption and disturbed morphologies, or by counting the close pairs per volume expected in mergers. About $\tau_{\rm merger}$, it is assumed based on theoretical models.

Moreover, we can define another related quantity, the *fractional merger rate*

$$\mathcal{R}_{\rm merger} = \frac{f_{\rm merger}}{\tau_{\rm merger}}, \tag{1.9}$$

where $f_{\rm merger} = n_{\rm merger}/n_{\rm galaxy}$ as the fraction of galaxies involved in merging and $n_{\rm galaxy}$ the total number density of galaxies. In the present-day Universe, reference values are $f_{\rm merger} \approx 0.01$, and $\mathcal{R}_{\rm merger} \approx 0.02\,{\rm Gyr}^{-1}$, for the latter assuming as timescale $\tau_{\rm merger} \approx 0.5\,{\rm Gyr}$ (for more details, see to Cimatti, Fraternali, & Nipoti 2019).

1.8.1 The two-phase formation scenario of ETGs

The ETGs that we observe in the present-day Universe are usually referred to as *red and dead galaxies*, because of their colours and the lacking formation of new stars. The theory of the formation of ETGs is not fully understood, and sometimes is still controversial. However, it is almost accepted that ETGs are the outcome of a growth that happens in two steps, usually called *the two-phase formation scenario of ETGs* (see Naab et al., 2009; Oser et al., 2010; Hilz et al., 2013). Specifically, the most massive ETGs, usually belonging to the slow-rotator type (see Emsellem et al., 2004; Cappellari et al., 2007; Emsellem et al., 2007; Cappellari, 2016), are located into very massive halos ($M_{\rm vir} \gtrsim 10^{13}\,{\rm M}_{\odot}$), occupying the innermost parts of overdense regions like groups and clusters of galaxies (see section 1.7). At $z \gtrsim 2$, central galaxies are fed by streams of cold gas following the paths traced by filaments, experiencing several episodes of star formation. Regardless of the specific mechanisms that trigger star formation in galaxies, the first phase of the formation of ETGs is the *in situ* formation, i.e. stars formed as a consequence of a collapse of gas within the central galaxy.

At $z \lesssim 2$, however, the star formation within the central galaxy becomes highly inefficient because of the gradual consumption of the cold gas and the inefficiency of cold gas accretion. Hence, this second phase of ETG formation is mainly characterised by dry mergers, where stars formed *ex situ* are accreted onto the main progenitor. Star formation is negligible during the merger because of the scarcity of cold gas, so the merger remnant is basically a galaxy whose stellar mass is the sum of the stellar mass of its progenitors.

In Figure 1.11, the average fraction of the stellar mass formed in situ and ex situ as predicted by the hydrodynamical cosmological simulation presented in Oser et al. (2010) is shown as a function of redshift for massive ETGs: the transition at $z \approx 2$ is apparent.

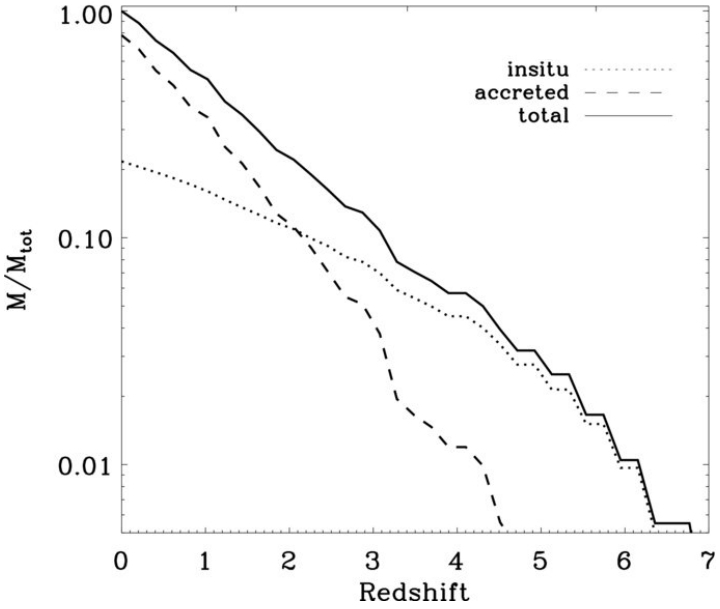

Fig. 1.11: The average stellar mass contents for the in-situ and ex-situ stellar populations (normalised to the total stellar mass at $z = 0$) as a function of redshift for massive ETGs (with virial masses of $12.7 \lesssim \log(M_{200}/\mathrm{M}_{\odot}) \lesssim 13.4$) in a cosmological hydrodynamical simulation. This is an adapted version of a plot taken from Oser et al. (2010).

1.9 Thesis structure

This Ph.D. thesis is mainly devoted at studying the merger-driven evolution of ETGs, how their stellar populations and scaling relations evolve through cosmic time, as well as looking for a new method for possibly deriving the dark matter mass in observed galaxies. In the following, the structure of this thesis is summarised.

- **The cosmic evolution of the stellar mass–velocity dispersion relation of early-type galaxies**

  In Chapter 2, we will present the first systematic study in the literature that traces the back-in-time evolution of the stellar mass–velocity dispersion relation in ETGs, performed by adopting a Bayesian hierarchical formalism.

- **The role of in-situ and ex-situ star formation in early-type galaxies: MaNGA versus IllustrisTNG**

  In Chapter 3, we will illustrate a comparison of the radial distributions of stellar properties such as the stellar metallicity and age, between observed ETGs in the MaNGA survey and simulated galaxies in the IllustrisTNG simulation suite, providing an explanation for these profiles in terms of stars formed in situ and ex situ.

- **Inferring the Dark Matter halo mass in galaxies from other observables with Machine Learning**

  In Chapter 4, we will show some preliminary results on a study intended to train a model with a state-of-the art machine learning technique, exploiting simulated galaxies from IllustrisTNG, whose main scope will be to derive a functional form for estimating the DM mass of halos that surround observed galaxies in the Universe.

- **Conclusions & Future Perspectives**

  Finally, in Chapter 5, we will sum up the results derived from the three projects above mentioned, discussing their main implications, and we will also present our future plans to pursue and extend the analysis carried out so far.

2 The cosmic evolution of the stellar mass–velocity dispersion relation of early-type galaxies

> *All truths are easy to understand once they are discovered; the point is to discover them.*
>
> — **Galileo Galilei**

In this Chapter, the first systematic study in literature concerning the evolution of the stellar mass–velocity dispersion relation in early-type galaxies is presented. The content of this Chapter is drawn from ***Cannarozzo, Sonnenfeld, & Nipoti (2020a)*** and ***Cannarozzo et al. (2020b)***.

2.1 Introduction

Since the late 1970s it was found empirically that present-day early-type galaxies (ETGs) follow scaling relations, i.e. correlations among global observed quantities, such as the Faber-Jackson relation (Faber & Jackson, 1976) between luminosity L and central stellar velocity dispersion σ_0, the Kormendy relation (Kormendy, 1977) between effective radius R_e and surface brightness (or luminosity), and the fundamental plane (Djorgovski & Davis, 1987; Dressler et al., 1987) relating σ_0, L and R_e. When estimates of the stellar masses are available, analogous scaling relations are found, replacing L with M_*: the M_*–R_e (stellar mass–size) relation, the M_*–σ_0 (stellar mass–velocity dispersion) relation and the stellar-mass fundamental plane (e.g., Hyde & Bernardi, 2009b; Auger et al., 2010; Zahid et al., 2016a). These scaling laws are believed to contain valuable information on the process of formation and evolution of ETGs. Any successful theoretical model of galaxy formation should reproduce these empirical correlations of the present-day population of ETGs (Somerville & Davé, 2015; Naab & Ostriker, 2017).

The observations strongly indicate that ETGs are not evolving passively. For instance, measurements of sizes and stellar masses of samples of quiescent galaxies at higher redshift imply that the M_*–R_e relation evolves with time: on average, for given stellar mass, galaxies were significantly more compact in the past (e.g. Ferguson et al., 2004; Damjanov et al., 2019). There are also indications that ETGs at higher redshift have, on average, higher stellar velocity dispersion than present-day ETGs of similar M_* (e.g. van de Sande et al., 2013; Belli et al., 2014a; Gargiulo et al., 2016; Belli et al., 2017; Tanaka et al., 2019). Interestingly, the stellar-mass fundamental plane, relating M_*, σ_0 and R_e appears to change little with redshift (Bezanson et al., 2013b, 2015; Zahid et al., 2016b). The observed behaviour of these scaling relations as a function of redshift represents a further challenge to models of galaxy formation and evolution. Furthermore, some studies in the literature discuss about the presence of a curvature in the scaling relations of ETGs (e.g., Hyde & Bernardi, 2009a; Bernardi et al., 2011a,b). In particular, the most massive ETGs have larger sizes, smaller velocity dispersions, and fainter surface brightnesses than what expected in the absence of curvature. In particular, Bernardi et al. (2011a,b) found that the M_*–R_e, M_*–b/a, M_*–colour and M_*–colour gradients scaling relations show a curvature, compatible with a scenario in which ETGs with $\log(M_*/\mathrm{M}_\odot) \gtrsim 11.3$ are subject to a recent stellar mass assembly history dominated by dry major mergers.

In the standard cosmological framework, structure formation in the Universe occured as a consequence of the collapse and virialisation of the dark matter halos, in which baryons infall and collapse, thus forming galaxies. Massive ETGs are believed to be the end products of various merging and accretion events. Given the old ages of the stellar populations of present-day ETGs, any relatively recent merger that these galaxies experienced must have had negligible associated star formation. Based on these arguments, a popular scenario for the late ($z \lesssim 2$) evolution of ETGs is the idea that these galaxies grow via dissipationless (or "dry") mergers. Interestingly, dry mergers make galaxies less compact: for instance, galaxies growing via parabolic dry merging increase their size as $R_\mathrm{e} \propto M_*^a$, with $a \gtrsim 1$, while their velocity dispersion evolves as $\sigma_0 \propto M_*^b$, with $b \lesssim 0$ (Nipoti, Londrillo, & Ciotti, 2003; Naab, Johansson, & Ostriker, 2009; Hilz, Naab, & Ostriker, 2013). Thus, the transformation of individual ETGs via dry mergers is a possible explanation of the observed evolution of the M_*–R_e, M_*–σ_0 and stellar-mass fundamental plane relations (Nipoti et al., 2009a, 2012; Oogi & Habe, 2013; Posti et al., 2014; Frigo & Balcells, 2017). Though this explanation is qualitatively feasible, it is not clear whether and to what extent dry mergers can explain quantitatively the observed evolution of these scaling laws. In this context, the stellar velocity dispersion σ_0 is a very interesting quantity to consider. Even for purely dry mergers of spheroids, σ_0 can increase, decrease of

stay constant following a merger, depending on the merger mass ratio and orbital parameters (Boylan-Kolchin et al., 2006; Naab et al., 2009; Nipoti et al., 2009b, 2012; Posti et al., 2014). Moreover, even slight amounts of dissipation and star formation during the merger can produce a non-negligible increase of the central stellar velocity dispersion with respect to the purely dissipationless case (Robertson et al., 2006; Ciotti et al., 2007).

In a cosmological context, the next frontier in the theoretical study of the scaling relations of ETGs is the comparison with observations of the evolution measured in hydrodynamic cosmological simulations. A quantitative characterisation of the evolution of the observed scaling relations of the ETGs is thus crucial to use them as test beds for theoretical models. On the one hand, the evolution of the observed stellar mass–size relation is now well established, being based on relatively large samples of ETGs out to $z \approx 3$ (Cimatti, Nipoti, & Cassata 2012; van der Wel et al. 2014). On the other hand, given that measuring the stellar velocity dispersion requires spectroscopic observations with relatively high resolution and signal-to-noise ratio, the study of the redshift evolution of correlations involving σ_0, such as the M_*–σ_0 relation and the stellar-mass fundamental plane, is based on much smaller galaxy samples than those used to study the stellar mass–size relation. This makes it more difficult to characterise quantitatively the evolution of these scaling laws out to significantly high redshift.

In this Chapter, we focus on the stellar mass–velocity dispersion relation of ETGs with the aim of improving the quantitative characterisation of the observed evolution of this scaling law. We build an up-to-date sample of massive ETGs with measured stellar mass and stellar velocity dispersion by collecting and homogenising as much as possible available state-of-the-art literature data. In particular, we consider galaxies with stellar masses higher than $10^{10.5}\,\mathrm{M}_\odot$ and we correct the observed stellar velocity dispersion to σ_e, the central line-of-sight stellar velocity dispersion within an aperture of radius R_e, so in our case $\sigma_0 = \sigma_\mathrm{e}$. We analyse statistically the evolution of the M_*–σ_e relation without resorting to binning in redshift and using a Bayesian hierarchical approach. As a result of this analysis we provide the posterior distributions of the hyper-parameters describing the M_*–σ_e relation in the redshift range $0 \lesssim z \lesssim 2.5$, under the assumption that, at given redshift, $\sigma_\mathrm{e} \propto M_*^{\beta}$. We explore both the case of redshift independent β and the case in which β is free to vary with redshift.

The Chapter is organised as follows. Section 2.2 describes the galaxy sample and the criteria adopted to select ETGs. We present the statistical method in section 2.3 and our results in section 2.4. Our results are discussed in section 2.5. Section 2.6

concludes. Throughout this Chapter, we adopt a standard Λ cold dark matter cosmology with $\Omega_{\rm m} = 0.3$, $\Omega_\Lambda = 0.7$ and $H_0 = 70\,{\rm km\,s^{-1}Mpc^{-1}}$. All stellar masses are calculated assuming a Chabrier (2003) initial mass function (IMF).

2.2 Galaxy sample

To study the evolution of the stellar mass–velocity dispersion relation of ETGs we build a sample of galaxies consisting in a collection of various subsamples of ETGs in the literature. Our definition of what constitutes an ETG is based mainly on morphology, with the addition of cuts on emission line equivalent width of [O II] aimed at removing star-forming galaxies (as explained in the rest of this section). Our goal is to build a sample spanning a redshift range as large as possible. At the same time, in order to make an accurate inference, it is important to 1) select galaxies and measure their stellar mass and velocity dispersion in a homogeneous way and 2) ensure that, at any given redshift and stellar mass, our selection criteria do not depend, either directly or indirectly, on velocity dispersion. With our main focus on accuracy, we first define a *fiducial sample* of galaxies, for which conditions 1) and 2) above are satisfied. We drew our fiducial sample from the Sloan Digital Sky Survey (SDSS; Eisenstein et al., 2011) and the Large Early Galaxy Astrophysics Census (LEGA-C; van der Wel et al., 2016). For the galaxies in this sample we strictly apply consistent selection criteria and measure their stellar masses using photometric data from the first data release of the Hyper Suprime-Cam (HSC; Miyazaki et al., 2018) Subaru Strategic Program (Aihara et al., 2018, DR1). The two surveys cover the redshift range $0 \lesssim z \lesssim 1$ and, most importantly, have well defined selection functions, which is critical to meet condition 2).

We then define a second *high-redshift* sample, consisting of stellar mass and velocity dispersion measurements of galaxies at $0.8 \lesssim z \lesssim 2.5$ from various independent studies. For the galaxies in this high-redshift sample, we only require that the definitions of stellar mass and stellar velocity dispersion are the same as those of the fiducial sample. We also define an *extended* sample, obtained by combining the fiducial and high-redshift samples. In building our samples, we include only galaxies with stellar mass higher than a minimum mass $M_{*,\rm min}$, which in general depends both on the survey and on z (see subsection 2.2.1 and subsection 2.2.2): in all cases $M_{*,\rm min} \geq 10^{10.5}{\rm M}_\odot$, which we adopt as absolute lower limit in stellar mass.

Our strategy is to carry out our inference on both the fiducial and the extended samples. Given the way the samples are built, we expect our results at $z < 1$ to

be more robust (i.e. less prone to observational biases), but it is nevertheless very interesting to examine trends out to $z \approx 2.5$, as probed by our extended sample. In the following two subsections we describe in detail how measurements for these samples are obtained.

2.2.1 The fiducial sample

Our fiducial sample consists of two sets of galaxies. The first set is drawn from the data release 12 (DR12; Alam et al., 2015) of the SDSS. In particular, we consider only objects belonging to the main spectroscopic sample (Strauss et al., 2002), which was built using observations up to SDSS DR7. The second set is selected from the LEGA-C survey DR2 (Straatman et al., 2018). The LEGA-C DR2 contains spectra of 1,922 objects obtained with the Visible Multi-Object Spectrograph (VIMOS; Le Fèvre et al., 2003) on the Very Large Telescope (VLT). LEGA-C targets were selected by applying a cut in $K_{\rm s}$-band magnitude to a parent sample of galaxies with photometric redshift in the range $0.6 < z < 1.0$ drawn from the Ultra Deep Survey with the VISTA telescope (UltraVISTA; Muzzin et al., 2013a).

ETG selection

As anticipated, our definition of ETG is based mostly on morphology. For the morphological classification we opted for visual inspection because the number of galaxies of our sample is relatively small. Valid alternatives, which are necessarily preferable for larger data sets, are automated morphological classification algorithms (e.g. Domínguez Sánchez et al. 2018). Before the visual inspection, we applied a pre-selection based on star formation activity: we removed star-forming galaxies from our sample, under the assumption that they are mostly associated with a late-type or irregular morphology. We relied on the presence of emission lines in the spectra of our galaxies as an indicator of star formation activity. In particular, we applied a selection based on the equivalent width of the forbidden emission line doublet of [O II], $\mathrm{EW}([\mathrm{O\,II}])\ \lambda\lambda 3726, 3729$: we included only those galaxies that have $\mathrm{EW}([\mathrm{O\,II}]) \geq -5\,\text{Å}$, where $\mathrm{EW}([\mathrm{O\,II}])$ of SDSS and LEGA-C galaxies are obtained from the respective data release catalogues. Although [O II] is not a perfect indicator of star formation activity, as it can suffer from contamination from emission by an active galactic nucleus, and other spectral lines could be used in its place (Hβ, for example), these lines are in general not accessible in the spectra of most LEGA-C galaxies, as they are redshifted outside the available spectral range. For the sake

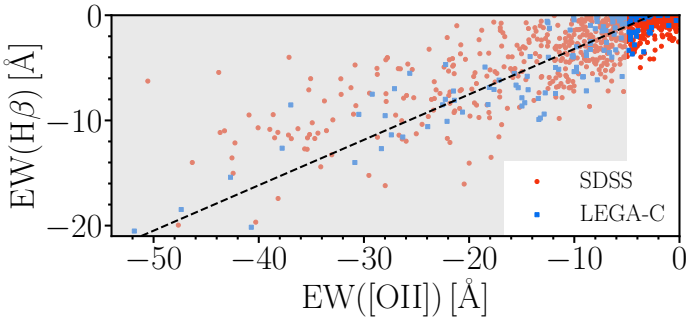

Fig. 2.1: Equivalent width of Hβ, EW(Hβ), as a function of equivalent width of [O II], EW([O II]), for galaxies drawn from the original catalogues of SDSS (circles) and LEGA-C (squares). For LEGA-C galaxies, we show only objects with signal-to-noise ratio > 10. The black dashed line represents a linear fit to the data. Galaxies in the shaded region of the diagram (EW([O II]) < -5 Å) are excluded from our sample of ETGs.

of homogeneity in our selection criteria, and in order to keep the high end of the redshift distribution of the LEGA-C galaxies in our sample, we used [O II] as a first step towards obtaining a sample of ETGs. Nevertheless, we found a good correlation between EW([O II]) and EW(Hβ) for those galaxies drawn from the original catalogues of SDSS and LEGA-C for which both measurements are available (see Figure 2.1).

Although half of the LEGA-C galaxies do not have values of EW([O II]) in the DR2 catalogue, these are for the most part objects at the low end of the redshift range, $z < 0.8$.

The second step in our selection is to include only galaxies with an early-type morphology, according to visual inspection. We used imaging data from the Wide layer of the HSC DR1, for this purpose. The Wide layer of HSC covers approximately 108 square degrees. The number of SDSS main sample galaxies present in this dataset is ≈ 2000, which, while only a small fraction of the total number of SDSS galaxies, is still sufficiently large to carry out a statistical analysis of the stellar mass–velocity dispersion relation. LEGA-C targets are located in a $\simeq 1.3\,\mathrm{deg}^2$ region, for the most part overlapping with the Cosmic Evolution Survey (COSMOS; Scoville et al., 2007) area. HSC DR1 data from the Ultra Deep layer are available for most (≈ 1700) of the objects in the LEGA-C DR2.

The motivation for using HSC data is in its high depth (i-band 26 mag detection limit for a point source in the Wide layer) and good image quality (typical i-band seeing is $0.6''$). This is particularly important for the LEGA-C galaxies, which are much fainter and have smaller angular sizes compared to the SDSS ones, due to their

higher redshift. For each galaxy with available HSC DR1 data, we obtained cutouts in the g, r, i, z and y filters, then visually inspected colour-composite RGB images made using the $g-, r-$ and $i-$band data. We removed objects showing any presence of discs, spiral arms, as well as galaxies for which a single Sérsic model (Sérsic, 1968) does not provide a qualitatively good description of the surface-brightness distribution (e.g., irregular galaxies). Such objects account for roughly 50% of the inspected galaxies. Examples of successful and unsuccessful Sérsic fits are shown in Figure 2.2 and Figure 2.3, respectively.

Additionally, a few percent of the objects were removed because of contamination from stars, and an even smaller fraction was eliminated because of the presence of close neighbours that make it difficult to carry out accurate photometric measurements. Although this last step could in principle introduce a bias in the inferred M_*–σ_e relation in case this varies as a function of environment, given the small fraction of objects with close neighbours removed, any such bias will in any case be very small.

In Figure 2.4 and Figure 2.5 we show colour-composite images of example sets of SDSS galaxies included and excluded from our sample on the basis of our morphological classification.

Photometric measurements

Our procedure for measuring stellar masses of the galaxies in the fiducial sample consisted in fitting stellar population synthesis models to broadband photometric data. Although photometric measurements for these galaxies are available from the literature, we chose to carry out new measurements using photometric data from the HSC survey. The data from the HSC survey are much deeper and have a much higher image quality compared to the SDSS data. This is important, because it allows for a cleaner detection and masking of foreground contaminants, and allows for a better characterisation of the faint extended envelope of massive galaxies (see e.g. Huang et al., 2018). Moreover, by using the same data and procedure to estimate the stellar masses of the galaxies in the SDSS and LEGA-C samples, our inference on the evolution of the M_*–σ_e relation is less prone to possible systematic effects related to the photometric measurements.

We estimated the g, r, i, z and y magnitudes of each galaxy by fitting a Sérsic surface brightness distribution to the data in these five bands simultaneously. In particular, we obtained 201×201 pixel ($\approx 34'' \times 34''$) sky-subtracted cutouts of each

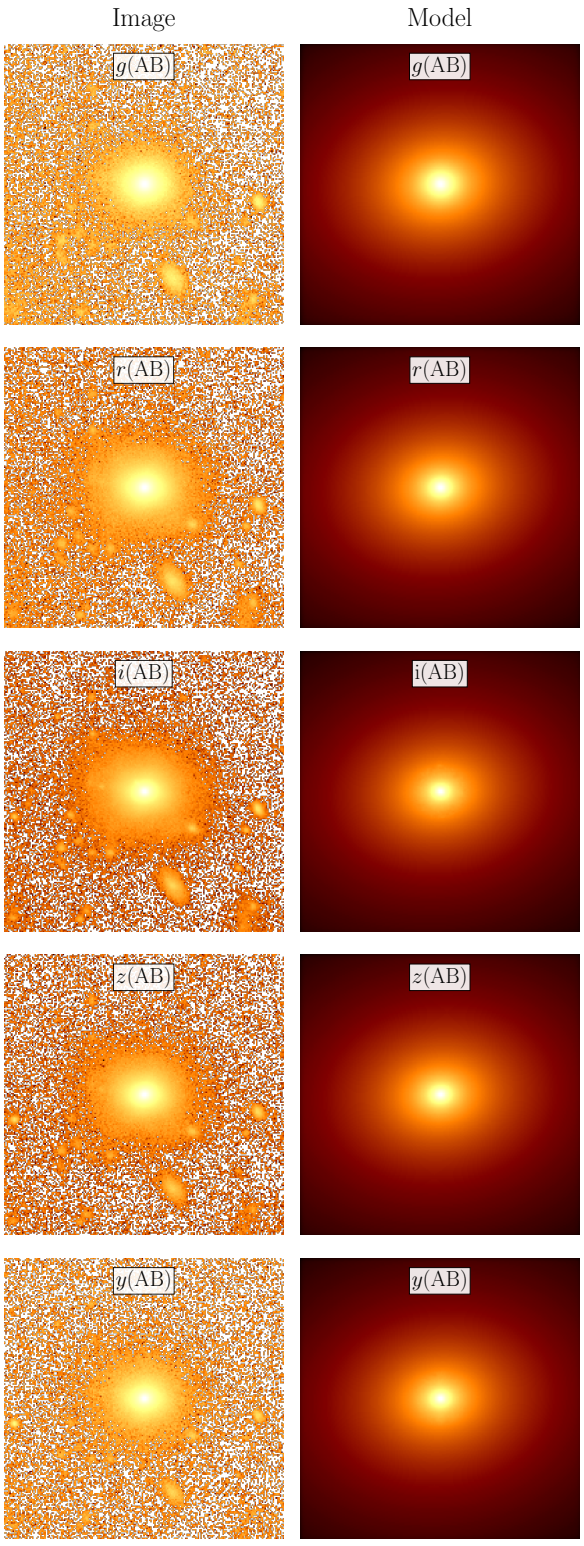

Fig. 2.2: A succesful case of Sérsic model in the g, r, i, z and y filters (from the top to the bottom) for one galaxy (HSC ID #42648136191078699) of the fiducial sample. Left panels show the original images of the galaxy in the five filters, while right panels illustrate the corresponding models.

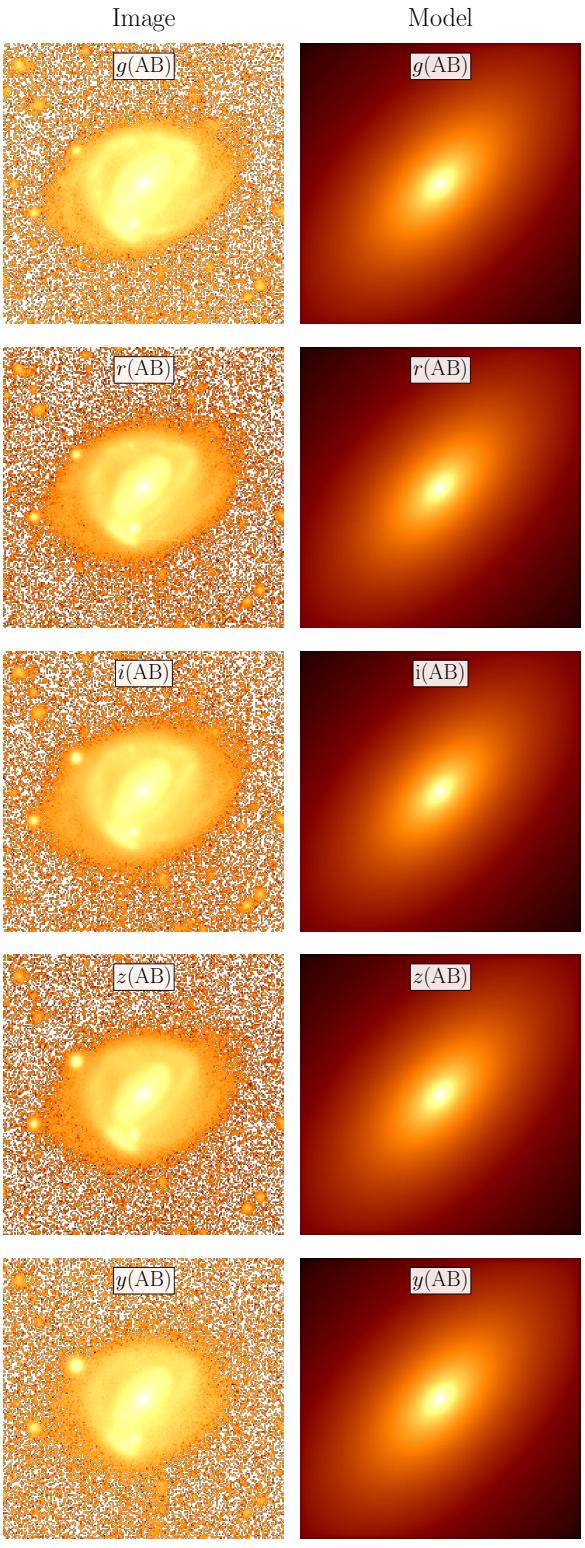

Fig. 2.3: Same as Figure 2.2, but for one galaxy (HSC ID #41214944259116180) of the fiducial sample for which the Sérsic fit is unsuccessful.

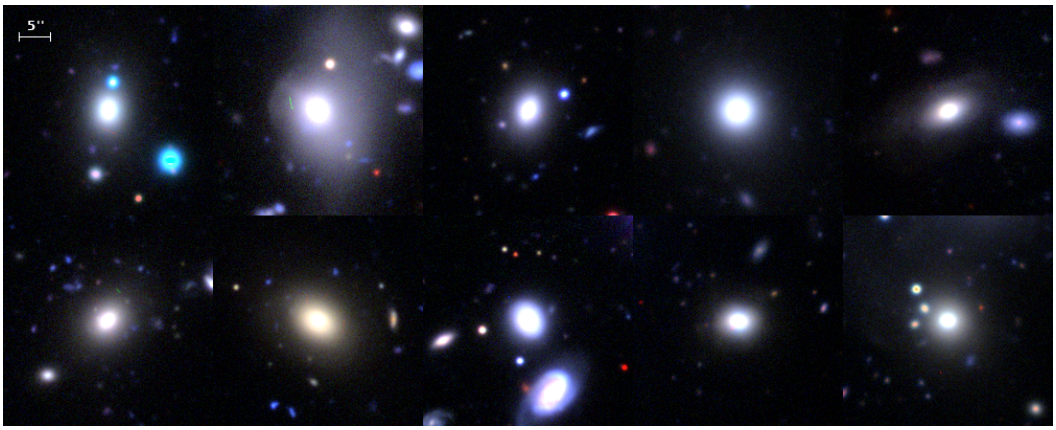

Fig. 2.4: Colour-composite HSC images of a set of SDSS main sample ETGs that passed our selection in EW([O II]) and our visual inspection.

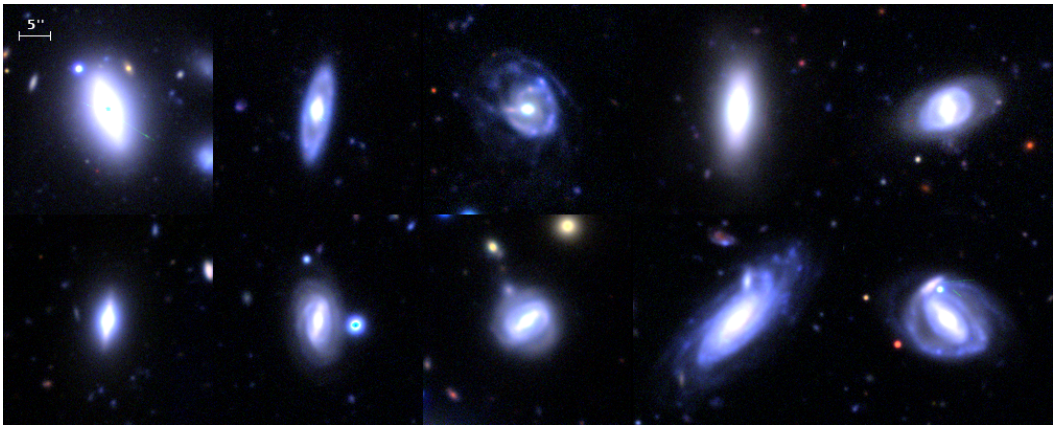

Fig. 2.5: Colour-composite HSC images of a set of SDSS main sample galaxies that passed our selection in EW([O II]), but were rejected in our visual inspection step, due to the presence of disks and/or spiral arms.

galaxy in each band, we fitted the five-band data simultaneously with a seeing-convolved Sérsic surface brightness profile with elliptical isophotes and spatially uniform colours, while iteratively masking out foreground or background objects using the software SExtractor (Bertin & Arnouts, 1996).

Saturated pixels were also masked, using the masks provided by HSC DR1. We added in quadrature a 0.05 magnitude systematic uncertainty to the observed flux in each band, to account for zero-point calibration errors in the HSC DR1 photometry, which have been shown to be on this order of magnitude or smaller (see Aihara et al., 2018).

An important data reduction step on which our measurements rely is the sky subtraction. We checked the robustness of the sky subtraction by repeating the analysis on a subset of galaxies, using the more recent data from the HSC data release 2[1] (DR2 Aihara et al., 2019). The HSC DR2 used a substantially different sky subtraction method, compared to the DR1 (see subsection 4.1 in Aihara et al., 2019). The corresponding difference in flux leads to an average difference of 0.03 dex on the stellar masses, with a 0.07 dex scatter. While the scatter is well within the observational uncertainty on the stellar mass, this bias is a potential systematic effect that is difficult to correct for and should in principle be taken into account in our global error budget. However, it does not affect the conclusions of our study: our main goal is to measure the slope and evolution of the M_*–σ_e relation, which are robust to overall shifts in the stellar mass measurements of the sample.

Stellar mass measurements

To infer stellar masses, we fitted the observed g, r, i, z and y fluxes with composite stellar population models. These were obtained using the BC03 stellar population synthesis (SPS) code (Bruzual & Charlot, 2003), with semi-empirical stellar spectra from the BaSeL 3.1 library (Westera et al., 2002), Padova 1994 stellar evolution tracks (Fagotto et al., 1994a,b,c) and a Chabrier IMF. We considered star formation histories with an exponentially declining star formation rate and we applied a prior on metallicity based on the mass–metallicity relation measured by Gallazzi et al. (2005). We sampled the posterior probability distribution of stellar mass, age (time since the initial burst of star formation), star formation rate decline timescale, metallicity and dust attenuation with a Markov Chain Monte Carlo (MCMC), following the method introduced by Auger et al. (2009). We then considered the posterior

[1]The HSC DR2 was released when the bulk of our analysis was complete.

probability distribution in log-stellar mass, marginalised over the other parameters, and approximated it as a Gaussian with mean equal to

$$\log M_*^{\rm obs} = \frac{\log M_*^{(84)} + \log M_*^{(16)}}{2} \tag{2.1}$$

and standard deviation

$$\sigma_{M_*} = \frac{\log M_*^{(84)} - \log M_*^{(16)}}{2}, \tag{2.2}$$

where $\log M_*^{(84)}$ and $\log M_*^{(16)}$ are the 84-th and 16-th percentile of the distribution, respectively. We refer to Sonnenfeld et al. (2019) for more details. In Appendix 2.A, we compare our estimates of stellar mass with those of Mendel et al. (2014, M14 hereafter) for the SDSS galaxies of our sample.

A complete sample

In order to accurately infer the M_*–$\sigma_{\rm e}$ relation, it is necessary that the selection criteria used to define our sample do not introduce spurious correlations between these two variables. A sufficient condition to achieve this is working with a sample that, at any given redshift, is highly complete in stellar mass, or is randomly drawn from a complete sample. For the SDSS sample, we achieved this condition by first estimating, at each redshift z, the minimum stellar mass above which our sample is 99% complete, $M_{*,\rm min}(z)$, and then removing from the sample all galaxies with stellar mass below this value. To estimate $M_{*,\rm min}(z)$ of the SDSS sample we proceeded as follows. The SDSS main sample, from which our galaxies are drawn, is complete down to an $r-$band Petrosian magnitude $r_{\rm P}$ of 17.77 (Strauss et al., 2002). At any redshift, this value of $r_{\rm P}$ corresponds to a range of values of the stellar mass, with a spread that is due to scatter in the stellar mass-to-light ratio and to a mismatch between the definition of Petrosian and Sérsic magnitudes. We can nevertheless define the ratio between the observed stellar mass and the observed-frame SDSS $r-$band Petrosian luminosity L_r and consider its distribution $\mathrm{P}(M_*/L_r)$. We then made narrow redshift bins and, approximating $\mathrm{P}(M_*/L_r)$ as a Gaussian, used the mean and standard deviation of the sample of M_*/L_r values in each bin to find the 99-th percentile of this distribution, $M_*/L_r|_{99}$. Finally, we obtained $M_{*,\rm min}(z)$ by multiplying $M_*/L_r|_{99}$ by the Petrosian luminosity corresponding to the limiting value $r_{\rm P} = 17.77$.

In Figure 2.6, we illustrate an application of this procedure on three redshift bins: in the upper panel, we show values of stellar mass as a function of $r_{\rm P}$, while in the

lower panel we show the corresponding distributions in M_*/L_r. The 99-th percentile of the $\mathrm{P}(M_*/L_r)$ distribution and the corresponding value of $M_{*,\mathrm{min}}(z)$ are shown as dashed lines in the two panels.

We estimated $M_{*,\mathrm{min}}(z)$ in a series of bins in the redshift range $0.05 < z < 0.20$. Outside this interval, the number of galaxies per redshift bin becomes small, and it is more difficult to obtain an accurate estimate of $M_{*,\mathrm{min}}$. We therefore only included SDSS galaxies in this redshift range, with a stellar mass larger than the value of $M_{*,\mathrm{min}}$ at the corresponding redshift. We approximated the function $M_{*,\mathrm{min}}(z)$ as a quadratic polynomial for this purpose. In the upper panel of Figure 2.7, we show the initial distribution in stellar mass as a function of redshift of our SDSS main sample ETGs composed by 2127 sources (grey dots), as well as the final sample (black dots), which consists of 413 objects, obtained after applying the cut in stellar mass. The solid curve shows $M_{*,\mathrm{min}}(z)$: our SDSS sample is more than 99% complete above this stellar mass.

LEGA-C primary targets have been selected on the basis of their photometric redshift and K_s-band magnitude, as obtained from the UltraVISTA survey photometric data (Muzzin et al., 2013a). Specifically, according to Straatman et al. (2018), primary targets have been selected in the photometric redshift range $0.6 < z_{\mathrm{photo}} < 1$ and applying a redshift-dependent K_s-magnitude selection $K_s < K_{s,\mathrm{max}}(z_{\mathrm{photo}})$, with $K_{s,\mathrm{max}}(z_{\mathrm{photo}}) = 20.7 - 7.5 \log\left[(1 + z_{\mathrm{photo}})/1.8\right]$. For the sake of robustness, in order to avoid contamination from objects with incorrect photo-z, we apply a more conservative selection adopting a constant K_s limit, $K_s < 20.36 = K_{s,\mathrm{max}}(1)$. We then obtained $M_{*,\mathrm{min}}(z)$ for the LEGA-C sample using the method described above for the SDSS sample, simply replacing r_P with the UltraVISTA K_s-band magnitude. The resulting distribution in redshift and stellar mass is shown in the lower panel of Figure 2.7. From a sample of 492 galaxies selected in morphology, K_s-band magnitude and EW([O II]) (grey dots), after selecting only galaxies with stellar mass above $M_{*,\mathrm{min}}(z)$, our LEGA-C sample of ETGs reduces to 178 objects[2] (black dots).

The LEGA-C DR2 sample, however, does not include all galaxies brighter than the stated magnitude limit, as the survey was not finished at the time of that data release. Instead, the targets included in DR2 were selected according to a K_s-dependent probability, $\mathrm{P}(K_s)$. The resulting sample is therefore incomplete, but the incompleteness rate $\mathrm{P}(K_s)$ is a known quantity, provided in the LEGA-C DR2. In

[2]The number of LEGA-C galaxies selected on morphology, K_s-band magnitude, and with a measurement of $\mathrm{EW}([\mathrm{O\,II}]) \geq -5$ Å or without a measurement of $\mathrm{EW}([\mathrm{O\,II}])$ is equal to 492. By applying also the selection on stellar mass, we obtain a sample of 292 objects. Among these 292 galaxies, around 40% are excluded because the doublet of [O II] is out of the observed range, ending up with a sample composed by 178 ETGs.

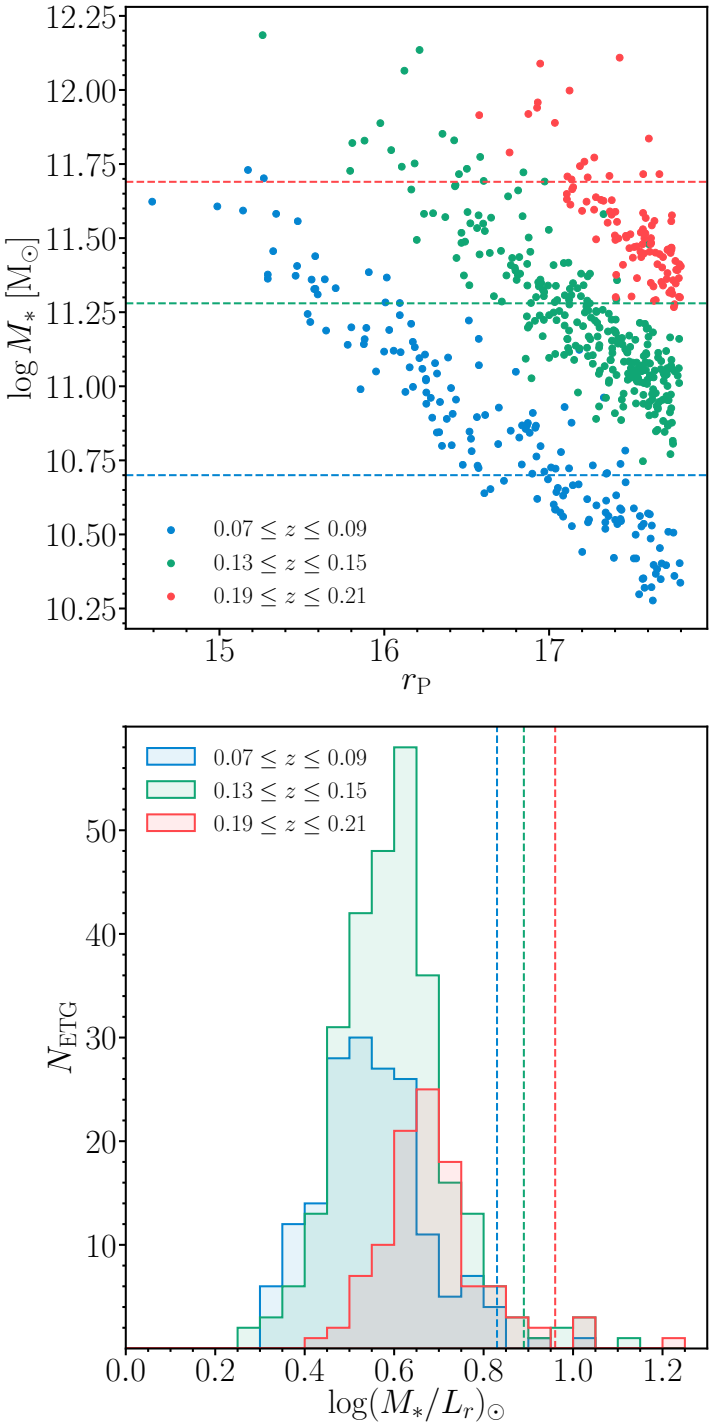

Fig. 2.6: Stellar mass as a function of SDSS $r-$band Petrosian magnitude, for SDSS main sample ETGs in three narrow redshift bins (upper pannel). Horizontal dashed lines mark, in each redshift bin, the stellar mass above which an ETG drawn from the SDSS main sample has more than 99% probability of entering our sample. Distribution in the ratio between stellar mass and observed-frame $r-$band Petrosian luminosity of the galaxies in the three redshift bins shown in the upper panel (lower panel). The 99-th percentile of each distribution is marked by a vertical dashed line. This value, multiplied by the Petrosian luminosity corresponding to the limiting $r-$band magnitude of the SDSS main sample, $r_\mathrm{P} = 17.77$, gives the 99% completeness limit shown in the upper panel.

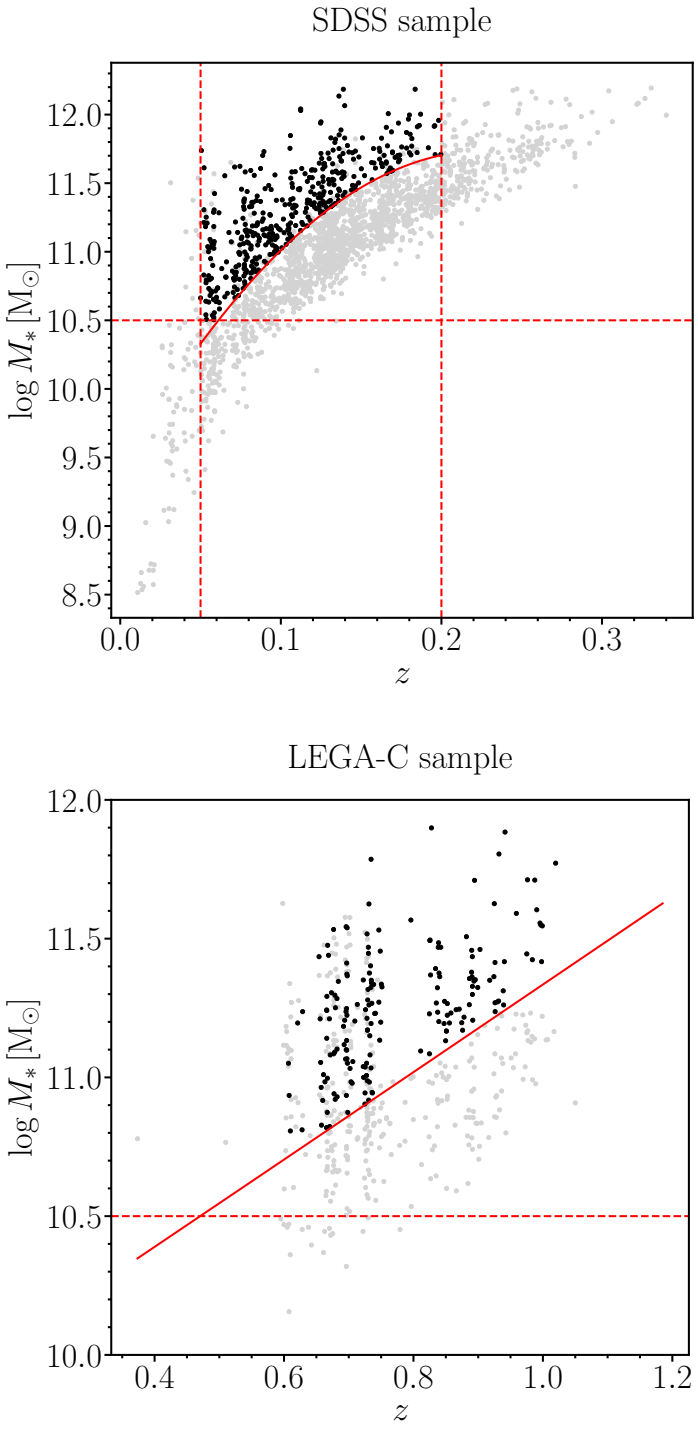

Fig. 2.7: Stellar mass as a function of redshift for SDSS (upper panel) and LEGA-C (lower panel) galaxies. The solid curves represent the empirical 99% mass-completeness limits. The horizontal dashed lines represent the absolute lower stellar mass limit $10^{10.5}\,\mathrm{M}_\odot$, while the vertical dashed lines are the lowest ($z = 0.05$) and highest ($z = 0.20$) redshift limits imposed in the SDSS galaxy selection. In the upper panel, grey dots represent all the 2127 SDSS main sample galaxies morphologically selected and with $\mathrm{EW}([\mathrm{O\,II}]) \geq -5$ Å, while black dots are the 413 objects above the mass-completeness limit, with $\log(M_*/\mathrm{M}_\odot) > 10.5$ in the redshift range $0.05 < z < 0.2$. In the lower panel, grey dots are the 492 LEGA-C galaxies selected in morphology, EW([O II]) and K_s-band magnitude, while the black dots represent the final LEGA-C sample of 178 ETGs above the mass-completeness limit.

Tab. 2.1: Summary table of the selection steps adopted to build the final SDSS and LEGA-C samples.

Selection step	$N_{\rm ETG}$
SDSS sample	
SDSS main sample galaxies selected on morphology and $\mathrm{EW}([\mathrm{O\,II}])$	2127
SDSS galaxies at $0.05 \leq z \leq 0.2$ with $M_* > 10^{10.5}\,\mathrm{M}_\odot$ and $M_* > M_{*,\mathrm{min}}(z)$	413
LEGA-C sample	
LEGA-C galaxies selected on morphology, $\mathrm{EW}([\mathrm{O\,II}])$ and K_s-band magnitude	492
LEGA-C galaxies with $M_* > 10^{10.5}\,\mathrm{M}_\odot$ and $M_* > M_{*,\mathrm{min}}(z)$	178

order to obtain an unbiased inference of the M_*–σ_e relation, it is then sufficient to re-weight each measurement by the inverse of $\mathrm{P}(K_s)$. In Table 2.1, we summarise the selection steps used to obtain the final SDSS and LEGA-C samples.

Velocity dispersion measurements

For each SDSS galaxy, we obtain, from the DR12 catalogue, the value and relative uncertainty of the line-of-sight stellar velocity dispersion measured in the $1.5''$ radius fiber of the SDSS spectrograph, which we label σ_ap. We convert this measurement into an estimate of the central velocity dispersion integrated within an aperture equal to the half-light radius, σ_e, by applying the following correction:

$$\sigma_\mathrm{e} = \sigma_\mathrm{ap} \times \left(\frac{R_\mathrm{e}}{1.5''}\right)^{-\delta}, \tag{2.3}$$

where R_e is the half-light radius and $\delta = 0.066$ (Cappellari et al., 2006).

Velocity dispersion measurements provided in the LEGA-C DR2 are converted to values of the central velocity dispersion σ_e applying the aperture correction

$$\sigma_\mathrm{e} = 1.05\,\sigma_\mathrm{ap}, \tag{2.4}$$

Tab. 2.2: Properties of the subsamples of ETGs used to build our fiducial (SDSS and LEGA-C) and high-redshift (vdS13, B14, G15 and B17) samples. Column 1: subsample name. Column 2: redshift range. Column 3: stellar mass range in logarithm. Column 4: number of galaxies.

Sample	z	$\log(M_*/\mathrm{M}_\odot)$	N_{ETG}
SDSS	$(0.05; 0.20)$	$(10.50; 12.19)$	413
LEGA-C	$(0.60; 1.02)$	$(10.80; 11.90)$	178
vdS13	$(0.81; 2.19)$	$(10.53; 11.69)$	56
B14	$(1.02; 1.60)$	$(10.59; 11.35)$	26
G15	$(1.26; 1.41)$	$(11.04; 11.49)$	4
B17	$(1.52; 2.44)$	$(10.60; 11.68)$	24

which is a good approximation for galaxies in the redshift range of the LEGA-C sample (van de Sande et al., 2013; Belli et al., 2014a). The distributions in redshift and in stellar mass of the SDSS and LEGA-C subsamples and of the fiducial sample are shown in Figure 2.8 (see also Table 2.2).

2.2.2 The high-redshift and extended samples

Our high-redshift sample of ETGs is a sample of 110 galaxies with $\log(M_*/\mathrm{M}_\odot) > 10.5$ in the redshift range $0.8 \lesssim z \lesssim 2.5$, built as follows. We obtain measurements of the stellar mass and stellar velocity dispersion of ETGs out to $z \approx 2.5$ from a variety of studies. In order of increasing median redshift, we take 26 galaxies drawn from the LRIS sample presented in Belli et al. (2014a, hereafter B14), including only those galaxies for which $\mathrm{EW}([\mathrm{O\,II}]) \geq -5\,\text{Å}$ (as done for the fiducial sample; subsection 2.2.1), 56 galaxies from van de Sande et al. (2013, hereafter vdS13), 4 galaxies from Gargiulo et al. (2015, hereafter G15), and 24 galaxies from Belli et al. (2017, hereafter B17). The main properties of each of these subsamples are summarised in Table 2.2. Among the original sample of 73 galaxies of vdS13, only 5 galaxies are presented for the first time, while the remaining 68 sources are collected from different studies. We removed 17 of these 73 ETGs because they are already included as part of either B14's or B17's samples. All the galaxies in the high-redshift samples are classified as ETGs, based on their UVJ colours, morphology and/or spectra. Of course, given the more heterogeneous selection, our extended sample is not as self-consistent as our fiducial sample, and, due to the known correlations between σ_{e} and some structural or spectral properties of ETGs (Zahid & Geller,

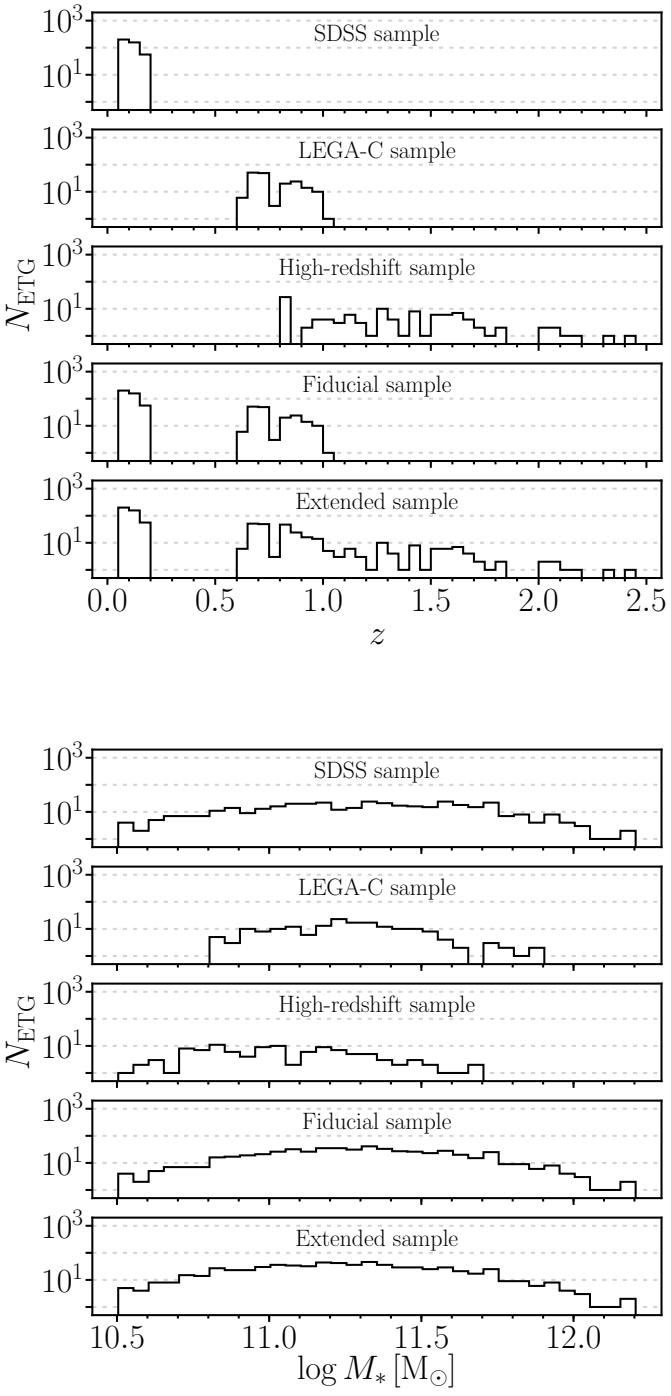

Fig. 2.8: Distributions of the subsamples and samples of ETGs in redshift (upper panel) and stellar mass (lower panel). From the top to the bottom, the SDSS subsample, the LEGA-C subsample, the high-redshift sample (vdS13+B14+G15+B17 subsamples), the fiducial sample (SDSS+LEGA-C subsamples) and the extended sample (fiducial sample+high-resdhift sample) distributions are shown.

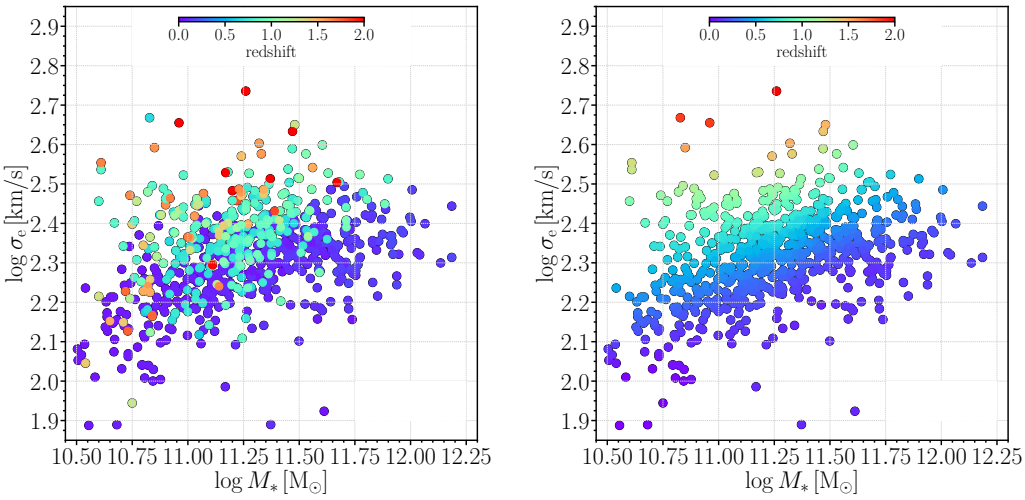

Fig. 2.9: Redshift distribution of the extended sample on the $M_*-\sigma_e$ plane. In the left panel each galaxy is colour-coded as a function of its redshift, while in the right panel the redshift distribution is smoothed by means of the two-dimensional Locally Weighted Regression (LOESS, Cleveland & Devlin, 1988) using the Python implementation of Cappellari et al. (2013, available at `https://www-astro.physics.ox.ac.uk/~mxc/software/`).

2017), we cannot exclude that selection biases have non-negligible effects when the high-redshift sample is considered. However, for the vast majority of these galaxies, stellar masses are measured by fitting SPS models to broadband imaging data and by scaling the total flux to match that measured by fitting a Sérsic surface brightness profile to high-resolution images from *Hubble Space Telescope* (HST). The details of the SPS models are very similar to those we adopted in our measurement of the stellar masses of the fiducial sample. In all these subsamples stellar masses are computed assuming Chabrier IMF and central velocity dispersions are given within an aperture of radius R_e. Our extended sample, obtained by combining the fiducial and high-redshift samples, consists of 701 ETGs with $M_* \gtrsim 10^{10.5}\,M_\odot$ in the redshift interval $0 \lesssim z \lesssim 2.5$. The distributions in redshift and in stellar mass of the high-redshift and extended samples are shown in Figure 2.8.

Finally, in Figure 2.9 the scatter distribution of the extended sample on the $M_*-\sigma_e$ plane colour-coded as a function of redshift is illustrated, suggesting that the evolution of the relation between $\log\sigma_e$ and $\log M_*$ may be described by assuming a linear function with a positive slope, whose normalisation should increase towards higher redshifts.

2.3 Method

We use a Bayesian hierarchical method to infer the distribution of stellar velocity dispersion as a function of stellar mass and redshift for the ETGs in our samples. This method allows us to properly propagate observational uncertainties, to disentangle intrinsic scatter from observational errors and to correct for Eddington bias (Eddington, 1913), which is introduced when imposing a lower cutoff to the stellar mass distribution. Throughout this section stellar masses are expressed in units of $\mathrm{M}_{\odot}$.

2.3.1 Bayesian hierarchical formalism

We describe each galaxy in our sample by its redshift, stellar mass and central stellar velocity dispersion. We refer to these parameters collectively as $\boldsymbol{\Theta} = \{\log M_*, \log \sigma_\mathrm{e}, z\}$. These represent the true values of the three quantities, which are in general different from the corresponding observed values. We assume that the values of $\boldsymbol{\Theta}$ are drawn from a probability distribution, described in turn by a set of *hyper-parameters* $\boldsymbol{\Phi}$:

$$\mathrm{P}(\boldsymbol{\Theta}) = \mathrm{P}(\boldsymbol{\Theta}|\boldsymbol{\Phi}). \tag{2.5}$$

Our goal is to infer plausible values of the hyper-parameters, which summarise the distribution of our galaxies in the $(\log M_*, \log \sigma_\mathrm{e}, z)$ space, given our data. We will describe in detail the functional form of the distribution $\mathrm{P}(\boldsymbol{\Theta}|\boldsymbol{\Phi})$ in subsection 2.3.2.

Using Bayes' theorem, the posterior probability distribution of the hyper-parameters given the data $\boldsymbol{d}$ is

$$\mathrm{P}(\boldsymbol{\Phi}|\boldsymbol{d}) \propto \mathrm{P}(\boldsymbol{\Phi})\mathrm{P}(\boldsymbol{d}|\boldsymbol{\Phi}), \tag{2.6}$$

where $\mathrm{P}(\boldsymbol{\Phi})$ is the prior probability distribution of the model hyper-parameters and $\mathrm{P}(\boldsymbol{d}|\boldsymbol{\Phi})$ is the likelihood of observing the data given the model.

The data consist of observed stellar masses, stellar velocity dispersions and redshifts,

$$\boldsymbol{d} \equiv \{\log M_*^{\mathrm{obs}}, \log \sigma_\mathrm{e}^{\mathrm{obs}}, z^{\mathrm{obs}}\}, \tag{2.7}$$

and related uncertainties. Since measurements on different galaxies are independent of each other, the likelihood term can be written as

$$\mathrm{P}(\boldsymbol{d}|\boldsymbol{\Phi}) = \prod_i \mathrm{P}(\boldsymbol{d}_i|\boldsymbol{\Phi}), \tag{2.8}$$

where $\boldsymbol{d}_i$ is the data relative to the i-th galaxy. For each galaxy in our sample, the likelihood of the data depends only on the true values of the redshift, stellar mass and velocity dispersion, $\boldsymbol{\Theta}$, and not on the hyper-parameters $\boldsymbol{\Phi}$. In order to compute the $\mathrm{P}(\boldsymbol{d}_i|\boldsymbol{\Phi})$ terms in Equation 2.8, then, we need to marginalise over all possible values of the individual object parameters $\boldsymbol{\Theta}_i$:

$$\mathrm{P}(\boldsymbol{d}_i|\boldsymbol{\Phi}) = \int \mathrm{d}\boldsymbol{\Theta}_i \mathrm{P}(\boldsymbol{d}_i, \boldsymbol{\Theta}_i|\boldsymbol{\Phi}) = \int \mathrm{d}\boldsymbol{\Theta}_i \mathrm{P}(\boldsymbol{d}_i|\boldsymbol{\Theta}_i)\mathrm{P}(\boldsymbol{\Theta}_i|\boldsymbol{\Phi}). \tag{2.9}$$

This allows us to evaluate the posterior probability distribution, Equation 2.6, provided that a model distribution $\mathrm{P}(\boldsymbol{\Theta}|\boldsymbol{\Phi})$ is specified, priors are defined and the shape of the likelihood is known. The method is hierarchical in the sense that there exists a hierarchy of parameters: individual object parameters $\boldsymbol{\Theta}_i$ are drawn from a distribution that is, in turn, described by a set of hyper-parameters.

As explained in subsection subsection 2.2.1, the LEGA-C sample is not representative of a complete sample, but each galaxy was included with a K_s magnitude-dependent probability $\mathrm{P}(K_s)$, so that brighter galaxies are over-represented (see figure 2 of Straatman et al., 2018). To correct for this, we re-weight the contribution of each LEGA-C measurement to the likelihood by a factor proportional to $1/P(K_s)$: we transform Equation 2.8 to

$$\mathrm{P}(\boldsymbol{d}|\boldsymbol{\Phi}) = \prod_i \mathrm{P}(\boldsymbol{d}_i|\boldsymbol{\Phi})^{w_i}, \tag{2.10}$$

where w_i is given by

$$w_i = \frac{1/P(K_{s,i})}{\langle 1/P(K_s)\rangle} \tag{2.11}$$

for LEGA-C galaxies and $w_i = 1$ otherwise. The normalisation of the weights given in the equation above ensures that the effective number of LEGA-C data points equals the number of LEGA-C galaxies.

2.3.2 The model

The purpose of our model is to summarise the distribution in stellar mass and velocity dispersion of our samples of ETGs with a handful of parameters, $\boldsymbol{\Phi}$, that can provide an intuitive description of the M_*–σ_e relation. In the absence of a well-established theoretically motivated model, we opt for an empirical one, that we describe in this subsection.

The dependent variable of our model is the central velocity dispersion, $\sigma_{\rm e}$, while stellar mass and redshift are independent variables. As such, it is useful to write the probability distribution of individual galaxy parameters as

$$\mathrm{P}(\mathbf{\Theta}|\mathbf{\Phi}) = \mathrm{P}(\log M_*, z|\mathbf{\Phi})\mathrm{P}(\log \sigma_{\rm e}|\log M_*, z, \mathbf{\Phi}). \tag{2.12}$$

Here, $\mathrm{P}(\log M_*, z|\mathbf{\Phi})$ describes the prior probability distribution for a galaxy in our sample to have logarithm of the true stellar mass $\log M_*$ and true redshift z. This probability depends on some hyper-parameters, which may vary between different subsamples. Our galaxies have been selected by applying a lower cut to the observed stellar masses, $M_*^{\rm obs} > M_{*,\rm min}$. We then expect the probability distribution in the true stellar mass to go to zero for low values of M_*. We also expect $\mathrm{P}(\log M_*, z|\mathbf{\Phi})$ to vanish for very large values of M_*, as there are few known galaxies with $M_* > 10^{12}$. For simplicity, we assume that $\mathrm{P}(\log M_*, z|\mathbf{\Phi})$ separates as follows:

$$\mathrm{P}(\log M_*, z|\mathbf{\Phi}) = \mathrm{P}(\log M_*|\mathbf{\Phi})\mathrm{P}(z|\mathbf{\Phi}), \tag{2.13}$$

where $\mathrm{P}(\log M_*|\mathbf{\Phi})$ is a skew Gaussian distribution in $\log M_*$,

$$\mathrm{P}(\log M_*|\mathbf{\Phi}) \propto \frac{1}{\sqrt{2\pi\sigma_{\sigma_*}^2}} \exp\left\{-\frac{(\log M_* - \mu_*)^2}{2\sigma_*^2}\right\} \mathcal{E}(\log M_*|\mathbf{\Phi}), \tag{2.14}$$

with

$$\mathcal{E}(\log M_*|\mathbf{\Phi}) = 1 + \mathrm{erf}\left(\alpha_* \frac{\log M_* - \mu_*}{\sqrt{2\sigma_*}}\right), \tag{2.15}$$

where the three hyper-parameters μ_*, σ_*, α_* are modelled as

$$\mu_* = \mu_{*,0} + \mu_{*,s} \log\left(\frac{1+z}{1+z^{\rm piv}}\right), \tag{2.16}$$

$$\sigma_* = \sigma_{*,0} + \sigma_{*,s} \log\left(\frac{1+z}{1+z^{\rm piv}}\right) \tag{2.17}$$

and

$$\alpha_* = const. \tag{2.18}$$

Since this is a prior on the stellar mass distribution, and since the typical uncertainty on the stellar mass measurements is much smaller than the width of this distribution (as shown in section 2.4), the particular choice of the functional form of $\mathrm{P}(\log M_*|\mathbf{\Phi})$ does not matter in practice, because the likelihood term dominates over the prior. The main role of the prior is downweighting extreme outliers and measurements with very large uncertainties. The term $\mathrm{P}(z|\mathbf{\Phi})$ in Equation 2.13 describes the redshift distribution of the galaxies in our sample. As we show below, this term

does not enter the problem, because uncertainties on the observed redshifts can be neglected.

The second term on the right hand side of Equation 2.12 is the core of our model. With it, we wish to capture the following features of the M_*–σ_e relation: its normalisation (i.e. the amplitude of the stellar velocity dispersion at a given value of the stellar mass) and its redshift evolution, the correlation between velocity dispersion and stellar mass, and the amplitude of the intrinsic scatter in σ_e at fixed M_* and redshift. With these requirements in mind, we assume that the logarithm of the stellar velocity dispersion is normally distributed, with a mean that can scale with redshift and stellar mass and with a variance that can evolve with redshift:

$$\mathrm{P}(\log\sigma_\mathrm{e}|\log M_*, z, \mathbf{\Phi}) = \frac{1}{\sqrt{2\pi\sigma_\sigma^2}}\exp\left\{-\frac{(\log\sigma_\mathrm{e}-\mu_\sigma)^2}{2\sigma_\sigma^2}\right\}. \tag{2.19}$$

We adopt the following functional form for the mean of this distribution:

$$\mu_\sigma = \mu_0^\mathrm{SDSS} + \beta\log\left(\frac{M_*}{M_*^\mathrm{piv}}\right) + \zeta\log\left(\frac{1+z}{1+z^\mathrm{piv}}\right). \tag{2.20}$$

In general, the slope β is allowed to depend on z as

$$\beta = \beta_0^\mathrm{SDSS} + \eta\log\left(\frac{1+z}{1+z^\mathrm{piv}}\right). \tag{2.21}$$

We perform our analysis considering two different cases: the first is a *constant-slope* case (model $\mathcal{M}_\mathrm{const}$), i.e. Equation 2.21 with $\eta = 0$; in the second, which we refer to as the *evolving-slope* case (model $\mathcal{M}_\mathrm{evo}$), η is a free hyper-parameter. For the standard deviation σ_σ in Equation 2.19, namely the intrinsic scatter of our relation, we adopt the form

$$\sigma_\sigma = \psi_0^\mathrm{SDSS} + \xi\log\left(\frac{1+z}{1+z^\mathrm{piv}}\right). \tag{2.22}$$

In equations (2.20-2.22) $M_*^\mathrm{piv} = 10^{11.321}$ and $z^\mathrm{piv} = 0.10436$, i.e. the median values of stellar mass and redshift of the SDSS ETGs, respectively, while the quantities μ_0^SDSS, β_0^SDSS and ψ_0^SDSS are the median values of the hyper-parameters μ_0, β_0 and ψ_0 obtained when fitting Equation 2.19 to the ETGs of the SDSS subsample with

$$\mu_\sigma = \mu_0 + \beta_0\log\left(\frac{M_*}{M_*^\mathrm{piv}}\right) \qquad \text{and} \qquad \sigma_\sigma = \psi_0, \tag{2.23}$$

i.e. neglecting any dependence on z. In order to prevent the redshift dependence of the relation from being influenced by any redshift dependence within the SDSS sample, which constitutes $\approx 60\%$ of the extended sample, we assume the model in

Equation 2.23 as the *zero point* at $z^{\rm piv}$ for our redshift-dependent models, because our main interest is to trace the evolution of the relation at higher redshift ($z \gtrsim 0.5$). Hereafter, we will refer to the model in Equation 2.23 applied to the SDSS subsample as model $\mathcal{M}^{\rm SDSS}$.

Allowing for intrinsic scatter is an important feature of our model. Neglecting it leads typically to underestimating the slope of the M_*–$\sigma_{\rm e}$ relation (see e.g. Auger et al., 2010). Our choice for the functional form of the distribution in velocity dispersion introduced above is somewhat arbitrary. Although there could exist alternative distributions that fit the data equally well as our model or better, however, exploring such distributions is beyond the scope of this work.

2.3.3 Sampling the posterior probability distribution functions of the model hyper-parameters

Our goal is to sample the posterior probability distribution function (PDF) of the model hyper-parameters $\mathbf{\Phi}$ given the data $\boldsymbol{d}$, $\mathrm{P}(\mathbf{\Phi}|\boldsymbol{d})$. For this purpose, we use an MCMC approach, using a Python adaptation of the affine-invariant ensemble sampler of Goodman & Weare (2010), `emcee` (Foreman-Mackey et al., 2013). For each set of values of the hyper-parameters, we need to evaluate the likelihood of the data. This is given by the product over the galaxies in our sample of the integrals in Equation 2.9. Using $\log M_*$, $\log \sigma_{\rm e}$ and z as the integration variables and omitting the subscript i in order to simplify the notation, Equation 2.9 reads

$$
\begin{aligned}
&\mathrm{P}(\log M_*^{\rm obs}, \log \sigma_{\rm e}^{\rm obs}, z^{\rm obs}|\mathbf{\Phi}) = \\
&\quad = \iiint \mathrm{d}\log M_* \, \mathrm{d}\log \sigma_{\rm e} \, \mathrm{d}z \times \\
&\qquad \times \mathrm{P}(\log M_*^{\rm obs}, \log \sigma_{\rm e}^{\rm obs}, z^{\rm obs}|\log M_*, \log \sigma_{\rm e}, z) \times \\
&\qquad \times \mathrm{P}(\log M_*, \log \sigma_{\rm e}, z|\mathbf{\Phi}) = \\
&\quad = \iiint \mathrm{d}\log M_* \, \mathrm{d}\log \sigma_{\rm e} \, \mathrm{d}z \times \\
&\qquad \times \mathrm{P}(\log M_*^{\rm obs}|\log M_*) \, \mathrm{P}(\log \sigma_{\rm e}^{\rm obs}|\log \sigma_{\rm e}) \, \delta(z^{\rm obs} - z) \times \\
&\qquad \times \mathrm{P}(\log M_*|\mathbf{\Phi}) \mathrm{P}(z|\mathbf{\Phi}) \mathrm{P}(\log \sigma_{\rm e}|\log M_*, z, \mathbf{\Phi}).
\end{aligned}
\tag{2.24}
$$

In the last line, we have used equations (2.12) and (2.13), and we have approximated the likelihood of observing redshift $z^{\rm obs}$ as a delta function, in virtue of the very small uncertainties on the redshift (typical errors are $< 10^{-4}$). As a result, the redshift distribution term $\mathrm{P}(z|\mathbf{\Phi})$ becomes irrelevant, as it contributes to the integral only through a multiplicative constant that we can ignore.

Assuming a Gaussian likelihood in $\log \sigma_{\rm e}^{\rm obs}$ for the term $\mathrm{P}(\log \sigma_{\rm e}^{\rm obs} | \log \sigma_{\rm e})$, the integral over $\mathrm{d} \log \sigma_{\rm e}$ can be performed analytically, as we show in Appendix 2.B. We also assume a Gaussian likelihood for the measurements of $\log M_*^{\rm obs}$,

$$\mathrm{P}(\log M_*^{\rm obs} | \log M_*) = \frac{\mathcal{A}(\log M_*)}{\sqrt{2\pi\sigma_{M_*}^2}} \exp\left\{ -\frac{(\log M_* - \log M_*^{\rm obs})^2}{2\sigma_{M_*}^2} \right\}, \tag{2.25}$$

with one caveat: we are only selecting galaxies with $\log M_*^{\rm obs} > \log M_{*,\rm min}$, where $\log M_{*,\rm min}$ is derived from the mass-completeness limits at a given redshift for SDSS and LEGA-C galaxies (see section 2.2.1) and it is assumed to be constant and equal to 10.5 for all the ETGs of the high-redshift sample. The likelihood must be normalised accordingly:

$$\int_{\log M_{*,\rm min}}^{\infty} \mathrm{d} \log M_*^{\rm obs} \, \frac{\mathcal{A}(\log M_*)}{\sqrt{2\pi\sigma_{M_*}^2}} \exp\left\{ -\frac{(\log M_* - \log M_*^{\rm obs})^2}{2\sigma_{M_*}^2} \right\} = 1. \tag{2.26}$$

In other words, the probability of measuring any value of the stellar mass larger than $M_{*,\rm min}$, given that a galaxy is part of our sample, is one. We perform the final integration over $\log M_*$ numerically with a Monte Carlo method (see Appendix 2.B). We assume flat priors on all model hyper-parameters.

2.3.4 Bayesian evidence

In our analysis, we consider models with different numbers of free hyper-parameters. To evaluate the performance of a given model in fitting the data, we rely on the *Bayesian evidence* $\mathcal{Z}$ that is the average of the likelihood under priors for a given model $\mathcal{M}$:

$$\mathcal{Z} = \mathrm{P}(\boldsymbol{d}|\mathcal{M}) = \int \mathrm{d}\boldsymbol{\Theta} \, \mathrm{P}(\boldsymbol{d}|\boldsymbol{\Theta}, \mathcal{M}) \, \mathrm{P}(\boldsymbol{\Theta}|\mathcal{M}). \tag{2.27}$$

We remark that, in our approach, the parameters $\boldsymbol{\Theta}$ are described by a set of global hyper-parameters $\boldsymbol{\Phi}$. When comparing two models, say models $\mathcal{M}_1$ and $\mathcal{M}_2$, we are interested in computing the ratio of the posterior probabilities of the models

$$\frac{\mathrm{P}(\mathcal{M}_1|\boldsymbol{d})}{\mathrm{P}(\mathcal{M}_2|\boldsymbol{d})} = \mathcal{B} \frac{\mathrm{P}(\mathcal{M}_1)}{\mathrm{P}(\mathcal{M}_2)}, \tag{2.28}$$

where

$$\mathcal{B} \equiv \frac{\mathrm{P}(\boldsymbol{d}|\mathcal{M}_1)}{\mathrm{P}(\boldsymbol{d}|\mathcal{M}_2)} = \frac{\mathcal{Z}_1}{\mathcal{Z}_2} \tag{2.29}$$

is the *Bayes factor*. When $\mathcal{B} \gg 1$, $\mathcal{M}_1$ provides a better description of the data than $\mathcal{M}_2$, and vice versa when $\mathcal{B} \ll 1$. The value of the Bayes factor is usually compared

Tab. 2.3: Jeffreys' scale (Jeffreys, 1961), giving the strength of evidence in the comparison of two models having Bayes factor $\mathcal{B}$ (equation 2.29).

$\lvert \ln \mathcal{B} \rvert$	Strength of evidence
$0 - 1$	Inconclusive
$1 - 2.5$	Weak evidence
$2.5 - 5$	Strong evidence
> 5	Decisive evidence

with the reference values of the empirical *Jeffreys' scale* (Jeffreys, 1961), reported in Table 2.3. Given two different models, the quantity $\lvert \ln \mathcal{B} \rvert$ is a measure of the strength of evidence that one of the two models is preferable. We compute the Bayesian evidence $\mathcal{Z}$ of a model exploiting the *nested sampling* technique (Skilling, 2004). Briefly, the nested sampling algorithm estimates the Bayesian evidence reducing the n-dimensional evidence integral (where n is the number of the parameters of a given model) into a 1D integral that is less expensive to evaluate numerically. In practice, we evaluate $\mathcal{Z}$ for a model using the MULTINEST algorithm (see Feroz & Hobson, 2008; Feroz et al., 2009) included in the Python module PyMultiNest (Buchner et al., 2014). For details about the estimates of the Bayesian evidence and the algorithm exploited to compute them, we refer the interested readers to Feroz & Hobson (2008) and Buchner et al. (2014).

2.4 Results

In this section we present the results obtained applying the Bayesian method described in section 2.3 to our fiducial and extended samples of ETGs (see section 2.2).

In subsection 2.3.2 we have introduced three models: model $\mathcal{M}^{\mathrm{SDSS}}$ (representing the present-day M_*–σ_e relation), model $\mathcal{M}_\mathrm{const}$ (representing the evolution of the M_*–σ_e relation with redshift-independent slope β) and model $\mathcal{M}_\mathrm{evo}$ (representing the evolution of the M_*–σ_e relation with redshift-dependent slope β). In models $\mathcal{M}_\mathrm{const}$ and $\mathcal{M}_\mathrm{evo}$ the intrinsic scatter of the M_*–σ_e relation is allowed to vary with redshift. In addition to these models, we also explore simpler models in which the intrinsic scatter is assumed to be independent of redshift. These models are named $\mathcal{M}_\mathrm{const,NES}$ and $\mathcal{M}_\mathrm{evo,NES}$, where NES stands for *non-evolving scatter*. In summary, we take into account five models: model $\mathcal{M}^{\mathrm{SDSS}}$, represented by Equation 2.23, models $\mathcal{M}_\mathrm{const}$ and $\mathcal{M}_\mathrm{evo}$, described by Equation 2.20 (the former obtained by

Tab. 2.4: Hyper-parameters used in the models. Column 1: name of the model. Column 2: name of the hyper-parameter. Column 3: description of the hyper-parameter. Column 4: uniform priors used in the models ("low" and "up" indicate, respectively, the lower and upper bounds). For those hyper-parameters showing two ranges for prior assumptions, the first refers to the fiducial sample and the second to the extended sample. $M_*^{\rm piv}$ and $z^{\rm piv}$ are the median values of stellar mass and redshift of the SDSS ETGs (subsection 2.3.2).

Model	Hyper-parameter	Description	Prior (low; up)
$\mathcal{M}^{\rm SDSS}$	μ_0	Median value of $\log\sigma_{\rm e}$ at $M_*^{\rm piv}$	(1; 3)
	β_0	Index of the M_*–$\sigma_{\rm e}$ relation: $\sigma_{\rm e}\propto M_*^{\beta_0}$	(0; 1)
	ψ_0	Intrinsic scatter in $\log\sigma_{\rm e}$	(0; 1)
	$\mu_{*,0}$	Normalisation of the mean of Gaussian prior of $\log M_*$	(10; 13)
	$\mu_{*,s}$	Slope of the mean of Gaussian prior of $\log M_*$	(15; 30)
	$\sigma_{*,0}$	Normalisation of the standard deviation in the Gaussian prior of $\log M_*$	(0; 2)
	$\sigma_{*,s}$	Slope of the standard deviation in the Gaussian prior of $\log M_*$	(−10; 10)
	α_*	Skewness parameter in the Gaussian prior of $\log M_*$	(−5; 15)
$\mathcal{M}_{\rm evo}$	$\mu_0^{\rm SDSS}$	Median value of $\log\sigma_{\rm e}$ at $M_*=M_*^{\rm piv}$ and $z=z^{\rm piv}$	$\simeq 2.287$
	$\beta_0^{\rm SDSS}$	Index of the M_*–$\sigma_{\rm e}$ relation at $z=z^{\rm piv}$: $\sigma_{\rm e}\propto M_*^{\beta_0^{\rm SDSS}}$	$\simeq 0.176$
	η	Index of the $\beta-(1+z)$ relation: $\beta\propto(1+z)^{\eta}$	(−2; 2)
	ζ	Index of the $\sigma_{\rm e}-(1+z)$ relation: $\sigma_{\rm e}\propto(1+z)^{\zeta}$	(−2; 2)
	$\psi_0^{\rm SDSS}$	Median value of ψ_0 of the intrinsic scatter at $z=z^{\rm piv}$	$\simeq 0.075$
	ξ	Index of the $\sigma_\sigma-(1+z)$ relation: $\sigma_\sigma\propto(1+z)^{\xi}$	(−2; 2)
	$\mu_{*,0}$	Normalisation of the mean of Gaussian prior of $\log M_*$	(7; 13)
	$\mu_{*,s}$	Slope of the mean of Gaussian prior of $\log M_*$	(0; 10) || (−5; 5)
	$\sigma_{*,0}$	Normalisation of the standard deviation in the Gaussian prior of $\log M_*$	(−5; 5)
	$\sigma_{*,s}$	Slope of the standard deviation in the Gaussian prior of $\log M_*$	(−10; 10)
	α_*	Skewness parameter in the Gaussian prior of $\log M_*$	(−15; 15)
$\mathcal{M}_{\rm const}$	α_*	Same as $\mathcal{M}_{\rm evo}$, but with $\eta=0$ Skewness parameter in the Gaussian prior of $\log M_*$	(−10; 10) || (−15; 15)
$\mathcal{M}_{\rm evo,NES}$		Same as $\mathcal{M}_{\rm evo}$, but with $\xi=0$	
$\mathcal{M}_{\rm const,NES}$	$\sigma_{*,s}$	Same as $\mathcal{M}_{\rm evo}$, but with $\eta=\xi=0$ Slope of the standard deviation in the Gaussian prior of s$\log M_*$	(−10; 10) || (−5; 5)
	α_*	Skewness parameter in the Gaussian prior of $\log M_*$	(−10; 10) || (−15; 15)

assuming $\eta = 0$ in Equation 2.21), and the models $\mathcal{M}_{\rm const,NES}$ and $\mathcal{M}_{\rm evo,NES}$, which are the same as $\mathcal{M}_{\rm const}$ and $\mathcal{M}_{\rm evo}$, respectively, but with $\xi = 0$ in Equation 2.22. A description of the hyper-parameters used for each model is provided in Table 2.4. Model $\mathcal{M}^{\rm SDSS}$ is applied to the SDSS subsample. The other four models are applied twice, once to the fiducial sample and once to the extended sample (we use the superscripts *fid* and *ext* to indicate that a model is applied, respectively, to the fiducial and extended samples).

The model-data comparison is performed as described in section 2.3. We validated our method by applying it to a mock data set similar to the our SDSS data set (see Appendix 2.C). Each MCMC run (see subsection 2.3.3) uses 50 random walkers running for 1000 steps to reach the convergence of the hyper-parameter distribution. The resulting inferences on the hyper-parameters used in model $\mathcal{M}^{\rm SDSS}$ are shown in Figure 2.10. The SDSS galaxies are described by $\sigma_{\rm e} \propto M_*^{\beta_0}$ with $\beta_0 \simeq 0.176$. The normalisation $\mu_0 \simeq 2.287$ is such that galaxies with $M_* = 10^{11}{\rm M}_\odot$ have $\sigma_{\rm e} \simeq 170\,{\rm km\,s^{-1}}$ and the intrinsic scatter is $\simeq 0.075$ dex in $\sigma_{\rm e}$ at fixed M_*. The posterior distributions of the hyperparameters μ_0, β_0 and ψ_0 are relatively narrow (Figure 2.10), with 1σ scatter of at most few percent (Table 2.5), so our SDSS sample of ETG is sufficiently numerous for our purposes, even if it contains only a small fraction of the massive ETGs of the entire SDSS sample. Our results on the present-day M_*–$\sigma_{\rm e}$ relation are broadly consistent with previous analyses (see subsection 2.5.2 for details).

The median values of the hyper-parameters of all models, with the corresponding 1σ uncertainties, are listed in Table 2.5. In order to compare the models we compute the Bayesian evidence $\mathcal{Z}$ of each model (subsection 2.3.4), using a configuration of 400 live points in the nested sampling algorithm. The resulting $\mathcal{Z}$ and the Bayes factors are listed in Table 2.6. The performances of models $\mathcal{M}_{\rm const}$ and $\mathcal{M}_{\rm evo}$ are relatively poor when applied to both the fiducial and the extended samples, so in the following we focus on model $\mathcal{M}_{\rm const,NES}$ and $\mathcal{M}_{\rm evo,NES}$: in Figure 2.11 and Figure 2.12, we show the inferences of these two models applied to both the fiducial and the extended samples.

2.4.1 Fiducial sample ($0 \lesssim z \lesssim 1$)

The model with the highest Bayesian evidence, among those applied to the fiducial sample, is $\mathcal{M}^{fid}_{\rm const,NES}$ (see Table 2.6). Model $\mathcal{M}^{fid}_{\rm evo,NES}$, though with slightly lower evidence, describes the data as well as model $\mathcal{M}^{fid}_{\rm const,NES}$, according to Jeffreys'

Tab. 2.5: Inferred median and 68% posterior credible intervals of the hyper-parameters of the models.

Model	μ_0	β_0	ψ_0	$\mu_{*,0}$	$\mu_{*,s}$	$\sigma_{*,0}$	$\sigma_{*,s}$	α_*
$\mathcal{M}^{\rm SDSS}$	$2.287^{+0.004}_{-0.004}$	$0.176^{+0.011}_{-0.011}$	$0.075^{+0.003}_{-0.003}$	$10.990^{+0.017}_{-0.016}$	$23.533^{+0.792}_{-0.910}$	$0.356^{+0.020}_{-0.018}$	$-5.690^{+1.358}_{-1.095}$	$6.969^{+4.725}_{-2.868}$

Model	η	ζ	ξ	$\mu_{*,0}$	$\mu_{*,s}$	$\sigma_{*,0}$	$\sigma_{*,s}$	α_*
$\mathcal{M}^{fid}_{\rm const}$	$--$	$0.390^{+0.031}_{-0.031}$	$0.033^{+0.026}_{-0.023}$	$9.827^{+0.259}_{-0.213}$	$5.616^{+0.955}_{-1.054}$	$0.457^{+0.199}_{-0.193}$	$-0.841^{+0.937}_{-0.908}$	$3.993^{+4.089}_{-2.579}$
$\mathcal{M}^{fid}_{\rm evo}$	$0.248^{+0.150}_{-0.156}$	$0.415^{+0.034}_{-0.035}$	$0.028^{+0.027}_{-0.024}$	$9.855^{+0.226}_{-0.220}$	$5.455^{+0.995}_{-0.913}$	$0.428^{+0.211}_{-0.191}$	$-0.684^{+0.920}_{-0.950}$	$5.727^{+5.763}_{-4.083}$
$\mathcal{M}^{ext}_{\rm const}$	$--$	$0.474^{+0.024}_{-0.023}$	$0.025^{+0.019}_{-0.019}$	$11.147^{+0.168}_{-0.158}$	$-0.172^{+0.322}_{-0.348}$	$0.249^{+0.088}_{-0.075}$	$0.210^{+0.301}_{-0.271}$	$0.062^{+1.421}_{-1.126}$
$\mathcal{M}^{ext}_{\rm evo}$	$0.179^{+0.101}_{-0.106}$	$0.505^{+0.028}_{-0.029}$	$0.019^{+0.021}_{-0.022}$	$11.156^{+0.140}_{-0.121}$	$-0.197^{+0.300}_{-0.319}$	$0.240^{+0.062}_{-0.079}$	$0.209^{+0.286}_{-0.254}$	$0.061^{+1.031}_{-0.952}$
$\mathcal{M}^{fid}_{\rm const,NES}$	$--$	$0.398^{+0.028}_{-0.031}$	$--$	$9.853^{+0.282}_{-0.220}$	$5.538^{+0.951}_{-1.029}$	$0.415^{+0.202}_{-0.181}$	$-0.657^{+0.846}_{-0.868}$	$3.267^{+3.894}_{-2.494}$
$\mathcal{M}^{fid}_{\rm evo,NES}$	$0.264^{+0.146}_{-0.142}$	$0.417^{+0.035}_{-0.034}$	$--$	$9.867^{+0.211}_{-0.204}$	$5.408^{+0.934}_{-0.870}$	$0.408^{+0.211}_{-0.179}$	$-0.625^{+0.900}_{-0.921}$	$5.195^{+5.947}_{-3.571}$
$\mathcal{M}^{ext}_{\rm const,NES}$	$--$	$0.478^{+0.021}_{-0.021}$	$--$	$11.142^{+0.174}_{-0.171}$	$-0.148^{+0.272}_{-0.302}$	$0.246^{+0.084}_{-0.076}$	$0.203^{+0.325}_{-0.274}$	$0.093^{+1.289}_{-1.036}$
$\mathcal{M}^{ext}_{\rm evo,NES}$	$0.180^{+0.103}_{-0.095}$	$0.506^{+0.029}_{-0.027}$	$--$	$11.192^{+0.138}_{-0.166}$	$-0.120^{+0.271}_{-0.285}$	$0.238^{+0.081}_{-0.071}$	$0.177^{+0.292}_{-0.246}$	$-0.281^{+1.103}_{-0.704}$

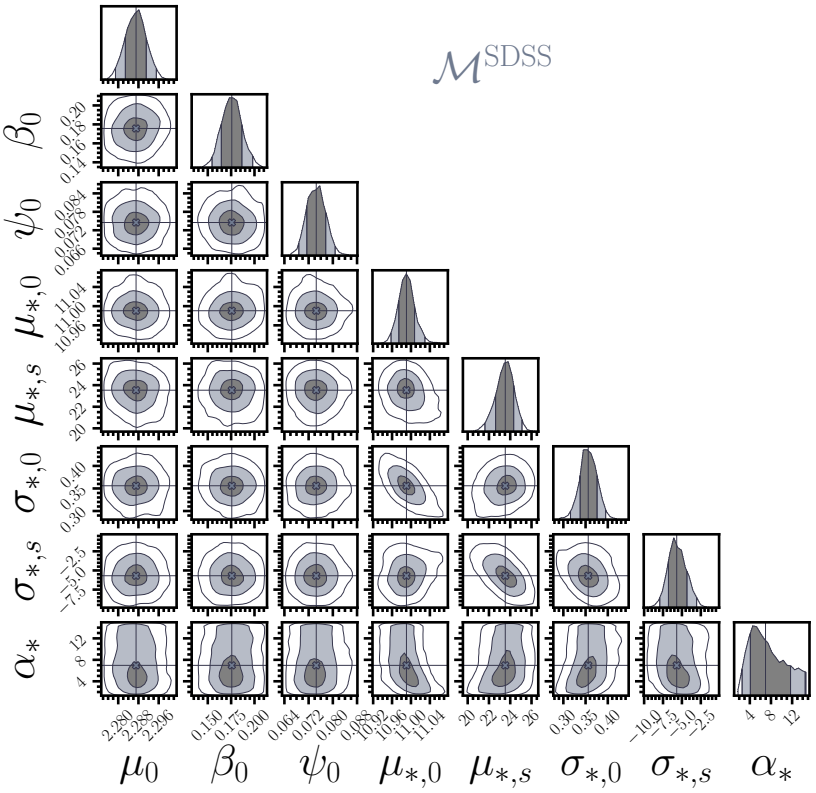

Fig. 2.10: Posterior probability distributions of the hyper-parameters for model $\mathcal{M}^{\rm SDSS}$ (see Tables 2.4 and 2.5). In the 1D distributions (upper panel of each column) the vertical solid lines and colours delimit the 68, 95 and 99.7-th quantile based posterior credible interval. In the 2D distributions (all the other panels) the contours enclose the 68, 95 and 99.7 percent posterior credible regions. The dashed lines indicate the median values of the hyper-parameters.

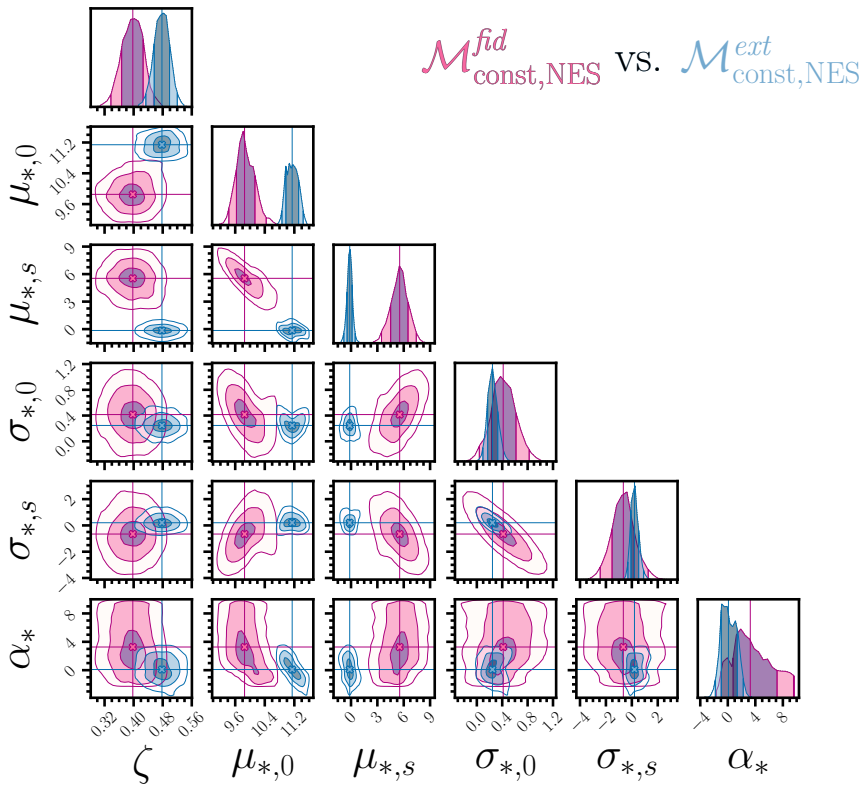

Fig. 2.11: Same as Figure 2.10, but for models $\mathcal{M}^{fid}_{\mathrm{const,NES}}$ (pink contours) and $\mathcal{M}^{ext}_{\mathrm{const,NES}}$ (azure contours; see Tables 2.4 and 2.5).

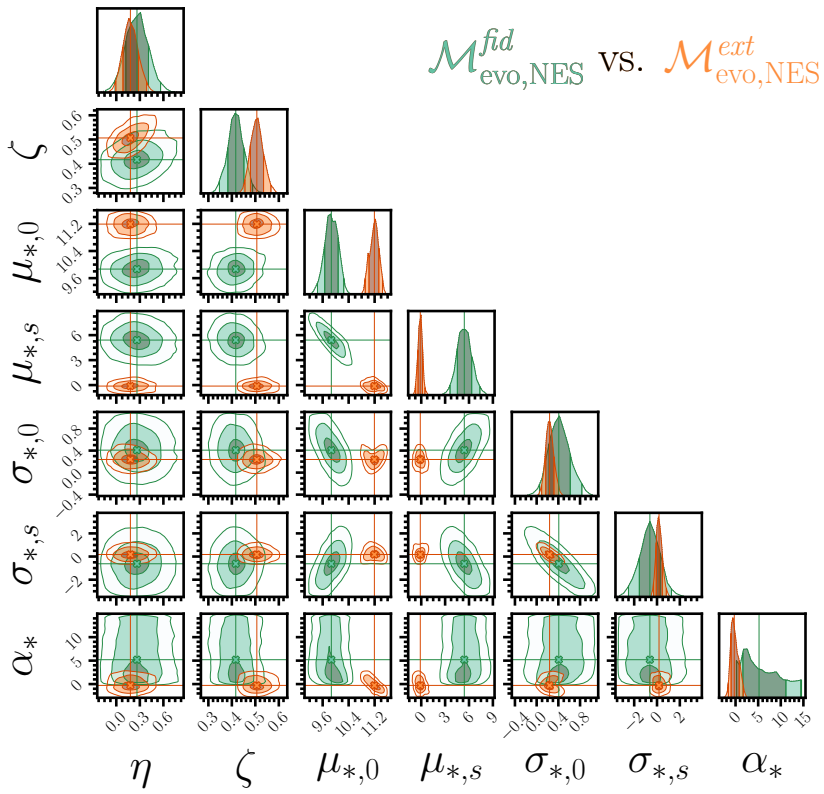

Fig. 2.12: Same as Figure 2.10, but for models $\mathcal{M}^{fid}_{\rm evo,NES}$ (green contours) and $\mathcal{M}^{ext}_{\rm evo,NES}$ (orange contours; see Tables 2.4 and 2.5).

Tab. 2.6: Logarithm of the Bayesian evidence, $\ln \mathcal{Z}$, and logarithm of the Bayes factor, $\ln \mathcal{B}$, of the models. The values of $\mathcal{B}$ are relative to the Bayesian evidence of model $\mathcal{M}^{fid}_{\rm const,NES}$ for the fiducial sample and of model $\mathcal{M}^{ext}_{\rm const,NES}$ for the extended sample, i.e. the models with the highest evidences for given sample.

Model	$\ln \mathcal{Z}$	$\ln \mathcal{B}$
$\mathcal{M}^{fid}_{\rm const}$	241.791 ± 0.204	-2.269 ± 0.391
$\mathcal{M}^{fid}_{\rm evo}$	240.645 ± 0.216	-3.415 ± 0.403
$\mathcal{M}^{fid}_{\rm const,NES}$	244.060 ± 0.187	$--$
$\mathcal{M}^{fid}_{\rm evo,NES}$	243.710 ± 0.197	-0.350 ± 0.384
$\mathcal{M}^{ext}_{\rm const}$	284.705 ± 0.225	-2.653 ± 0.431
$\mathcal{M}^{ext}_{\rm evo}$	283.908 ± 0.235	-3.450 ± 0.441
$\mathcal{M}^{ext}_{\rm const,NES}$	287.358 ± 0.206	$--$
$\mathcal{M}^{ext}_{\rm evo,NES}$	286.584 ± 0.222	-0.774 ± 0.428

scale[3] (Table 2.3), while models $\mathcal{M}^{fid}_{\rm const}$ and $\mathcal{M}^{fid}_{\rm evo}$ are rejected with strong evidence. Thus, based on our analysis of the fiducial sample, we conclude that at $z \lesssim 1$ the normalisation of the M_*–$\sigma_{\rm e}$ relation changes with z, while the intrinsic scatter is independent of redshift; the slope β is either constant or increasing with redshift (see Figure 2.13).

The median M_*–$\sigma_{\rm e}$ relations found for models $\mathcal{M}^{fid}_{\rm const,NES}$ and $\mathcal{M}^{fid}_{\rm evo,NES}$ at three representative redshifts are shown in the left panels of Figure 2.14. Quantitatively, according to model $\mathcal{M}^{fid}_{\rm const,NES}$, in the redshift interval $0 \lesssim z \lesssim 1$, the M_*–$\sigma_{\rm e}$ relation is well described by a power law $\sigma_{\rm e} \propto M_*^{\beta}$ with redshift-independent slope $\beta \simeq 0.18$ and intrinsic scatter $\simeq 0.08\,{\rm dex}$ in $\sigma_{\rm e}$ at given M_*. At fixed M_*, $\sigma_{\rm e} \propto (1+z)^{\zeta}$, with $\zeta \simeq 0.40$, so galaxies of given M_* tend to have higher $\sigma_{\rm e}$ at higher redshift: the median velocity dispersion at fixed M_* is a factor ≈ 1.3 higher at $z = 1$ than at $z = 0$. According to model $\mathcal{M}^{fid}_{\rm evo,NES}$, $\sigma_{\rm e}$ varies with M_* and z as $\sigma_{\rm e} \propto {M_*}^{\beta(z)}(1+z)^{\zeta}$, with $\zeta \simeq 0.42$ and $\beta(z) \simeq 0.16 + 0.26\log(1+z)$. For instance, at $z = 1$, the slope of the M_*–$\sigma_{\rm e}$ relation is $\beta \simeq 0.24$. The time variation of $\sigma_{\rm e}$ at given M_* depends on M_*: at $M_* = 10^{11}\,{\rm M}_\odot$ it is similar to that inferred according model $\mathcal{M}^{fid}_{\rm const,NES}$ (Figure 2.13, upper panel).

[3] The difference between models $\mathcal{M}^{fid}_{\rm const}$ and $\mathcal{M}^{fid}_{\rm evo}$ is that $\mathcal{M}^{fid}_{\rm evo}$ has the additional hyper-parameter η (model $\mathcal{M}^{fid}_{\rm evo}$ reduces to model $\mathcal{M}^{fid}_{\rm const}$ for η=0). We note that the posterior distribution of η found for model $\mathcal{M}^{fid}_{\rm evo}$ is such that $\eta = 0$ within 2σ from the median.

In summary, the evolution of the M_*–σ_e relation in the redshift range $0 \lesssim z \lesssim 1$ can be roughly described by

$$\log\left(\frac{\sigma_e}{\mathrm{km\,s^{-1}}}\right) \simeq 2.21 + 0.18\log\left(\frac{M_*}{10^{11}\mathrm{M_\odot}}\right) + 0.40\log(1+z), \tag{2.30}$$

based on the median values of the hyper-parameters of model $\mathcal{M}^{fid}_{\mathrm{const,NES}}$, or

$$\log\left(\frac{\sigma_e}{\mathrm{km\,s^{-1}}}\right) \simeq [0.16 + 0.26\log(1+z)]\log\left(\frac{M_*}{10^{11}\mathrm{M_\odot}}\right) + \\ + 0.42\log(1+z) + 2.22, \tag{2.31}$$

based on the median values of the hyper-parameters of model $\mathcal{M}^{fid}_{\mathrm{evo,NES}}$, with redshift-independent intrinsic scatter $\simeq 0.08\,\mathrm{dex}$ in σ_e at a given M_*.

2.4.2 Extended sample ($0 \lesssim z \lesssim 2.5$)

The results obtained for the extended sample are very similar to those obtained for the fiducial sample. The model with the highest Bayesian evidence is model $\mathcal{M}^{ext}_{\mathrm{const,NES}}$ (Table 2.6), but the performance of model $\mathcal{M}^{ext}_{\mathrm{evo,NES}}$ is comparable on the basis of Jeffreys' scale (see Table 2.3). Models $\mathcal{M}^{ext}_{\mathrm{const}}$ and $\mathcal{M}^{ext}_{\mathrm{evo}}$ are rejected with strong evidence. Thus, on the basis of our data, over the redshift range $0 \lesssim z \lesssim 2.5$ the M_*–σ_e relation of ETGs evolves in time by changing its normalisation, with redshift-independent intrinsic scatter, and with slope either constant or increasing with redshift (see Figure 2.13).

The median M_*–σ_e relations of models $\mathcal{M}^{ext}_{\mathrm{const,NES}}$ and $\mathcal{M}^{ext}_{\mathrm{evo,NES}}$ at five representative redshifts are shown in the right panels of Figure 2.14. Quantitatively, according to model $\mathcal{M}^{ext}_{\mathrm{const,NES}}$, in the redshift interval $0 \lesssim z \lesssim 2.5$, the M_*–σ_e relation is well described by a power law $\sigma_e \propto M_*^{\beta}$ with slope $\beta \simeq 0.18$ and intrinsic scatter $\simeq 0.08\,\mathrm{dex}$ in σ_e at given M_*: at fixed M_*, $\sigma_e \propto (1+z)^{\zeta}$, with $\zeta \simeq 0.48$, so galaxies of given M_* tend to have higher σ_e at higher redshift. For instance, the median velocity dispersion at fixed M_* is a factor ≈ 1.7 higher at $z = 2$ than at $z = 0$. According to model $\mathcal{M}^{ext}_{\mathrm{evo,NES}}$, σ_e varies with M_* and z as $\sigma_e \propto M_*^{\beta(z)}(1+z)^{\zeta}$, with $\zeta \simeq 0.51$ and $\beta(z) \simeq 0.17 + 0.18\log(1+z)$ (so $\beta \simeq 0.26$ at $z = 2$; Figure 2.13, lower panel). The time variation of σ_e at given M_* depends on M_*, but at $M_* = 10^{11}\,\mathrm{M_\odot}$ is similar to that obtained with model $\mathcal{M}^{ext}_{\mathrm{const,NES}}$ (Figure 2.13, upper panel)

In summary, the evolution of the M_*–σ_e relation in the redshift range $0 \lesssim z \lesssim 2.5$ can be roughly described by

$$\log\left(\frac{\sigma_e}{\mathrm{km\,s^{-1}}}\right) \simeq 2.21 + 0.18\log\left(\frac{M_*}{10^{11}\mathrm{M_\odot}}\right) + 0.48\log(1+z), \tag{2.32}$$

based on the median values of the hyper-parameters of model $\mathcal{M}^{ext}_{\mathrm{const,NES}}$, or

$$\log\left(\frac{\sigma_e}{\mathrm{km\,s^{-1}}}\right) \simeq [0.17 + 0.18\log(1+z)]\log\left(\frac{M_*}{10^{11}\mathrm{M_\odot}}\right) + \\ + 0.51\log(1+z) + 2.21, \tag{2.33}$$

based on the median values of the hyper-parameters of model $\mathcal{M}^{ext}_{\mathrm{evo,NES}}$, with redshift-independent intrinsic scatter $\simeq 0.08\,\mathrm{dex}$ in σ_e at a given M_*.

2.4.3 Comparing the results for the fiducial and extended samples

Among the hyper-parameters of model $\mathcal{M}_{\mathrm{const,NES}}$, only ζ, which quantifies the redshift dependence of σ_e at given M_*, contains physical information on the M_*–σ_e relation: the other five hyper-parameters describe properties of the galaxy sample. Thus, when comparing the inferences obtained for model $\mathcal{M}_{\mathrm{const,NES}}$ applied to the fiducial and extended samples (Figure 2.11), we must focus on the inference on ζ. For model $\mathcal{M}_{\mathrm{evo,NES}}$, instead, the physical information is contained in the hyper-parameters η and ζ, which must be considered when comparing the inferences for models $\mathcal{M}^{fid}_{\mathrm{evo,NES}}$ and $\mathcal{M}^{ext}_{\mathrm{evo,NES}}$ (Figure 2.12). While the differences in the distributions of η between $\mathcal{M}^{fid}_{\mathrm{evo,NES}}$ and $\mathcal{M}^{ext}_{\mathrm{evo,NES}}$ are well within 1σ, the differences in the distributions of ζ are between 1σ and 2σ for both pairs of models ($\mathcal{M}^{fid}_{\mathrm{const,NES}}$-$\mathcal{M}^{ext}_{\mathrm{const,NES}}$ and $\mathcal{M}^{fid}_{\mathrm{evo,NES}}$-$\mathcal{M}^{ext}_{\mathrm{evo,NES}}$). Thus, while we find no significant differences in η, the extended-sample data prefer a somewhat higher value of ζ than the fiducial-sample data, suggesting that the evolution of σ_e at a given M_* might be stronger at higher redshift.

However, we recall that the extended sample is not as homogeneous and complete as the fiducial sample, so the aforementioned difference in ζ could be produced by some observational bias. For instance, while for the fiducial sample we selected ETGs on the basis of morphology and strength of emission lines, in some of the subsamples of the high-redshift sample (Belli et al. 2014b and Belli et al. 2017), ETGs were selected using also the so-called UVJ colour-colour diagram, which is a useful tool to separate passive and star-forming galaxies (e.g. Moresco et al., 2013). To quantify

the effect of these different selection criteria, we performed the following test. Using UVJ colour measures from the UltraVISTA survey (Muzzin et al. 2013a), we placed the LEGA-C galaxies of our fiducial sample in the UVJ diagram, finding that 90% of them lie in the locus of passive galaxies (see Cannarozzo et al. 2020b). We then modified our fiducial sample by excluding the remaining 10% of the LEGA-C galaxies and applied model $\mathcal{M}^{fid}_{\rm const,NES}$ to this modified fiducial sample, finding inferences on the hyper-parameters (in particular $\zeta = 0.408^{+0.032}_{-0.031}$) in agreement within 1σ with those of $\mathcal{M}^{fid}_{\rm const,NES}$ shown in Figure 2.11. This test, presented in Appendix 2.D, indicates that the results obtained for the extended sample should be independent of whether the UVJ-colour selection is used as additional criterion to define the sample of ETGs. Of course the selection of the extended sample is heterogeneous also in other respects, so we cannot exclude that there are other non-negligible biases.

As a more general comment, we note that, for both the fiducial and the extended samples, the results on the evolution of the M_*–$\sigma_{\rm e}$ relation hold within the assumption that the slope and the normalisation vary as power laws of $1+z$. Our inferences on the redshift intervals in which we have no galaxies ($0.2 < z < 0.6$) or very few galaxies ($z > 1.75$) in our samples (Figure 2.8) clearly rely on this assumption and are thus driven by the properties of galaxies in other redshift intervals.

2.5 Discussion

2.5.1 Potential systematics

Our inference relies on measurements of the stellar mass and central velocity dispersion of galaxies. Both these quantities are subject to systematic effects that could in principle affect our results. The biggest systematics are those affecting the stellar mass measurements, which we discuss here.

Stellar mass measurements are the result of fits of Sérsic profiles to broad band photometric data, from which luminosities and colours are derived and subsequently fitted with stellar population synthesis models. One possible source of systematics is a deviation of the true stellar density profile of a galaxy from a Sérsic profile. For instance, as shown by Sonnenfeld et al. (2019) in their study of a sample of massive ellipticals at $z \sim 0.6$, it is difficult to distinguish between a pure Sérsic model and a model consisting of the sum of a Sérsic and an exponential component, even with relatively deep data from the HSC survey: differences between the two

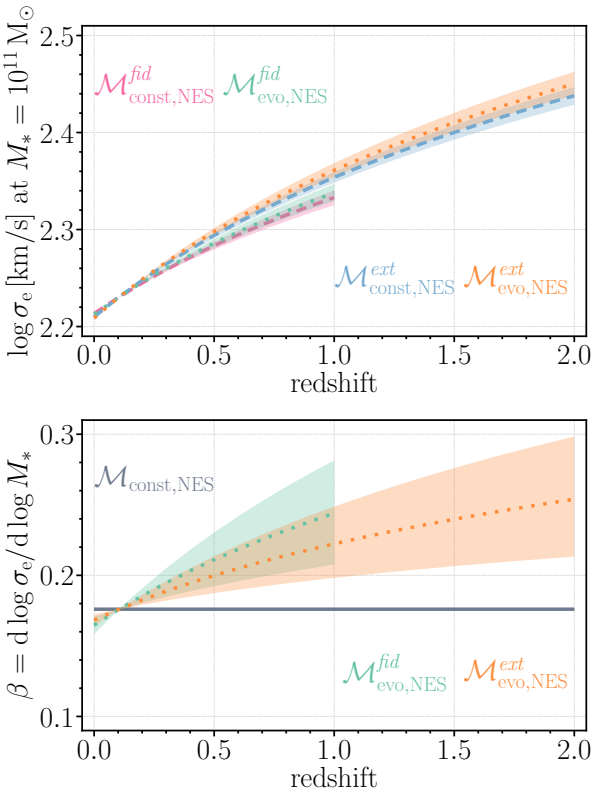

Fig. 2.13: Median central stellar velocity dispersion σ_e at $M_* = 10^{11}\,M_\odot$ (upper panel) and slope β of the M_*–σ_e relation (lower panel) as functions of redshift for models $\mathcal{M}^{fid}_{\rm const,NES}$ (pink dashed curve), $\mathcal{M}^{fid}_{\rm evo,NES}$ (green dotted curves), $\mathcal{M}^{ext}_{\rm const,NES}$ (azure dashed curve) and $\mathcal{M}^{ext}_{\rm evo,NES}$ (orange dotted curves). In the lower panel the curves for models $\mathcal{M}^{fid}_{\rm const,NES}$ and $\mathcal{M}^{ext}_{\rm const,NES}$ are identical, and are represented by the grey solid line. The curves are obtained by computing, at given x, the median value of y (where x and y are the quantities in abscissa and ordinate, respectively) among all the values sampled by the posterior distribution obtained with the MCMC; similarly, the shaded bands, which we will refer to as 1σ uncertainty bands, are defined by computing the 16% and the 84% of the distribution of y, at given x, for the same sampling.

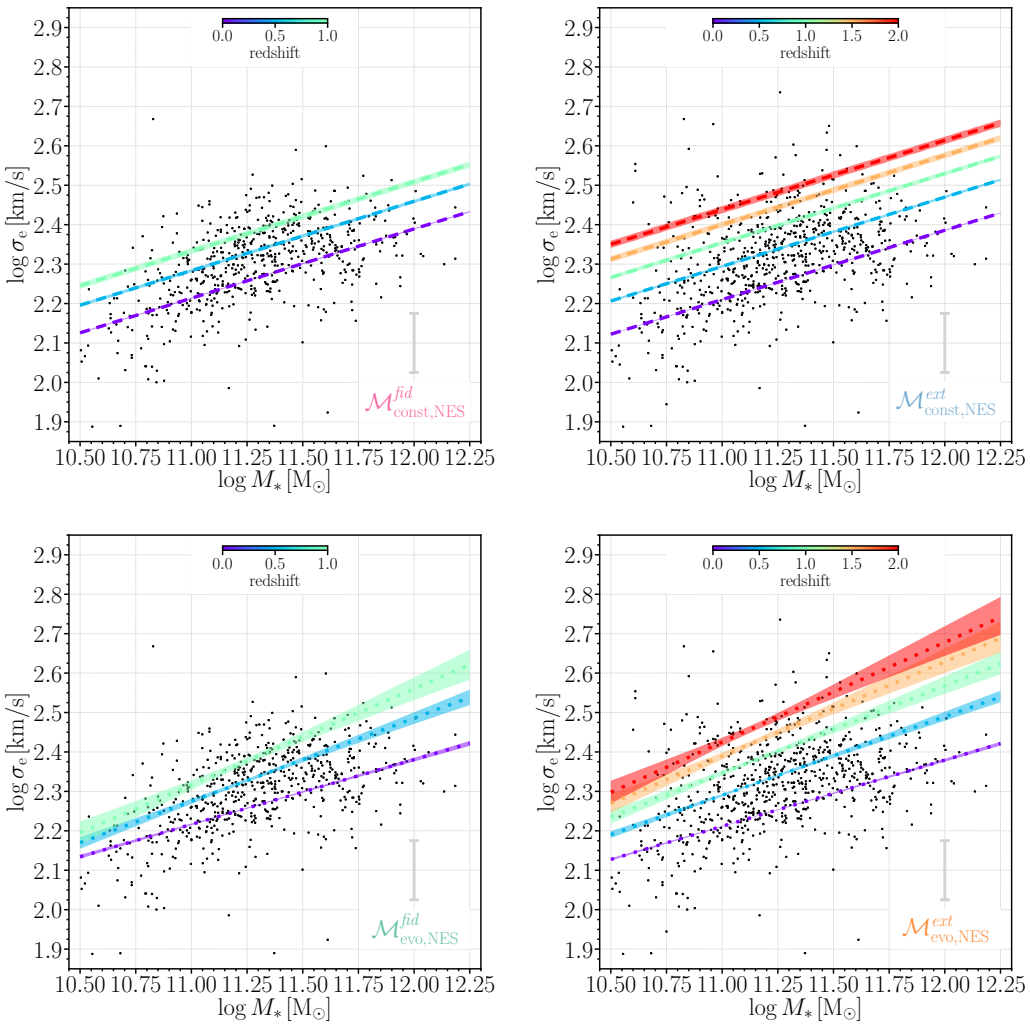

Fig. 2.14: Central stellar velocity dispersion as a function of stellar mass. In the left panels the curves represent the median relations of the fiducial-sample models $\mathcal{M}^{fid}_{\rm const,NES}$ (upper panel) and $\mathcal{M}^{fid}_{\rm evo,NES}$ (lower panel), at $z = 0$, $z = 0.5$ and $z = 1$. In the right panels the curves represent the median relations of the extended-sample models $\mathcal{M}^{ext}_{\rm const,NES}$ (upper panel) and $\mathcal{M}^{ext}_{\rm evo,NES}$ (lower panel), at $z = 0$, $z = 0.5$, $z = 1$, $z = 1.5$ and $z = 2$. The bands indicate the 1σ uncertainty ranges. The median relations and the 1σ bands are computed as described in the caption of Figure 2.13. The grey error bars represent the redshift-independent intrinsic scatter. The dots indicate the positions in these diagrams of the ETGs of the fiducial (left panels) and extended (right panels) samples.

models only arise at large radii and can lead to variations in the estimated luminosity on the order of 0.1 dex. Secondly, our models assume implicitly that the stellar population parameters of a galaxy are spatially constant. However, if these vary as a function of radius, a bias on the inferred stellar masses could be introduced. More generally, the stellar population synthesis models on which our M_* measurements are based are known to be subject to systematics (see e.g. Conroy, 2013a). Most importantly, uncertainties on the stellar IMF can lead to a global shift of the stellar mass distribution, affecting the inference on the normalisation of the M_*–σ_e relation μ_0, and/or the slope of the relation β_0, in case the IMF varies as a function of mass. Additionally, gradients in the IMF can also introduce biases: along with M_*/L gradients at fixed IMF, these are particularly relevant if our measurements are used to quantify the stellar component to the dynamical mass of a galaxy (see e.g. Bernardi et al., 2018; Li et al., 2018; Sonnenfeld et al., 2018; Domínguez Sánchez et al., 2019, and related discussions).

All of these systematic effects are common to virtually all estimates of the M_*–σ_0 relation in the literature and are difficult to address, given our current knowledge on the accuracy of our models of galaxy stellar profiles and stellar populations. Nevertheless, they should be taken into consideration when comparing our observations with theoretical models.

2.5.2 Comparison with previous works

In this section we compare our results on the M_*–σ_e relation with previous works in the literature, which we briefly describe in the following.

- Auger et al. (2010) study a sample of 59 ETGs (morphologically classified as ellipticals or S0s) identified as strong gravitational lenses in the Sloan Lens ACS Survey (SLACS) (Bolton et al., 2008; Auger et al., 2009) with a mean redshift $z \approx 0.2$. The stellar masses of these ETGs span the range $11 < \log(M_*/\mathrm{M}_\odot) < 12$. Auger et al. (2010) report fits of the M_*–$\sigma_{\mathrm{e}/2}$ relation both allowing and not allowing for the presence of intrinsic scatter ($\sigma_{\mathrm{e}/2}$ is the velocity dispersion within an aperture $R_\mathrm{e}/2$).

- Hyde & Bernardi (2009a) extract 46410 ETGs from the SDSS DR4 with parameters updated to the DR6 values (Adelman-McCarthy et al., 2008), selecting galaxies with $60 < \sigma_{\mathrm{e}/8}/(\mathrm{km\,s^{-1}}) < 400$, where $\sigma_{\mathrm{e}/8}$ is the stellar velocity dispersion measured within an aperture $R_\mathrm{e}/8$, in the redshift range $0.07 < z \leq 0.35$. Hyde & Bernardi (2009a) fit the distribution of $\log \sigma_{\mathrm{e}/8}$

as a function of $\log M_*$ both with a linear function, over the stellar mass range $10.5 < \log(M_*/\mathrm{M}_\odot) < 11.5$, and with a quadratic function, in the range $9.5 < \log(M_*/\mathrm{M}_\odot) < 12$.

- Damjanov et al. (2018) estimate the M_*–σ_0 relation of 565 quiescent galaxies of the hCOS20.6 sample, with $10.5 < \log(M_*/\mathrm{M}_\odot) < 11.4$, in the redshift range $0.2 < z < 0.5$. The velocity dispersions, corrected to an aperture of $3\,\mathrm{kpc}$, can be taken as good approximations (to within $3-4\%$; I. Damjanov, private communication) of measurements of σ_e.

- Zahid et al. (2016a) analyse the M_*–σ_0 relation for massive quiescent galaxies out to $z \approx 0.7$. For our comparison, we use their power-law fit obtained for a subsample of 1316 galaxies drawn from the Smithsonian Hectospec Lensing Survey (SHELS; Geller et al. 2005) at $0.3 < z < 0.4$. Also in this case the velocity dispersions, which are corrected to an aperture of $3\,\mathrm{kpc}$, can be taken as measurements of σ_e.

- Belli et al. (2014a) measure σ_e and M_* for a sample of galaxies with median redshift $z \simeq 1.23$. We take from Zahid et al. (2016a) the best fit parameters of the M_*–σ_e relation for the sample of Belli et al. (2014a).

- Mason et al. (2015) study the redshift evolution of the M_*–σ_e relation, assuming redshift-independent slope determined by the low-z relation measured by Auger et al. (2010), finding that σ_e at fixed M_* increases with redshift as $(1+z)^{0.2}$ In particular, we consider here the fit of Mason et al. evaluated at $z = 0.35, 1.23$ and 2, taking as reference the fit of Auger et al. (2010) with non-zero intrinsic scatter.

In order to compare the results of the different works, we express all the fits in the form

$$\log\left(\frac{\sigma_\mathrm{e}}{\mathrm{km\,s^{-1}}}\right) = \mu + \beta \log\left(\frac{M_*}{M_*^\mathrm{piv}}\right) + \gamma\left[\log\left(\frac{M_*}{M_*^\mathrm{piv}}\right)\right]^2, \tag{2.34}$$

where $M_*^\mathrm{piv} = 10^{11.321}\,\mathrm{M}_\odot$ (Chabrier IMF). We correct for aperture the fits of Auger et al. (2010) and Hyde & Bernardi (2009a) using Equation 2.3, so $\log\sigma_\mathrm{e} = \log\sigma_{\mathrm{e}/8} - 0.06$ and $\log\sigma_\mathrm{e} = \log\sigma_{\mathrm{e}/2} - 0.02$. Except for the quadratic fit of Hyde & Bernardi (2009a), all the other fits assume $\gamma = 0$ in Equation 2.34. The values of the parameters of Equation 2.34 for the considered literature works are reported in Table 2.7. In Figure 2.20, we show the comparison between our models and the previous works at $z = 0.2$, 0.35, 1.23 and 2.

Tab. 2.7: Values of the parameters of Equation 2.34, according to the fits of the literature works that we compared with our model. $\gamma = 0$ in all cases, but in the case of the quadratic fit of Hyde & Bernardi (2009a), for which $\gamma = -0.044$.

Redshift	Reference	μ	β
$z \simeq 0.2$	Auger et al. (2010)	2.38	0.24
	Auger et al. (2010) with intrinsic scatter	2.38	0.18
	Hyde & Bernardi (2009a) Linear fit	2.32	0.29
	Hyde & Bernardi (2009a) Quadratic fit	2.32	0.24
$z \simeq 0.35$	Damjanov et al. (2018) hCOS20.6 ($0.2 < z < 0.5$)	2.37	0.25
	Zahid et al. (2016a) SHELS ($0.3 < z < 0.4$)	2.38	0.31
$z = 0.35$	Mason et al. (2015)	2.39	0.18
$z \simeq 1.23$	Belli et al. (2014a)	2.48	0.30
$z = 1.23$	Mason et al. (2015)	2.43	0.18
$z = 2$	Mason et al. (2015)	2.46	0.18

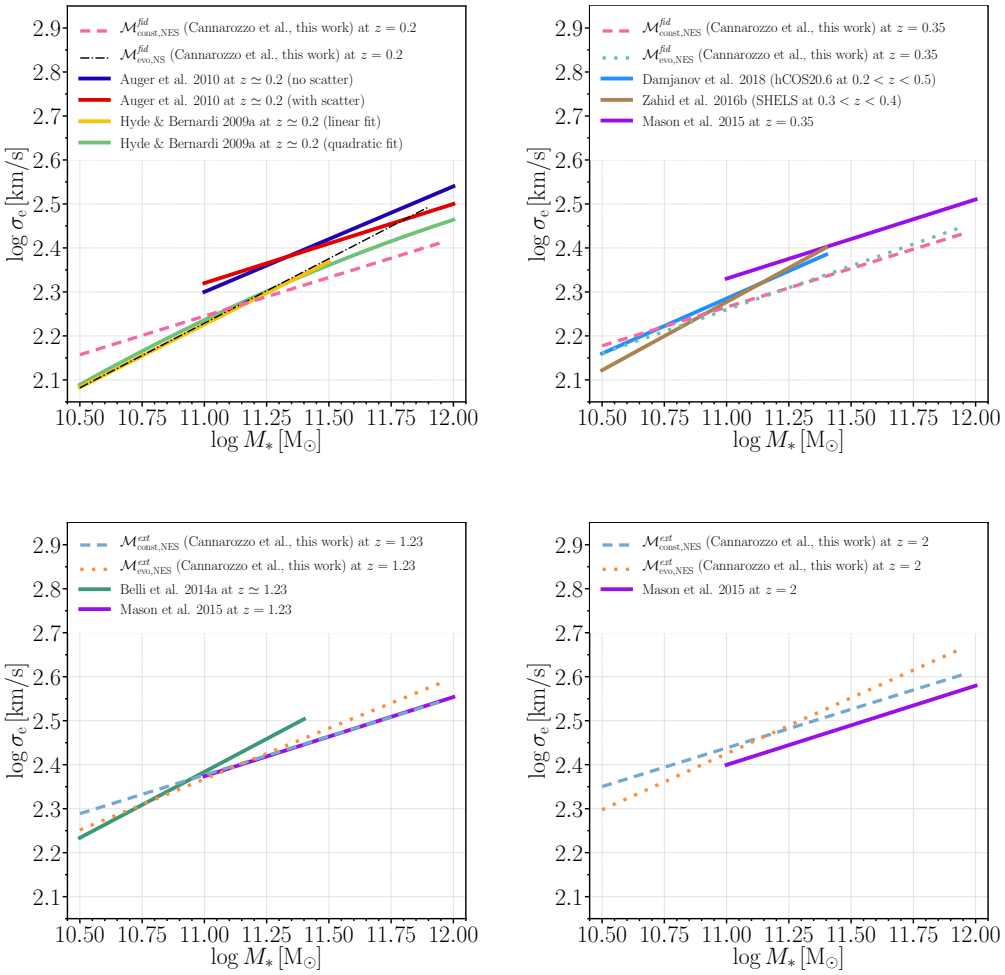

Fig. 2.15: Comparison between the median M_*–σ_e relations of our models $\mathcal{M}_{const,NES}$ (dashed curves) and $\mathcal{M}_{evo,NES}$ (dotted curves), and fits from the literature (solid curves) at $z = 0.2$ (upper left panel), $z = 0.35$ (upper right panel), $z = 1.23$ (lower left panel) and $z = 2$ (lower right panel). Upper left panel: the red and blue solid curves are the linear fits of Auger et al. (2010), including and not including the intrinsic scatter, respectively, while the gold and light green solid curves are the linear and the quadratic fits of Hyde & Bernardi (2009a), respectively. The thin dash-dotted curve is the median relation of model $\mathcal{M}^{fid}_{evo,NS}$, in which we assume zero intrinsic scatter (see text). Upper right panel: the azure curve is the linear fit for the hCOS20.6 galaxies ($0.2 < z < 0.5$) by Damjanov et al. (2018), the brown curve is the linear fit of Zahid et al. (2016a) for the SHELS sample ($0.3 < z < 0.4$) and the violet curve is the fit of Mason et al. (2015) evaluated at $z = 0.35$. Lower left panel: the green curve is the linear fit of Belli et al. (2014a) and the violet curve is the fit of Mason et al. (2015) evaluated at $z = 1.23$. Lower right panel: the violet curve is the fit of Mason et al. (2015) evaluated at $z = 2$. Each curve is shown over the stellar mass range spanned by the considered data set.

At $z = 0.2$ (upper left panel of Figure 2.20) we compare our results with Auger et al. (2010) and Hyde & Bernardi (2009a). The curve of model $\mathcal{M}^{fid}_{\rm const,NES}$ at $z = 0.2$ intersects the linear fit of Hyde & Bernardi (2009a), but has shallower slope, similar to the fits to lens ETGs of Auger et al. (2010), which however have $\approx 20\%$ higher normalisation, probably reflecting the fact that, at given stellar mass, higher velocity dispersion galaxies are more efficient lenses. At $z = 0.2$ the median relation of model $\mathcal{M}^{fid}_{\rm evo,NES}$, not shown in the plot, is very similar to that of model $\mathcal{M}^{fid}_{\rm const,NES}$. The steeper slope β of the fits of Hyde & Bernardi (2009a) can be ascribed to two main reasons: they exclude the highest-mass galaxies and they do not allow for intrinsic scatter in their model. The fact that the correlation is shallower at higher M_* is apparent from the shape of the quadratic fit of Hyde & Bernardi (2009a). The difference between the two fits of Auger et al. (2010) illustrates the effect on β of allowing for intrinsic scatter. As a further test of the importance of considering the intrinsic scatter in the model, we applied to the fiducial sample the analysis described in section 2.3, but assuming zero intrinsic scatter ($\sigma_\sigma = 0$ in equation 2.22) for models $\mathcal{M}_{\rm const}$ and $\mathcal{M}_{\rm evo}$. Based on the Bayesian evidence, in this case the best model is $\mathcal{M}^{fid}_{\rm evo,NS}$, i.e. an evolving-slope model with a null scatter (NS) that can be approximately described by

$$\log\left(\frac{\sigma_{\rm e}}{\rm km\,s^{-1}}\right) \simeq 2.21 + \beta(z)\left(\frac{M_*}{10^{11}{\rm M}_\odot}\right) + 0.46\log(1+z), \tag{2.35}$$

with $\beta(z) = 0.22 + 0.89\log(1+z)$. This model evaluated at $z = 0.2$ (dash-dotted curve in upper left panel of Figure 2.20) has slope $\beta \simeq 0.29$ and overlaps almost perfectly with the linear fit of Hyde & Bernardi (2009a).

In the upper right panel of Figure 2.20 we compare our models $\mathcal{M}^{fid}_{\rm const,NES}$ and $\mathcal{M}^{fid}_{\rm evo,NES}$ at $z = 0.35$ with the fits obtained by Mason et al. (2015) at the same redshift, by Damjanov et al. (2018) at $0.2 < z < 0.5$ and by Zahid et al. (2016a) for SHELS galaxies at $0.3 < z < 0.4$. Taking into account the differences in the stellar-mass range, and that Damjanov et al. (2018) and Zahid et al. (2016a) do not allow for the presence of intrinsic scatter, there is reasonable agreement among the five curves.

In the lower left panel of Figure 2.20 we compare our models $\mathcal{M}^{ext}_{\rm const,NES}$ and $\mathcal{M}^{ext}_{\rm evo,NES}$ at $z = 1.23$ (mean redshift of the sample of Belli et al. 2014a) with the linear fit obtained by Belli et al. (2014a) and that of Mason et al. (2015) at the same redshift. Considering that Belli et al. (2014a) do not allow for the presence of intrinsic scatter, the four curves are broadly consistent.

In the lower right panel of Figure 2.20 we compare the median relations of our models $\mathcal{M}^{ext}_{\rm const,NES}$ and $\mathcal{M}^{ext}_{\rm evo,NES}$ with the estimate of Mason et al. (2015) at $z = 2$, finding that our relations predict a higher velocity dispersion at the same stellar mass, which is a consequence of the fact that the Mason et al. (2015) find a weaker redshift dependence of the normalisation than our models.

Overall, we do find a satisfactory agreement among our results and previous works in the literature. Some of the differences pointed out above may be ascribed to different redshift distributions of the galaxy sample, stellar mass ranges, data and models used in the measurements of the stellar masses, selection criteria or fitting methods. For instance, it is apparent from Figure 2.20 that different studies consider different stellar mass intervals. Studies focusing on lower stellar masses tend to find steeper slopes than those focusing on higher stellar masses. Furthermore, allowing for the presence of intrinsic scatter when modelling the data leads to shallower slopes. Models allowing for the presence of intrinsic scatter, such as those presented in this work, are expected to provide a more correct description of the M_*–$\sigma_{\rm e}$ correlation.

2.5.3 Connection with the size evolution of ETGs

It is useful discuss the results here obtained for the evolution of the M_*–$\sigma_{\rm e}$ relation of ETGs in light of the well known evolution of the M_*–$R_{\rm e}$ relation: the redshift dependence of the median effective radius at fixed stellar mass can be parameterised as $R_{\rm e} \propto (1+z)^{a_{\rm R}}$. The value of $a_{\rm R}$ for ETGs appears to depend somewhat on the considered sample, mass and redshift intervals, ranging from $a_{\rm R} \approx -1.5$ (van der Wel et al. 2014; $0 \lesssim z \lesssim 3$) to $a_{\rm R} \approx -0.6$ (Cimatti et al. 2012; $0 \lesssim z \lesssim 2$). If all the ETGs in the considered redshift range were structurally and kinematically homologous (see, e.g., section 5.4.1 of Cimatti, Fraternali, & Nipoti 2019), we would have $\sigma_{\rm e}^2 \propto M_*/R_{\rm e}$ and thus, at fixed stellar mass M_*, $\sigma_{\rm e} \propto R_{\rm e}^{-1/2} \propto (1+z)^{\zeta_{\rm hom}}$, with $\zeta_{\rm hom} = -a_{\rm R}/2$. For $-1.5 \lesssim a_{\rm R} \lesssim -0.6$, we get $0.3 \lesssim \zeta_{\rm hom} \lesssim 0.75$. This toy model is consistent with our observational finding $\sigma_{\rm e} \propto (1+z)^{\zeta}$ with $0.4 \lesssim \zeta \lesssim 0.5$.

It must be stressed that the observed value of ζ must not be necessarily equal to $\zeta_{\rm hom}$. From a theoretical point of view, an observed evolution in $\sigma_{\rm e}$ different than predicted by the above toy model can be expected if ETGs do not evolve maintaining homology. For instance, dry merging, which is one of the processes believed to be responsible for the size and velocity dispersion evolution of ETGs (see Chapter 1), is known to produce non-homology, because it varies the shape and the kinematics of the stellar distribution, and the mutual density distributions of luminous and

dark matter (Nipoti et al., 2003; Hilz et al., 2013; Frigo & Balcells, 2017). We can quantify the effect of non-homology by defining the dimensionless parameter

$$k_* \equiv \frac{GM_*}{\sigma_\mathrm{e}^2 R_\mathrm{e}}, \tag{2.36}$$

such that galaxies that are structurally and kinematically homologous have the same value of k_*. If, at fixed M_*, $R_\mathrm{e} \propto (1+z)^{a_\mathrm{R}}$ and $\sigma_\mathrm{e} \propto (1+z)^{\zeta}$, the average value of k_* must vary with redshift as $k_* \propto (1+z)^{a_\mathrm{k}}$ with $a_\mathrm{k} = -(2\zeta + a_\mathrm{R})$. Thus, we have $\zeta \neq -a_\mathrm{R}/2$ if $a_\mathrm{k} \neq 0$, i.e. if, on average, galaxies at different redshift have different k_*. However, from an observational point of view, a significant evolution of k_* seems to be excluded. Defining the dynamical mass $M_\mathrm{dyn} \equiv 5\sigma_\mathrm{e}^2 R_\mathrm{e}/G$, the average ratio $M_*/M_\mathrm{dyn} \propto k_*$ is found to increase mildly with redshift (for galaxies with $M_* > 10^{11}\,\mathrm{M}_\odot$, it varies as $(1+z)^{0.17}$ from $\simeq 0.6$ at $z = 0$ up to $\simeq 0.9$ at $z > 1.5$; van de Sande et al. 2013), or even remain constant ($\simeq 0.7$ in the range $0 < z < 1.6$; Belli et al. 2014a), and the zero point of the stellar-mass fundamental plane (which also can be seen as a measure of the average k_*) varies only little with redshift (Bezanson et al., 2013a; Zahid et al., 2016b).

For our extended sample of galaxies we computed the median k_* by binning the galaxies in bins of either Sérsic index or redshift. We found that k_* decreases systematically for increasing n, ranging, on average, from $k_* \approx 4$ for $n = 2$ to $k_* \approx 1.5$ for $n = 10$, suggesting a moderate structural non-homology (see Bertin et al., 2002). The median k_* is ≈ 2.5 at $z = 0$ and tends to increase with redshift, but only by a factor of ≈ 1.5 from $z \approx 0$ to $z > 1$.

2.6 Conclusions

We have studied the evolution of the correlation between central stellar velocity dispersion σ_e (measured within R_e) and stellar mass M_* for massive ($M_* \gtrsim 10^{10.5}\,\mathrm{M}_\odot$) ETGs observed in the redshift range $0 \lesssim z \lesssim 2.5$. We have modelled the evolution of this scaling law using a Bayesian hierarchical method. This allowed us to optimally exploit the available observational data, without resorting to binning in either redshift or stellar-mass space. The main conclusions of this work are the following.

- On average, the central velocity dispersion of massive ($M_* \gtrsim 10^{10.5}\,\mathrm{M}_\odot$) ETGs increases with stellar mass following a power-law relation $\sigma_\mathrm{e} \propto M_*^{\beta}$ with either $\beta \simeq 0.18$, independent of redshift, or β increasing with redshift as

$\beta \simeq 0.16 + 0.26\log(1+z)$ in the redshift range $0 \lesssim z \lesssim 1$ probed by our fiducial sample.

- The normalisation of the M_*–σ_e relation increases with redshift: for instance, when $\beta \simeq 0.18$ independent of redshift, at fixed stellar mass $\sigma_\mathrm{e} \propto (1+z)^\zeta$ with $\zeta \simeq 0.4$ out to $z \approx 1$. In other words, a typical ETG of $M_* \approx 10^{11}\,\mathrm{M}_\odot$ at $z \approx 0$ has σ_e lower by a factor ≈ 1.3 than ETGs of similar stellar mass at $z \approx 1$.

- The intrinsic scatter of the M_*–σ_e relation is $\simeq 0.08$ dex in σ_e at given M_*, independent of redshift.

- Over the wider redshift range $0 \lesssim z \lesssim 2.5$, probed by our extended sample, we find results similar to those found for the $z \lesssim 1$ fiducial sample, with slightly stronger redshift dependence of the normalisation ($\zeta \simeq 0.5$) and weaker redshift dependence of the slope ($\mathrm{d}\beta/\mathrm{d}\log(1+z) \simeq 0.18$) when β varies with time. On average, the velocity dispersion of ETGs of $M_* \approx 10^{11}\,\mathrm{M}_\odot$ at $z = 2$ is a factor of ≈ 1.7 higher than that of $z = 0$ ETGs of similar stellar mass.

The results of this work confirm and strengthen previous indications that the M_*–σ_e relation of massive ETGs evolves with cosmic time. The theoretical interpretation of the observed evolution is not straightforward. Of course, the stellar mass of an individual galaxy can vary with time: it can increase as a consequence of mergers and star formation and decrease as a consequence of mass return by ageing stellar populations. In the standard paradigm, the first effect is dominant, so we expect that, as cosmic time goes on, an individual galaxy moves in the M_*–σ_e plane in the direction of increasing M_*. As pointed out in Chapter 1, the variation of σ_e for an individual galaxy is more uncertain: even pure dry mergers can make it increase or decrease depending on the merging orbital parameters and mass ratio. It is then clear that, at least qualitatively, the evolution shown in Figure 2.14 could be reproduced by individual galaxies evolving at decreasing σ_e, but, at least at the low-mass end, even an evolution of individual galaxies at constant or slightly increasing σ_e is not excluded. Remarkably, our results suggest that, on average, the stellar velocity dispersion of individual galaxies with $M_* \gtrsim 3 \times 10^{11}\mathrm{M}_\odot$ at $z \approx 1$ must decrease from $z \approx 1$ to $z \approx 0$ for them to end up on the median present-day M_*–σ_e relation.

An additional complication to the theoretical interpretation of the evolution of the scaling laws of ETGs is that it is not guaranteed that the high-z (say $z \approx 2$) ETGs are representative of the progenitors of all present-day ETGs. If the progenitors of some of the present-day ETGs were star-forming at $z \approx 2$, they would not be included in our sample of $z \approx 2$ ETGs: this is the so-called *progenitor bias*, which must be

accounted for when interpreting the evolution of a population of objects. However, the effect of progenitor bias should be small at least for the most massive ETGs in the redshift range $0 \lesssim z \lesssim 1$, in which the number density of quiescent galaxies shows little evolution (López-Sanjuan et al., 2012).

The theoretical interpretation of the evolution of the scaling relations of ETGs can benefit from the comparison of the observational data with the results of cosmological simulations of galaxy formation. In this approach, the progenitor bias can be taken into account automatically if simulated and observed galaxies are selected with consistent criteria. Moreover, in the simulations we can trace the evolution of individual galaxies, which is a crucial piece of information that we do not have for individual observed galaxies. The method presented in this Chapter is suitable to be applied to samples of simulated as well as observed galaxies. In the near future we plan to apply this method to compare the observed evolution of the M_*–σ_e relation of ETGs with the results of state-of-the-art cosmological simulations of galaxy formation.

Appendix 2.A: Comparison with independent estimates of the stellar mass of SDSS galaxies

In this work we have estimated the stellar masses of the SDSS and LEGA-C galaxies anew in a self-consistent way. As a sanity check and for comparison with other works, it is useful to compare our estimates with others available in the literature. For this purpose, we contrast here, for our SDSS sample of ETGs, our values of M_* with those obtained for the same galaxies by M14, who measured M_* for $\approx$ 660,000 galaxies of the SDSS DR7 Legacy Survey, relying on the photometric analysis of Simard et al. (2011) in the g and r bands, extended by M14 also to the u, i and z bands (we took M14's stellar mass estimates from the UPENN_PHOTDEC_MSTAR[4] catalogue of Meert et al. 2015).

Both our and M14's stellar masses are obtained by multiplying the galaxy luminosity L by the stellar mass-to-light ratio M_*/L, so it is interesting to compare independently estimates of these two quantities. Since our stellar masses are based on a Sérsic photometric fit, we limit our comparison to the stellar mass estimates of M14 based on the pure Sérsic fits of Simard et al. (2011). We calculate M14's stellar mass-to-light ratio in the r band M_*/L_r related to two different models considered: one based on a "dust-free" model (assuming zero dust extinction) and the other on a "dusty" model (assuming non-zero dust extinction). In Figure 2.16, we show, for the $\approx$ 2000 galaxies of our SDSS sample (see Table 2.1), the distributions of the ratios between our M_*/L_r and those of M14 (left panel), and of the ratios between our r-band luminosities L_r and those obtained by Simard et al. (2011) for pure Sérsic fits. The overall agreement is good, though, on average, our M_*/L_r tend to be slightly lower and our L_r slightly higher than those of M14 and Simard et al. (2011), respectively. In Figure 2.17 we show, for the same galaxies as in Figure 2.16, the dust-free (left panel) and dusty (right panel) stellar masses of M14 as functions of our stellar masses. In both cases, there is remarkably good agreement between our and M14's stellar masses: the linear fits are very close the 1:1 relation and the scatter is relatively small.

[4] Available at http://alan-meert-website-aws.s3-website-us-east-1.amazonaws.com/fit_catalog/download/index.html.

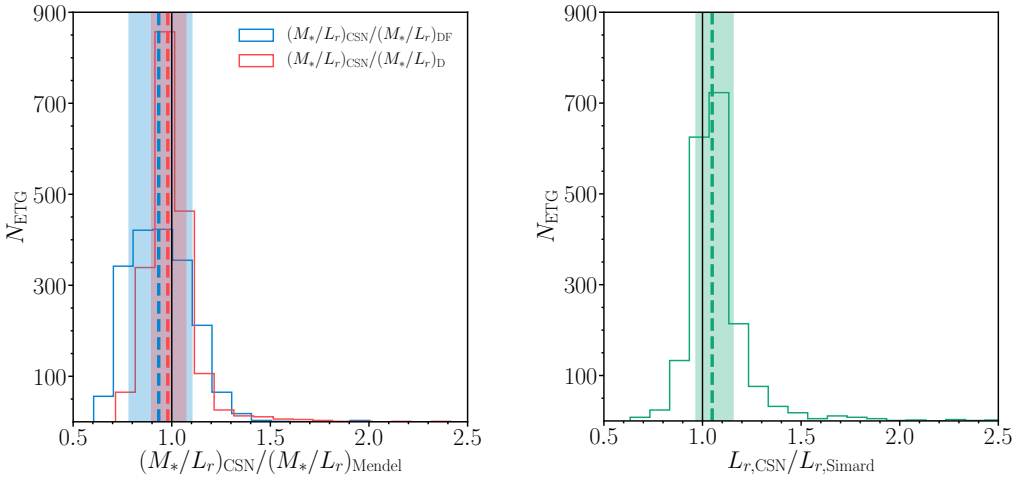

Fig. 2.16: Left panel: distribution of the ratio between our r-band stellar mass-to-light ratio ($(M_*/L_r)_{\rm CSN}$) and those obtained by M14 assuming dust-free ($(M_*/L_r)_{\rm DF}$, blue histogram) and dusty ($(M_*/L_r)_{\rm D}$, red histogram) models for the SDSS galaxies of our sample. Right panel: distribution of the ratio between our r-band luminosity ($L_{r,\rm CSN}$) and that of Simard et al. (2011) ($L_{r,\rm Simard}$) for the same galaxies as in the left panel. In both panels, the dashed lines represent the medians of the distributions, while the intervals between the 16-th and 84-th percentiles are indicated by the shaded areas.

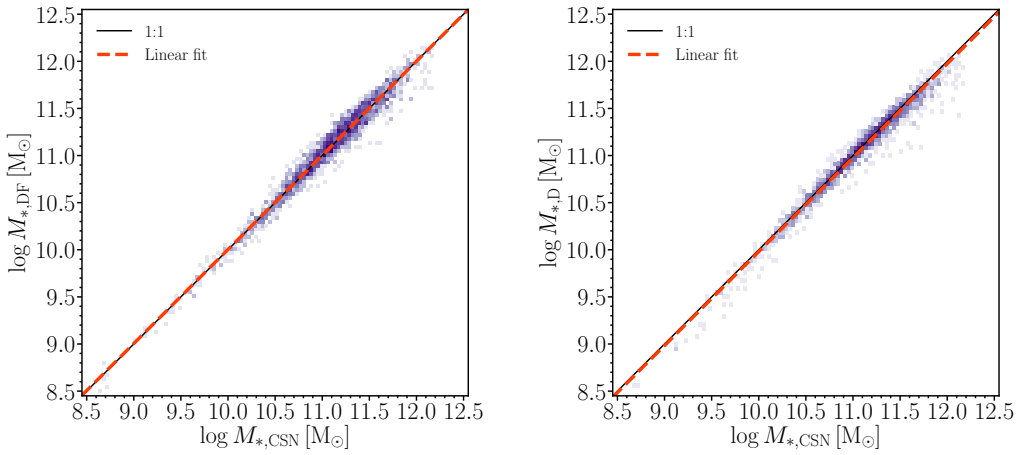

Fig. 2.17: Pure Sérsic fit stellar masses based on the dust-free (left panel) and dusty (right panel) models of M14 ($\log M_{*,\rm DF}$ and $\log M_{*,\rm D}$, respectively) as functions of our stellar masses ($\log M_{*,\rm CSN}$) for the SDSS galaxies of our sample. The distributions are represented as two-dimensional histograms: the darkest the colour of the pixel the highest the number of galaxies. In each panel, the solid line represents the 1:1 relation, while the dashed line is the linear fit to the data.

Appendix 2.B: Details of the calculation of the likelihood used in the model-data comparison

Here we provide some steps of the calculation of the likelihood in Equation 2.19. In this section all masses are in units of solar masses. By writing explicitly each term in Equation 2.8 for our case, we obtain

$$\mathrm{P}(\boldsymbol{d}|\boldsymbol{\Phi}) = \prod_{i=1}^{n} \int \mathrm{d}\log M_{*,i}\, \mathrm{d}\log \sigma_{\mathrm{e},i}\, \mathrm{d}z_i\, \mathrm{P}(\log M_{*,i}^{\mathrm{obs}}, \log \sigma_{\mathrm{e},i}^{\mathrm{obs}}, z_i^{\mathrm{obs}}|\log M_{*,i}, \log \sigma_{\mathrm{e},i}, z_i) \times \\ \times\, \mathrm{P}(\log M_{*,i}, \log \sigma_{\mathrm{e},i}, z_i|\boldsymbol{\Phi}). \tag{2.37}$$

As explained in subsection 2.3.2, we neglect the uncertainty on redshift, so that the first term on the right-side of Equation 2.37 becomes

$$\begin{aligned}\mathrm{P}(\log M_{*,i}^{\mathrm{obs}}, \log \sigma_{\mathrm{e},i}^{\mathrm{obs}}, z_i^{\mathrm{obs}}|\log M_{*,i}, \log \sigma_{\mathrm{e},i}, z_i) =& \mathrm{P}(\log M_{*,i}^{\mathrm{obs}}|\log M_{*,i}) \times \\ &\times \mathrm{P}(\log \sigma_{\mathrm{e},i}^{\mathrm{obs}}|\log \sigma_{\mathrm{e},i}) \times \\ &\times \delta(z_i^{\mathrm{obs}} - z_i).\end{aligned} \tag{2.38}$$

Therefore, we can rewrite Equation 2.19 for the i-th galaxy as follows:

$$\begin{aligned}\mathrm{P}(\log M_{*,i}^{\mathrm{obs}}, \log \sigma_{\mathrm{e},i}^{\mathrm{obs}}, z_i^{\mathrm{obs}}|\boldsymbol{\Phi}) = &\int \mathrm{d}\log M_{*,i} \frac{\mathcal{A}(\log M_{*,i})}{\sqrt{2\pi\sigma_{M_*,i}^2}} \exp\left\{-\frac{(\log M_{*,i} - \log M_{*,i}^{\mathrm{obs}})^2}{2\sigma_{M_*,i}^2}\right\} \times \\ &\times \quad \frac{1}{\sqrt{2\pi\sigma_*^2}} \exp\left\{-\frac{(\log M_{*,i} - \mu_*)^2}{2\sigma_*^2}\right\} \mathcal{E}(\log M_{*,i}|\boldsymbol{\Phi}) \times \\ &\times \int \mathrm{d}\log \sigma_{\mathrm{e},i} \frac{1}{\sqrt{2\pi\sigma_{\sigma_{\mathrm{e}},i}^2}} \exp\left\{-\frac{(\log \sigma_{\mathrm{e},i} - \log \sigma_{\mathrm{e},i}^{\mathrm{obs}})^2}{2\sigma_{\sigma_{\mathrm{e}},i}^2}\right\} \times \\ &\times \quad \frac{1}{\sqrt{2\pi\sigma_{\sigma,i}^2}} \exp\left\{-\frac{(\log \sigma_{\mathrm{e},i} - \mu_{\sigma,i})^2}{2\sigma_{\sigma,i}^2}\right\},\end{aligned} \tag{2.39}$$

where

$$\mu_{\sigma,i} = \mu_0 + \beta \log\left(\frac{M_{*,i}}{M_*^{\mathrm{piv}}}\right) + \zeta \log\left(\frac{1+z_i}{1+z^{\mathrm{piv}}}\right)$$

and (2.40)

$$\sigma_{\sigma_i} = \psi_0 + \xi \log\left(\frac{1+z}{1+z^{\mathrm{piv}}}\right).$$

Equation 2.39, the term $\mathcal{A}(\log M_*)$ allows to normalise the distribution over all values of the observed stellar mass. Specifically, $\mathcal{A}(\log M_*)$ ensures that the probability of having an ETG with $\log M_*^{\rm obs}$ between $\log M_{*,\rm min}$ (the lower bound of the considered observed stellar mass interval) and $+\infty$ is one:

$$\int_{\log M_{*,\rm min}}^{\infty} \mathrm{d}\log M_{*,i}^{\rm obs}\, \frac{\mathcal{A}(\log M_{*,i})}{\sqrt{2\pi\sigma^2_{M_*,i}}} \exp\left\{-\frac{(\log M_{*,i} - \log M_{*,i}^{\rm obs})^2}{2\sigma^2_{M_*,i}}\right\} = 1. \tag{2.41}$$

Hence, $\mathcal{A}(\log M_{*,i})$ is given by

$$\begin{aligned}\mathcal{A}(\log M_{*,i}) =& \frac{1}{\displaystyle\int_{\log M_*^{min}}^{\infty} \mathrm{d}\mathcal{M}'\, \frac{1}{\sqrt{2\pi\sigma^2_{M_*,i}}} \exp\left\{-\frac{(\log M_{*,i} - \mathcal{M}')^2}{2\sigma^2_{M_*,i}}\right\}} = \\ =& \left[\frac{\sqrt{\sigma^2_{M_*,i}}}{\frac{1}{2}\,\sigma^2_{M_*,i}\,\mathrm{erf}\left(\frac{\sqrt{2}}{2}\frac{\log M_{*,i} - \mathcal{M}}{\sigma^2_{M_*,i}}\right)}\right]_{\log M_*^{min}}^{+\infty}.\end{aligned} \tag{2.42}$$

In the previous two equations the term $\log M_{*,\rm min}$ is obtained from the mass-completeness limits at a given redshift for SDSS and LEGA-C ETGs (section 2.2.1), while for the high-redshift sample galaxies we assume a constant value of 10.5.

The integral term in $\mathrm{d}\log\sigma_{\mathrm{e},i}$ of Equation 2.39 can be written as

$$\begin{aligned}&\frac{1}{\sqrt{2\pi(\sigma^2_{\sigma_{\mathrm{e}},i} + \sigma^2_{\sigma,i})}} \exp\left\{-\frac{(\log\sigma_{\mathrm{e},i}^{\rm obs} - \mu_{\sigma,i})^2}{2(\sigma^2_{\sigma_{\mathrm{e}},i} + \sigma^2_{\sigma,i})}\right\} \times \\ &\times \int \mathrm{d}\log\sigma_{\mathrm{e},i}\, \frac{1}{\sqrt{2\pi\tilde{\sigma}_i^2}} \exp\left\{-\frac{(\log\sigma_{\mathrm{e},i} - \tilde{\mu}_i)^2}{2\tilde{\sigma}_i^2}\right\} = \\ &= \frac{1}{\sqrt{2\pi(\sigma^2_{\sigma_{\mathrm{e}},i} + \sigma^2_{\sigma,i})}} \exp\left\{-\frac{(\log\sigma_{\mathrm{e},i}^{\rm obs} - \mu_{\sigma,i})^2}{2(\sigma^2_{\sigma_{\mathrm{e}},i} + \sigma^2_{\sigma,i})}\right\},\end{aligned} \tag{2.43}$$

where

$$\tilde{\mu}_i = \frac{\log\sigma_{\mathrm{e},i}^{\rm obs}\,\sigma^2_{\sigma,i} + \mu_{\sigma,i}\,\sigma^2_{\sigma_{\mathrm{e}},i}}{\sigma^2_{\sigma,i} + \sigma^2_{\sigma_{\mathrm{e}},i}}$$

and (2.44)

$$\tilde{\sigma}_i = \sqrt{\frac{\sigma^2_{\sigma,i}\sigma^2_{\sigma_{\mathrm{e}},i}}{\sigma^2_{\sigma,i} + \sigma^2_{\sigma_{\mathrm{e}},i}}}.$$

By writing $\mu_{\sigma,i}$ explicitly, Equation 2.39 becomes

$$\begin{aligned}\mathrm{P}(\log M_{*,i}^{\mathrm{obs}}, \log \sigma_{\mathrm{e},i}^{\mathrm{obs}}, z_i^{\mathrm{obs}}|\mathbf{\Phi}) = \int \mathrm{d}\log M_{*,i} \frac{\mathcal{A}(\log M_{*,i})}{\sqrt{2\pi\sigma^2_{M_*,i}}} \exp\left\{-\frac{(\log M_{*,i} - \log M_{*,i}^{\mathrm{obs}})^2}{2\sigma^2_{M_*,i}}\right\} \times \\ \times \quad \frac{1}{\sqrt{2\pi\sigma_*^2}} \exp\left\{-\frac{(\log M_{*,i} - \mu_*)^2}{2\sigma_*^2}\right\} \mathcal{E}(\log M_{*,i}|\mathbf{\Phi}) \times \\ \times \quad \frac{1}{\sqrt{2\pi}\sigma_{\mathrm{eff},i}|\beta|} \exp\left\{-\frac{(\log M_{*,i} - \mu_{\mathrm{eff},i})^2}{2\sigma^2_{\mathrm{eff},i}}\right\}\end{aligned} \tag{2.45}$$

with

$$\mu_{\mathrm{eff},i} = \log M_*^{\mathrm{piv}} + \frac{\log \sigma_{\mathrm{e},i}^{\mathrm{obs}} - \mu_0 - \zeta\left[\log(1+z_i) - \log(1+z^{\mathrm{piv}})\right]}{\beta}$$

and (2.46)

$$\sigma_{\mathrm{eff},i} = \frac{(\sigma^2_{\sigma_{\mathrm{e}},i} + \sigma^2_{\sigma,i})}{\beta^2}.$$

$$\begin{aligned}\mathrm{P}(\log M_{*,i}^{\mathrm{obs}}, \log \sigma_{\mathrm{e},i}^{\mathrm{obs}}, z_i^{\mathrm{obs}}|\mathbf{\Phi}) = \frac{1}{|\beta|} \frac{1}{\sqrt{2\pi(\sigma^2_{M_*,i} + \sigma^2_{\mathrm{eff},i})}} \exp\left\{-\frac{(\log M_{*,i}^{\mathrm{obs}} - \mu_{\mathrm{eff},i})^2}{2(\sigma^2_{M_*,i} + \sigma^2_{\mathrm{eff},i})}\right\} \times \\ \times \int \mathrm{d}\log M_{*,i} \ \frac{1}{\sqrt{2\pi\sigma_i^{'2}}} \exp\left\{-\frac{(\log M_{*,i} - \mu_i^{'})^2}{2\sigma_i^{'2}}\right\} \ \times \\ \times \quad \mathcal{A}(\log M_{*,i}) \ \mathcal{S}(\log M_{*,i}),\end{aligned} \tag{2.47}$$

with

$$\mu_i^{'} = \frac{\log M_{*,i}\sigma^2_{\mathrm{eff},i} + \mu_{\mathrm{eff},i}\sigma^2_{M_*,i}}{\sigma^2_{\mathrm{eff},i}\sigma^2_{M_*,i}}$$

and (2.48)

$$\sigma_i^{'} = \sqrt{\frac{\sigma^2_{\mathrm{eff},i}\sigma^2_{M_*,i}}{\sigma^2_{\mathrm{eff},i} + \sigma^2_{M_*,i}}}.$$

We compute the integral term in Equation 2.47 numerically, using the trapezoidal rule.

Appendix 2.C: Mock sample

In order to check the reliability of our method, we performed some tests on mock samples. In the following, we provide an example of our method applied to a mock sample of around 400 ETGs, with properties similar to our SDSS subsample, generated as follows (masses are in units of $\mathrm{M}_\odot$ and velocity dispersions in units of $\mathrm{km\,s^{-1}}$):

- stellar masses M_*^{t} are generated extracting $\log M_*^{\mathrm{t}}$ from a normal distribution with mean 11.321 and standard deviation 0.358;
- the true velocity dispersions $\sigma_{\mathrm{e}}^{\mathrm{t}}$ are generated extracting $\log \sigma_{\mathrm{e}}^{\mathrm{t}} \equiv \mu^{\mathrm{t}}$ from a normal distribution with mean

$$\mu^{\mathrm{t}} = \mu_0^{\mathrm{mock}} + \beta_0^{\mathrm{mock}} \log\left(\frac{M_*^{\mathrm{t}}}{M_*^{\mathrm{mock}}}\right) \tag{2.49}$$

  and standard deviation 0.075 dex, where $M_*^{\mathrm{mock}} = 10^{11.321}$, $\mu_0^{\mathrm{mock}} = 2.287$, $\beta_0^{\mathrm{mock}} = 0.176$;
- the errors on the stellar masses σ_{M_*} are extracted from a normal distribution with mean 0.760 (the median stellar mass error in the SDSS sample) and standard deviation $\simeq 0.009$ (the standard deviation of the stellar mass error distribution in the SDSS sample);
- the errors on the velocity dispersions $\sigma_{\sigma_{\mathrm{e}}}$ are extracted from a normal distribution with mean 8.7 (the median stellar velocity dispersion error in the SDSS sample) and standard deviation 2.995 (the standard deviation of the stellar velocity dispersion error in the SDSS sample);
- the values of $\log M_*^{\mathrm{obs}}$ and $\log \sigma_{\mathrm{e}}^{\mathrm{obs}}$ are extracted from $\mathcal{N}(\mu = \log M_*^{\mathrm{t}},\, \sigma = \sigma_M)$ and $\mathcal{N}(\mu = \log \sigma_{\mathrm{e}}^{\mathrm{t}},\, \sigma = \sigma_{\sigma_{\mathrm{e}}})$, respectively;
- galaxies with $\log M_*^{\mathrm{obs}} < 10.5$ are excluded, so for the mock $\log M_{*,\mathrm{min}} = 10.5$.

For simplicity, we assume that all galaxies are at $z = z^{\mathrm{piv}}$, so that the mean and standard deviation of the skew prior in Equation 2.14 used to model the stellar mass distribution reduces to $\mu_* = \mu_{*,0}$ and $\sigma_* = \sigma_{*,0}$.

In order to sample the PDFs of the model applied to our mock catalogue (hereafter model $\mathcal{M}^{\mathrm{mock}}$), we perform a MCMC run (see subsection 2.3.3), using 50 random walkers running for 1000 steps to reach the convergence of the hyper-parameter distribution. In Figure 2.18 we show the posterior PDFs of all hyper-parameters

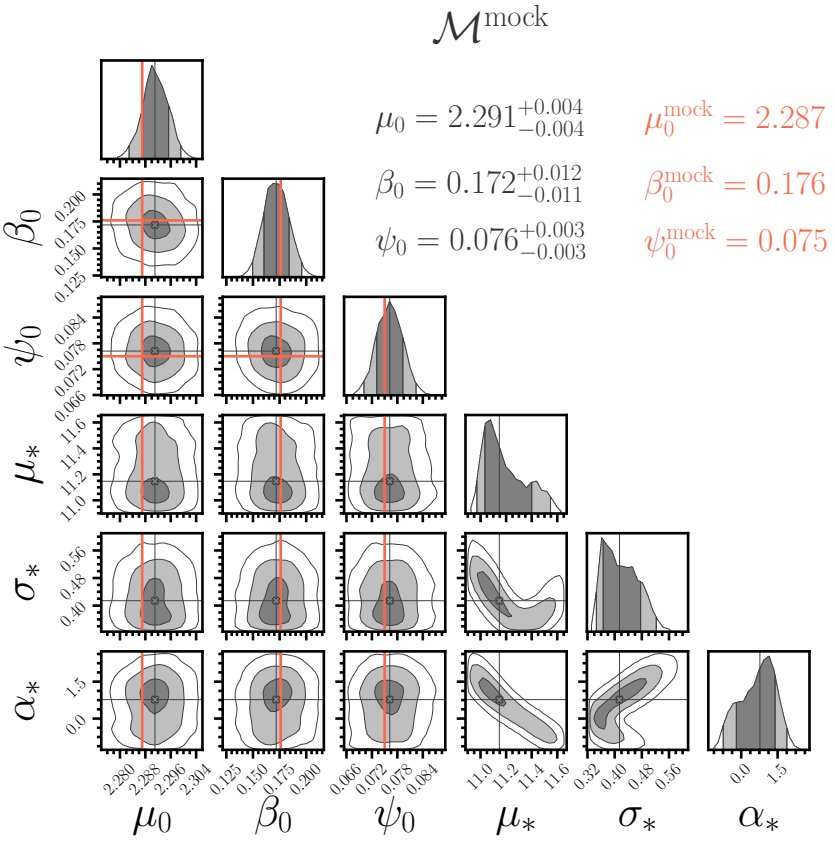

Fig. 2.18: Same as Figure 2.10, but for model $\mathcal{M}^{\rm mock}$ (dark grey contours). The thick orange solid lines indicate the input values of the hyper-parameters $\mu_0^{\rm mock}$, $\beta_0^{\rm mock}$ and $\psi_0^{\rm mock}$.

and report the median values of the hyper-parameters μ_0, β_0 and ψ_0 with their 1σ uncertainties. The input values of the hyper-parameters are all recovered within 1σ.

Appendix 2.D: Testing a different definiton of ETG

One of the properties of ETGs is to be passive and EW([O II]) is only one of the possible diagnostics for the star formation rate. Another indicator is the position of galaxies within the UVJ colour-colour diagram, in which the loci of passive and star-forming galaxies are separate (e.g., Cimatti, Fraternali, & Nipoti, 2019). For instance, Belli et al. (2014a), from which part of the galaxies of the high-redshift sample are taken, select using a UVJ-based criterion. In principle, this different selection criterion can induce spurious evolution when the extended sample is considered. In this appendix we analyse the effect of adding a UVJ-based selection to the criteria used for the fiducial sample.

The model with the highest value of Bayesian evidence explored in this work, named model $\mathcal{M}_{\rm const,NES}$, has six hyper-parameters: ζ, $\mu_{*,0}$, $\mu_{*,\rm s}$, $\sigma_{*,0}$, $\sigma_{*,\rm s}$ and α_* (see section 2.4 for details). We repeated the same analysis by considering a modified fiducial sample. In particular, we changed the selection criterion for the galaxies of the LEGA-C sample: in addition to the criteria used for the fiducial sample, we exclude galaxies that are star-forming on the basis of their position in the UVJ colour-colour diagram, as done in Muzzin et al. (2013a). In the top panel of Figure 2.20, the UVJ diagram for the LEGA-C sample of 178 ETGs illustrated in section 2.4 is shown (the UVJ colours are taken from the UltraVISTA catalogue of Muzzin et al. 2013b). In this diagram the locus of passive galaxies is the area above and to the left of the broken line: about 90% of the LEGA-C galaxies of the fiducial sample are in this area. Excluding galaxies that are outside the locus of passive galaxies in the UVJ diagram of Figure 2.20, we end up with a modified fiducial sample, consisting of 161 instead of 178 LEGA-C galaxies, in addition to the SDSS galaxies.

We applied model $\mathcal{M}_{\rm const,NES}$ to this modified fiducial sample (hereafter model $\mathcal{M}^{\textit{fid,UVJ}}_{\rm const,NES}$) and compared the results with those obtained for the original fiducial sample (hereafter model $\mathcal{M}^{\textit{fid}}_{\rm const,NES}$). The posterior distributions of the hyper-parameters of models $\mathcal{M}^{\textit{fid,UVJ}}_{\rm const,NES}$ and $\mathcal{M}^{\textit{fid}}_{\rm const,NES}$, shown in the bottom panel of Figure 2.20, are in agreement within 1σ. In particular, for model $\mathcal{M}^{fid,UVJ}_{\rm const,NES}$, the normalisation of the M_*–$\sigma_{\rm e}$ scaling relation evolves with $\zeta = 0.408^{+0.032}_{-0.031}$, consistent with $0.398^{+0.028}_{-0.031}$ obtained by model $\mathcal{M}^{fid}_{\rm const,NES}$. This analysis suggests that, at least as far as the UVJ selection is concerned, the results of the extended sample shown in section 2.4 are not biased.

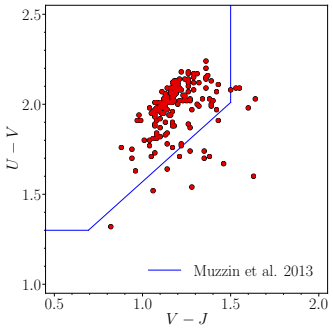

Fig. 2.19: UVJ colour-colour diagram for the LEGA-C sample of 178 ETGs (red dots). The broken line separates quiescent (upper-left region) and star-forming galaxies (lower-right region) as in Muzzin et al. (2013a).

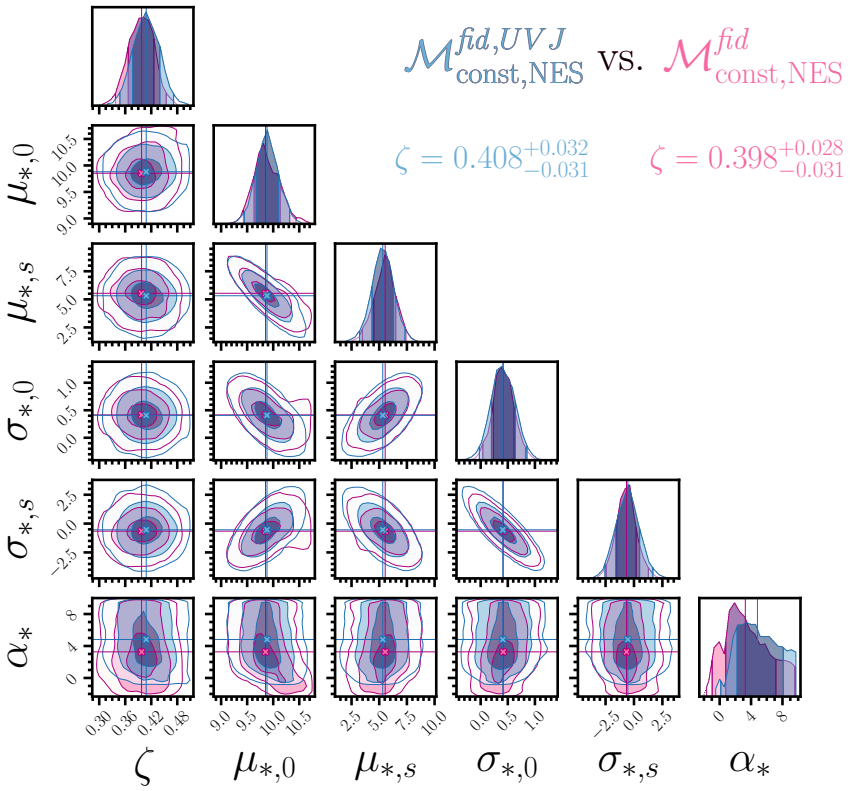

Fig. 2.20: Posterior probability distributions of the hyper-parameters for the M_*–$\sigma_{\rm e}$ models $\mathcal{M}^{fid}_{\rm const,NES}$ (purple contours) and $\mathcal{M}^{fid,UVJ}_{\rm const,NES}$ (blue contours). In the 1D distributions (top panel of each column) the vertical solid lines and colours delimit the 68, 95 and 99.7-th quantile based posterior credible interval. In the 2D distributions (all the other panels) the contours enclose the 68, 95 and 99.7 percent posterior credible regions. The lines indicate the median values of the hyper-parameters.

3

The role of in-situ and ex-situ star formation in early-type galaxies: MaNGA versus IllustrisTNG

> *If I have seen further than others, it is by standing upon the shoulders of giants.*
>
> **— Isaac Newton**

A possible way to understand the formation and evolution scenario of galaxies consists in the exploitation of numerical simulations that reproduce real objects. In this Chapter we present a work that deals with the comparison of observed galaxies from the MaNGA survey with simulated galaxies from the IllustrisTNG simulation, disentangling for the latter the role of in-situ and ex-situ stellar populations. This Chapter is based on ***Cannarozzo et al. (a, in prep. to be submitted to MNRAS soon)***.

3.1 Introduction

The spatial distributions of metallicity, chemical abundances, age and other properties of stellar populations in a galaxy enclose all the evolutionary processes occurred across cosmic time.

In the context of the standard cosmological framework, an early-type galaxy (ETG) may experience several episodes of accretion of material from the intergalactic medium or via mergers that can dramatically change the whole system. A natural outcome of the merger-driven evolution experienced by ETGs is the evolution of internal scaling relations. Indeed, as described in section 1.6, historically we know that ETGs show relations that link, for instance, the stellar luminosity (or

interchangeably the stellar mass) to the velocity dispersion (Faber & Jackson, 1976), to the size (Kormendy, 1977), or, more generally, involving these three properties together in the so-called Fundamental Plane (Djorgovski & Davis, 1987; Dressler et al., 1987). The improvement of technologies together with the increasing of the statistics in the newest surveys led the astrophysicists to study those relations at different redshifts. Indeed, massive ETGs at high redshifts are found to be compact, with an effective radius $R_{\rm e}$ smaller than that of galaxies in the present-day Universe (e.g., Ferguson et al., 2004; van der Wel et al., 2014; Damjanov et al., 2019). As we have seen in Chapter 2, also the stellar mass–velocity dispersion relation, $M_*-\sigma_{\rm e}$, evolves: on average, for given stellar mass, the lower the redshift, the lower the velocity dispersion (e.g., van de Sande et al., 2013; Belli et al., 2014a; Gargiulo et al., 2016; Belli et al., 2017; Tanaka et al., 2019; Cannarozzo et al., 2020a).

An intriguing result obtained from cosmological simulations that model the formation of ETGs is the so-called *two-phase formation scenario* (e.g., Naab et al., 2009; Oser et al., 2010; Hilz et al., 2013, see subsection 1.8.1). According to this scenario, in an early phase ($z \gtrsim 2$), the stellar component within massive galaxies is mainly constituted by stars that formed *in situ*, i.e. in the same galaxy. Subsequently, as a consequence of multiple minor and major mergers, an ETG accretes stars formed *ex situ*, i.e. in other galaxies, hence modifying the total mass, the size and stellar properties in general.

A possible way to investigate how the progenitor stellar populations settled in the final galaxy remnants would be to perform high-resolution simulations. For instance, by exploiting a set of N-body dissipationless binary merging simulations, in Nipoti et al. (2020) we studied the effect of dry mergers on the final distribution of the initial mass function (IMF) mismatch parameter $\alpha_{\rm IMF}$[1], finding that these encounters tend to flatten the $\alpha_{\rm IMF}$ profiles, because of the mixing of the stellar populations of the two progenitors. On the other side, hydrodynamical cosmological simulations can help the study of the evolution of stellar population properties, taking into account the aspects of a cosmological evolution of systems. In this context, as found by Rodriguez-Gomez et al. (2016) for galaxies in the Illustris simulation suite (Genel et al., 2014; Vogelsberger et al., 2014a,b; Sijacki et al., 2015), stars formed in situ tend to be more dominant in the innermost regions of galaxies, while stars accreted from other systems tend to lie in the outer parts.

[1]The IMF mismatch parameter $\alpha_{\rm IMF}$ (Treu et al., 2010) is defined as the ratio between $(M_*/L)_{\rm true}$, i.e. the true stellar mass-to-light ratio of an ensemble of stars in a given band, and $(M_*/L)_{\rm ref}$, i.e. the stellar mass-to-light ratio in the same band that one would infer adopting a reference IMF, for example the Salpeter (1955), the Kroupa (2001), or the Chabrier (2003) IMF.

The presence of initial gradients in stellar metallicity can be determined by the first episodes of star formation (e.g., Larson, 1974; Thomas et al., 2005) and a natural consequence is the production of metallicity profiles that decrease going towards the external regions of galaxies, while stellar age profiles remain almost constant. As show in Hirschmann et al. (2015) and Cook et al. (2016), the large number of mergers and interactions occurred in galaxies cause the presence of shallow metallicity profiles and almost flat (or slightly positive) age gradients, because of the mix of stars with different metallicities and the accumulation of old stellar populations in the outer regions, respectively. On the contrary, a lack of late-time minor mergers in galaxies produces metallicity profiles substantially negative, causing the formation of metal-poor regions in the outskirts of galaxies (e.g., Kobayashi, 2004; Pipino et al., 2010; Taylor & Kobayashi, 2017).

In the last decades, the integral field spectroscopy (IFS) technique has been exploited in many surveys: SAURON (Spectroscopic Areal Unit for Research on Optical Nebulae; Bacon et al., 2001; de Zeeuw et al., 2002), ATLAS^{3D} (Cappellari et al., 2011), CALIFA (Calar Alto Legacy Integral Field Array survey; Sánchez et al., 2016), SAMI (Sydney-Australian-Astronomical-Observatory Multi-object Integral-Field Spectrograph Croom et al., 2012; Bryant et al., 2015), MASSIVE (Ma et al., 2014) and MaNGA (Mapping Nearby Galaxies at Apache Point Observatory; Bundy et al., 2015). The main advantage of IFS is to obtain simultaneously spectra in different regions of a given source, spatially resolving morphological and kinematic aspects. Indeed, each pixel is associated with a spectrum (the so-called *spaxel*, i.e. spectral pixel), providing a measure of the flux at different wavelengths. These spatially-resolved surveys allow to study in detail the properties of stellar populations in individual objects, therefore not limiting the analysis only to the study of gradients, but revealing the 2D spatial distribution over the entire galaxy on the plane of the sky.

By analysing a set of ETGs with $\log(M_*/\mathrm{M}_\odot) > 10.3$ in SAURON, Kuntschner et al. (2010) found that stellar metallicity gradients become shallower with increasing stellar mass, while stellar age remain constant. Also Li et al. (2018) using MaNGA galaxies with $9 < \log(M_*/\mathrm{M}_\odot) < 12.3$ found metallicity gradients consistent with those of Kuntschner et al. (2010). Moreover, Li et al. (2018) found that the stellar metallicity gradients show a strong dependence on stellar velocity dispersion: they peak (being most negative) at velocity dispersions of around $100\,\mathrm{km\,s^{-1}}$. The interpretation of this radial dependence is in terms of a different evolutionary scenario for galaxies with different velocity dispersions. In particular, metallicity gradients tend to flatten at high velocity dispersions suggesting a rising role of mergers that redistribute stellar populations in these galaxies. However, the studies

conducted so far that involve IFS surveys are sometimes in contrast. For example, also Goddard et al. (2017b) picked ETGs from MaNGA with $9 < \log(M_*/\mathrm{M}_\odot) < 11.5$: although, the galaxies were drawn from the same survey as done by Li et al. (2018), the authors derived metallicity profiles that become steeper going towards the high-mass tail. A consistent result was found by Zheng et al. (2017), for ETGs in the MaNGA survey with $8.5 < \log(M_*/\mathrm{M}_\odot) < 11.5$. In Greene et al. (2015), subsequently extended in Greene et al. (2019) to larger radii, ETGs with $\log(M_*/\mathrm{M}_\odot) > 11.6$ show shallow metallicity gradients and radius-independent age and α-element abundances relative to the iron, i.e. $[\alpha/\mathrm{Fe}]$. Recently, by analysing a sample of 96 passive brightest cluster galaxies (BCGs) from the SAMI survey, Santucci et al. (2020) found negative metallicity gradients that tend to become shallower as the stellar mass increases, slightly positive age gradients and almost zero $[\alpha/\mathrm{Fe}]$ gradients, the latter tending to become a bit more negative as the mass increases. This study revealed also that there are no significant differences in the stellar profiles of the analysed properties between central and satellite galaxies, both at fixed stellar mass and as a function of halo mass, highlighting for the two galaxy populations follow a similar formation scenario, which appears to be independent of the environment. The differences found among the various studies (also when using the same galaxy survey) may depend on a combination of different selection criteria adopted to identify ETGs, stellar mass ranges considered, as well as methods used to retrieve properties and their profiles.

Despite the relatively large number of IFS surveys, understanding whether a stellar population in a galaxy either formed in situ or was accreted from another progenitor is not a trivial argument. In a recent work, Oyarzún et al. (2019), making use of more than 1000 ETGs with $10 < \log(M_*/\mathrm{M}_\odot) < 12$ from the MaNGA survey, studied the radial distributions of metallicity adopting three different stellar fitting codes, i.e. FIREFLY, PROSPECTOR and PPXF. They found that, regardless of the fitting code used, metallicity profiles in galaxies with $\log(M_*/\mathrm{M}_\odot) > 11$ tend to become flatter in the outer regions, interpreting this feature as a signature of accretion. In order to understand the presence of this flattening, the authors built a simple toy model. Specifically, they assumed that the low-mass tail of galaxies in their sample is representative of galaxies mainly constituted by stars formed in situ. As the mass increases, the flattening in the metallicity profiles becomes more prominent at $R \gtrsim 1\,R_\mathrm{e}$. Hence, for the high-mass end of galaxies, the inner part of the profiles ($R \lesssim 1\,R_\mathrm{e}$) is associated to the in-situ stellar population, while the external parts are mainly dominated by stars accreted from other galaxies. Quantitatively, they infer the role of ex-situ stars that, within $R \approx 2R_\mathrm{e}$, is around 20% of the total stellar

mass in ETGs with $\log(M_*/\mathrm{M}_\odot) < 10.5$, while in ETGs with $\log(M_*/\mathrm{M}_\odot) > 11.5$ this fraction reaches even 80% of the stellar mass content.

In this work, we propose a more realistic model to provide an interpretative scenario for the radial distributions of stellar properties in real ETGs in terms of in-situ and ex-situ stellar components. Specifically, we compare the profiles of stellar mass surface density, metallicity, age and velocity dispersion for observed galaxies drawn from the MaNGA survey with those for in-situ and ex-situ stellar populations (information that is directly accessible from simulations) in ETGs extracted from the IllustrisTNG project. On the one hand, we make use of MaNGA galaxies because, up to now, MaNGA represents the largest spatially-resolved survey (≈ 10000 nearby galaxies) that exploits the IFS technique. On the other hand, IllustrisTNG is a suite of state-of-the-art magneto-hydrodynamic cosmological galaxy formation simulations that sheds light on the physical processes occurring into galaxies across cosmic time. This Chapter is organised as follows. In section 3.2 we describe the galaxy sample and the criteria adopted to select ETGs. The methods to obtain radial profiles are described in section 3.3. Our results are discussed in section 3.4. Section 3.5 concludes. Throughout this Chapter, we assume a ΛCDM cosmological framework with the cosmological parameters derived from Planck Collaboration et al. (2016), i.e. $\Omega_{\Lambda,0} = 0.6911$, $\Omega_{m,0} = 0.3089$, $\Omega_{b,0} = 0.0486$, and $H = 67.74\,\mathrm{km\,s^{-1}Mpc^{-1}}$.

3.2 Galaxy samples

In order to provide an explanation for radial profiles of stellar properties in observed ETGs in the present-day Universe, in this work we compare galaxies drawn from the MaNGA survey with simulated galaxies taken from the hydrodynamical cosmological simulation suite IllustrisTNG. In the following, we describe the samples used for our analysis, the selection criteria, the properties of the observed and simulated ETGs, and the method adopted to directly compare the two samples.

3.2.1 The MaNGA survey

The MaNGA survey (Bundy et al., 2015; Yan et al., 2016a), one of the three parts of the fourth generation of SDSS (York et al., 2000; Gunn et al., 2006; Blanton et al., 2017) mapped, through the 2.5 m telescope Apache Point Observatory, ≈ 10000 galaxies in the redshift range $0.01 \lesssim z \lesssim 0.15$, providing for each source spatially-resolved spectra. MaNGA was designed to map a representative sample of galaxies

with $\log(M_*/\mathrm{M}_\odot) > 9$. This sample is taken from an extended version of the original NASA-Sloan Atlas (NSA `v1_0_1`[2]; Blanton et al., 2011) catalogue. By exploiting all the advantages of the IFS technique (Smee et al., 2013; Drory et al., 2015; Law et al., 2015), galaxies in MaNGA are observed with a set of 17 hexagonal bundles, each composed by fibers with a total diameter that varies from $12''$ (with 19 fibers) to $32''$ (with 127 fibers). Each fiber has a diameter of $2''$. MaNGA achieves a uniform radial coverage of galaxies to $1.5\,R_\mathrm{e}$ and $2.5\,R_\mathrm{e}$, for $\approx 2/3$ (*Primary Sample*) and $\approx 1/3$ (*Secondary Sample*) of the final sample, respectively. The observations provide a wavelength coverage in the range $3600-10300\,\text{Å}$, with a spectral resolution of $R \sim 1400$ at $\lambda \sim 4000\,\text{Å}$ and $R \sim 2600$ at $\lambda \sim 9000\,\text{Å}$. A value of $R \sim 2000$ corresponds to a velocity dispersion of around $70\,\mathrm{km\,s^{-1}}$ (see Smee et al., 2013).

The MaNGA observations used in this work were previously reduced by the Data Reduction Pipeline (DRP; Law et al., 2016; Yan et al., 2016b). In this work, both the de-projected distances and stellar kinematic maps are computed using the Data Analysis Pipeline (DAP; Westfall et al., 2019) for MaNGA. The MaNGA galaxies forming our observed sample are drawn from the SDSS Data Release 15 (DR15; Aguado et al., 2019), a sample of the first 4675 observed MaNGA sources[3].

In order to study the behaviour of radial profiles of some stellar properties in observed ETGs, but concurrently reducing the presence of effects of systematic biases caused by different assumptions, priors and fitting methods (Conroy, 2013b), we rely on measurements derived from two full spectral fitting codes: FIREFLY[4] (Maraston & Strömbäck, 2011; Comparat et al., 2017; Goddard et al., 2017a; Wilkinson et al., 2017; Maraston et al., 2020) and PROSPECTOR[5] (Leja et al., 2017; Johnson et al., 2019). In addition, we take into account the estimates of velocity dispersion obtained by using the PPXF code[6] (Cappellari & Emsellem, 2004; Cappellari, 2017). In the following we briefly summarise the settings adopted for the three stellar population fitting codes.

- FIREFLY (Fitting IteRativEly For Likelihood analYsis) is a χ^2 minimisation fitting code for deriving the stellar population properties. This code aims at disentangling stars and dust, subtracting the low-order continuum shape before fitting spectra. A set of simple stellar populations (SSPs) with a variety of age and metallicity are considered iteratively, in order to minimise the χ^2 fitting procedure, allowing FIREFLY to fit non-parametric SFHs. For our

[2]Available at `https://www.sdss.org/dr15/manga/manga-target-selection/nsa/`.
[3]Available at `https://www.sdss.org/dr15/manga/manga-data/`.
[4]Available at `https://github.com/FireflySpectra/firefly_release`.
[5]Available at `https://github.com/bd-j/Prospector`.
[6]Available at `http://www-astro.physics.ox.ac.uk/~mxc/software/`.

scope, we adopt the stellar population models of Maraston & Strömbäck (2011), the MILES stellar library (Sánchez-Blázquez et al., 2006; Vazdekis et al., 2010) and a Chabrier (2003) IMF. The set of SSPs used are spread over the range 6.5 Myr−15 Gyr in age, while metallicity can assume values in the range $-2.3 \leq \log(Z_*/Z_\odot) \leq 0.3$. The library covered wavelength range is $4000-7400$ Å. We include only spectra with $S/N > 10$ (see Goddard et al., 2017b; Wilkinson et al., 2017), and we mask emission lines.

- PROSPECTOR is a code able to infer stellar population properties from photometric and/or spectroscopic data with flexible models. It is based on the original stellar population synthesis code FSPS[7] (Conroy et al., 2009; Conroy & Gunn, 2010). PROSPECTOR is able to sample the posterior distribution of a stellar population parameter space (externally defined by users) and provides uncertainties and degeneracies. We adopt the MILES stellar population library, the MIST isochrones (Choi et al., 2016; Dotter, 2016) and a Kroupa (2001) IMF[8]. Our fit procedure explores a ten-dimensional parameter space. In this fit, the dust optical depth in V-band, stellar mass, stellar velocity dispersion and mass-weighted metallicities are taken into account. Moreover, non-parametric SFHs with a continuity prior are considered. Following the same approach described in Leja et al. (2019), our parameter space considers the SFR spanning over the following time bins: $0\,\mathrm{Myr} < t < 30\,\mathrm{Myr}$; $30\,\mathrm{Myr} < t < 100\,\mathrm{Myr}$; $100\,\mathrm{Myr} < t < 330\,\mathrm{Myr}$; $330\,\mathrm{Myr} < t < 1.1\,\mathrm{Gyr}$; $1.1\,\mathrm{Gyr} < t < 3.6\,\mathrm{Gyr}$; $3.6\,\mathrm{Gyr} < t < 11.7\,\mathrm{Gyr}$; $11.7\,\mathrm{Gyr} < t < 13.7\,\mathrm{Gyr}$.

  The priors used for our PROSPECTOR runs are listed in Table 3.1. Finally, the posterior distributions are obtained exploiting the Dynamic Nested Sampling package dynesty (Speagle, 2020).

- The Penalized Pixel-Fitting method (PPXF) code derives the stellar or gas kinematics and stellar population from absorption-line spectra of galaxies, using a maximum penalized likelihood method. The original approach was presented in Cappellari & Emsellem (2004) and then improved in Cappellari (2017). Since the high robustness in inferring stellar and gas kinematics, PPXF has been used to estimate velocity dispersions for our observed ETGs. Specifically, the penalisation of the non-well-fitted pixels minimises the mismatch with the used templates. We ran PPXF with the included libraries based on MILES.

[7] Available at `https://github.com/cconroy20/fsps`.

[8] For our purpose, the assumption of a Kroupa IMF or a Chabrier IMF for retrieving stellar population properties is almost indistinguishable.

Tab. 3.1: List of priors used for our PROSPECTOR runs. Column 1: parameter. Column 2: prior.

Parameter	Prior
Star formation history	Continuity
dust2	TopHat $(0, 1)$
Stellar metallicity $\log(Z_*/Z_\odot)$	TopHat $(-2, 0.3)$
Formed stellar mass $M_*/\mathrm{M}_\odot$	LogUniform$(10^7, 10^{12})$
Velocity dispersion σ_* [$\mathrm{km\,s^{-1}}$]	TopHat $(0.1, 400)$

For a more extended description about the stellar fitting codes used and the method, we refer the reader to Oyarzún et al. (2019).

3.2.2 IllustrisTNG simulations

In this work, we extract simulated ETGs from *The Next Generation* Illustris project (hereafter, IllustrisTNG[9]; Marinacci et al., 2018; Naiman et al., 2018; Nelson et al., 2018; Pillepich et al., 2018a; Springel et al., 2018), the successor to the original Illustris[10] simulation suite (Genel et al., 2014; Vogelsberger et al., 2014a,b; Sijacki et al., 2015). This is a state-of-the art magneto-hydrodynamic cosmological simulation that models the formation and evolution of galaxies within the ΛCDM framework. As its predecessor, IllustrisTNG exploits all the advantages of the *unstructured moving-mesh* hydrodynamics method AREPO (Springel, 2010), but improving for instance the numerical methods, the subgrid physical model, and the recipe for galaxy feedback both from stellar component and AGN. In particular, IllustrisTNG is equipped with a novel dual mode (thermal and kinetic) AGN feedback that shapes and regulates the stellar component within massive systems, maintaining a realistic gas fraction. Also the feedback from galactic winds has been improved to have better representation of low- and intermediate-massive galactic systems (Weinberger et al., 2017; Pillepich et al., 2018b).

The IllustrisTNG model was calibrated to significantly reduce the tensions between the original Illustris suite and the observations. For instance, some discrepancies concern the SFR density as a function of time, the stellar-to-halo mass relation in the present-day Universe, the stellar mass function, as well as the black hole

[9]Official website at `https://www.tng-project.org`.
[10]Official website at `https://www.illustris-project.org`.

mass−stellar mass relation or the black hole mass−halo mass relation, and the gas amount within virial radii.

The IllustrisTNG simulation suite consists of three simulation volumes: IllustrisTNG50 (Nelson et al., 2019; Pillepich et al., 2019), IllustrisTNG100 and IllustrisTNG300. The three runs have different box sizes, with sides of about $50\,\mathrm{Mpc}$, $100\ \mathrm{Mpc}$ and $300\,\mathrm{Mpc}$, respectively. The project assumes a ΛCDM cosmology and the cosmological parameters, drawn from Planck Collaboration et al. (2016), are $\Omega_{\Lambda,0} = 0.6911$, $\Omega_{m,0} = 0.3089$, $\Omega_{b,0} = 0.0486$, $\sigma_8 = 0.8159$, $n_s = 0.9667$ and $h = 0.6774$. The starting redshift of each run is set at $z = 127$ using the Zeldovich approximation and the simulations evolve down to $z = 0$.

For our scope, we make use of the highest-resolution version of the medium volume size IllustrisTNG100, i.e. IllustrisTNG100-1. This run includes 2×1820^3 resolution elements. The dark matter and baryonic mass resolutions are $m_{\mathrm{DM}} = 7.5 \times 10^6\,\mathrm{M}_\odot$ and $m_{\mathrm{b}} = 1.4 \times 10^6\,\mathrm{M}_\odot$. The softening length employed for this version for both the dark matter and stellar components is $\epsilon = 0.74\,\mathrm{kpc}$, while an adaptive gas gravitational softening is used, with a minimum $\epsilon_{\mathrm{gas,min}} = 0.125\,\mathrm{ckpc}/h$ (in comoving units). In particular, we take into account the properties of subhalos of the snapshot $\#91$, corresponding to $z = 0.1$, i.e. the mean redshift of galaxies in the MaNGA survey.

In-situ & ex-situ stars in IllustrisTNG galaxies

In the last decade, a few cosmological simulations have indicated that especially the most massive galaxies grew in mass as well as in size accreting stars during their evolution. The fraction of stars accreted onto a galaxy strictly depends on the stellar or DM halo masses (e.g., Oser et al., 2010; Lackner et al., 2012). From the original Illustris simulation suite, Rodriguez-Gomez et al. (2016) derived the fraction of the ex-situ stellar component accreted onto systems with stellar masses from $10^9\,\mathrm{M}_\odot$ up to $10^{11}\,\mathrm{M}_\odot$. They found that this fraction increases from $\lesssim 10\%$ of the total stellar amount, to beyond 50% in the most massive galaxies. A similar analysis has been conducted on the IllustrisTNG runs: Pillepich et al. (2018a), by analysing stellar masses within different apertures, i.e. $< 10\,\mathrm{kpc}$, $< 30\,\mathrm{kpc}$, the total central galaxy with intracluster light (excluding satellites), and $> 100\,\mathrm{kpc}$, found that at $z = 0$ the low-mass tail of galaxies are mainly formed by in-situ stellar particles, while the central galaxies of the most massive halos ($\log(M_{\mathrm{200c}}/\mathrm{M}_\odot) > 14$) accreted even more than 80% of their total stellar mass via mergers and accretion events. Moreover, by considering stellar masses within an aperture larger than $100\,\mathrm{kpc}$, the ex-situ

fraction is found to be dramatically dominant at these distances, exceeding even 90% of the total stellar population. The relevant contribution in massive systems of the ex-situ stars reaches around 60% in the innermost regions ($< 10\,\mathrm{kpc}$).

In the following, we adopt the same definition of in-situ and ex-situ stars used in Pillepich et al. (2014), Rodriguez-Gomez et al. (2016), Pillepich et al. (2018a), and Tacchella et al. (2019), exploiting the baryonic merger trees of Rodriguez-Gomez et al. (2015):

- *in-situ stars* are those stellar particles that, at the time of their formation, formed in a galaxy lying in the main progenitor branch of the merger tree;
- *ex-situ stars* are those stellar particles that, at the time of their formation, formed and were gravitationally bound to a halo outside the main progenitor branch of a given halo and later accreted onto it.

3.2.3 ETG selection

The comparison of observations and simulations is not trivial under several points of view. In our case, the first issue arises when we want to select ETGs. IllustrisTNG simulations were calibrated in order to reproduce different properties of galaxies in the present-day Universe, including the colour bimodality (see section 1.3). Nelson et al. (2018) take into account three different models for deriving $ugriz$ magnitudes for simulated galaxies, comparing them with those of SDSS galaxies. One model (Model A) considers the intrinsic stellar particle emission in each subhalo, not accounting for attenuation due to the presence of dust. The other two models take into account the contribution of dust: the *unresolved dust model* (Model B) is introduced to account for the presence of gas clouds surrounding young stellar population; the *resolved dust model* (Model C), instead, improves the unresolved model, following the distribution of neutral gas in galaxies, adding also the attenuation caused by the presence of metals. In their paper, Nelson et al. (2018) discuss in detail the results using the colours derived through Model C, providing the supplementary data catalogue SDSS Photometry, Colors, and Mock Fiber Spectra[11]. IllustrisTNG colours were compared with the observed colours of galaxies in the present-day Universe ($z < 0.1$) drawn from the SDSS DR12 (Alam et al., 2015). The distributions of $(g-r)$ colours in each mass bin well recover the colour bimodality shown by SDSS galaxies. In particular, the blue and red galaxy populations show a peak at $(g-r) \approx 0.4$ and ≈ 0.8, respectively. Moreover, the colour bimodality tends to disappear above

[11] Available at https://www.tng-project.org/data/downloads/TNG100-1/.

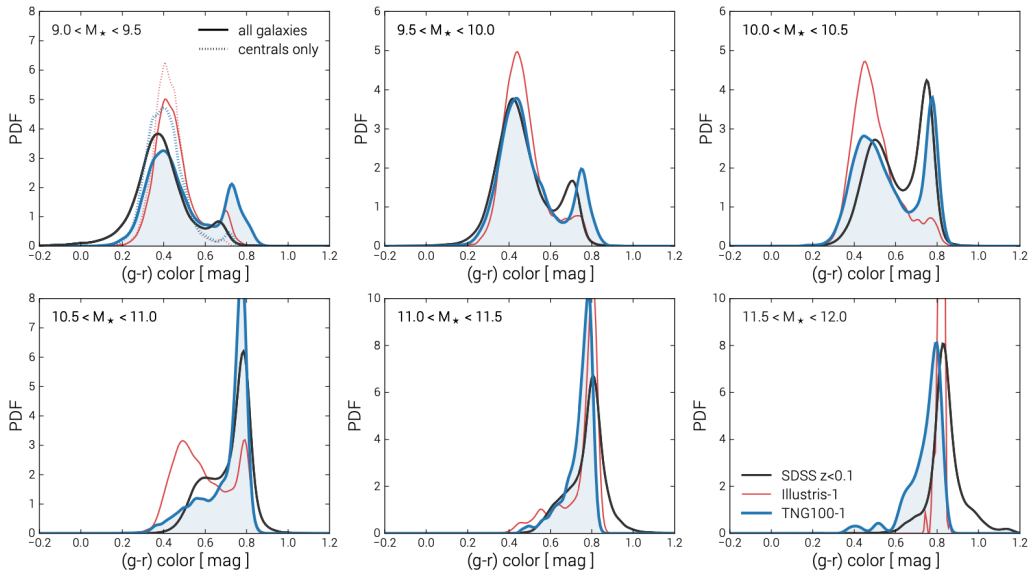

Fig. 3.1: Distributions of simulated $(g-r)$ colours at different mass bins in IllustrisTNG100-1 (blue curve) compared with SDSS (black curve) and Illustris-1 (red curve) estimates. This plot is taken from Nelson et al. (2018).

$M_* \simeq 10^{10.5}\,\mathrm{M}_\odot$, where the red population dominates. Tacchella et al. (2019) studied the connection between the star formation activity and morphology of central galaxies in IllustrisTNG, by adopting as morphological indicators the spheroid-to-total ratio, S/T, and the concentration of stellar mass density profiles, C_{82}, defined as $5 \times \log(r_{80}/r_{20})$, with r_{80} and r_{20} the radii including the 80% and 20% of the total stellar mass, respectively. In particular, they found that the S/T parameter strongly correlates with $(g-r)$ colours: S/T is higher for redder colours and higher stellar masses (while, at fixed mass, C_{82} is found to be weakly dependent on colour).

In order to compare as homogeneously as possible observed and simulated galaxies we apply a simple selection based on $(g-r)$ colours, identifying hereafter ETGs as *Red Galaxies*, i.e. those galaxies with $(g-r) > 0.6$, since $(g-r) \simeq 0.6$ marks the transition value between the blue cloud and the red sequence of galaxies. As discussed by Nelson et al. (2018), by looking at the colour–mass diagrams, beyond the excellent agreement found between simulations and observations, some second-order discrepancies arise, such as the flatter slope of the red sequence for simulated galaxies. However, these discrepancies are negligible for our scope. For this comparison, to select ETGs in our observed MaNGA sample, we retrieve the $ugriz$ Petrosian magnitudes from the NSA catalogue. Moreover, our MaNGA sample was pre-selected on the basis of the equivalent width of the emission line $\mathrm{H}\alpha$, including only objects with $\mathrm{EW}(\mathrm{H}\alpha) \geq -3\,\text{Å}$.

In Appendix 3.C we test a different selection criterion for ETGs based on the star formation rate, following one of the approaches described in Donnari et al. (2019), finding consistent results with those presented here.

3.2.4 Stellar mass estimates

Another potential source of systematic effects when comparing observations and simulations concerns the estimate of stellar masses. Indeed, differences in the measurements of stellar masses can be caused by several factors, such as the fitting method used to derive luminosities and colours that, in turn, depend on the stellar population synthesis models and libraries assumed, etc. Sonnenfeld et al. (2019) discuss the differences in deriving luminosity of galaxies in massive ETGs observed with the Hyper-Supreme Cam (HSC; Miyazaki et al., 2018) Subaru Stratyegic Program (Aihara et al., 2018, DR1), assuming either a simple Sérsic fit or a Sérsic+Exponential fit. The difference between the two methods can cause a variation of around $0.1\,\mathrm{dex}$ on the measurements of luminosity for the same object. Moreover, as already discussed in subsection 2.5.1, a different assumption of IMF can imply a global shift of stellar masses and the potential presence or IMF radial variations can introduce biases.

Given the wide variety of systematic effects on the final estimate of stellar masses, as done for the ETG selection criteria described above, in the following we present the results for two definitions of masses available in the UPENN_PHOTDEC_MSSTAR[12] catalogue of Meert et al. (2015). The two stellar masses for the MaNGA ETGs we use here, obtained multiplying the stellar mass-to-light ratios (M_*/L) from Mendel et al. (2014) by the luminosities from the PyMorph SerExp (Sérsic+Exponential) photometry, assume M_*/L fitting models which either account or do not account for the effects of dust extinction (Table 3 and Table 5 of Mendel et al. 2014, respectively). We refer to these two estimates as SerExp Dusty and Dust-free stellar masses, respectively. For simplicity's sake, in section 3.4 we will discuss the results limiting the analysis only to the SerExp Dusty stellar mass estimates for MaNGA ETGs, postponing in Appendix 3.A the comparison with the SerExp Dust-free measurements.

In order to compare MaNGA and IllustrisTNG stellar masses as similarly as possible, for the latter we consider the 2D projected stellar mass defined as the sum of all bound stellar particles within a *circle* of radius $R = 2R_{\mathrm{hm}}$, where R_{hm} is the radius of a circle containing half of the projected mass. This is the same mass definition

[12] Available at http://alan-meert-website-aws.s3-website-us-east-1.amazonaws.com/fit_catalog/download/index.html.

adopted by Ardila et al. (2021), where the authors discuss the fact that the agreement between observed and simulated galaxies considerably depends on the definition of mass adopted. In Figure 3.2, the comparison between the above-mentioned projected 2D stellar mass within $2R_{\rm hm}$ ($M_*^{\rm 2hmr,2D}$) and the 3D mass estimate, i.e. the mass defined as the sum of all stellar particles gravitationally bound within a *sphere* of radius $r = 2r_{\rm hm}$, where $r_{\rm hm}$ is the radius of a sphere containing half of the 3D total stellar mass ($M_*^{\rm 2hmr,3D}$) is shown for our initial IllustrisTNG galaxy sample of ≈ 3000 subhalos with total mass (i.e., the mass defined as the sum of all star particles gravitationally bound, $M_*^{\rm tot,3D}$) $\log(M_*^{\rm tot,3D}/{\rm M}_\odot) \geq 10.5$. As clearly visible, the difference between the two mass estimates increases with mass, underlying the importance of adopting the stellar mass definition as similar as possible to that of observations.

Hereafter, we will refer to $M_*^{\rm 2hmr}$ or, equivalently, to *2hmr mass* as the projected mass within a circle of radius $R = 2R_{\rm hm}$, and, in general, we will consider only projected masses for simulated galaxies.

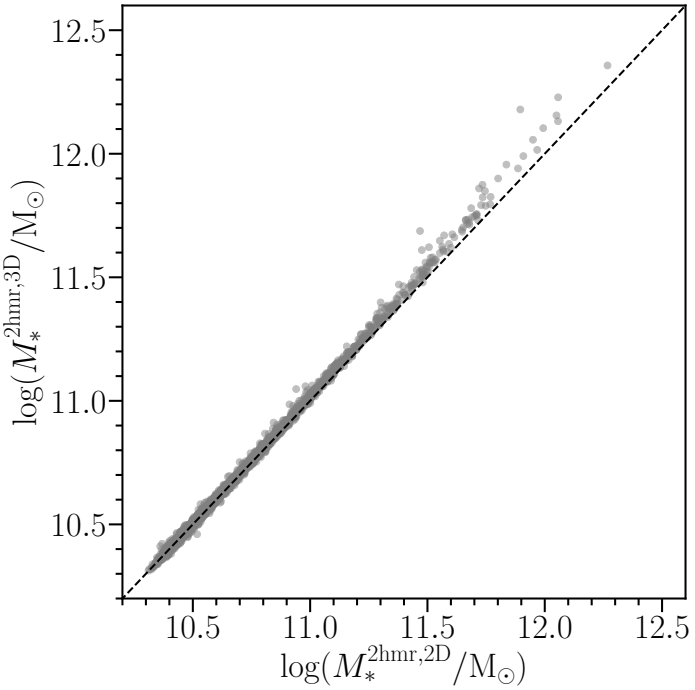

Fig. 3.2: Comparison between the 2D stellar mass within $2R_{\rm hm}$ ($M_*^{\rm 2hmr,2D}$, x-axis) and the 3D stellar mass within $2r_{\rm hm}$ ($M_*^{\rm 2hmr,3D}$, y-axis) for the IllustrisTNG starting sample of ≈ 3000 subhalos with $\log(M_*^{\rm tot,3D}/{\rm M}_\odot) \geq 10.5$.

For completeness, in Appendix 3.C, we study the effect of adopting different definitions of stellar mass. In particular, we consider for IllustrisTNG the stellar mass

Tab. 3.2: Summary table of the MaNGA and IllustrisTNG samples. Column 1: sample. Column 2: stellar mass range in logarithm. Column 3: mean value. Column 4: median value. Stellar masses are in units of $\mathrm{M}_{\odot}$.

Red galaxy samples

Sample	N_{ETG}	(min $\log M_*$; max $\log M_*$)	$\log \bar{M}_*$	$\log M_*\|_{\mathrm{med}}$
MaNGA SerExp Dusty	700	(10.50; 12.26)	11.12	11.12
MaNGA SerExp Dust-free	717	(10.51; 12.37)	11.21	11.21
IllustrisTNG100 2hmr	1543	(10.50; 12.27)	10.83	10.76

within a projected aperture of $30\,\mathrm{kpc}$ and for MaNGA the mass estimates derived from Sérsic and Petrosian fits (drawn from the original NSA catalogue) and the mass defined as the sum of the masses included in the 5 concentric annuli used to derive the profiles of stellar properties from FIREFLY and PROSPECTOR. Based on this exploration, we conclude that our main results are independent of the specific definitions of M_*.

In Table 3.2, we summarise the properties of the final IllustrisTNG and MaNGA (for the latter reporting both the SerExp Dusty and SerExp Dust-free stellar masses) *Red galaxy samples*, i.e. objects with $\log(M_*/\mathrm{M}_{\odot}) \geq 10.5$ and $(g-r) > 0.6$. In Figure 3.3 the colour–mass diagrams (left panel) and the mass distributions of the MaNGA galaxies (assuming the SerExp Dusty masses) compared with the IllustrisTNG sample (right panel) are illustrated. Although the MaNGA and IllustrisTNG galaxies are similarly distributed over the colour–mass diagrams, we note that the samples are very different in the distributions of stellar masses. Indeed, while MaNGA sample, by construction, show an almost uniform distribution over the entire range in stellar mass, IllustrisTNG peaks at the low-mass end and rapidly decrease, becoming lower than the MaNGA sample in counts above $10^{11}\,\mathrm{M}_{\odot}$.

Concerning our MaNGA Red galaxies, we verified the reliability of the adopted selection to identify ETGs, checking the morphological type assigned by the MaNGA MORPHOLOGY DEEP LEARNING DR15 CATALOGUE[13]. This catalogue, presented in Fischer et al. (2019), is built by exploiting the Deep Learning method for identifying the morphology of galaxies as described in Domínguez Sánchez et al. (2020) for all the objects of MaNGA DR15. In brief, the Deep Learning methodology relies on a Convolutional Neural Network trained on the morphological catalogues of Nair & Abraham (2010) and Willett et al. (2013). The resulting catalogue provides

[13]Available at https://www.sdss.org/dr15/data_access/value-added-catalogs/?vac_id=manga-morphology-deep-learning-dr15-catalogue.

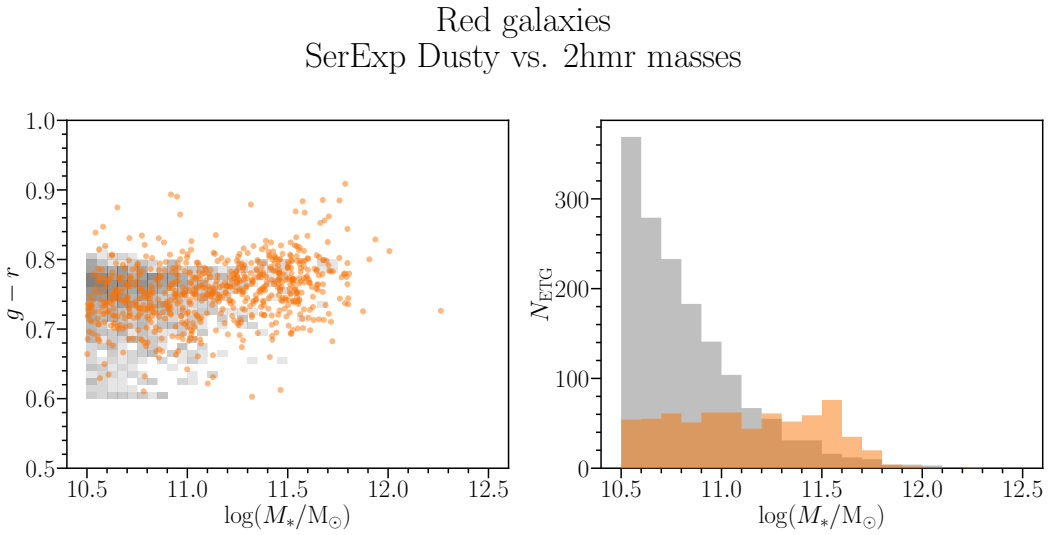

Fig. 3.3: Red galaxy samples with with $(g-r) > 0.6$. Left panel: the scatter distribution indicates the MaNGA sample assuming the SerExp Dusty masses (orange dots). The 2D histogram indicates the IllustrisTNG colour-selected sample, assuming the 2hmr mass. Right panel: 1D histograms of the mass distributions for the MaNGA (orange histogram) and the IllustrisTNG (grey histogram) estimates.

the `T-Type` morphological parameter by applying the methodology on the Nair & Abraham (2010) catalogue, while the other available parameters are derived by using the Galaxy Zoo 2 (Willett et al., 2013) catalogue. For our scope, we identify ETGs as in Domínguez Sánchez et al. (2020), i.e. requiring a T-Type ≤ 0, otherwise sources are late-type galaxies (LTGs). The left panel of Figure 3.4 illustrates the distribution of the morphological type for our MaNGA Red Galaxy sample. A fraction of $\approx 84\%$ of the whole galaxy sample effectively shows a morphology compatible with an E/S0 type, of which $\approx 27\%$ with a probability of being a lenticular (see right panel). Similar fractions are found also for the MaNGA sample using the Dust-free mass estimates.

3.3 Methods

In this work we compare the radial distributions of some stellar population properties, such as age or metallicity, in observed and simulated galaxies. In the following we describe the method used to retrieve the radial profiles from the 2D maps. In particular, we make use of mass-weighted stellar metallicity and age for both MaNGA and IllustrisTNG galaxies. We tested also the luminosity-weighted measurements for MaNGA galaxies finding no significant difference between the two choices.

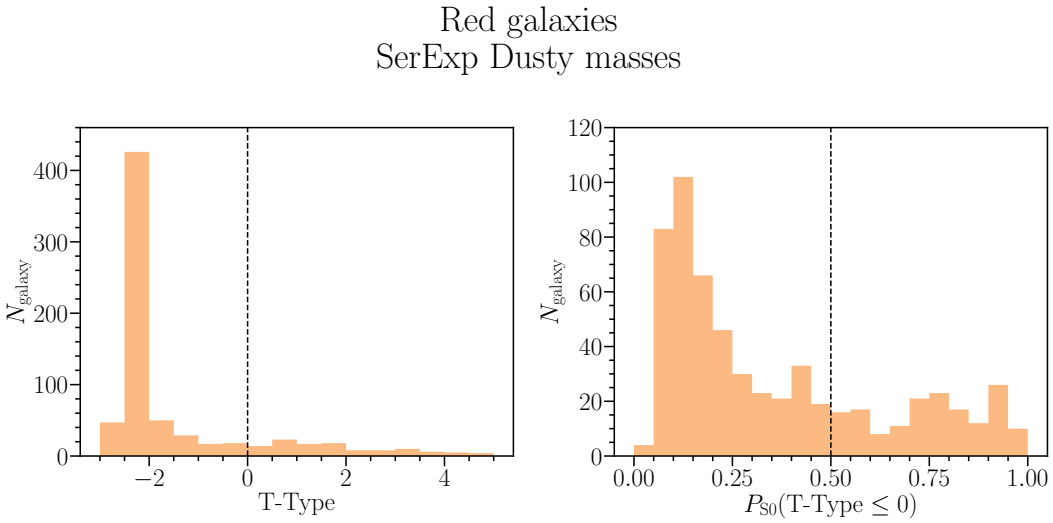

Fig. 3.4: Distributions of the T-Type (left panel) and $P_{\rm S0}$ (right panel) morphological parameters for our MaNGA Red Galaxy sample. A value of T-Type ≤ 0 identifies an ETG, i.e. a system with a E/S0 morphology, otherwise the source is a LTG. The parameter $P_{\rm S0}$ gives the probability for each galaxy of being a S0 lenticular galaxy (with $P_{\rm S0} > 0.5$) rather than a pure elliptical (with $P_{\rm S0} < 0.5$). In both panels, the black dashed lines divide the plots between ETGs and LTGs, and between pure ellipticals and lenticulars, respectively.

3.3.1 Radial profiles for MaNGA galaxies

To obtain the stellar properties in each MaNGA galaxy at different galactocentric distances we adopt the approach described in Oyarzún et al. (2019), but considering a radial binning in physical units (not in units of effective radii). Specifically, by considering the axis ratio of each source obtained from r-band photometric images, elliptical polar radii are associated to spaxels. Afterward, we bin into five concentric elliptical annuli each galaxy map, assuming the following radii as the edges of each bin: $R/\mathrm{kpc} = \{0;\ 2;\ 4;\ 10;\ 20;\ 100\}$.

The next step after radial binning consists in the shift of spectra to the rest-frame taking the stellar systemic velocity from DAP as a reference. A Voronoi binning is then applied to the maps, considering a minimum $S/N = 10$ in each bin. Spectra belonging to the same annulus are co-added and, after running pPXF with the MILES library, they are stacked to estimate the line-of-sight stellar mean velocity and velocity dispersion. For a more detailed description of the methods used to obtain the radial profiles, we refer the reader to Oyarzún et al. (2019).

3.3.2 Radial profiles for IllustrisTNG galaxies

In order to compare simulated galaxies with observations, we apply the same method presented in Ardila et al. (2021). We firstly project the 3D particle distributions of the simulated galaxies on 2D maps. For each object, the 2D map is composed by 300 pixels per side, with a resolution of $1\,\mathrm{kpc}$ per pixel (for a total physical side length of the map of $300\,\mathrm{kpc}$). For extracting the 1D stellar profiles we then use the same methodology presented in Huang et al. (2018) and also used in Ardila et al. (2021), that we briefly summarise in the following. To obtain the 1D stellar mass surface density profiles we use the projected 2D stellar mass maps. We applied `galsbp`, the galaxy surface brightness profile function included in the `kungpao` package[14]. Galaxy centroids are identified by means of `extract`, a function included in the `sep` library, and the `ellipse` algorithm allows to fit concentric elliptical isophotes on the source. The position angle and ellipticity of the isophotes used are the mean values from the 2D fitting procedure of the galaxy maps. The radial binning of isophotes is spaced uniformly in log over the range $0-150\,\mathrm{kpc}$. Concerning metallicity, age and velocity dispersion profiles, for each map we use the same center coordinates and ellipticity of isophotes computed during the fitting procedure of stellar mass surface density maps. Therefore, to derive mass-weighted stellar properties, each pixel for example in the metallicity maps is weighted by the corresponding value of mass in that pixel. The entire procedure is applied to both the in-situ and ex-situ stellar populations, starting from their 2D stellar property maps.

For a more detailed description about the methods used to obtain the radial profiles, we refer the reader to Huang et al. (2018) and Ardila et al. (2021).

Another aspect to be taken into account when comparing simulated and observed objects concerns the effect of degradation in observations due to the finite spatial resolution. Together with the profiles derived from the original IllustrisTNG maps, we obtain the corresponding profiles from PSF-convolved maps. Specifically, we associate to each simulated galaxy an angular diameter distance, assuming as redshift of the source the one obtained by fitting the $z-M_*$ distribution of the MaNGA sample used for the comparison (see Appendix 3.B). Afterwards, for each galaxy we compute its mock MaNGA resolution and then, for smoothing its original map, we compute the corresponding 2D Gaussian filter kernel to be used defined as

$$\sigma_{\mathrm{kernel},i} = \sqrt{\mathcal{R}^2_{\mathrm{MaNGA},i} - \mathcal{R}^2_{\mathrm{TNG}}}, \tag{3.1}$$

[14]The `kungpao` library is avavilable at `https://github.com/dr-guangtou/kungpao/`.

where $\mathcal{R}_{\rm TNG} = 1\,{\rm kpc}$, while $\mathcal{R}_{{\rm MaNGA},i} = \sin({\rm PSF}_{\rm MaNGA}) d_{A,i}$, with ${\rm PSF}_{\rm MaNGA} = 2.5''$ ($\simeq 1.21 \times 10^{-5}$ in radians), and $d_{A,i}$ the angular diameter distance (in kpc) for the i-th galaxy in the IllustrisTNG sample determined as described above. For example, at $z = 0.05$, $\mathcal{R}_{\rm MaNGA} \simeq 2.52\,{\rm kpc}$. In Appendix 3.B, the $z-M*$ planes for the SerExp Dusty and Dust-free stellar mass samples are shown with their fitting forms.

3.3.3 Building stellar mass bins

For comparing the profiles of the stellar properties of MaNGA and IllustrisTNG galaxies, we firstly subdivide galaxies in bins of stellar mass and then we compute the median profile in each stellar mass bins.

To consider similarly observed and simulated galaxies, we select objects adopting two diverse criteria of binning. The first choice consists in comparing galaxies in the same *stellar mass bins*, i.e. we select galaxies in the three bins $10.5 < \log(M_*/{\rm M}_\odot) < 11$, $11 < \log(M_*/{\rm M}_\odot) < 11.5$, and $\log(M_*/{\rm M}_\odot) > 11.5$. The second choice, instead, relies on a selection made at fixed number density. Therefore, to associate similar galaxies, we make a number density matching, building *number-density-based stellar mass bins* starting from the stellar mass functions (SMFs) of each sample. For our scope, we compute the SMF for our IllustrisTNG galaxy sample, and we take from Table 1 of Bernardi et al. (2017) the observed (i.e., error-broadened) SMFs associated to the Dusty ($\mathbf{\Phi}_{\rm Obs}^{\rm M14_d}$) and Dust-free ($\mathbf{\Phi}_{\rm Obs}^{\rm M14_{d-f}}$) mass estimates from Mendel et al. (2014) with the SerExp photometry of Meert et al. (2015). For every SMF we computed the cumulative stellar mass function (CSMF) as the sum of the number counts of galaxies with stellar masses greater than a given value $M_{*,i}$:

$$n(> M_{*,i}) = \int_{M_{*,i}}^{+\infty} \mathbf{\Phi}(M'_*)\, {\rm d}M'_*. \tag{3.2}$$

In this context, it would be useful to check whether and to what extent the results depend on the bin selection. In Figure 3.5, the CSMFs for the IllustrisTNG and for the two mass definitions used for the MaNGA galaxies are shown, in which we highlighted the three number-density-based stellar mass bins, while in Table 3.3, we list the values of stellar mass for the three CSMFs corresponding to their cut values in number density of Figure 3.5. For an easier comparison with the results obtained using the stellar mass bins as above, the number-density-based stellar mass bins are built starting from the values of number density of the MaNGA galaxy CSMFs corresponding to the stellar mass values $\log(M_*/{\rm M}_\odot) = 10.5,\, 11.0,\, 11.5$.

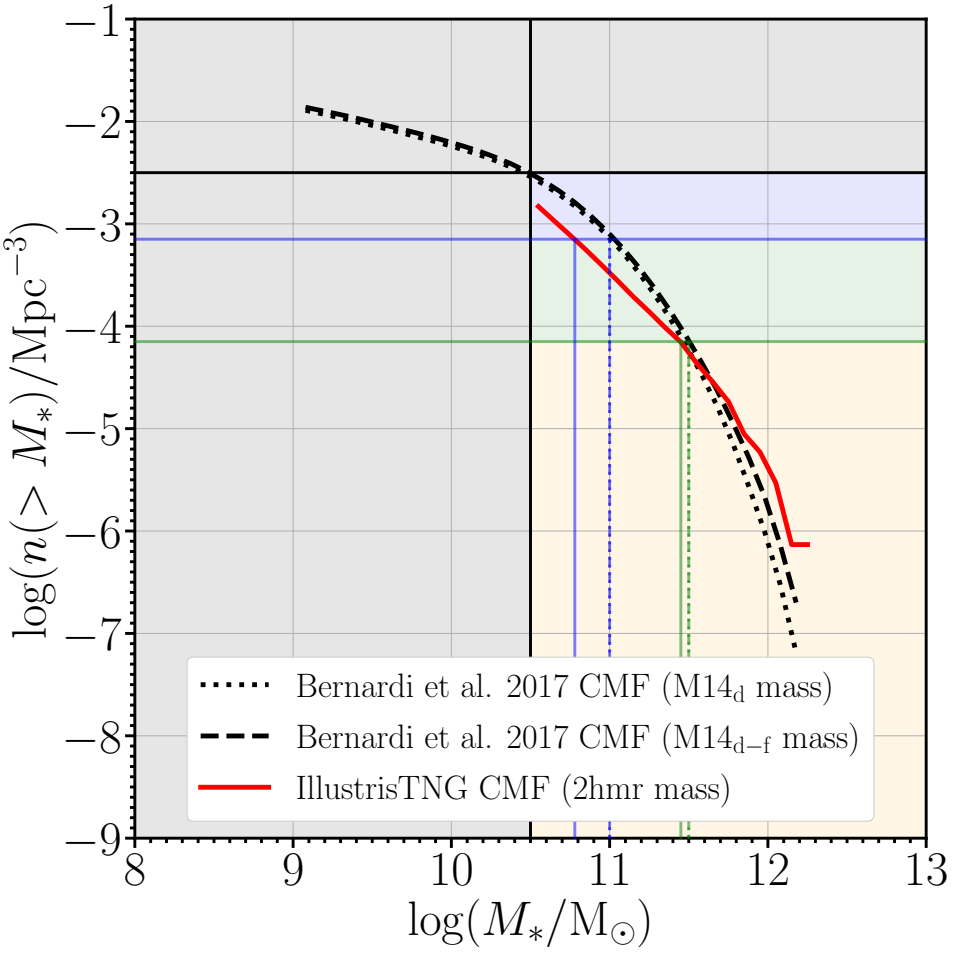

Fig. 3.5: Cumulative stellar mass functions for the IllustrisTNG (red solid curve) and the MaNGA samples for the SerExp Dusty (black dotted curve) and the Dust-free (black dashed curve) stellar mass measurements. The CSMFs are compared at the same number-density-based stellar mass bins built deriving the values of number density of the MaNGA galaxy CSMFs corresponding to the stellar mass values $\log(M_*/\mathrm{M}_\odot) = 10.5, 11.0, 11.5$: from -2.50 to -3.15 (blue shaded region), from -3.15 to -4.15 (green shaded region), and below -4.15 (yellow shaded region). The vertical lines trace the stellar mass values of each galaxy sample corresponding to their number density value, following the same formalism in colours and curve styles. The grey shaded regions correspond to value of stellar masses and/or number densities excluded by our selection.

Tab. 3.3: Values of stellar mass corresponding to each number density value for the three CMFs. Column 1: number density in logarithm. Column 2: stellar mass in logarithm for the MaNGA Dusty/Dust free model samples. Column 3: stellar mass in logarithm for the IllustrisTNG sample.

Red galaxy samples

$\log(n/\mathrm{Mpc}^{-3})$	$\log(M_*/\mathrm{M}_\odot)_{\mathrm{MaNGA}}$	$\log(M_*/\mathrm{M}_\odot)_{\mathrm{TNG}}$
-2.50	10.50	10.50
-3.15	11.00	10.78
-4.15	11.50	11.45

3.3.4 Building median radial profiles with errors

In order to account for the errors associated to MaNGA measurements, the profiles are obtained by computing in each radial bin the median value (and its errors) of all the estimates in that bin, exploiting a Bayesian hierarchical approach. Specifically, we assume that each stellar property X in any radial bin has a Gaussian distribution, so that its likelihood can be written as

$$\mathrm{P}(X^{\mathrm{inf}}|X^{\mathrm{data}},\sigma_X^{\mathrm{data}},\mu,\sigma) = \frac{1}{\sqrt{2\pi\sigma_X^2}}\exp\left\{-\frac{(X^{\mathrm{data}}-\mu)^2}{2\sigma_X^2}\right\}, \tag{3.3}$$

where X^{inf} is the quantity we would like to infer in each radial bin (e.g., the logarithm of the stellar mass surface density), while X^{data} and σ_X^{data} are the data values and the related uncertainties, respectively. The variance in Equation 3.3 has the form

$$\sigma_X^2 = {\sigma_X^{\mathrm{data}}}^2 + \sigma^2. \tag{3.4}$$

In Equation 3.3 and in Equation 3.4, μ and σ are the two *hyper-parameters* of our Bayesian hierarchical approach and represent the mean value and the intrinsic scatter of the distribution of the quantity X^{inf}, respectively. In table Table 3.4, we list the priors adopted for each property.

The stellar properties of MaNGA galaxies are sampled adopting a Markov Chain Monte Carlo (MCMC) approach, using for each run 10 random walkers and 150 steps to reach the convergence of the hyper-parameter distribution. For our scope, we use the Python adaptation of the affine-invariant ensemble sampler of Goodman & Weare (2010), emcee by Foreman-Mackey et al. (2013). For the IllustrisTNG profiles, the median values and the corresponding 1σ uncertainties in each radial bin are obtained applying a bootstrap method with 1000 random extractions.

Tab. 3.4: Hyper-parameters used to compute MaNGA profiles. Column 1: stellar property. Column 2: Prior on the mean (low; up). Column 3: Prior on the intrinsic scatter (low; up).

Stellar property	$(\min \mu; \max \mu)$	$(\min \sigma; \max \sigma)$
Surface density $\log(\Sigma_*/\mathrm{M}_\odot\mathrm{kpc}^{-2})$	$(7; 11)$	$(0; 5)$
Metallicity $\log(Z_*/Z_\odot)$	$(-1; 1)$	$(0; 1)$
Age [Gyr]	$(0; 13)$	$(0; 5)$
Velocity dispersion $\sigma_*/\mathrm{km\,s}^{-1}$	$(80; 340)$	$(10; 100)$

3.4 Results

In this section, we show the median radial profiles of the stellar mass surface density, metallicity, age and velocity dispersion for both MaNGA and IllustrisTNG Red galaxies, comparing the profiles in stellar mass bins (subsection 3.4.1), and briefly discussing the differences for the cases in which galaxies are subdivided in number-density-based stellar mass bins (subsection 3.4.2).

3.4.1 Comparing profiles in stellar mass bins

In the following, we describe the radial profiles in stellar mass bins of IllustrisTNG and MaNGA ETGs. For the latter we focus on the SerExp Dusty model stellar masses, postponing to Appendix 3.A a comparison with the SerExp Dust-free model stellar mass. In all the plots, we show only the median profiles and their uncertainties for both MaNGA and IllustrisTNG stellar properties, omitting, for clarity reasons, the intrinsic scatters of the distributions. However, they are comparable with those of the profiles shown in Appendix 3.C. The hatched area up to $\approx 2.1\,\mathrm{kpc}$ in each plot indicates three times the force resolution of the stellar particles of IllustrisTNG galaxies, i.e. the region might be affected by numerical effects.

The top panels of Figure 3.6 show the profiles of stellar mass surface densities for the total stellar population (i.e. in-situ & ex-situ stars) of IllustrisTNG (black curves) and the estimates from FIREFLY (yellow dots) and PROSPECTOR (green squares) for MaNGA ETGs in the log-mass bins (in solar units) from 10.5 to 11 (left panel), from 11 to 11.5 (middle panel), and above 11.5 (right panel). In each stellar mass bin, we find a satisfying agreement at all radii between the two MaNGA measurements, with a small systematic shift to higher values of the stellar mass surface density

obtained by PROSPECTOR, compatible with the systematic shift in mass estimates (for the same galaxy, PROSPECTOR infers a stellar mass that, on average, is higher than the estimate obtained by FIREFLY by $\approx 0.15-0.2\,\mathrm{dex}$). In each stellar mass bin, IllustrisTNG reproduces remarkably well the surface densities of MaNGA ETGs.

The top panels of Figure 3.7 show the median profiles of the stellar mass surface density for the in-situ (red dashed curves) and ex-situ (blue dotted curves) stellar populations in the three different mass bins. In the mass range $10.5 < \log(M_*/\mathrm{M}_\odot) < 11$, on the average, the in-situ stellar component is found to be dominant out to $\approx 30\,\mathrm{kpc}$, radius beyond which the ex-situ stars tend to become slightly more relevant. The central mass bin, i.e. $11 < \log(M_*/\mathrm{M}_\odot) < 11.5$, reveals the rising role of the ex-situ stars in these ETGs: in this case, the profiles of the two populations almost overlap over the entire range in radius. Above $\log(M_*/\mathrm{M}_\odot) \approx 11.5$, the ex-situ stars dominate at all radii. Therefore, to sum up, we do find that below $\log(M_*/\mathrm{M}_\odot) \approx 11$, the most relevant stellar component (at least $20-30\,\mathrm{kpc}$) is the in-situ population, whereas beyond the ex-situ stars become dominant across the entire range of radii. The shapes of the in-situ and ex-situ profiles depend on the mass bin. Going towards the high-mass tail of ETGs, the two stellar mass surface density profiles become more and more similar to each other. The latter result, together with the fact that the ex-situ stars are the most important stellar component in these systems, corroborate previous findings on IllustrisTNG from Pillepich et al. (2018a) and Tacchella et al. (2019), for which the stellar mass assembly history of these massive galaxies are mainly marked by a major-merger-driven evolution. Major mergers not only allow ex-situ stellar populations to settle even in the innermost regions of galaxies, but also mix homogeneously the two stellar components at all radii, causing the formation of similar surface density profiles (that only differ in normalisation). The result predicted by IllustrisTNG might be in light tension with previously scenarios for which massive ETGs are the results of a merger-driven evolution mainly marked by minor mergers (e.g., Naab et al., 2009; Oser et al., 2010; Hilz et al., 2013). As discussed in Tacchella et al. (2019), the ex-situ stellar mass fraction increases with stellar mass. The interpretation of this difference in galaxies with stellar mass below and above $M_* \approx 10^{11}\,\mathrm{M}_\odot$ is due to the main formation channels of galaxies. Especially in galaxies with $M_* \gtrsim 10^{11}\,\mathrm{M}_\odot$, major mergers start to be relevantly more important than minor mergers. Figure 3.8 reports some details about the merger activity of the IllustrisTNG ETGs: specifically, in the first row the fractions of the in-situ and ex-situ stellar components are illustrated, while in the second row the ex-situ fractions coming from all mergers and only from major mergers are made explicit; in the third row the whole number of minor and major mergers experienced by galaxies are displayed; in the last row the redshifts of the last minor and major

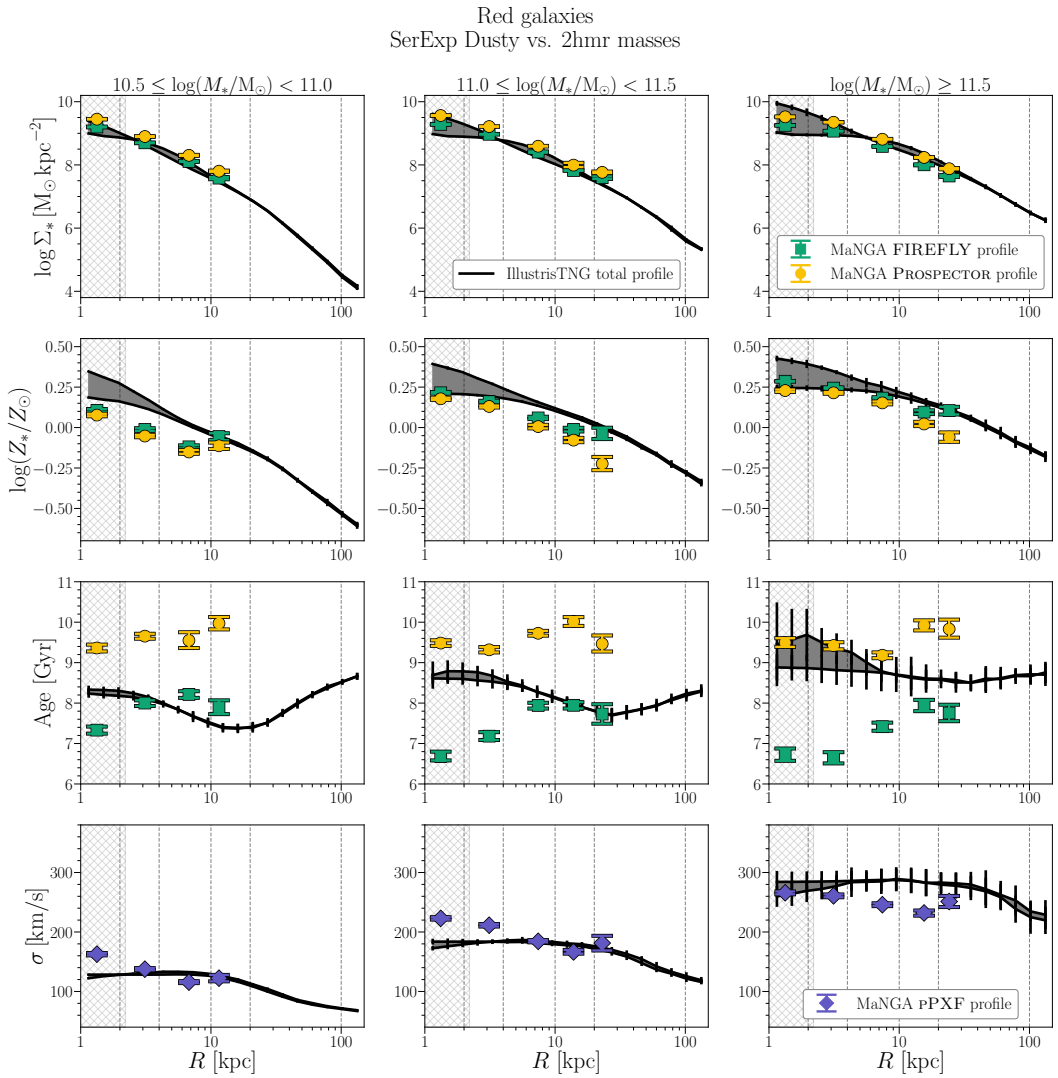

Fig. 3.6: Radial profiles of (from the top to the bottom) stellar mass surface density, metallicity, age, and velocity dispersion in three bins of stellar mass for MaNGA and IllustrisTNG Red galaxies. For MaNGA ETGs we use the Dusty model masses, while for IllustrisTNG ETGs we use the 2hmr masses. The green, yellow and violet dots represent the median estimates for MaNGA ETGs from FIREFLY, PROSPECTOR and pPXF codes, respectively, in the 5 radial bins identified by the grey dashed lines. The two black curves represent the median value of each stellar property for the total stellar populations in IllustrisTNG galaxies in 20 radial bins spaced uniformly in log over the range $0-150\,\mathrm{kpc}$, both obtained from the original maps and from the maps convolved with the MaNGA PSF, respectively. The black shaded area is the region that lies in between the profiles obtained from the original and the convolved IllustrisTNG maps. The errorbars represent the 1σ uncertainties on the median for MaNGA and IllustrisTNG estimates. The hatched area (0:2.1 kpc) shows 3x the force resolution of the stellar particles in IllustrisTNG.

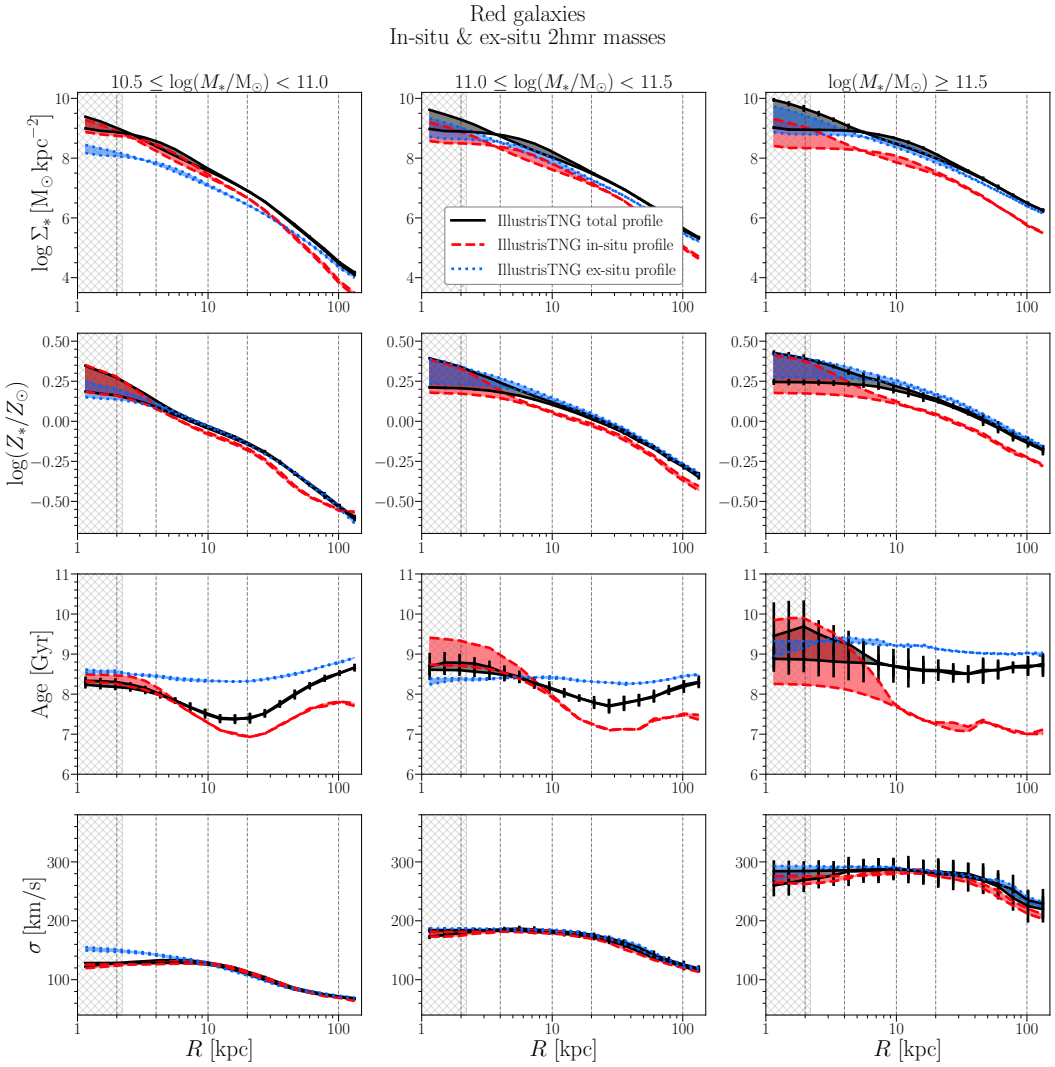

Fig. 3.7: Radial profiles of (from the top to the bottom) stellar mass surface density, metallicity, age, and velocity dispersion in three bins of stellar mass for IllustrisTNG Red galaxies. The black solid, red dashed and blue dotted curves (and their shaded areas) are the same as in Figure 3.6, but for the total, the in-situ, and the ex-situ stellar populations, respectively. The errorbars represent the 1σ uncertainties on the median for IllustrisTNG estimates. The hatched area (0:2.1 kpc) shows 3x the force resolution of the stellar particles in IllustrisTNG.

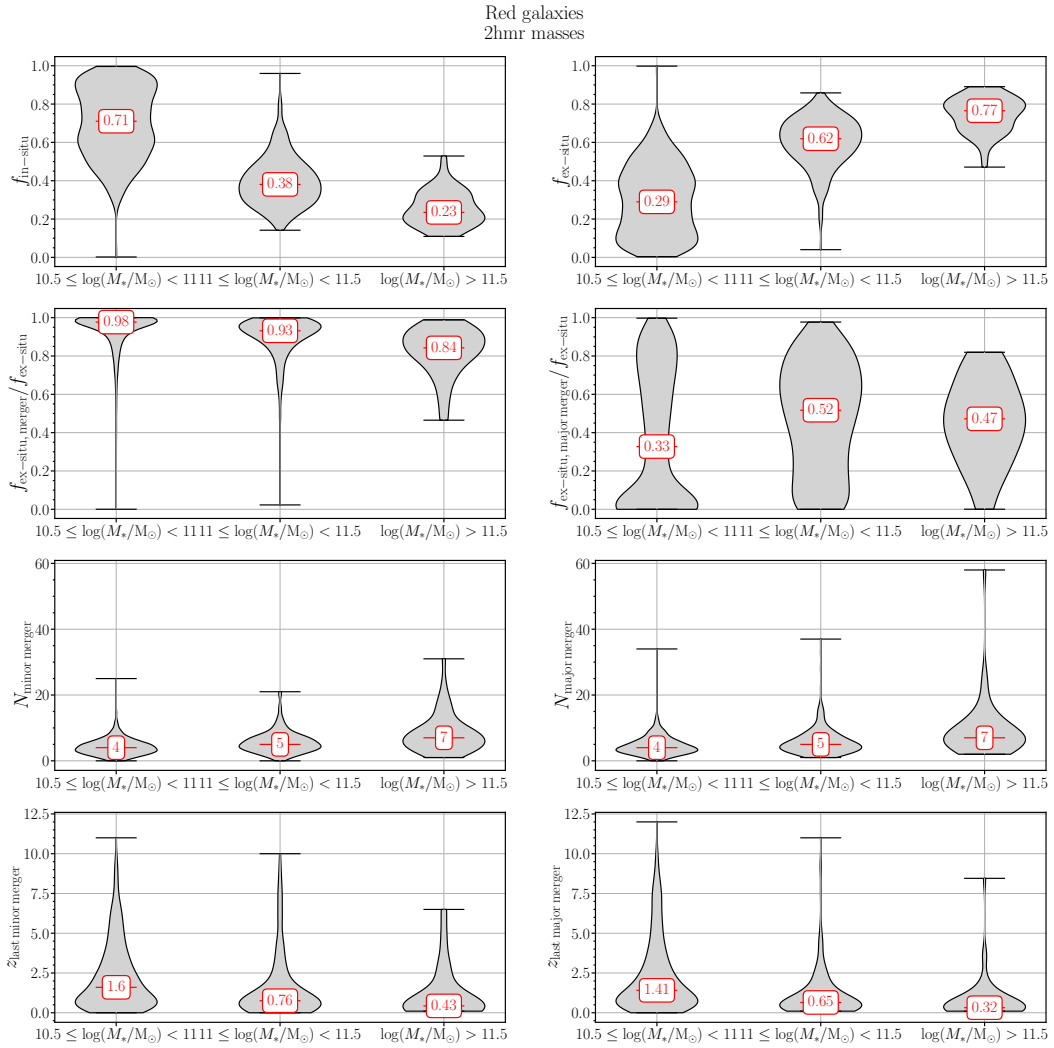

Fig. 3.8: Violin plots of eight properties related to the merger history of the IllustrisTNG ETGs. First row: fractions of the in-situ (left panel) and the ex-situ (right panel) stellar components. Second row: fractions of the ex-situ stellar component due to all mergers ($0 < \mu_* < 1$, excluding stars stripped from surviving galaxies), and only due to major mergers (right panel) normalised to the total ex-situ stellar fraction. Third row: number of minor (left panel) and major (right panel) mergers. Fourth row: redshifts of the lasts minor (left panel) and major (right panel) mergers. All the distributions are shown for the three stellar mass bins as in Figure 3.6 and in Figure 3.7. For each violin plot the median value of the corresponding distribution is reported.

mergers are shown. For each stellar mass bin, the data distributions are presented as *violin plots*, which provide the probability density of a sample of data, smoothed by a kernel density estimator. The shape of each violin plot represents the frequency of data, so that the larger the violin's body, the higher the density of data at a given y-axis value. The complementary behaviour of the in-situ and ex-situ stellar mass fractions in the two top panels of Figure 3.8 confirms the rising importance of the accreted stars going towards the high-mass tail of ETGs. In particular, the median distribution of the ex-situ stellar fraction grows from around 29% of the total stellar mass for galaxies with $10.5 < \log(M_*/\mathrm{M}_\odot) < 11$ up to $\approx 77\%$ for the most massive systems. As in Rodriguez-Gomez et al. (2015, 2016), by defining μ_* as the *stellar mass ratio* between the two progenitors of a given galaxy, a *major merger* is identified by a $\mu_* > 1/4$, while a *minor merger* is defined by $1/10 < \mu_* < 1/4$. However, the fraction of accreted stars from other galaxies is not only due to major and minor mergers: indeed, the remaining fraction includes stars from the so-called *very minor mergers*, i.e. with $\mu_* < 1/10$, as well as stripped stars from surviving galaxies. As illustrated in the left panel of the second row of Figure 3.8, the analysis of the ex-situ fraction from all mergers (i.e. major, minor, and very minor mergers) relative to the total ex-situ fraction, reveals that, on average, more than 80% of stars are accreted via mergers. Specifically, this relative fraction reduces from $\approx 98\%$ to $\approx 84\%$ towards the most massive galaxies. The remaining percentage of stars, instead, are those stripped from other surviving galaxies, which increases as the stellar mass goes up. By isolating the role of major mergers (see the right panel in the second row), their contribution presents broad distributions, with median values of around 50% (relative to the whole ex-situ stellar fraction) for ETGs with $\log(M_*/\mathrm{M}_\odot) > 11$. Furthermore, looking at the distributions of the number of major and minor mergers occurred in the IllustrisTNG ETGs, the two plots clearly show the relevance of major mergers in producing the final remnants. Finally, during their stellar mass assembly history, IllustrisTNG ETGs experienced, on average, their last major mergers in each stellar mass bin more recently than the last minor mergers, with a median redshift that decreases from $z \simeq 1.41$ in the low-mass bin to $z \simeq 0.32$ for ETGs with $\log(M_*/\mathrm{M}_\odot) > 11.5$.

The second row of plots in Figure 3.6 illustrates the metallicity profiles in the three mass bins. The two MaNGA profiles show similar radial distributions, that differ mainly in normalisation: on average, FIREFLY provides for the same galaxy an estimate of metallicity higher than the one made by PROSPECTOR by $\approx 0.1\,\mathrm{dex}$. The stellar metallicity from IllustrisTNG tends, on average, to be slightly higher in normalisation, but, in particular in the intermediate and high mass bins, it is quite similar to the metallicity estimated by FIREFLY. In this case, we stress also the

importance of applying a smoothing using the MaNGA PSF on the original maps of simulated objects. Indeed, in all the mass bins the metallicity profiles from the original maps (upper black curves in the plots) are steeper than those obtained from the convolved maps, the latter giving a metallicity lower by $\approx 0.15-0.2\,\mathrm{dex}$ in the innermost parts. Concerning in-situ and ex-situ stellar metallicity (second row of plot in Figure 3.7), IllustrisTNG galaxies are characterised by ex-situ stars that are more metal rich than the in-situ population, and this gap increases as increasing stellar mass.

The radial distributions of stellar age (third row of plots in Figure 3.6) derived from FIREFLY and PROSPECTOR show a common behaviour in the three stellar mass bins: a systematic shift in age is found between the two stellar fitting codes that, on average, for the same galaxy assign an age to the stellar population at each radius that differs of around $2\,\mathrm{Gyr}$. The systematic difference in age obtained by the two codes may be partially explained in terms of the *age-metallicity degeneracy*: the red colours that characterise old stellar populations can be explained also assuming a higher metallicity, and viceversa (Worthey, 1994). Indeed, for the same sample of ETGs, on average, FIREFLY derives a bit more metal-rich and younger stellar populations with respect to the estimates from the PROSPECTOR code. However, most of the substantial discrepancy between the two estimates of stellar age should be ascribed to the different fitting methods and libraries used by FIREFLY and PROSPECTOR, as discussed in subsection 3.2.1. The large gap between the two stellar age profiles can be taken as a measure of the uncertainty on the age of the observed galaxies of our sample. It is clear that these age profiles have little constraining power on theoretical models, implying that the almost flat IllustrisTNG profiles lies in between. Moreover, qualitatively speaking, we observe that, while at the low-mass tail IllustrisTNG reproduces better the age predicted by FIREFLY, analysing the most massive systems, these tend to be more representative of the ages provided by PROSPECTOR, at least within the first 10 kpc. The analysis of the radial distributions of age for the in-situ and ex-situ stellar populations in the simulated ETGs (third rows of plots in Figure 3.7) shows that, below $\log(M_*/\mathrm{M}_\odot) \approx 11$, the ex-situ component is older (up to $+1.5\,\mathrm{Gyr}$) than the in-situ one over the entire range in radius, whereas the inner regions ($R \lesssim 7\,\mathrm{kpc}$) of galaxies with $\log(M_*/\mathrm{M}_\odot) \gtrsim 11$ are composed by stars with similar ages.

Finally, the bottom panels in Figure 3.6 display the radial profiles of stellar velocity dispersion for simulated and observed ETGs, the latter obtained using the PPXF code. Below $\log(M_*/\mathrm{M}_\odot) \approx 11.5$, albeit PPXF profiles tend to be slightly steeper than the IllustrisTNG ones, we found a good agreement between the two measurements. Above $\log(M_*/\mathrm{M}_\odot) \approx 11.5$, the velocity dispersion profiles of both MaNGA and

IllustrisTNG galaxies are almost flat out to $R \approx 40\,\mathrm{kpc}$. However, we find an almost constant discrepancy between the two profiles, with velocity dispersions for the simulated ETGs generally higher by $30-40\,\mathrm{km\,s^{-1}}$ (that will be discussed in subsection 3.4.3), but enough compatible within the uncertainties. The line-of-sight velocity dispersion profiles for in-situ and ex-situ stellar populations (the bottom panels in Figure 3.7) almost coincide in the intermediate and high mass bins, while in the low-mass bin the velocity dispersion is higher in the centre for the in-situ component. For given gravitational potential, the line-of-sight velocity dispersion profile of a given component depends both on its intrinsic velocity distribution and its density distribution. In the low-mass bin, the higher central velocity dispersion of the in-situ component can be qualitatively explained by its shallower surface density profile (top-left panel in Figure 3.7).

3.4.2 Comparing profiles in number-density-based stellar mass bins

The same analysis performed using a selection in number-density-based stellar mass bins, rather than in stellar mass bins, does not reveal crucial differences from the previous results. As illustrated in Figure 3.9, the most evident exceptions concern the central bins of the stellar properties analysed. In particular, the discrepancy between the radial profiles of the stellar mass surface density increases, highlighting a tendency of the simulated galaxies to assume lower values. On the contrary, the discrepancy of the stellar metallicity profiles between the MaNGA and IllustrisTNG reduces. Age profiles are not significantly affected by this selection. Instead, concerning velocity dispersion, in this case there is a better agreement between the observed and simulated profiles in the last bin, to the detriment of the central bin, where the IllustrisTNG profile is systematically lower than that of MaNGA. The same considerations are valid for in-situ and ex-situ stellar profiles in Figure 3.10 if compared with Figure 3.7.

3.4.3 Central versus satellite galaxies

The analysis of radial distributions of stellar physical properties can be extended to central and satellite galaxies, by disentangling their role in both IllustrisTNG and MaNGA samples. Halos and subhalos in IllustrisTNG are detected by SUBFIND, the subhalo finder code developed by Springel et al. (2001). An IllustrisTNG subhalo is classified as central if it is the most massive subhalo of each friends-of-friends

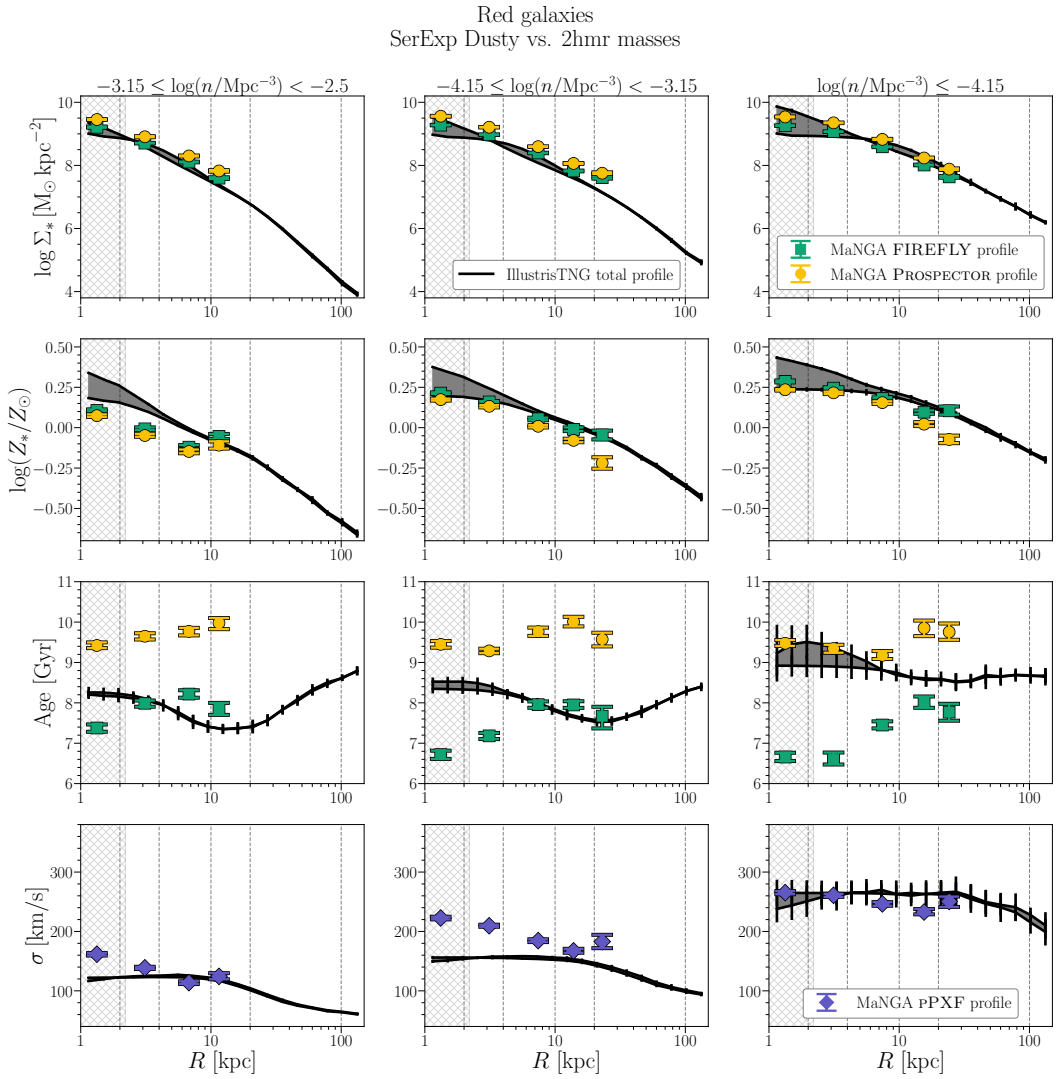

Fig. 3.9: Same as Figure 3.6, but in number-density-based stellar mass bins.

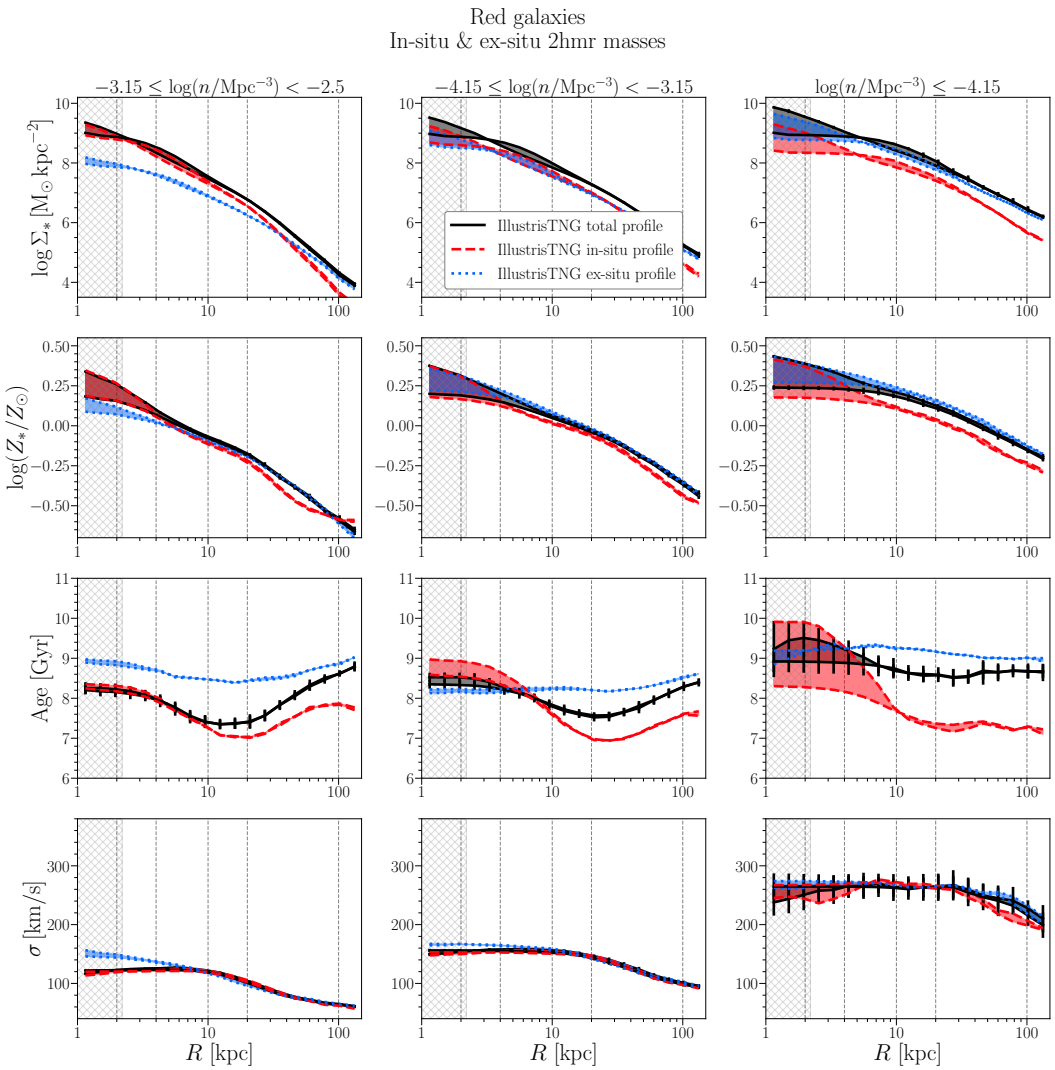

Fig. 3.10: Same as Figure 3.7, but in number-density-based stellar mass bins.

(FoF) halo (flag `is_primary==1`). Otherwise, subhalos are classified as satellites. Concerning MaNGA galaxies, to separate ETGs into central and satellite galaxies we rely on the classification provided by Yang et al. (2007), obtained for a sample of more than 300,000 galaxies from SDSS DR4 (Adelman-McCarthy et al., 2006). In the following we will show the results of this analysis only for the convolved profiles of Red galaxy samples, using for MaNGA the SerExp Dusty masses and for IllustrisTNG the 2hmr masses. The same analysis carried out on the other samples return results consistent with those described here. The stellar mass surface density (Figure 3.11), metallicity (Figure 3.12), age (Figure 3.13), and velocity dispersion (Figure 3.14) profiles in the three stellar mass bins as in Figure 3.6 are displayed. The darkest curves (black, red and blue) indicate the radial distributions for IllustrisTNG central galaxies (for the total, in-situ, and ex-situ stellar components), while the lightest curves (grey, pink and cyan) refer to satellites. The green, yellow and violet dots indicate the estimate derived by FIREFLY, PROSPECTOR and pPXF for centrals, while azure, redbrick and orange are those related to satellites. The profiles for MaNGA central and satellite galaxies show, within the uncertainties, similar results for all the stellar properties analysed in this work. The only exception concerns two median estimates derived by FIREFLY, in the radial bins $4-10\,\mathrm{kpc}$ and $10-20\,\mathrm{kpc}$ for galaxies within the range $10.5 < \log(M_*/\mathrm{M}_\odot) < 11$ (the top-left panel of Figure 3.13), for which satellites have slightly older stellar populations than the central counterparts. However, these differences are quite small if compared with the discrepancies between FIREFLY and PROSPECTOR measurements.

In the IllustrisTNG stellar mass surface density profiles, no significant differences between central and satellite galaxies are found at all masses, at least out to $\approx 30\,\mathrm{kpc}$ from the centers. Moreover, even in this case, centrals and satellites share the same behaviour for the in-situ and ex-situ stellar populations over the entire range in stellar mass considered. Although one would expect that central galaxies should accrete more ex-situ stars than satellites, a possible explanation for this similarity (that we plan to investigate in the future) is that most satellites have been recently accreted onto the main halo and acquired a significant fraction of their ex-situ component when they were centrals of other halos. Also stellar metallicity profiles for the two galaxy populations in IllustrisTNG almost overlap at all radii and masses. The stellar age radial distributions for the total stellar components for centrals and satellites are consistent to each other, showing only a small difference for the median age of the most massive systems ($M_* > 10^{11.5}\,\mathrm{M}_\odot$), for which centrals appear to be slightly older (but consistent within the uncertainties) than satellite galaxies.

The analysis made on the radial profiles of velocity dispersion in IllustrisTNG reveals the most impactful result: though centrals and satellites have a common behaviour

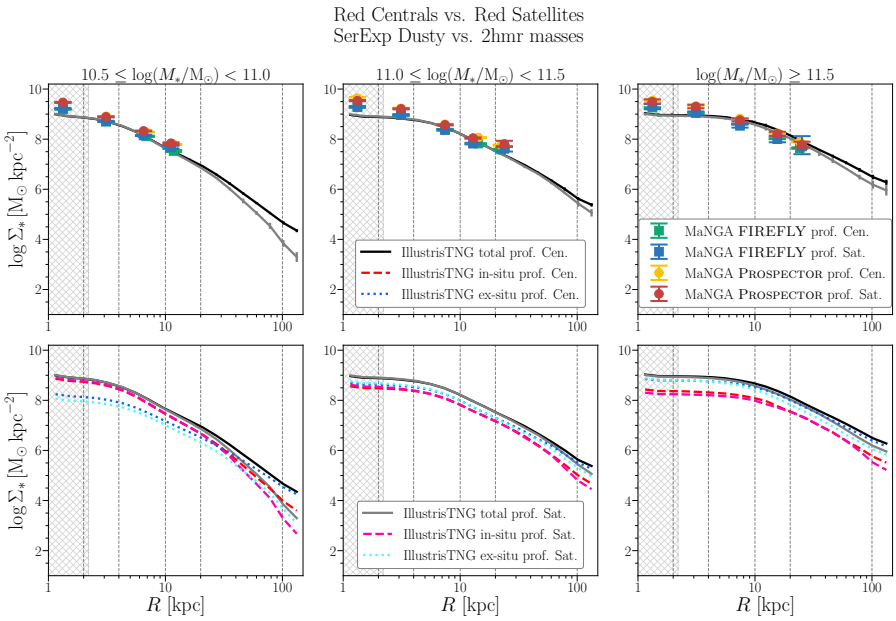

Fig. 3.11: Top panels: radial profiles for stellar mass surface density in three bins of stellar mass for MaNGA and IllustrisTNG Red central and satellite galaxies. For MaNGA ETGs we use the Dusty model masses, while for IllustrisTNG ETGs we use the 2hmr masses. The green and yellow dots represent the median estimates for MaNGA central ETGs from FIREFLY and PROSPECTOR codes, while the azure and redbrick dots are the median values obtained for MaNGA satellites ETGs, in the 5 radial bins identified by the grey dashed lines. The errorbars represent the 1σ uncertainties for MaNGA and IllustrisTNG estimates. The black and grey curve represent the median value of each stellar property for the total stellar populations in central and satellite IllustrisTNG galaxies in 20 radial bins spaced uniformly in log over the range $0-150\,\mathrm{kpc}$, both obtained from the maps convolved with the MaNGA PSF. Bottom panels: the red dashed and blue dotted curves represent the in-situ and the ex-situ stellar components for centrals, while the pink dashed and cyan dotted curves indicate the in-situ and ex-situ stellar components for satellites. For clarity reasons, we omit the errobars for the plots in the lower panels. The hatched area (0:2.1 kpc) shows 3x the force resolution of the stellar particles in IllustrisTNG.

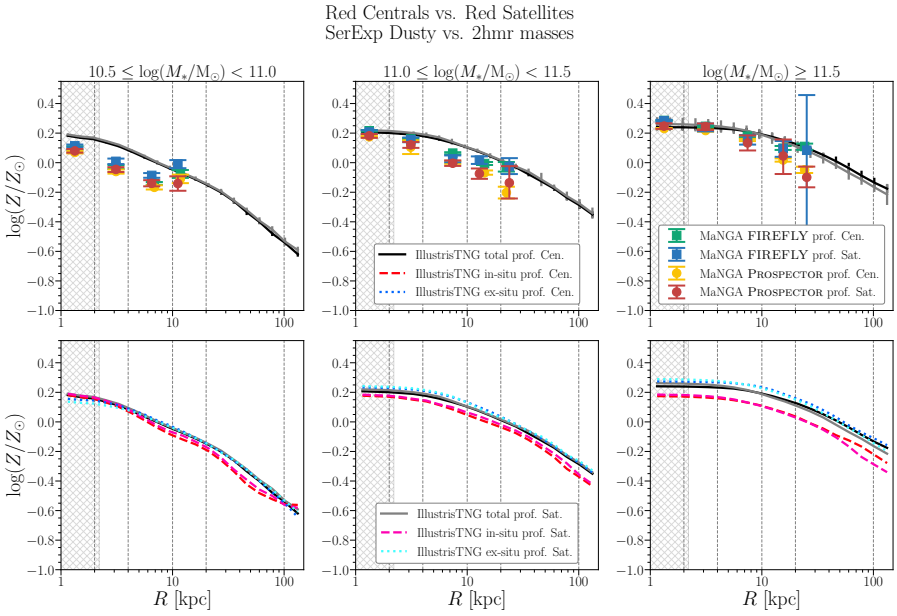

Fig. 3.12: Same as in Figure 3.11, but for stellar metallicity.

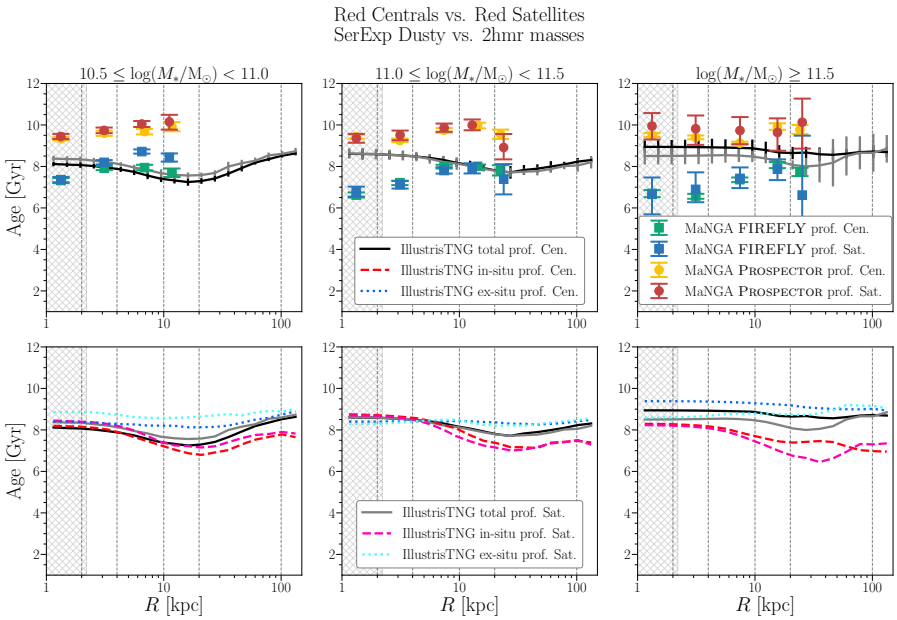

Fig. 3.13: Same as in Figure 3.11, but for stellar age.

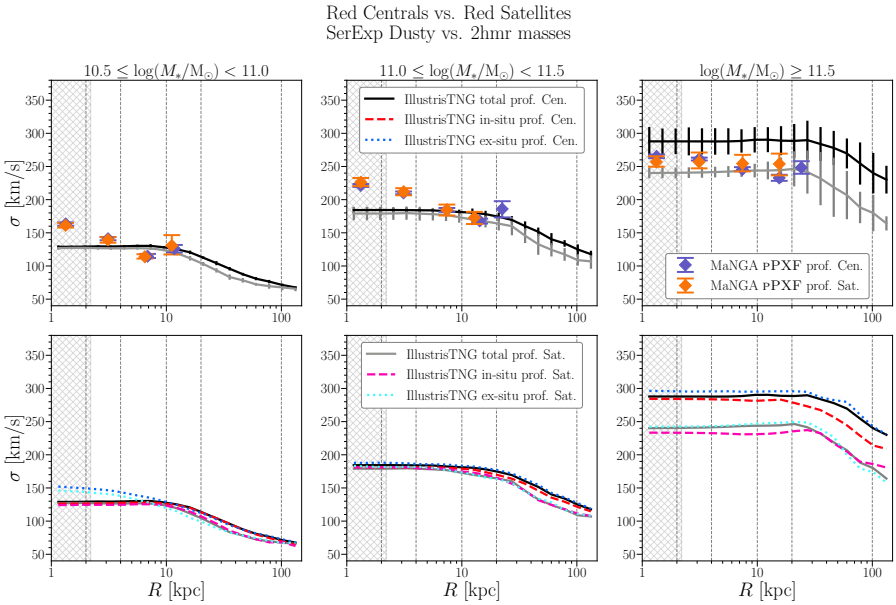

Fig. 3.14: Same as in Figure 3.11, but for stellar velocity dispersion. The violet and orange diamonds represent the median estimates for MaNGA central and satellite ETGs from pPXF code, respectively.

for systems with $M_* < 10^{11.5}\,\mathrm{M}_\odot$, central galaxies in the high-mass tail exhibit, at fixed radius, a systematic shift with respect to the median profile of satellites that generally is of $\approx +50\,\mathrm{km\,s^{-1}}$, while satellites agree within the errors with estimates derived by pPXF for both the observed populations. Albeit the study of the dark matter content in galaxies is out of the scope of this project, a possible explanation for the significant difference in velocity dispersion between IllustrisTNG centrals and satellites may reside on the large amount of dark matter in central simulated galaxies. As discussed in Lovell et al. (2018), whose study is focused only on central galaxies of IllustrisTNG, the simulation predicts an important enhancement of the dark matter content in the inner regions of subhalos. Hence, this high fraction of dark matter, that dominates galaxies at $z \approx 0$, may be the responsible of this high velocity dispersion especially for the most massive central galaxies.

3.4.4 Comparison with recent works in literature exploiting MaNGA data

So far, we have discussed the contrast made between MaNGA and IllustrisTNG, finding a reasonable similarity between the two samples and the radial distributions of the analysed stellar properties. In this section, we compare our outcomes with some recent works in literature based on MaNGA galaxies.

Using a sample of 366 ETGs, selected as such by adopting the Galaxy Zoo morphological classification (Lintott et al., 2011; Willett et al., 2013) and then visually inspected, with masses in the range $9.9 < \log(M_*/\mathrm{M}_\odot) < 10.8$, Parikh et al. (2018, 2019) analysed the radial gradients of stellar age, metallicity, $[\alpha/\mathrm{Fe}]$, $[\mathrm{Na}/\mathrm{Fe}]$, and IMF slope out to one half-radii. If we consider in our sample only galaxies with stellar mass lower than $10^{10.8}\,\mathrm{M}_\odot$[15], we find a satisfying consistency with the stellar age and metallicity gradients provided by Parikh et al. (2018, 2019).

Bernardi et al. (2019) show stellar population gradients for a sample of MaNGA DR15 elliptical galaxies subdivided into slow and fast rotators, making considerations on the role of environment as well. ETGs are identified as in Domínguez Sánchez et al. (2020), i.e. applying the same morphological approach described in subsection 3.2.4 based on T-Type ≤ 0, considering both pure ellipticals and lenticulars. Moreover, the authors subdivide galaxies into slow and fast rotators, where the former are expected to be characterised by a merger-dominated stellar mass assembly history. Among the stellar population properties taken into account, they found that fast rotators are more metal rich, but poor in α-elements, and younger than slow rotators. Even in that work, the study of the stellar populations gradients are extended out $1\,R_\mathrm{e}$, and their age and metallicity gradients are qualitative compatible with our estimates. One of the most relevant outcomes of Bernardi et al. (2019) is that slow rotators become dominating above $\log(M_*/\mathrm{M}_\odot) \approx 11.5$: at this stellar mass, where also the size-mass relation slope changes (see Bernardi et al., 2011a), ellipticals are found to be almost central galaxies[16]. Moreover, as the mass increases, ETGs tend to move from fast to slow rotators, the latter mainly assembled via the two-phase formation scenario (see Cappellari, 2016), result in agreement with findings from IllustrisTNG. As an extension of the Bernardi et al. (2019) work, in Domínguez Sánchez et al. (2020) the authors focus their study on stellar properties of S0 lenticular galaxies, highlighting a bimodality in this galaxy population depending on stellar mass. Above $\log(M_*/\mathrm{M}_\odot) \approx 10.5$, indeed, these galaxies are characterised by stronger age and velocity dispersion gradients, with, instead, negligible gradients in metallicity.

In a recent work, Pulsoni et al. (2020) analyse the photometric and kinematic properties out to $15\,R_\mathrm{e}$ of ETGs stellar halos for 1114 objects in IllustrisTNG100 (together with other 80 sources in IllustrisTNG50), with $10.3 < \log(M_*/\mathrm{M}_\odot) < 12$ and selected in $g - r$ colours (pretty similiarly with the selection adopted in this work) and in the angular momentum–ellipticity plane. IllustrisTNG ETGs are

[15] The median effective radius for our MaNGA ETGs with stellar mass lower than $10^{10.8}\,\mathrm{M}_\odot$, i.e. the highest mass considered in Parikh et al. (2018, 2019), is $\lesssim 3\,\mathrm{kpc}$.

[16] Bernardi et al. (2019) make use of the Yang et al. (2007) environmental catalogue used also in this work.

compared with some observational survey, including MaNGA galaxies. Looking at the distribution of galaxies in the angular momentum–ellipticity plane within $1\,R_{\rm e}$, a percentage of the IllustrisTNG galaxies lie in a region where no observed ETGs are found: these are basically elongated, triaxial systems. However, when simulated galaxies with an intemediate-to-major axis ratio $p < 0.6$ at $1\,R_{\rm e}$ are removed - the centrally elongated objects -, the simulated ETGs reflect the location in the plane of observed galaxies, except for a region where a large fraction of MaNGA S0 with an angular momentum parameter > 0.7 is present.

3.5 Conclusions

In this work we made a consistent comparison between ETGs with $M_* \gtrsim 10^{10.5}\,{\rm M}_\odot$ taken from the state-of-the-art spatially-resolved MaNGA survey and the magneto-hydrodynamic cosmological simulation IllustrisTNG100. The main scope of this project was to provide an interpretative scenario of the stellar mass assembly history of ETGs that we observe in the present-day Universe, disentangling the role of in-situ and ex-situ stellar populations in simulated galaxies, through the analysis of the radial distributions of stellar mass surface density, metallicity, age, as well as velocity dispersion.

Our main results are summarised here below.

- We do find a remarkable agreement between observations and simulations in the stellar mass surface density radial profiles. This agreement is observed at all radii, at any stellar mass as well as considering different definitions of ETGs and/or stellar mass definitions.

- Generally, IllustrisTNG galaxies profiles reproduce quite well the metallicity, age and velocity dispersion radial distributions of MaNGA galaxies. Concerning metallicity, the shape of the PSF-convolved profiles for IlllustrisTNG galaxies is similar to those of MaNGA ETGs, in particular for galaxies with $M_* \gtrsim 10^{11}\,{\rm M}_\odot$, differing at most in normalisation. The age of observed ETGs are highly uncertain. The age profiles of stellar populations in IllustrisTNG are found to lie in between the profiles predicted by FIREFLY and PROSPECTOR. Finally, for galaxies $M_* < 10^{11.5}\,{\rm M}_\odot$, we find a rather good agreement also for the radial distributions of velocity dispersion for both simulated and observed ETGs. However, the very massive systems of IllustrisTNG tend to overpredict the velocity dispersion, over the entire range of radii, even by $\approx +50\,{\rm km\,s^{-1}}$.

- By separating central and satellite galaxies for both IllustrisTNG and MaNGA ETGs, we find that there are not relevant differences in all the profiles between the two galaxy populations, except for the velocity dispersion profiles of massive systems ($M_* > 10^{11.5}\,\mathrm{M}_\odot$). Indeed, we find that, while satellites are in a good agreement with the MaNGA velocity dispersion profiles, central galaxies tend to have velocity dispersion at all radii higher than observed ETGs by around $50\,\mathrm{km\,s^{-1}}$.

- The behaviour of the in-situ and ex-situ stellar mass surface density profiles identifies two different scenarios for the merger-driven history of these objects, corroborating previous outcomes from Pillepich et al. (2018a) and Tacchella et al. (2019): galaxies with $M_* < 10^{11}\,\mathrm{M}_\odot$ are mainly dominated by the in-situ stellar populations out to $\approx 20{-}30\,\mathrm{kpc}$; going towards the high-mass tail of galaxies ($M_* \gtrsim 10^{11}\,\mathrm{M}_\odot$), in these systems the role of the ex-situ stars becomes as relevant as that of the in-situ component, being even totally dominating for very massive ETGs ($M_* \gtrsim 10^{11.5}\,\mathrm{M}_\odot$).

- The similar shapes found for the radial distributions of the stellar mass surface density for both in-situ and ex-situ stars (see Figure 3.7 and Figure 3.10) as well as the detailed analysis of the merger history (see Figure 3.8) of simulated ETGs reveal that especially galaxies with $M_* \gtrsim 10^{11}\,\mathrm{M}_\odot$ experienced across cosmic time a merger-driven evolution mainly marked by major merger events. Indeed, major mergers allow both to explain the presence of a significant percentage of ex-situ stars that are able to penetrate even in the innermost part of galaxies, and also that the two stellar components are well homogenised at all radii, showing similar stellar mass surface density profiles.

This study sheds light on the current state of both cosmological simulations and stellar fitting codes used in observations. On the one hand, this work contributes to improve our understanding of the comparison between simulated and real objects, allowing to check whether and to what extent the physical models implemented in cosmological simulations are able to well describe the scenario of formation and evolution of galaxies (see also van de Sande et al., 2019). On the other hand, we showed that the estimates of some properties, like the stellar age, strongly depends on the choice of the fitting methods, models and libraries used to retrieve their estimates in observed sources, confirming previous works in the literature (e.g., Conroy, 2013b) about the necessity of improving current recipes.

For the future, we plan to extend the analysis to other stellar physical properties, like single chemical abundances. In order to provide a more complete scenario behind the cosmic evolution of the ETGs that we observe at $z = 0$, in simulations we will

reconstruct the merger history of individual progenitors, to take a look at the spatial distributions of their stellar properties and how these vary during their merging history. Finally, we will make use of the newest IllustrisTNG50 simulation which, though characterised by a smaller physical volume and thus a lower statistics, it benefits from a higher mass resolution that could allow us to make a more reliable comparison at smaller scales of galaxies with data from current and upcoming surveys.

Appendix 3.A: Comparing the results obtained using the SerExp Dusty and SerExp Dust-free model masses for MaNGA ETGs

In section 3.4, we have discussed the radial distributions of stellar properties of IllustrisTNG ETGs with those of MaNGA galaxies, using for the latter the stellar masses from the SerExp Dusty model taken from Meert et al. (2015). We applied again the same analysis using the masses from the SerExp Dust-free model for MaNGA ETGs. The colour-mass diagram and the mass distribution for this MaNGA sample compared with the IllustrisTNG galaxies is shown in Figure 3.15 (as in Figure 3.3). Similarly to what found for the MaNGA sample using the SerExp Dusty masses, using the MaNGA Morphology Deep Learning DR15 catalogue of Fischer et al. (2019), we do find that a percentage of around 84% of entire sample shows a typical ETG morphology, of which 23% with a high probability ($P_{\rm S0} > 50\%$) of being a lenticular galaxy.

The analysis of the profiles in stellar mass bins considering the SerExp Dust-free stellar mass measurements for MaNGA (Figure 3.17) shows an overall similar behaviour than that for the SerExp Dusty mass sample (Figure 3.6), with only few exceptions[17]:

- with Dust-free model masses, MaNGA ETGs, at fixed mass bin, tend to be slightly more metal poor than with Dusty model masses;
- similarly, at fixed mass bin, stellar ages tend to be slightly younger with the Dust-free model than with the Dusty model;
- in this case, the MaNGA velocity dispersion profiles are, on average, shifted down by around $20\,{\rm km\,s^{-1}}$ with respect to those of the Dusty model sample.

The same analysis performed using a selection in number-density-based stellar mass bins (Figure 3.18), rather than in stellar mass bins, does not reveal any significant difference from the results in Figure 3.9, except for the velocity dispersion profiles, where the median profile tends to assume lower values (similarly to the effect in Figure 3.17), showing a slightly better agreement with the IllustrisTNG profiles.

[17] The IllustrisTNG profiles shown in Figure 3.6, Figure 3.7 and in Figure 3.17 are the same, as well as the profiles selected in number-density-based stellar mass bins in Figure 3.9, Figure 3.10 and in Figure 3.18.

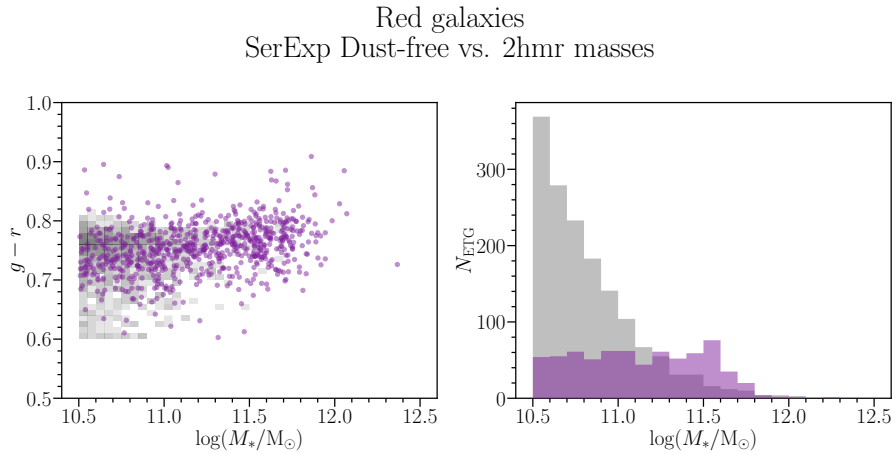

Fig. 3.15: Same as Figure 3.3, but for the SerExp Dust-free model stellar mass for MaNGA galaxies.

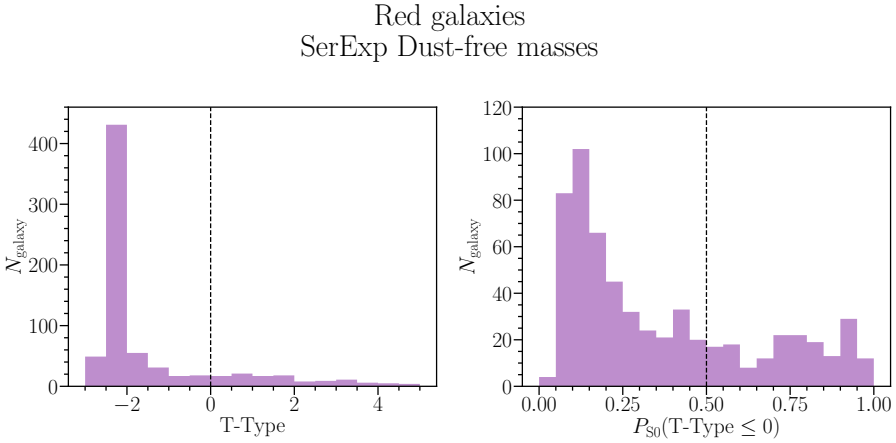

Fig. 3.16: Same as Figure 3.4, but for the SerExp Dust-free model stellar mass for MaNGA galaxies.

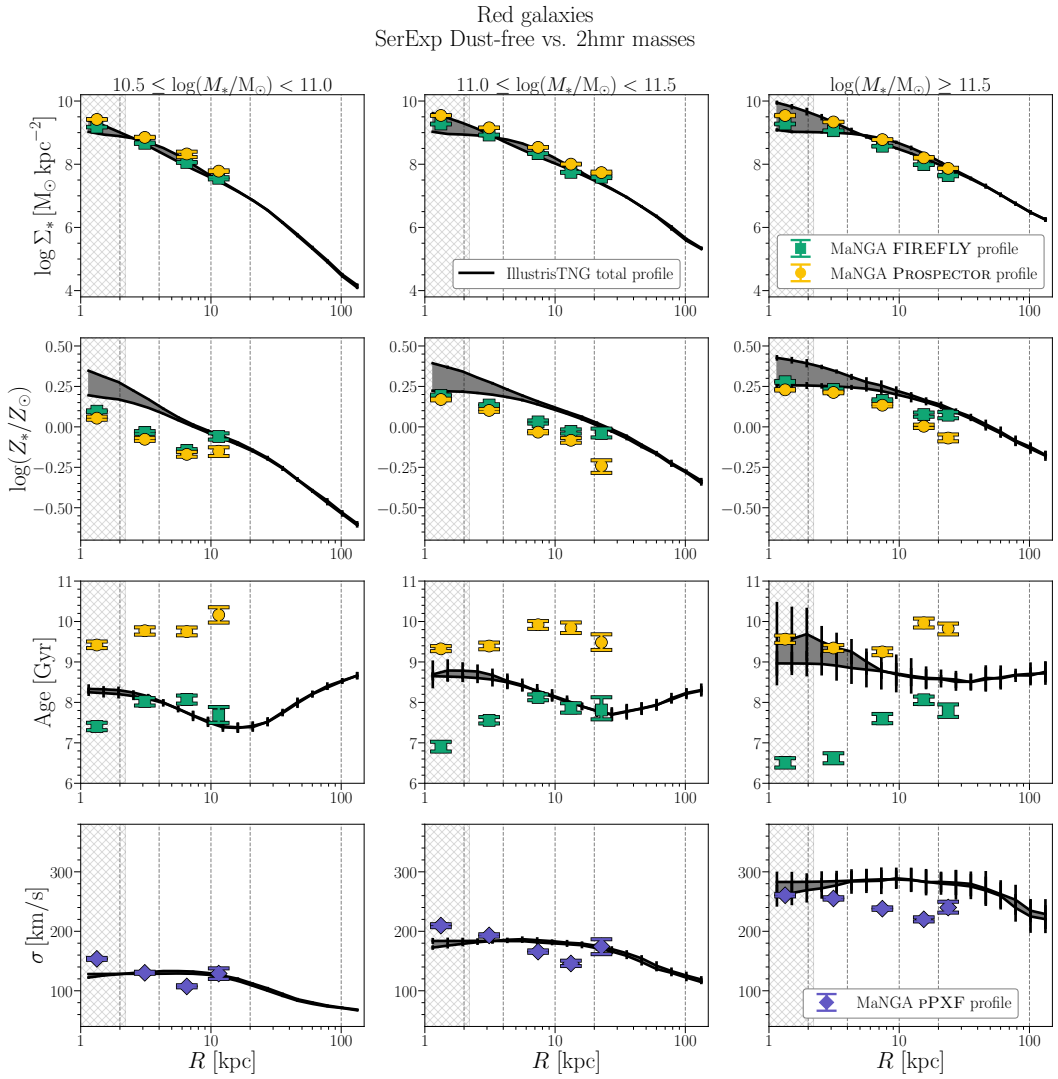

Fig. 3.17: Same as Figure 3.6, but for the Dust-free model masses for MaNGA ETGs.

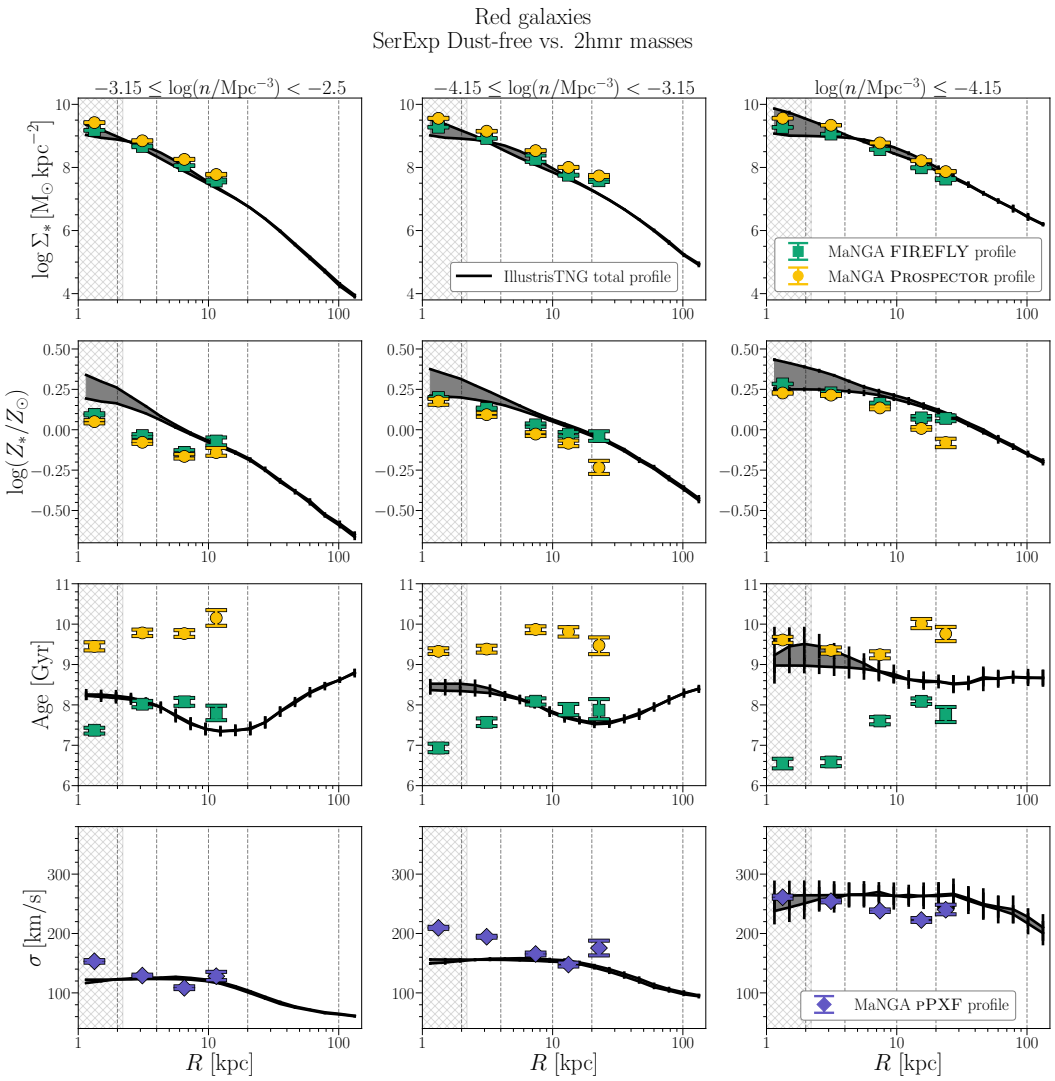

Fig. 3.18: Same as Figure 3.6, but in number-density-based stellar mass bins and for the Dust-free model masses for MaNGA ETGs.

Appendix 3.B: Computing the angular diameter distances to convolve IllustrisTNG maps

As described in subsection 3.3.2, in order to account for the effects of MaNGA resolution on simulated galaxies, for each stellar property we consider two limit-case profiles: given an IllustrisTNG ETG, one profile is computed directly from the original 2D stellar property map, while the other profile is derived from a map previously convolved with a 2D Gaussian filter kernel $\sigma_{\rm kernel}$.

For computing the kernel of each simulated galaxy, we use Equation 3.1, where $\mathcal{R}_{\rm TNG} = 1\,{\rm kpc}$ is the IllustrisTNG resolution of the original maps, while $\mathcal{R}_{{\rm MaNGA},i} = \sin({\rm PSF}_{\rm MaNGA}) d_{A,i}$ is the resolution of the i-th MaNGA ETGs, that depends on ${\rm PSF}_{\rm MaNGA} = 2.5''$ and the angular diameter distance $d_{A,i}$ of the i-th MaNGA galaxy. To measure $d_{A,i}$ we rely on the `angular_diameter_distance` function of the Python package AstroPy, that takes in input the redshift of the i-th source.

Since MaNGA was built in such a way that the most massive galaxies are located at higher redshifts, we fit the $z-M_*$ distribution of each MaNGA sample considered (so taking into account also the different definitions of the MaNGA masses for a given sample) and we assign to each IllustrisTNG galaxy the corresponding redshift value depending on its stellar mass.

In particular, the functional form adopted for fitting the $z-M_*$ distributions in MaNGA is

$$z = a\, e^{b \log(M_*/{\rm M}_\odot)}, \tag{3.5}$$

where a and b are the two parameters used for each fit. In Figure 3.19, the $z-M_*$ scatter distributions with the corresponding fits for the SerExp Dusty (left panel) and Dust-free (right panel) model masses are shown. Thus, these fits are used to assign the redshifts to the IllustrisTNG ETGs on the basis of their stellar masses, to compute their angular diameter distance, and then the kernel used to convolve their stellar property maps.

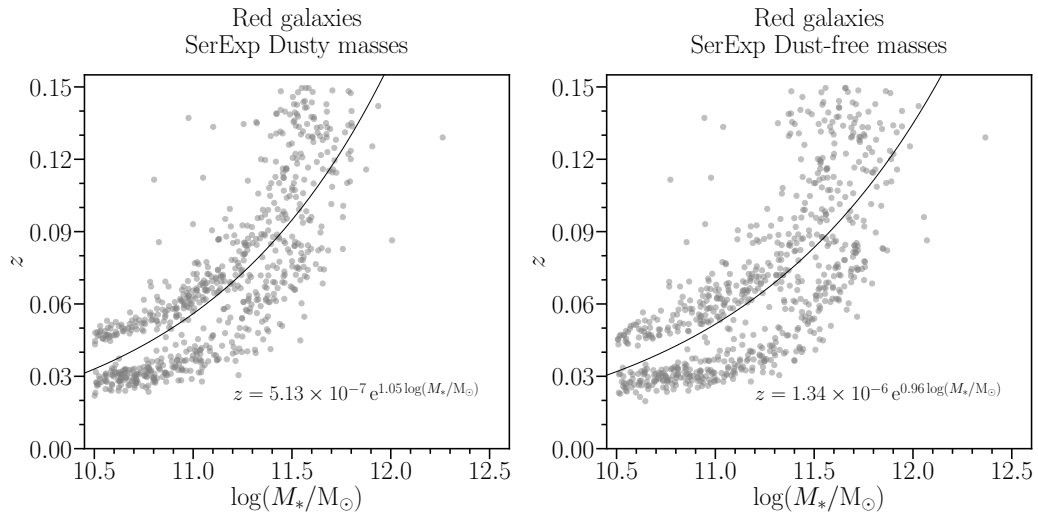

Fig. 3.19: The $z-M_*$ scatter distributions of the Red galaxy samples of MaNGA, using the SerExp Dusty model (left panel) and the SerExp Dust-free model (right panel) masses. The black solid curves trace the fit of each distribution. In each plot the corresponding fit functional form is reported. The two stripes of dots in each panel trace the Primary sample (the lower cloud) and the Secondary sample (the upper cloud) of the MaNGA total sample.

Appendix 3.C: Testing other definitions of ETGs and stellar masses

In subsection 3.2.3 and subsection 3.2.4 we presented the criteria adopted to select as homogeneously as possible ETGs from MaNGA and IllustrisTNG, as well as the definitions used for comparing stellar masses. Specifically, we selected ETGs as those galaxies characterised by colours $(g-r) > 0.6$, and for stellar masses we adopted the two mass estimates derived by Meert et al. (2015) using the PyMorph SerExp Dusty and Dust-free model stellar masses for MaNGA, and for IllustrisTNG we consider as stellar mass the sum of all stellar particles included within a projected area of radius twice the half-mass radius.

In order to check the reliability of our results, we extended our analysis to another definition of ETG and we adopted different stellar mass definitions for both MaNGA and IllustrisTNG samples. In particular, the other definition of ETGs tested here is presented in Donnari et al. (2019, see their Table 2), considering ETGs those galaxies having a measure of star formation rate below $1\,\mathrm{dex}$ the star-forming main sequence of galaxies:

$$\log\left(\frac{\mathrm{SFR}}{\mathrm{M_{\odot}yr^{-1}}}\right) = \alpha(z)\log\left(\frac{M_*}{\mathrm{M_{\odot}}}\right) + \beta(z), \tag{3.6}$$

assuming as α and β those at $z = 0$ reported in Table 3 of Donnari et al. (2019), i.e. $\alpha(z = 0) = 0.8$ and $\beta(z = 0) = -8.15$. MaNGA and IllustrisTNG galaxies selected by applying the above-mentioned selection criterion constitute the so-called *Quiescent galaxy samples*.

Concerning the estimates of stellar masses, we consider as further definition for IllustrisTNG galaxies the sum of all star particles within a projected aperture of $30\,\mathrm{kpc}$, while for MaNGA we use the masses derived from a Sérsic fit and a Petrosian fit included in the NSA catalogue, as well as the mass defined as the sum of the masses in the 5 concentric annuli estimated by FIREFLY and PROSPECTOR.

Overall, in all the cases shown in the following, we find a very high consistency with the results presented in section 3.4, corroborating the robustness of our study and its implications. Given the soundness of the results, for conciseness, here we will present results only for profiles derived from the original IllusrtisTNG maps (i.e. not derived from the convolved maps) and in stellar mass bins (i.e. not in number-density-based stellar mass bins).

In Figure 3.20 we show the colour–mass diagrams and the stellar mass distributions for the MaNGA and IllustrisTNG Quiescent galaxy samples, adopting for MaNGA the SerExp Dusty model and the SerExp Dust-free model stellar masses, while for IllustrisTNG the 2hmr stellar masses. The profiles for both MaNGA and IllustrisTNG Quiescent galaxies with these stellar masses are shown in Figure 3.21 (assuming for MaNGA the Dusty model masses) and in Figure 3.22 (assuming for MaNGA the Dusty model masses).

In Figure 3.23 we show the colour–mass diagrams and the stellar mass distributions for the MaNGA and IllustrisTNG Red galaxy samples, adopting for MaNGA the NSA Sérsic and Petrosian stellar masses, and the stellar masses included into the 5 radial bins computed by FIREFLY and PROSPECTOR, while for IllustrisTNG the stellar masses within an aperture of $30\,\mathrm{kpc}$. The profiles for both MaNGA and IllustrisTNG Red galaxies with these stellar masses are shown in Figure 3.24 (assuming for MaNGA the NSA Sérsic masses), in Figure 3.25 (assuming for MaNGA the NSA Petrosian masses), and in Figure 3.26 (assuming for MaNGA the masses within the 5 radial bins computed by FIREFLY and PROSPECTOR).

Finally, in Figure 3.27 we show the colour–mass diagrams and the stellar mass distributions for the MaNGA and IllustrisTNG Quiescent galaxy samples, adopting for MaNGA the NSA Sérsic and Petrosian stellar masses, and the stellar masses included into the 5 radial bins computed by FIREFLY and PROSPECTOR, while for IllustrisTNG the stellar masses within an aperture of $30\,\mathrm{kpc}$. The profiles for both MaNGA and IllustrisTNG Quiescent galaxies with these stellar masses are shown in Figure 3.28 (assuming for MaNGA the NSA Sérsic masses), in Figure 3.29 (assuming for MaNGA the NSA Petrosian masses), and in Figure 3.30 (assuming for MaNGA the masses within the 5 radial bins computed by FIREFLY and PROSPECTOR).

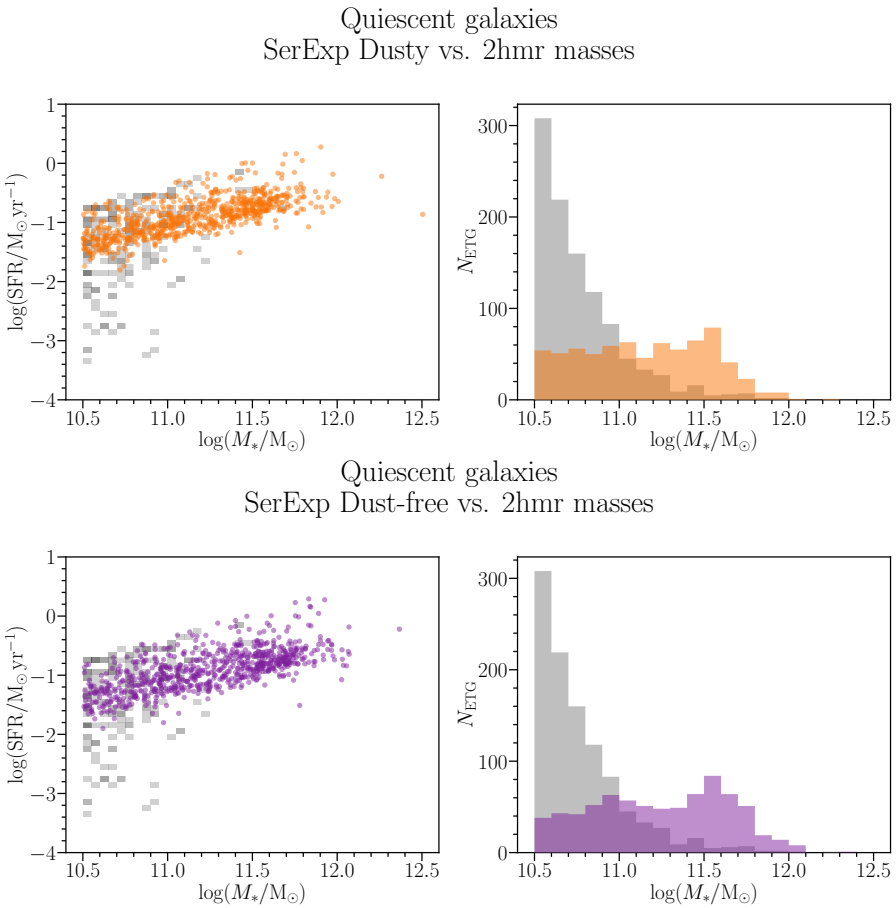

Fig. 3.20: Same as in Figure 3.3, but for Quiescent galaxies, i.e. galaxies with star formation rate below 1 dex the star-forming main sequence of galaxies, using the SerExp Dusty (top panels) and the SerExp Dust-free (bottom panels) stellar masses.

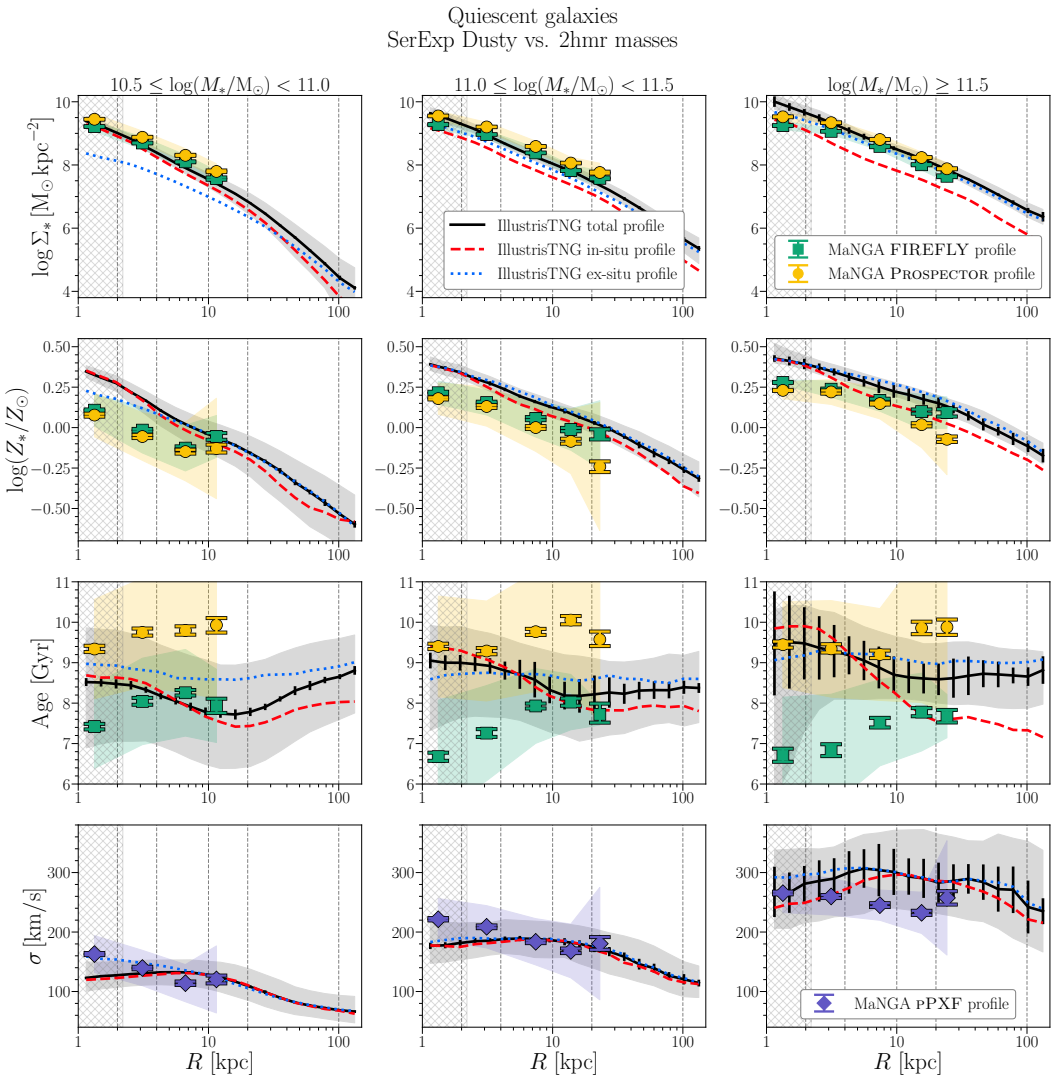

Fig. 3.21: Radial profiles of (from the top to the bottom) stellar mass surface density, metallicity, age, and velocity dispersion in three bins of mass for MaNGA and IllustrisTNG Quiescent galaxies. For MaNGA ETGs we use the Dusty model masses, while for IllustrisTNG ETGs we use the 2hmr masses. The green, yellow and violet dots represent the median estimates for MaNGA ETGs from FIREFLY, PROSPECTOR and pPXF codes, respectively, in the 5 radial bins identified by the grey dashed lines.The black solid, red dashed and blue dotted curves represent the median profiles of each stellar property for the total, the in-situ and the ex-situ stellar populations in IllustrisTNG galaxies in 20 radial bins spaced uniformly in log over the range $0-150\,\mathrm{kpc}$ obtained from the original maps. The black, green, yellow and violet shaded areas indicate the 68% intrinsic scatter distributions for IllustrisTNG, FIREFLY, PROSPECTOR, and pPXF profiles, respectively. The error-bars represent the 1σ uncertainties on the median for MaNGA and IllustrisTNG estimates. The hatched area (0:2.1 kpc) shows 3x the force resolution of the stellar particles in IllustrisTNG.

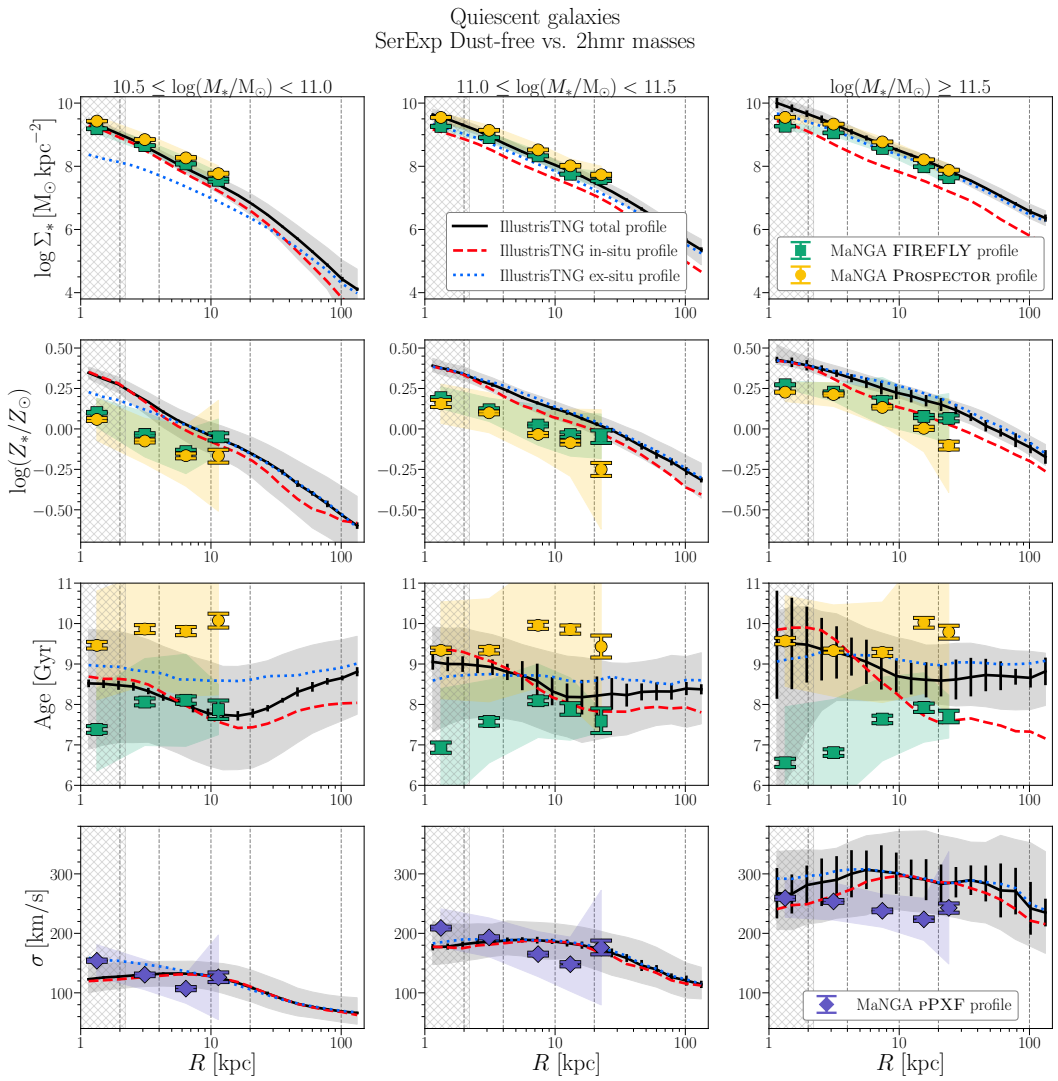

Fig. 3.22: Same as Figure 3.21, but assuming the SerExp Dust-free model masses for MaNGA galaxies.

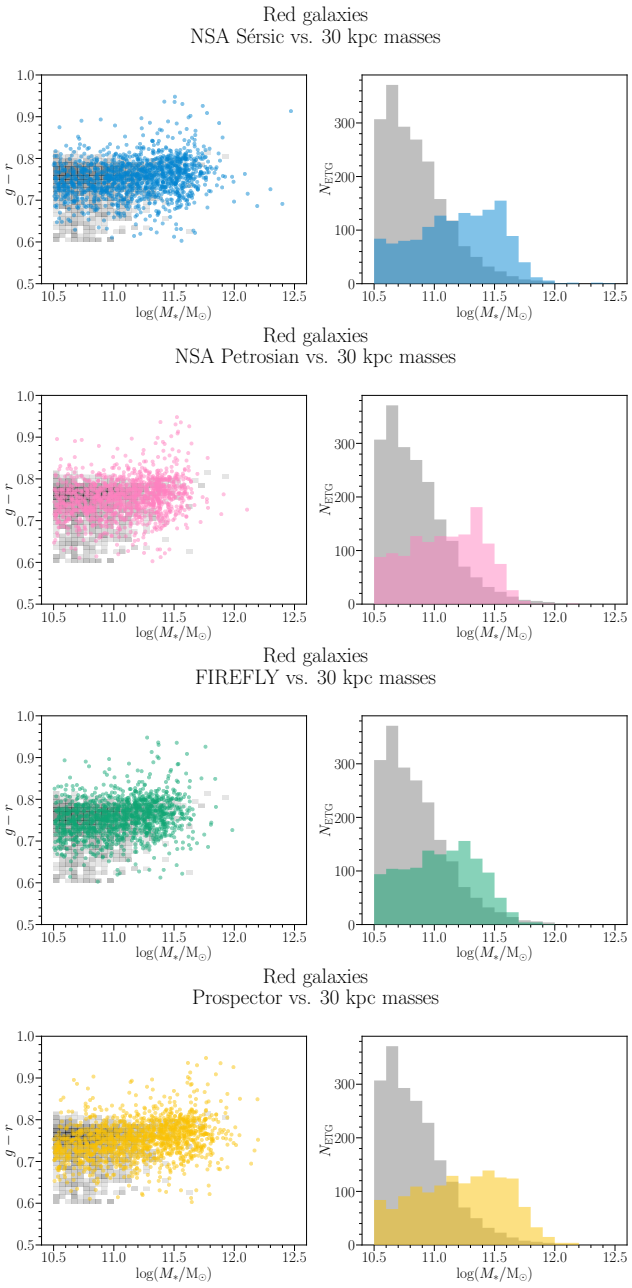

Fig. 3.23: Same as Figure 3.20, but for Red galaxies. For MaNGA galaxies we adopt, from the top to the bottom panels, the NSA Sérsic masses (blue dots and histograms), the NSA Petrosian masses (pink dots and histograms) and the masses included into the 5 radial bins computed by FIREFLY (green dots and histograms) and PROSPECTOR (yellow dots and histograms), while for IllustrisTNG galaxies we assume the masses within an aperture of 30 kpc (grey 1D and 2D histograms).

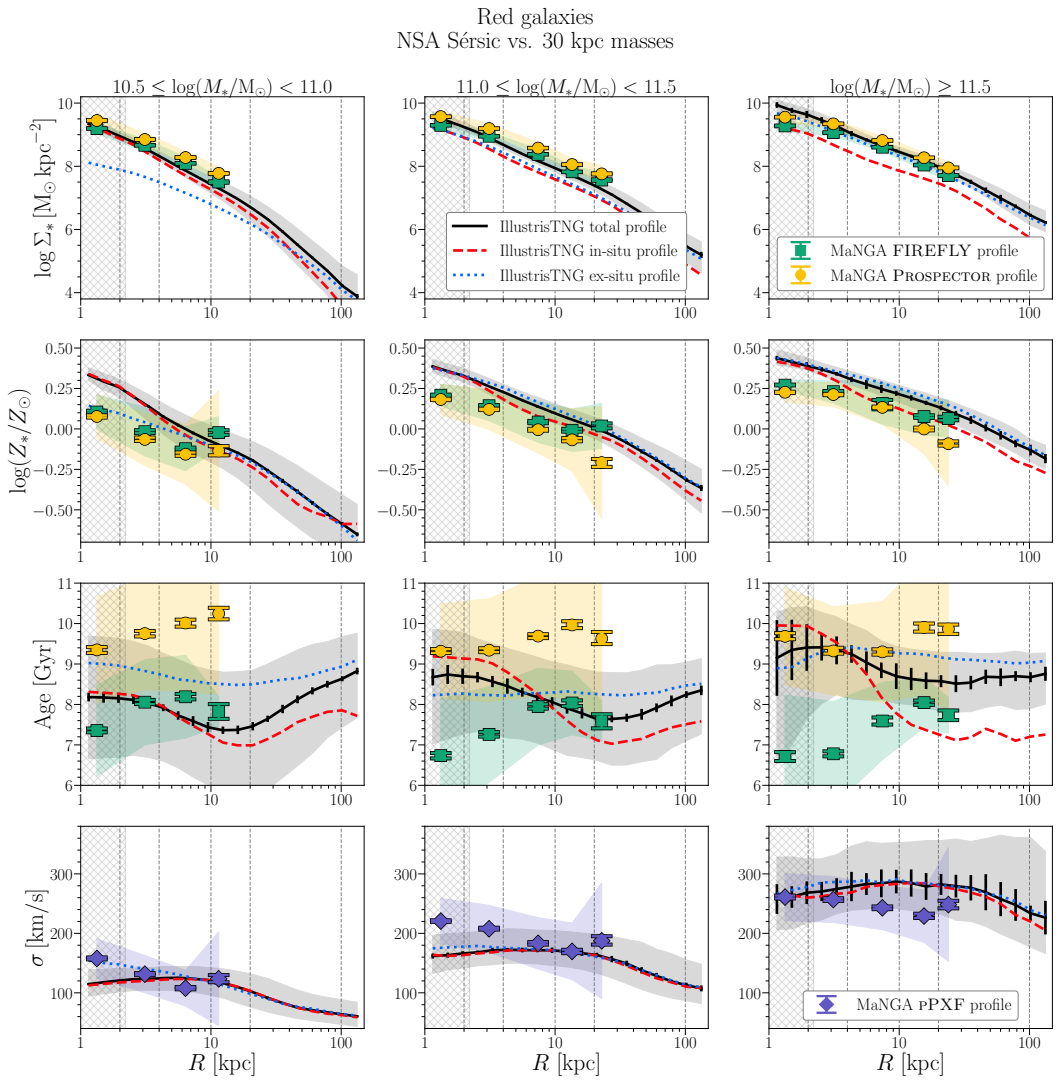

Fig. 3.24: Same as Figure 3.21, but for Red galaxies and assuming the NSA Sérsic masses for MaNGA galaxies, and the masses within 30 kpc for IllustrisTNG galaxies.

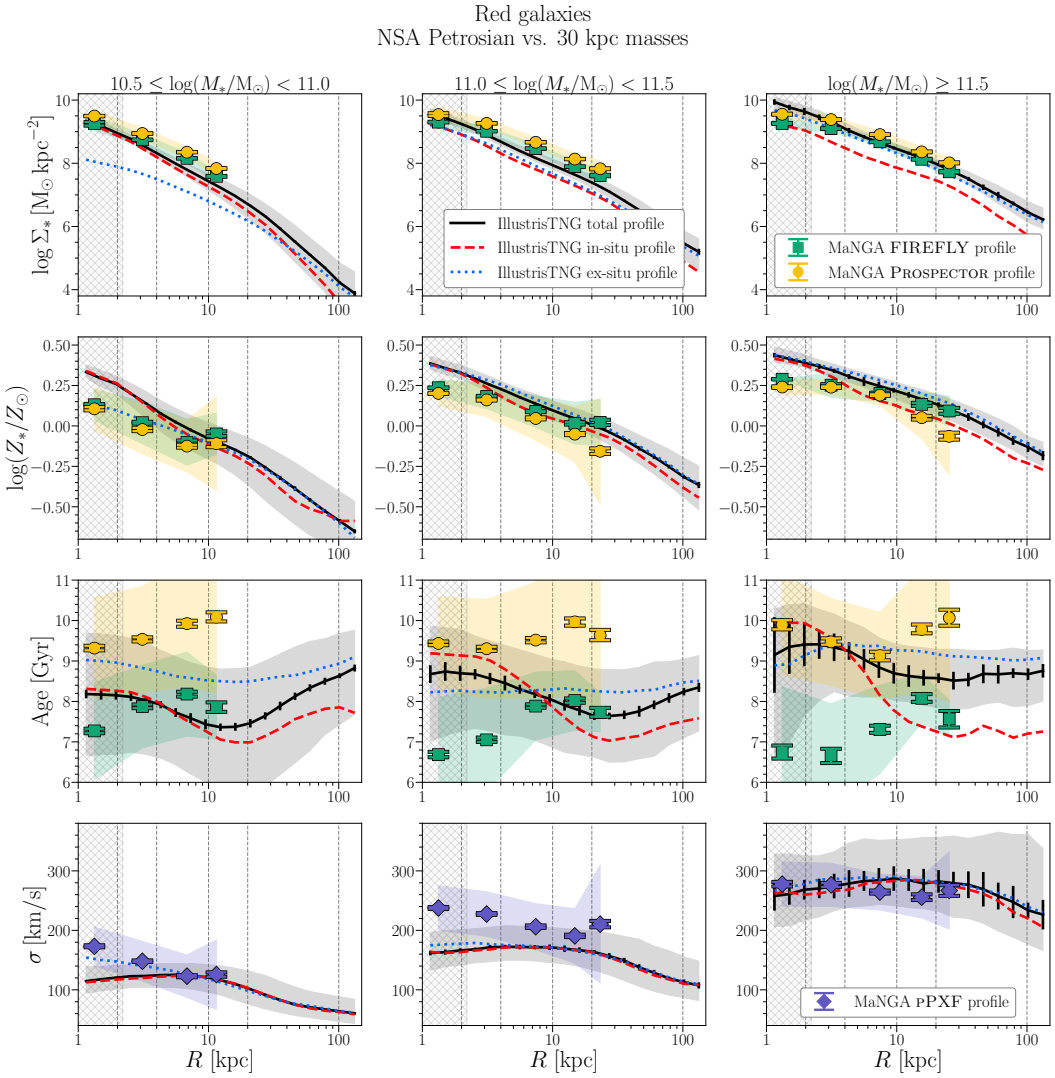

Fig. 3.25: Same as Figure 3.21, but for Red galaxies and assuming the NSA Petrosian masses for MaNGA galaxies, and the masses within 30 kpc for IllustrisTNG galaxies.

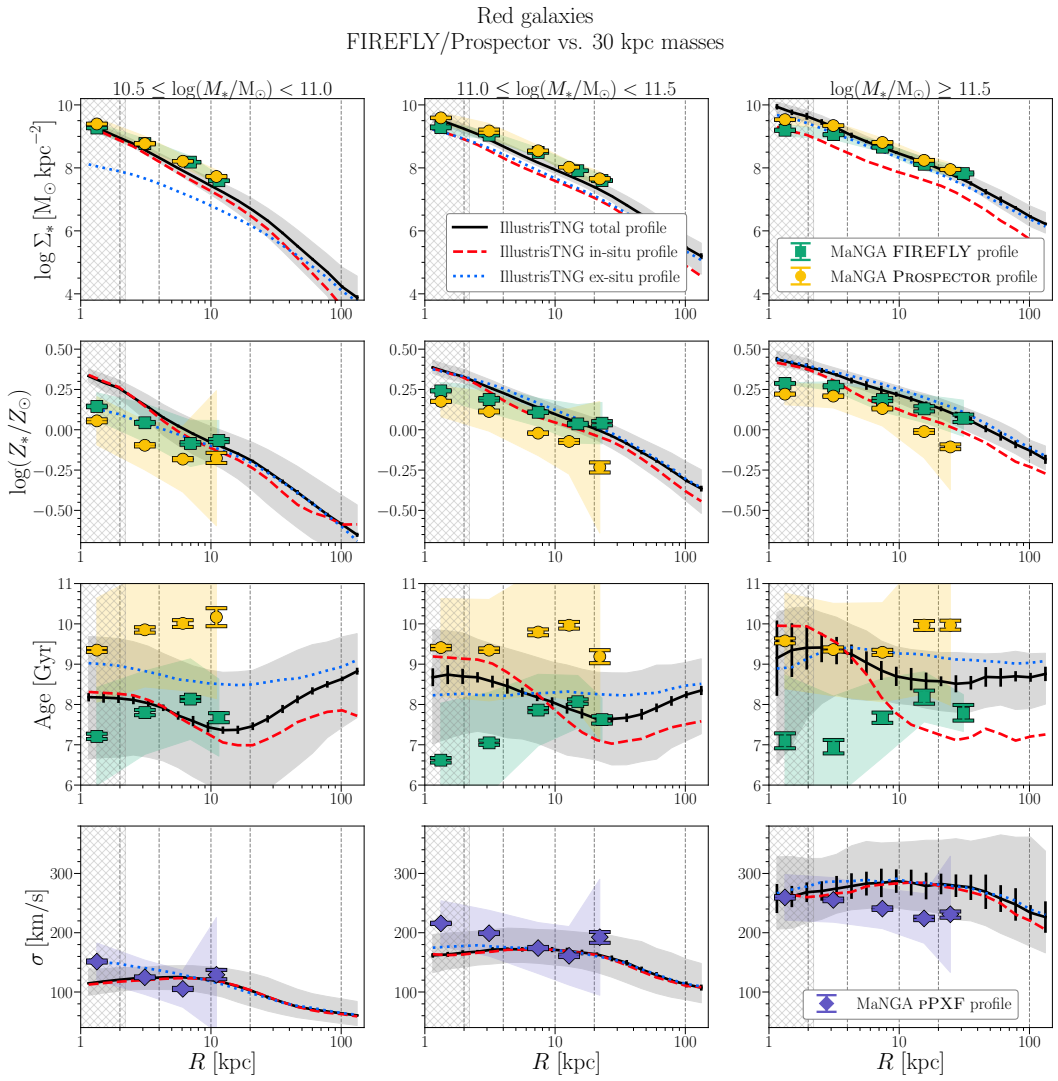

Fig. 3.26: Same as Figure 3.21, but for Red galaxies and assuming the masses within the 5 radial bins computed by FIREFLY and PROSPECTOR for MaNGA galaxies, and the masses within 30 kpc for IllustrisTNG galaxies.

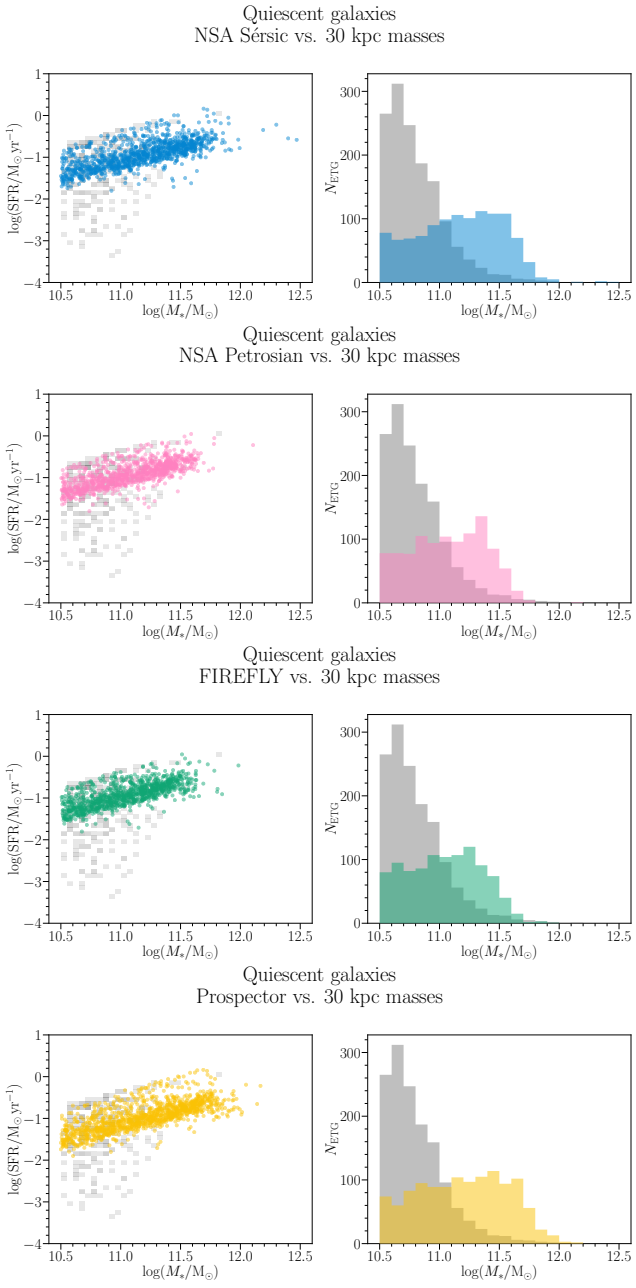

Fig. 3.27: Same as Figure 3.23, but for Quiescent galaxies.

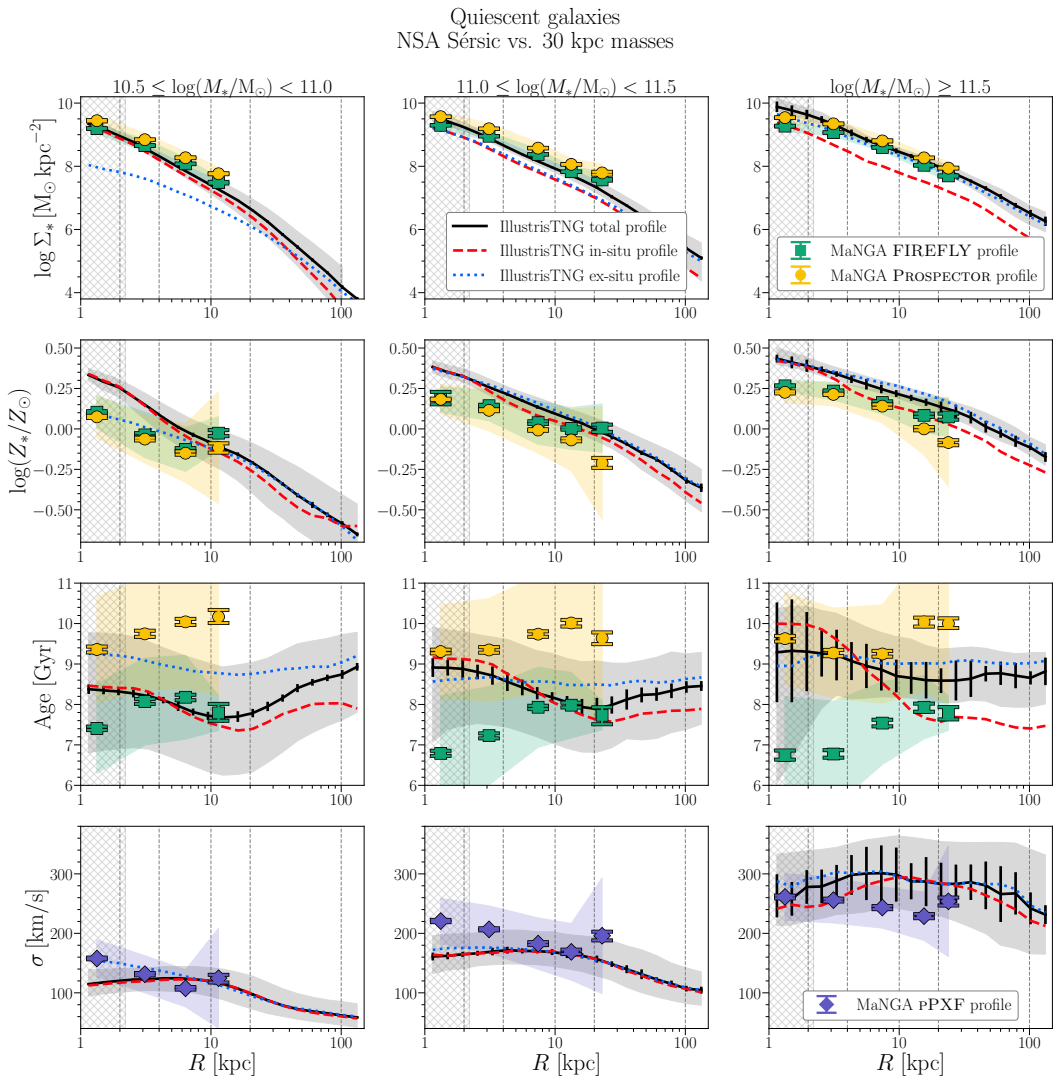

Fig. 3.28: Same as Figure 3.21, but assuming the NSA Sérsic masses for MaNGA galaxies, and the masses within 30 kpc for IllustrisTNG galaxies.

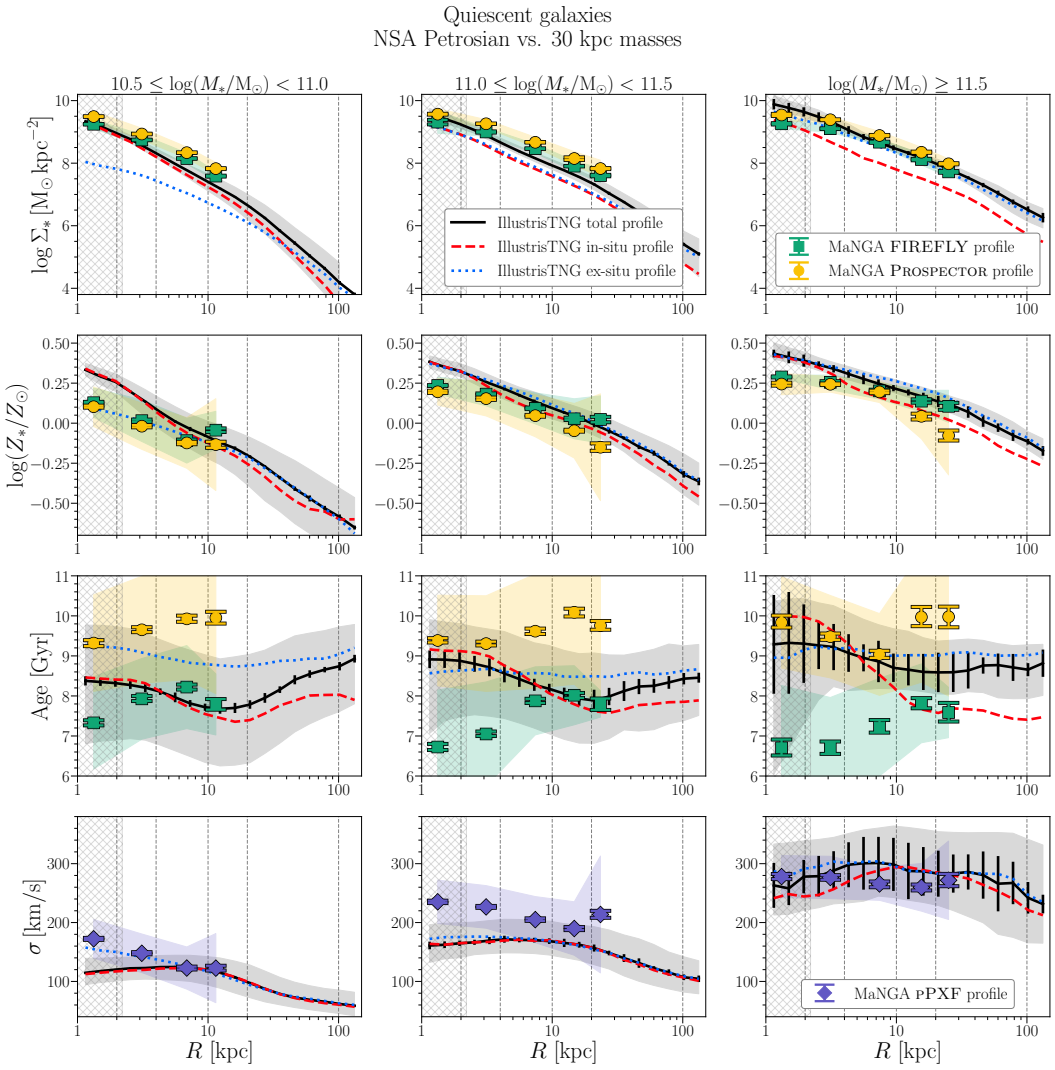

Fig. 3.29: Same as Figure 3.21, but assuming the NSA Petrosian masses for MaNGA galaxies, and the masses within 30 kpc for IllustrisTNG galaxies.

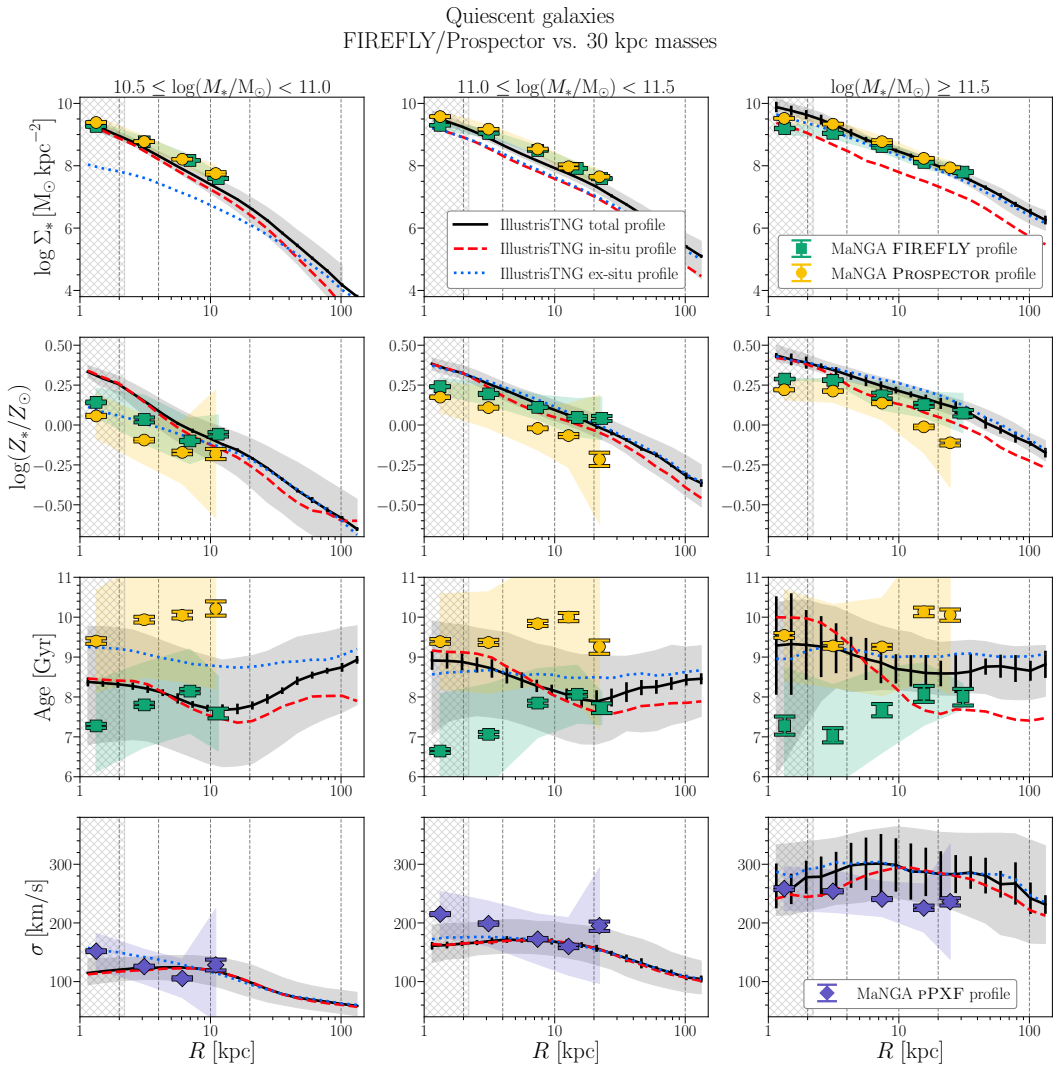

Fig. 3.30: Same as Figure 3.21, but assuming the masses within the 5 radial bins computed by FIREFLY and PROSPECTOR for MaNGA galaxies, and the masses within 30 kpc for IllustrisTNG galaxies.

4

Inferring the Dark Matter halo mass in galaxies from other observables with Machine Learning

> *Everything should be made as simple as possible, but not simpler.*
>
> **— Albert Einstein**

In 2019, I was awarded *Marie Skłodkowska-Curie grant* by the *Horizon2020-MSCA-RISE-2017 Project 777822 GHAIA "Geometric and Harmonic Analysis with Interdisciplinary Applications"* to carry out a project on the scientific area of *Data Analysis and Machine Learning*. This Chapter is based on an ongoing project that will be presented in ***Cannarozzo et al. (b, in prep.)***.

4.1 Introduction

In the last few years, the astrophysical research has been increasingly approaching the world of artificial intelligence methods. This is mainly due to the fast growth of data and the large amount of information coming from surveys. Astrophysics has been entering into the so-called *Big Data age*, making this science the ideal branch in which data analysis, machine and deep learning techniques are becoming essentials.

The impelling need of developing and improving machine learning (ML) methods finds fertile ground in the current and next generations of telescopes and surveys: Atacama Large Millimeter Array (ALMA; Wootten & Thompson, 2009), the Large Synoptic Survey Telescope (LSST; Ivezić et al., 2019), the Square Kilometer Array (SKA; Dewdney et al., 2009), as well as the upcoming Euclid mission (Laureijs et al., 2011), the James Webb Space Telescope (JWST; Gardner et al., 2006), the Nancy Grace Roman Space Telescope (Dressler et al., 2012; Green et al., 2012; Spergel et

al., 2015), etc. But we do not have to wait for future surveys to deal with big amount of astrophysical data: we are already used to the immense volumes of surveys like the Sloan Digital Sky Survey (SDSS; York et al., 2000), Pan-STARRS (Kaiser et al., 2010), Gaia (Gaia Collaboration et al., 2016) and the Dark Energy Surveys (DES; Abbott et al., 2018; Troxel et al., 2018). Artificial intelligence allows us to shed light on intricate relations among data, predict and infer hidden information and manage quickly a huge amount of data for a wide range of tasks.

4.1.1 The importance of machine learning in astrophysics

The constant growth of interest in ML techniques for astrophysics and cosmology is due to the extreme necessity to develop algorithms able to identify objects and their properties, but, at the same time, to weave together information from different telescopes facilities.

Among the vastness of ML methods, we recognise two main subgroups: the *supervised* and *unsupervised* ML algorithms. Supervised ML consists in using a set of features to learn the relationship with a specific target variable. This link can be exploited to make the inference of the target on a test sample. In contrast to classical fitting procedures for which a model is preset, supervised ML methods allow to build a model that adapts itself to the input sample. The supervised ML techniques generally consist of three main steps: the *training step*, the *validation step* and the *test step*. During the training step, the method learns the relationship between a given training set and the target. The second step allows to validate the predictions made by the model to find the best set of parameters. Finally, during the test step, the model is applied to a subsample in order to infer the target variable on the basis of what the model learned. Supervised ML problems can be grouped into two classes: *classification* and *regression* models. In the case of classification, a method provides capabilities for mapping input to output labels, or in other words to assign a given category to the target, for example classifying a brilliant source as a star or a galaxy. Regression methods, instead, are implemented to map input to a continuous output. If the variable varies over a range, regression allows to estimate it from a set of features as done, for instance, for the derivation of redshift from photometric measurements. Among the supervised learning methods we count *linear regression*, *logistic regression*, *decision trees* and *random forests*, and *neural networks*.

Unsupervised ML tools are used when one is interested in learning about the mutual connections in data, without using given labels. Hence, the aim of this class of methods is to identify hidden structures in measurements that were previously

undetected to understand more about the input data. Unlike supervised ML, this kind of methods cannot be applied to problems like regression or classification, since the user does not know which might be the output from data. In this large class of methods, we identify *clustering analysis*, *dimensionality reduction* and *visualisation*.

In the last years, many novel approaches that exploit ML techniques have been developed in astrophysics. For example, ML methods are used to classify objects like galaxies (e.g., Huertas-Company et al., 2008; Chattopadhyay et al., 2019; Pérez-Carrasco et al., 2019) or variable stars and transients (Richards et al., 2011; Carrasco-Davis et al., 2019), to disentangle components kinematically in simulated galaxies (Obreja et al., 2018, 2019) and to retrieve redshift of sources (e.g., Tagliaferri et al., 2003; Luken et al., 2019; Norris et al., 2019; Salvato et al., 2019).

In this framework, ML can be used also to find relations between dark matter (DM) halos and their host galaxies. For example, by training a neural network architecture on a cosmological simulation performed with RAMSES-RT, Sullivan et al. (2018) provided a prediction of the baryon fraction content in DM halos using their physical features, while Agarwal et al. (2018) used the Mufasa simulation to connect galaxy features to halo features. Recently, Moster et al. (2020) presented *GalaxyNet*, a deep neural network which allows to link the properties of galaxies and of their haloes. Specifically, GalaxyNet finds these connections between observed properties and simulated DM halos by directly training the algorithm with observed data, exploiting a reinforcement learning method.

A more detailed presentation of supervised and unsupervised ML applied to astrophysical problems, and a discussion of the pros and cons of the techniques, is provided in Baron (2019).

4.1.2 Linking DM halos to other galactic properties

An important aspect to be investigated in order to link DM halos to their host galaxies concerns our knowledge on how the diverse galaxy properties correlate with their halos, as well as, how a given property can be a good estimator for the mass of DM halos. The idea behind the connection that should subsist between DM halo mass and other galaxy properties lies at the basis of galaxy formation and evolution theory. Indeed, this connection should find origin during the process of structure formation, when galaxies formed as the result of baryon condensation inside the gravitational wells yielded by DM halos (e.g. Rees & Ostriker, 1977; White & Rees, 1978; Fall & Efstathiou, 1980; Blumenthal et al., 1984). The entire process gives rise

to the so-called *galaxy-halo connection*. Given this connection between DM halos and galaxies, we expect also that the biggest halos host the biggest galaxies, and they grow in tandem through cosmic time.

As discussed in Wechsler & Tinker (2018), the existence of a relationship between the DM halo and its galaxy does not specify directly which galaxy properties are more linked to their halo, and in particular which are the more useful to infer its mass. The most well-known relation between the DM halo and its host galaxy is the so-called stellar-to-halo mass relation (SHMR), that can be derived for example from galaxy formation models or parametrised models (Kravtsov et al., 2004; Moster et al., 2010; Leauthaud et al., 2011; Tinker et al., 2017; Wechsler & Tinker, 2018; Behroozi et al., 2019; Girelli et al., 2020). From an observational point of view, other approaches to estimate the mass of halos in single objects relies on the measurements of some observed properties, for example by exploiting gravitational lensing effects (e.g., Mandelbaum et al., 2006, 2016), or kinematics (e.g., More et al., 2009; Wojtak & Mamon, 2013; Lange et al., 2019), or estimates derived from X-ray observations (e.g., Kravtsov et al., 2018). Although the galaxy stellar mass can be considered as the primary property strictly linked to the DM mass, it could be useful to look for other possibilities. For instance, the gas in galaxies is expected to be another crucial property, but deriving complete and statistical relevant samples with reliable measurements of gas (e.g., mass, size) is very demanding. More generally, we can think whether and to what extent the correlation between the DM halo mass and whole baryon mass gives more constraints on the correlation with respect to the SHMR. This aspect has been largely studied with the Tully-Fisher relation (e.g., McGaugh et al., 2000) as well as with clustering analysis of HI-selected sources (e.g., Guo et al., 2017), finding so far estimates of scatter similar to those coming from the classic SHMR.

Together with possible primary properties directly linked to DM halos, we have to bear in mind that they show, in turn, other relations with other quantities. An example is given by the stellar mass which exhibits several further correlations: for example, the $M_* - M_{\rm BH}$ relation (e.g., Magorrian et al., 1998; Reines & Volonteri, 2015), or the relations with the stellar and gas metallicities (e.g., Tremonti et al., 2004; Gallazzi et al., 2005; Gallazzi et al., 2006; Mannucci et al., 2010; Mingozzi et al., 2020). Hence, because of the complexity of the problem and the high number of features that might be related to the DM halo in a galaxy, the study of the galaxy-halo connection can be performed, as we will present in this ongoing work, exploiting ML methods to shed light in this intricate network of possible relations among several galaxy properties.

The final aim of this project will be to derive a functional that allows to infer DM mass in galaxies exploiting observed properties. To do that, we train a model on the results of the IllustrisTNG simulations, by exploiting *Explainable Boosting Machine*, a state-of-the-art machine learning implementation of the Generalized Additive Models with pairwise interactions.

This Chapter is organised as follows. The machine learning method adopted in this work is presented in section 4.2. The preliminary results are illustrated in section 4.3. Section 4.4 concludes. Throughout this Chapter, we assume a ΛCDM cosmological framework with the cosmological parameters derived from Planck Collaboration et al. (2016), i.e. $\Omega_{\Lambda,0} = 0.6911$, $\Omega_{m,0} = 0.3089$, $\Omega_{b,0} = 0.0486$, and $H = 67.74\,\mathrm{km\,s^{-1}Mpc^{-1}}$. Stellar masses are estimated assuming a Chabrier (2003) initial mass function.

4.2 The Method

The main scope of this project will be to derive a functional form able to provide a prediction of the DM mass in a given galaxy using a bunch of observed properties, and not limiting, for instance, to the only use of the stellar mass as usually done, but extending the analysis to other quantities that may have hidden connections with their halo. In this context, the use of ML methods can help us to go through the dataset in input, train a model, and estimate the halo mass. For our goal, we exploit *Explainable Boosting Machine*, a state-of-the-art ML technique recently developed by Microsoft Research in the context of Generalized Additive Models with pairwise interactions.

4.2.1 Generalized additive models & GA^{2}Ms

Generalized additive models (GAMs) were firstly introduced by Hastie & Tibshirani (1990). From a mathematical point of view, a GAM is an additive model whose ability is to capture the role of the predictive features exploiting a series of smooth functions[1]. The basic idea behind GAMs is to simply link individual predictors and a dependent variable through a linear or nonlinear pattern.

Before seeing the architecture behind a GAM, we start from the simpler class of *General Linear Models* (GLMs, McCullagh & Nelder, 1989). In a GLM, the target

[1]Usually, spline functions are implemented in GAMs as smooth functions

variable y_i one would like to infer can be expressed as a summation of linear terms as

$$y_i = \beta_0 + \beta_1 x_{i1} + \cdots + \beta_p x_{ip}, \tag{4.1}$$

with an associated error term ε_i. Examples with the same functional form as in Equation 4.1 are the scaling relations of ETGs introduced in Chapter 1, like the Fundamental Plane (Equation 1.6). The simplest case of a linear model reduces to a one-variable dependence model called *Simple Linear Model* (SLM)

$$y_i = \beta_0 + \beta_1 x_{i1}. \tag{4.2}$$

The *linearity* of theses classes of models lies in the fact that y_i is a linear function of $x_{i1}, \ldots, x_{ip}$. The main limitation of these models is that, in many cases, treating a problem adopting SLMs may be restrictive in capturing the role of each predictor. Hence, ideally one would like to adopt a more complex, fully general model, like Random Forests, Neural Networks, or Boosted Trees, in which an arbitrary function may take into account all the predictors simultaneously

$$y_i = f_i(x_{i1}, \ldots, x_{ip}). \tag{4.3}$$

Between these two extreme cases of models, there is the family of Additive Models.

Let assume a training dataset $\mathcal{D} = \{(\boldsymbol{x}_i, y_i)\}_1^N$, where N is the size of the dataset, $\boldsymbol{x}_i = (x_{i1}, \ldots, x_{ip})$ denotes a feature vector composed by p features, and y_i is the target variable, that, in our case, would be the DM mass. With x_j we indicate the j-th variable within the space of features. The GAM formulation can be written as

$$g(E[y]) = \beta_0 + \sum_j f_j(x_j) = \beta_0 + f_1(x_1) + \cdots + f_p(x_p), \tag{4.4}$$

where y is the dependent variable that we would like to estimate, $E[y]$ indicates the expected value, g is the so-called *link function*, and for each functional term f_j, called *shape function*, $E[f_j] = 0$. The functional terms f_j are *non-parametric functions* whose shapes are completely determined by the data. This characteristic guarantees a great flexibility in the estimate of models without knowing *a priori* the hidden patterns of models.

In order to improve the accuracy of the model, we can add other terms to the standard GAM in Equation 4.4, for instance allowing for the presence of the *pairwise*

interactions obtaining a *Generalized Additive Model with pairwise interactions* (Lou et al., 2013, GA^{2}M):

$$g(E[y]) = \beta_0 + \sum_j f_j(x_j) + \sum_{i \neq j} f_{ij}(x_i, x_j). \tag{4.5}$$

A GA^{2}M computes all the "first-order" terms as a standard GAM and then identifies and sorts the possible k-th pairwise interactions required by the training dataset.

The high intelligibility of GAMs and GA^{2}Ms lies in the straightforward visualisations of the feature terms: indeed, the relationship between each variable x_j and the corresponding function f_j in a GAM can be visualised in the $f_j(x_j) - x_j$ plane, while the mutual interactions in a GA^{2}M can be represented as maps of $f_{ij}(x_i, x_j)$.

4.2.2 The Explainable Boosting Machine model

In ML we can identify a sort of tradeoff between two characteristics: *accuracy* and *intelligibility*. Accuracy is the quality of a method of being precise in making its tasks, whereas intelligibility represents the property of a method of being easily understandable and manageable. Among the most accurate methods (but less intelligible) we count for instance Random Forests, Neural Networks or Boosted Trees. These complex models are often more accurate than a linear model, but they tend to be less intelligible. Instead, methods like Logistic Regressions or Decision Lists are very intelligible, but usually not very accurate. Recently, Microsoft Research released a state-of-the-art ML method called Explainable Boosting Machine (EBM), a C++/Python fast implementation of the GA^{2}M algorithm presented in Lou et al. (2013).

EBM is part of InterpretML (Nori et al., 2019), an open-source Python-based package consisting in a unique framework that makes possible a direct comparison of different ML methods, with the help of an API platform for the visualisation. InterpretML contains two classes of methods:

- *glassbox* (or *whitebox*, or *transparent-box*) type is a ML class of algorithms with high intelligibility, so as to be easily understood;
- *blackbox* models are complex structures designed for providing an explanation to problems with a hidden pattern.

Among the supported techniques within the current version of InterpretML, we find EBM, Decision Tree, Decision Rule List and Linear & Logistic Regressions among the glassbox models, while the available blackbox explainers are SHAP Kernel Explainer, SHAP Tree Explainer, LIME, Morris Sensitivity Analysis and Partial Dependece.

Once a glassbox or blackbox technique is chosen, the user gives in input the dataset and InterpretML returns four kinds of explanations:

- *Data* gives an overview of the target variable in the training set and the relations between each training features and the target;
- *Performance* reports performances of the inference;
- *Global* explains the overall behaviour of all the features used for the inference;
- *Local* explains the behaviour of all the features used for the inference in each entry of the test sample.

After the explanation step, all the information concerning the prediction of the model, the training and test samples are stored and usable for visualisation through an interactive dashboard.

In particular, for our scope, we exploit EBM, an implementation of GAM and GA^{2}M that basically learns the 1D and 2D functions reported in Equation 4.4 and Equation 4.5. To learn, EBM makes use of state-of-the-art ML techniques like *bagging* and *boosting*. The great advantage of EBM is that it is not only highly accurate, but, being a complete glassbox method, it is also even more intelligible than a classic linear or logistic regression models.

In EBM, both the 1D and 2D functions help in making the final prediction of the target variable. The link function g (see Equation 4.5) receives the summation of each term from the functions and then it provides the estimate of the target. Finally, given the nature of the method, the role of each feature is sorted based on the overall importance it has in making the final prediction.

Science with EBM

EBM has already been applied in diverse science fields and compared with other ML methods. In the following, we briefly describe a specific application to show the potentiality of such method.

At the beginning of this section, we discussed about the existing tradeoff between intelligibility and accuracy. In some cases, like healthcare, a very high accuracy is

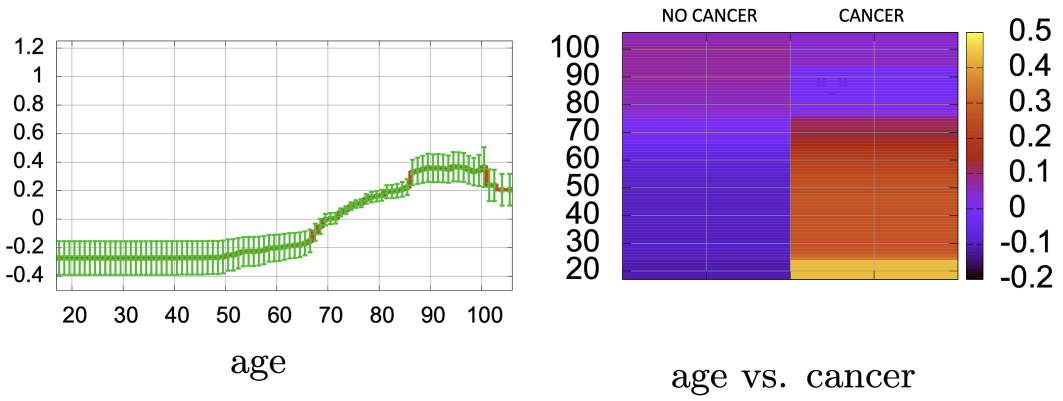

Fig. 4.1: The 1D age profile (left panel) and the 2D age−cancer map (right panel). The y-axis in the 1D profile and the colorbar in the 2D map represent the entire range of the POD. The green errorbars are ± 1 standard deviation of POD derived from bagging runs. The plots are adapted from Caruana et al. (2015).

required, but concurrently there is a crucial necessity of understanding, validating, testing and trusting about the prediction made upon a model. In Caruana et al. (2015), the authors present two healthcare studies approached with a GA^{2}M: the prediction of death caused by pneumonia and the probability of being readmitted in hospital for patients within 30 days after their releasing. We focus now on the first study. The main goal of this analysis is to predict the probability of death (POD) caused by pneumonia. Caruana et al. (2015) analysed a dataset of more than 1400 patients afflicted with pneumonia taken from a previous work of (Cooper et al., 1997). As done in the previous work, the dataset has been splitted into two subsets: a 70% of patients forms the training set and the remaining 30% is the test set. A number of 46 features per patient has been analysed: 18 features, such as age, temperature or SpO2 oxygen saturation, are continuous variables, while 28 features, such as gender, cancer or asthma, are discrete variables (e.g., having/not having asthma).

The necessity of inferring the POD caused by pneumonia is strictly related to necessity of knowing whether a patient has a high risk of death and so he needs to be hospitalised, or he can be treated as a low-risk patient. Another important information to know in this study is that a percentage of around 11% of patients in the sample died because of pneumonia.

Leaving out all further details of this study, we focus now on two examples of 1D and 2D shape functions predicted by the GA^{2}M. Among all the features taken into account by the model, the age turns out to have the most important role. On the left-hand side of Figure 4.1, the graph POD−age is shown. The x-axis spans over the range 18-106 years old. On the y-axis the POD is shown. In this case, the

score is such that POD=+1 implies an addition of 1 to the global score, taking into account also the role of all the other features and pairwise interactions. Roughly speaking, adding 1 means doubling the probability of dying because of pneumonia, while subtracting 1 implies a halving of that probability. Moreover, for an easier interpretation of the results, a score equal to 0 is associated to the mean of the feature on the x-axis, in this case 70 years old. The errorbars represents the ± 1 standard deviation of the variation of POD evaluated by 100 rounds of bagging.

In the age profile we can recognise some peculiarities of this feature. From 18 up to around 50 years old, the flat profile and negative value (≈ -0.27) suggest that, on average, the risk of dying because of pneumonia is low and constant over this range. From 50 to 66 years old, we observe a slow increase of the profile. In the range 67-70, the profile rises quickly. Given the small errorbars, this jump is real and not due to an oscillation of the fit procedure. A possible interpretation provided by the authors is that for this dataset, many patients around 65 years old have retired and this may cause a change in the lifestyle, health insurance and other factors. From 70 the POD rises to +0.2 at 82 and reaches +0.35 at age 86. This jump in the age profile is not straightforward to explain: maybe this change would be due to a combination of a different treatment intended for these patients, natural causes, as well as a lower statistics in the sample (suggested by the sudden widening of the errorbars). To provide an answer to the latter issue, it would be useful to train the model on other samples. Finally, after a more or less constant profile from 87 to 100, the score profile drops down to a value of POD around +0.2. As the previous case, this drastic change may be caused by a combination of factors: on the one hand, also in this range the statistics of the sample is not so high, however, on the other hand, people in this age interval are, as defined by the authors, *successful agers* endowed with an extraordinary genetics.

On the right-hand side of Figure 4.1, the pairwise interaction between the age and cancer coloured as a function of the POD is shown. The Boolean nature of the "cancer" feature has to be interpreted as having the cancer ($0 : +1$ range) and not having the cancer ($-1 : 0$ range). Focusing on the left part of the x-axis (i.e. people without cancer), this analysis suggests that, as expected, the older the patient, the higher the POD. The right side of the plot (i.e., patients affected by a cancer), instead, highlights a very high risk for the youngest people. This may be caused by an untreated cancer acquired during youth.

The studies conducted exploiting EBM cover a wide range of science fields. Concerning healthcare, EBM has been recently exploited also for testing the hypothesis that a ML technique with nonlinear interactions may improve the prediction of

admission in intensive care units due to COVID-19 (Zhou et al., 2020), or helping the identification of intravenous immunoglobulin-resistant patients (Wang et al., 2020b). EBM has been also compared with other ML methods (Agarwal et al., 2020; Darshana Abeyrathna et al., 2020; Yang et al., 2020), used for predicting recidivisms for different crimes (Wang et al., 2020a), or for making a prediction for the number of goals for soccer analytics (Decroos & Davis, 2019).

In astrophysics, Walmsley et al. (2020) used Bayesian convolutional neural networks (CNNs) to model and use the uncertainties of Galaxy Zoo volunteer responses to gather posteriors for galaxy morphologies. In their work, the authors exploited EBM to check whether the developed method is sensitive to non-morphological parameters such as mass, magnitude, etc.

For more details about GAM and GA^{2}M, the EBM architecture and the InterpretML environment we recommend the reader to refer to Lou et al. (2012, 2013), Caruana et al. (2015), Tan et al. (2018), Lengerich et al. (2019), Nori et al. (2019), Zhang et al. (2019), Chang et al. (2020), and Kaur et al. (2020).

4.3 An application to the cosmological simulation IllustrisTNG

Our scope is to understand the importance of some galactic features in the inference of DM mass in order to find a functional form useful to estimate the DM content in real galaxies. In this section we will present a preliminary study of the prediction of the DM mass in a sample of subhalos drawn from the IllustrisTNG simulation.

4.3.1 The training and test samples

As a first application, we selected from the $z = 0$ snapshot of IllustrisTNG100-1[2] central subhalos with a total mass $M_{\rm tot} > 10^{11}\,{\rm M}_\odot$, meaning by $M_{\rm tot}$ the sum of the masses of all particles and cells of all components in each subhalo. Our sample is composed by 15088 central subhalos and we randomly split it into a training sample (10561 subhalos) and a test sample (4527 subhalos) with a ratio of 70:30, following the same prescription used in Caruana et al. (2015, see section 4.2.2).

[2] A detailed description of the IllustrisTNG simulation suite is provided in subsection 3.2.2 of this manuscript.

For each subhalo we take into account 7 features:

- the stellar mass M_*;
- the gas mass $M_{\rm gas}$;
- the black hole mass $M_{\rm BH}$;
- the stellar metallicity Z_*;
- the gas metallicity $Z_{\rm gas}$;
- the black hole accretion rate $\dot{M}_{\rm BH}$;
- the star formation rate SFR.

In Table 4.1 we list the intervals and the mean values of $M_{\rm DM}$ and of each feature for the training sample, while in Figure 4.2 and Figure 4.3 the $M_{\rm DM}-$feature scatter distributions are shown, reporting above the Pearson correlation coefficient[3].

Tab. 4.1: Variables of the training sample. Column 1: Variable. Column 2: range of values in logarithm. Column 3: mean value.

Snapshot $z = 0$

Feature f	(min f; max f)	$\bar{f}$
$\log(M_{\rm DM}/{\rm M}_\odot)$	$(10.91; 14.54)$	11.40
$\log(M_*/{\rm M}_\odot)$	$(7.81; 12.57)$	9.49
$\log(M_{\rm gas}/{\rm M}_\odot)$	$(8.02; 13.76)$	10.37
$\log(M_{\rm BH}/{\rm M}_\odot)$	$(6.08; 10.09)$	7.04
$\log(Z_*/Z_\odot)$	$(-0.96; 0.43)$	-0.02
$\log(Z_{\rm gas}/Z_\odot)$	$(-1.10; 0.66)$	-0.05
$\log(\dot{M}_{\rm BH}/{\rm M}_\odot\,{\rm yr}^{-1})$	$(-8.79; -0.66)$	-3.47
$\log({\rm SFR}/{\rm M}_\odot\,{\rm yr}^{-1})$	$(-3.53; 2.00)$	-0.54

The next step consists in fitting the training sample with the EBM regressor. In addition to the 7 features listed above, we consider also the three most relevant pairwise interactions. Indeed, EBM evaluates all the possible pairwise interactions among the features, returning the k-th most relevant, where k is set by the user. In

[3]The specific choice of these 7 features made for the presented application is somewhat arbitrary, and one can of course explore cases with a different number of features. In the future, we will plan to consider other observables of galaxies such as the luminosity, colours, size, velocity dispersion, surface brightness, age, etc.

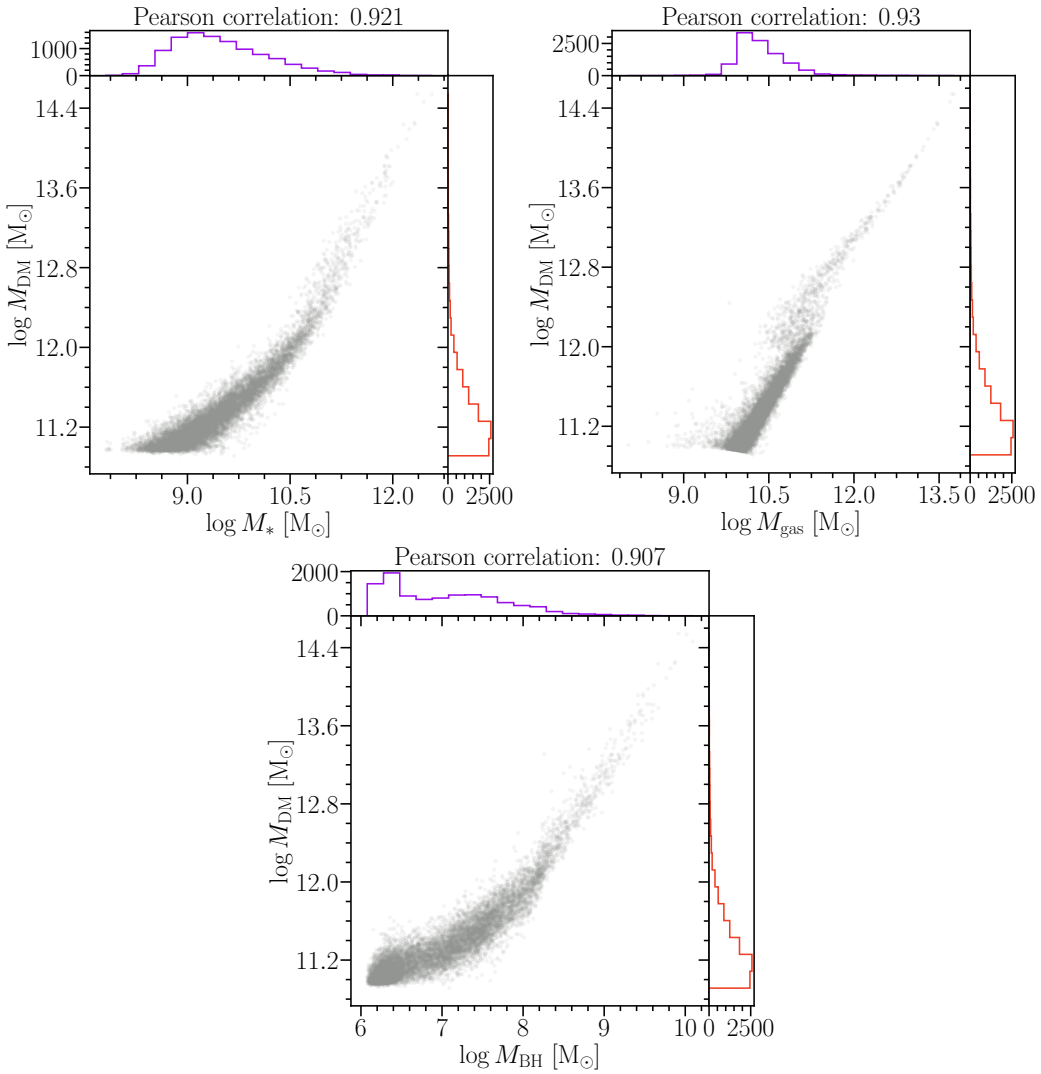

Fig. 4.2: Target variable $M_{\rm DM}$ as a function of the stellar mass M_* (upper left panel), the gas mass $M_{\rm gas}$ (upper right panel), and the black hole mass $M_{\rm BH}$ (lower panel) for the training sample. In each panel, the 1D red histogram on the y-right-axis represents the distribution of the target $M_{\rm DM}$, while the 1D violet histogram on the x-upper-axis represents the distribution of each feature. Above each plot the Pearson correlation coefficient is reported.

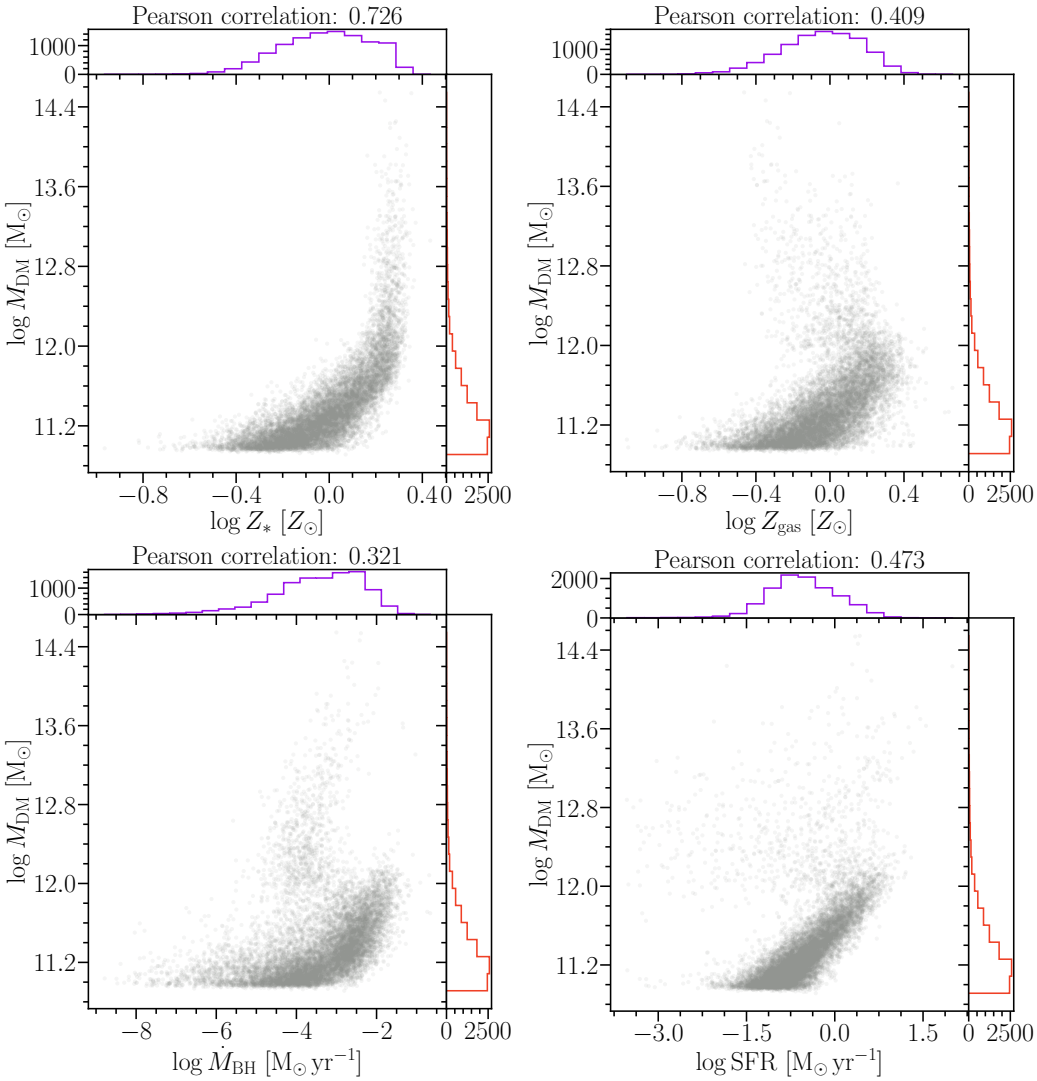

Fig. 4.3: Same as Figure 4.2, but for the stellar metallicity Z_* (upper left panel), the gas metallicity $Z_{\rm gas}$ (upper right panel), the black hole accretion rate $\dot{M}_{\rm BH}$ (lower left panel), and the star formation rate SFR (lower right panel).

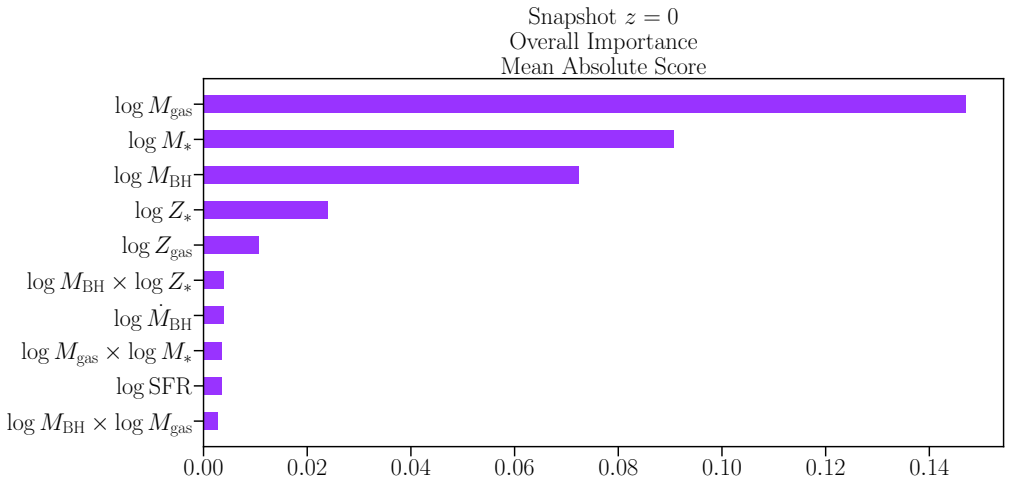

Fig. 4.4: Overall importance diagram of the 7 features and the 3 most relevant pairwise interactions used by EBM. The contribute of each term is additive thanks to the modularity of the GAM/GA^{2}Ms.

Figure 4.4, the overall importance of the features and of the three most important pairwise interactions is shown. As clearly visible from the plot, each term is playing a role in inferring the DM mass, but the gas mass, the stellar mass and the black hole mass have a significantly stronger role. The three most relevant pairwise interactions involve in turn the black hole mass and the stellar metallicity, the gas and stellar masses, and the gas and black hole mass. The length of each bar in Figure 4.4 is obtained by computing the mean of the absolute score for each term. EBM is an additive model, so it makes final predictions as functions of each individual feature. It predicts the target variable by disentangling the role of the features into a single or a pairwise "projections" on the target. An easy way to interpret it is to assign a score equal to 0 to the mean value of $M_{\rm DM}$ of the training sample, i.e. $\log(M_{\rm DM}/{\rm M}_\odot) \simeq 11.4$. When the model makes predictions, it will use each feature graph as a “look up table” to retrieve a score that the feature contributes to an individual prediction. Let us make an example on how the overall feature importance is estimated. For simplicity, let us assume two features, A and B, whose corresponding scores varies monotonically from -1 to +1 for A, while from $+0.2$ to $+0.6$ for the B feature. Although the mean value of B ($= 0.4$) is greater than the mean value of A ($= 0$), because of its stronger variation over its range, A is clearly contributing to the final prediction much more heavily than B, since its scores tend to be much bigger in absolute value.

Figure 4.5 and Figure 4.6 show the 1D shape functions for the seven individual features used by EBM, while in Figure 4.7 the 2D maps for the three most relevant

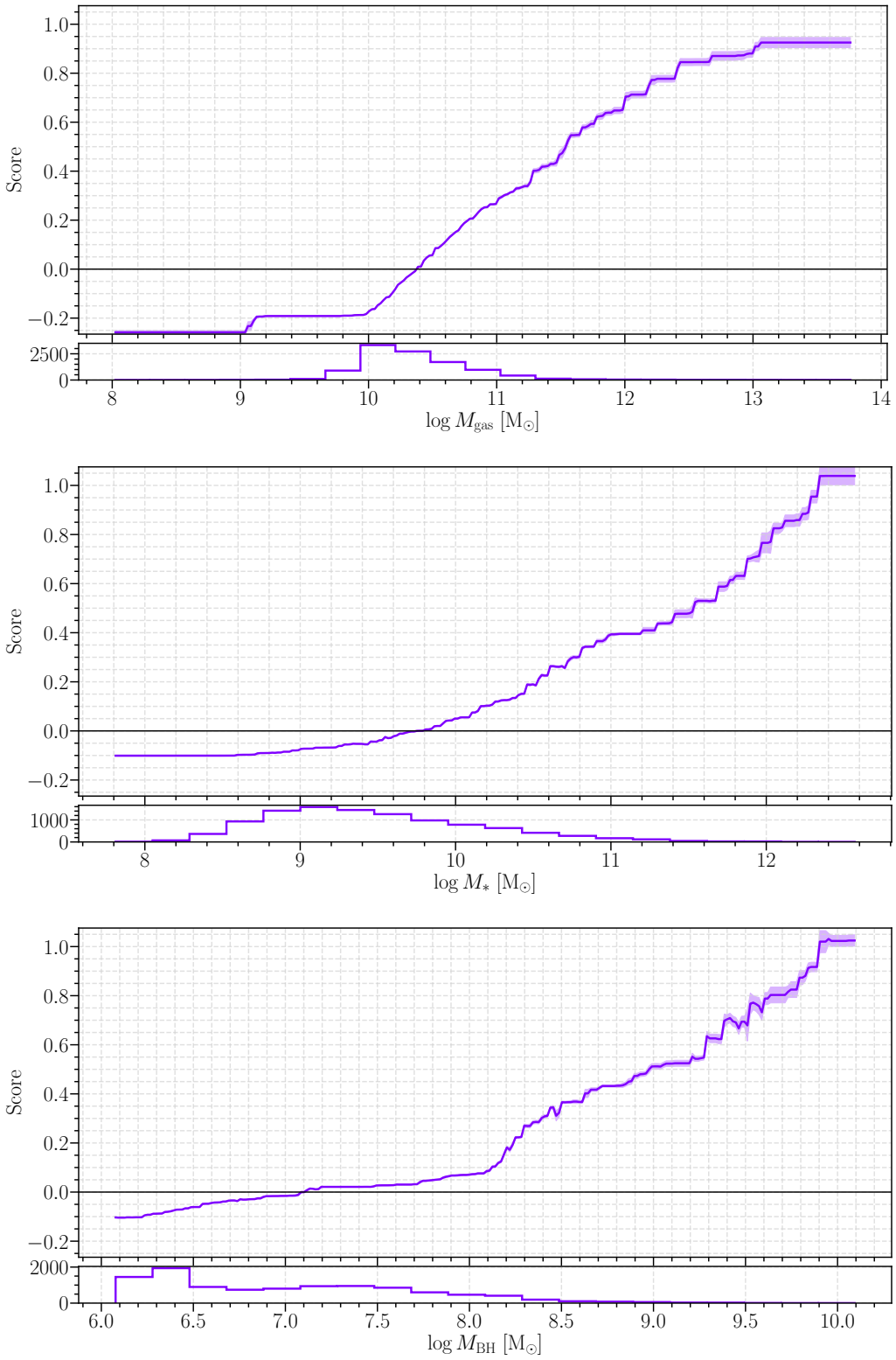

Fig. 4.5: Single feature score profiles for the gas mass (top panel), stellar mass (middle panel) and for the black hole mass (bottom panel). In each panel, the y-axis indicates the score, i.e. the value in units of $\log M_{\rm DM}$ to be added to the mean of DM mass value of the training sample, $\log(M_{\rm DM}/{\rm M}_\odot) \simeq 11.4$. The shaded regions represent the ± 1 standard deviation of the variation of score estimated by 100 rounds of bagging.

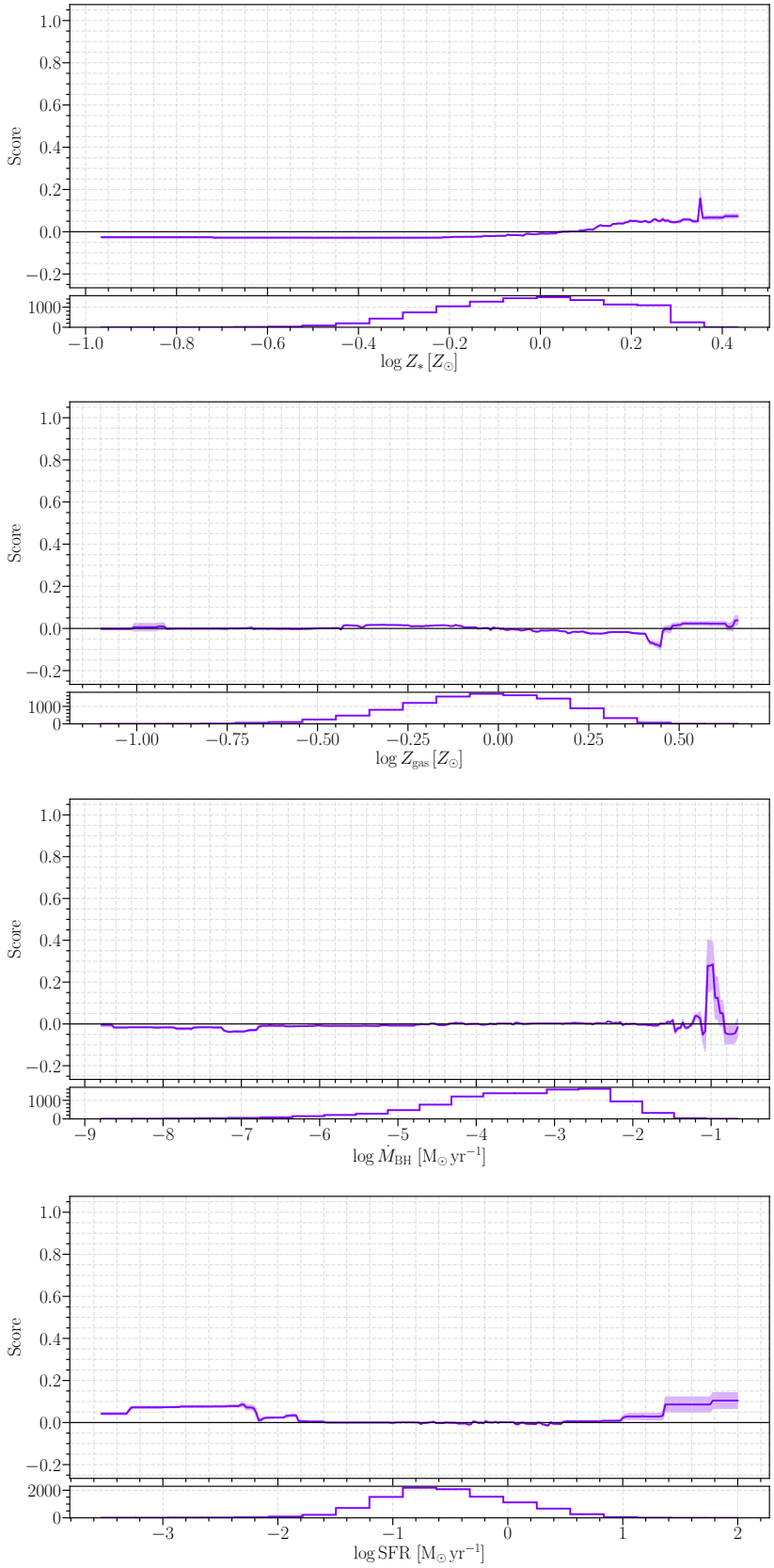

Fig. 4.6: Same as Figure 4.5, but (from top to bottom) for the stellar metallicity, the gas metallicity, the black hole accretion rate and the star formation rate.

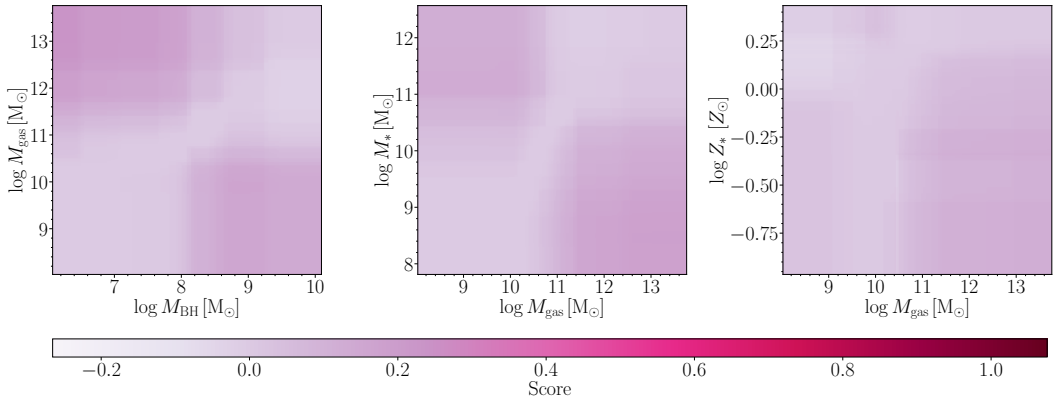

Fig. 4.7: Pairwise interaction 2D maps for the couples $\log M_{\rm gas} - \log M_{\rm BH}$ (left panel), $\log M_* - \log M_{\rm gas}$ (middle panel), and $\log Z_* - \log M_{\rm gas}$ (right panel). These maps are coloured as a function of the score with the same range of the y-axes as in the plots of Figure 4.5 and Figure 4.6.

pairwise interactions sorted by importance are displayed. Let focus first on the 1D shape functions. The three mass features vary widely and almost monotonically over their ranges, while the remaining four features tend to be constant (except for a few small oscillations). The way to interpret these graphs is the following: from the $M_{\rm gas}$ profile (upper panel of Figure 4.5) we can learn that, for instance, a subhalo with a gas mass of $\approx 10^{12}\,\mathrm{M}_\odot$ gives on average a contribution of $\approx +0.7\,\mathrm{dex}$ to the mean $\log M_{\rm DM}$ of the training sample, or analogously for a subhalo with a stellar mass of $\approx 10^{8}\,\mathrm{M}_\odot$ the score to be added to the mean $\log M_{\rm DM}$ is $\approx -0.1\,\mathrm{dex}$. Another way to read these plots is that a subhalo with a DM mass equal to the mean value, i.e. $\log(M_{\rm DM}/\mathrm{M}_\odot) \approx 11.4$, has, on average, a gas mass of $\approx 10^{10.4}\,\mathrm{M}_\odot$, a stellar mass of $\approx 10^{9.8}\,\mathrm{M}_\odot$, a black hole mass of $\approx 10^{7.2}\,\mathrm{M}_\odot$, etc. The low overall importance of the stellar and gas metallicities, the black hole accretion rate and the star formation rate (see Figure 4.4) is reflected in their score profiles (see Figure 4.6): except for a few small variations over their intervals, these features contribute very little to the final prediction.

The strong dependence of the DM mass on the gas, stellar and black hole masses can be explained in terms of a correlation between the DM halo and the baryonic component in a given galaxy. As already discussed in Wechsler & Tinker (2018), usually the most studied relation between the DM halo and its host galaxy is the SHMR, because the measurement of stellar mass (or luminosity) is relatively simple. For example, the estimate of the total gas amount in galaxies is very challenging and demanding. However, the possible correlation between halo masses and baryonic masses has been taken into account in some studies. An example can be the exploitation of the Tully-Fisher relation as done in McGaugh et al. (2000)

or the dependence of galaxy clustering on HI (e.g., Guo et al., 2017). Moreover, in Contreras et al. (2015) the authors studied with two different approaches which galactic properties show a correlation with DM halo mass, finding that, together with the stellar mass and the r-band magnitude, a good correlation is found also for the black hole mass.

Though the three baryonic components are crucial for the prediction of DM mass, explaining the detailed behaviour of each score profile is not so trivial and needs a deep-dive analysis of single subhalos in the target sample. An example is the hump-like structure in the stellar mass score profile at around $\log(M_*/\mathrm{M}_\odot) = 11$. A possible explanation may be found in the role of mergers in these massive galaxies, whose stellar mass growth is mainly dominated by the accretion of ex-situ stellar populations, as previously presented in section 3.4, and also found in Pillepich et al. (2018a) and Tacchella et al. (2019).

The 2D maps of the three most important pairwise interactions are shown in Figure 4.7. Looking at the position on the overall importance histogram in Figure 4.4, these interactions are found to be not so significant for the prediction of the DM mass, being comparable with the black hole accretion rate and star formation rate mean absolute scores ($\lesssim 0.004$).

The prediction obtained by EBM from the training sample can be now applied to the test sample. In Figure 4.8 two relative importance bar plots for two subhalos randomly chosen from the test sample are shown as an example. Above each plot, the value of the DM mass from the simulation $M_{\mathrm{DM}}^{\mathrm{true}}$ and that one predicted by EBM $M_{\mathrm{DM}}^{\mathrm{pred}}$ are provided. To obtain the predicted DM mass values for these two subhalos, all the terms in the histograms have to be added to the mean $\log M_{\mathrm{DM}}$ of the training sample.

Finally, in Figure 4.9, a comparison between the DM masses directly drawn from the simulation ($M_{\mathrm{DM}}^{\mathrm{true}}$) and those predicted by the model ($M_{\mathrm{DM}}^{\mathrm{pred}}$) for the subhalos in the test sample is illustrated: this distribution is very tight with a scatter $\lesssim \pm 0.06\,\mathrm{dex}$[4]. The distribution of the residuals around 0 is almost symmetric, even though a sort of bending at negative values is present for subhalos with $\log(M_{\mathrm{DM}}^{\mathrm{true}}/\mathrm{M}_\odot) < 11.4$, meaning that the predicted mass is systematically lower than the actual estimate. The reason for this bending is still unclear and we will investigate about its origin. It might be due to a selection bias in how the data are collected (we underline that for this first application, we selected subhalos with $\log(M_{\mathrm{tot}}/\mathrm{M}_\odot) > 11$).

[4]The analysis repeated considering only the gas mass, stellar mass, and black hole mass gives a consistent result, while accounting only for the stellar metallicity, gas metallicity, star formation rate, and black hole accretion rate (and excluding any pairwise interaction) the scatter increases up to $\approx \pm 0.15\,\mathrm{dex}$.

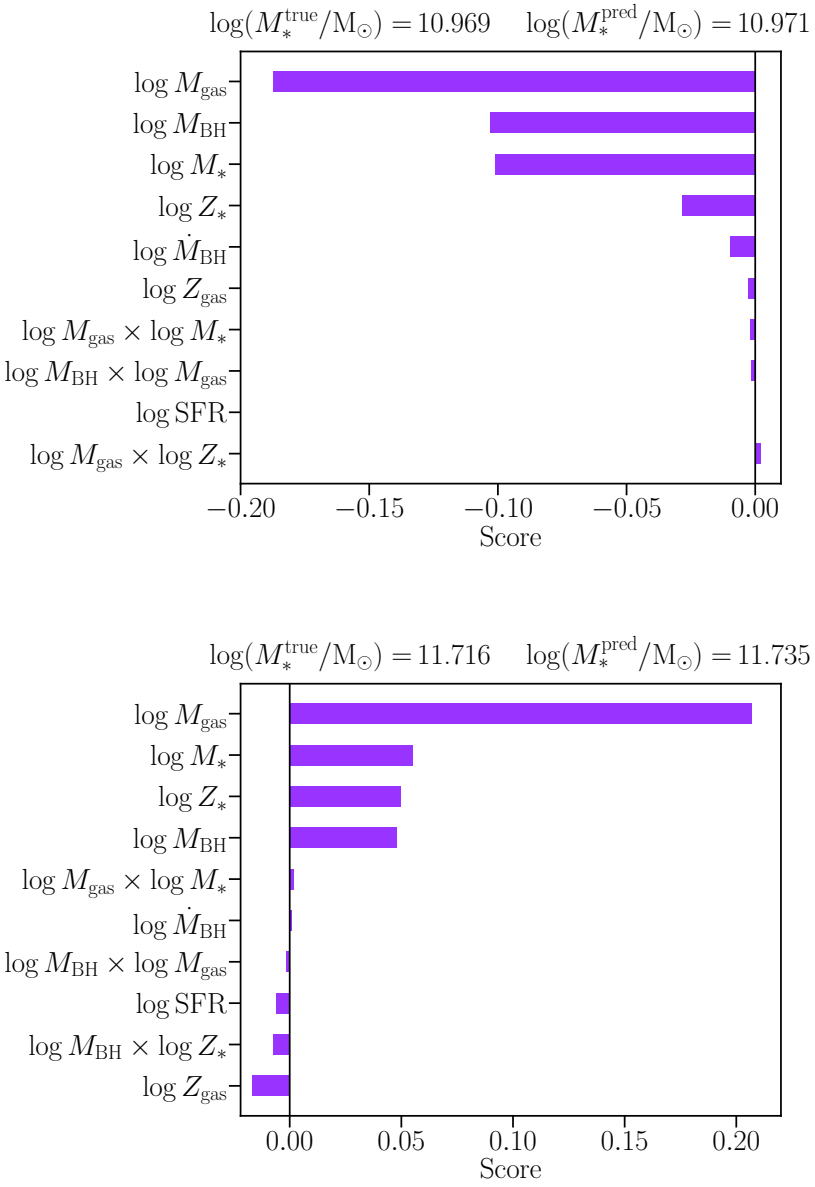

Fig. 4.8: Relative importance histograms of the single features and the three most significant pairwise interactions for two subhalos of the $z = 0$ test sample. Above each plot, the true DM mass ($M_{\rm DM}^{\rm true}$) and the mass predicted by the model ($M_{\rm DM}^{\rm pred}$) are reported.

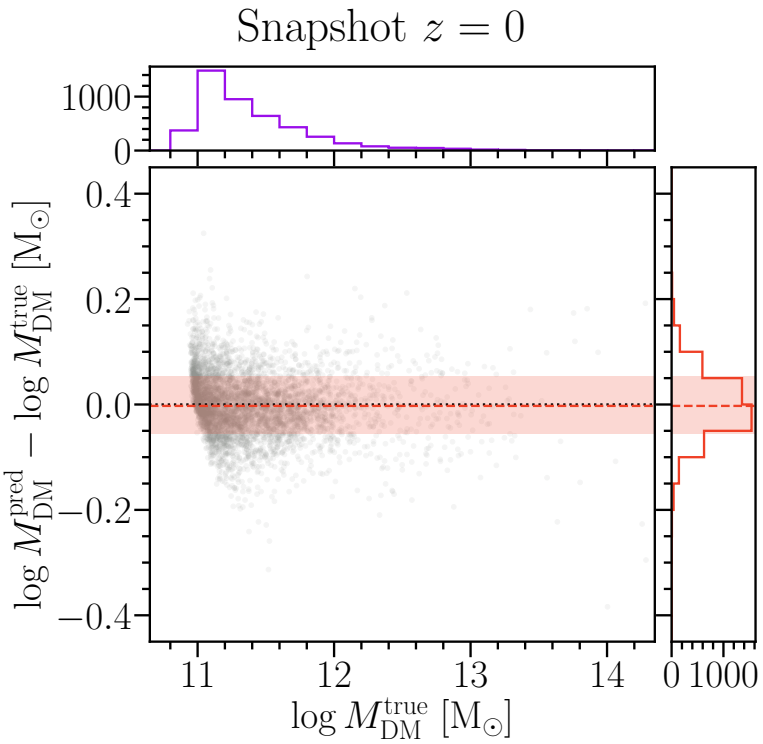

Fig. 4.9: Difference between the predicted and the true DM masses as a function of the true DM mass for the subhalos of the test sample at $z = 0$. The dotted black line represents $M_{\rm DM}^{\rm true} = M_{\rm DM}^{\rm pred}$. The red dashed line traces the median of the distribution, while the shaded region indicates the 68-th percentile of the distribution.

4.3.2 Predicting DM mass at different redshift

In this section we briefly discuss an extension of the previous analysis to higher redshifts. In particular, together with the subhalos taken from the $z = 0$ snapshot of IllustrisTNG100-1, we now apply the same approach to all the central subhalos with $\log(M_{\rm tot}/{\rm M}_\odot) > 11$ extracted from the snapshots at $z = 0.5$, $z = 1$, $z = 2$ and $z = 3$.

In Table 4.2, the number of subhalos in the training and test samples of each snapshot are listed, while Table 4.3-4.6 report the intervals and the mean values of the initial 7 features in each training samples as in Table 4.1.

Tab. 4.2: Number of subhalos in the training and test samples at snapshots $z = 0$, $z = 0.5$, $z = 1$, $z = 2$, $z = 3$. Column 1: redshift of the snapshot. Columns 2: number of subhalos in the training sample. Columns 3: number of subhalos in the test sample.

Snapshot	$N^{\rm train}$	$N^{\rm test}$
$z = 0$	10561	4527
$z = 0.5$	10987	4709
$z = 1$	10825	4640
$z = 2$	9011	3862
$z = 3$	6139	2632

Tab. 4.3: Same as Table 4.1, but for the $z = 0.5$ snapshot.

Snapshot $z = 0.5$

Feature f	(min f; max f)	$\bar{f}$
$\log(M_{\rm DM}/{\rm M}_\odot)$	$(10.92; 14.25)$	11.41
$\log(M_*/{\rm M}_\odot)$	$(7.59; 12.40)$	9.49
$\log(M_{\rm gas}/{\rm M}_\odot)$	$(8.86; 13.42)$	10.43
$\log(M_{\rm BH}/{\rm M}_\odot)$	$(6.08; 9.79)$	6.96
$\log(Z_*/Z_\odot)$	$(-1.00; 0.39)$	-0.06
$\log(Z_{\rm gas}/Z_\odot)$	$(-1.34; 0.65)$	-0.06
$\log(\dot{M}_{\rm BH}/{\rm M}_\odot\,{\rm yr}^{-1})$	$(-8.38; -0.19)$	-3.03
$\log({\rm SFR}/{\rm M}_\odot\,{\rm yr}^{-1})$	$(-3.58; 1.94)$	-0.26

Tab. 4.4: Same as Table 4.1, but for the $z = 1$ snapshot.

Snapshot $z = 1$

Feature f	(min f; max f)	$\bar{f}$
$\log(M_{\rm DM}/{\rm M}_\odot)$	$(10.88; 13.94)$	11.40
$\log(M_*/{\rm M}_\odot)$	$(7.63; 12.03)$	9.48
$\log(M_{\rm gas}/{\rm M}_\odot)$	$(8.66; 13.13)$	10.45
$\log(M_{\rm BH}/{\rm M}_\odot)$	$(6.07; 9.70)$	6.87
$\log(Z_*/Z_\odot)$	$(-1.04; 0.46)$	-0.10
$\log(Z_{\rm gas}/Z_\odot)$	$(-1.45; 0.59)$	-0.10
$\log(\dot{M}_{\rm BH}/{\rm M}_\odot\,{\rm yr}^{-1})$	$(-7.34; 0.07)$	-2.87
$\log({\rm SFR}/{\rm M}_\odot\,{\rm yr}^{-1})$	$(-3.42; 2.29)$	0.00

Tab. 4.5: Same as Table 4.1, but for the $z = 2$ snapshot.

Snapshot $z = 2$

Feature f	(min f; max f)	$\bar{f}$
$\log(M_{\rm DM}/{\rm M}_\odot)$	$(10.92; 13.51)$	11.35
$\log(M_*/{\rm M}_\odot)$	$(8.06; 11.97)$	9.38
$\log(M_{\rm gas}/{\rm M}_\odot)$	$(9.73; 12.59)$	10.44
$\log(M_{\rm BH}/{\rm M}_\odot)$	$(6.08; 9.58)$	6.66
$\log(Z_*/Z_\odot)$	$(-1.00; 0.46)$	-0.19
$\log(Z_{\rm gas}/Z_\odot)$	$(-1.43; 0.60)$	-0.16
$\log(\dot{M}_{\rm BH}/{\rm M}_\odot\,{\rm yr}^{-1})$	$(-6.63; 0.61)$	-2.69
$\log({\rm SFR}/{\rm M}_\odot\,{\rm yr}^{-1})$	$(-2.19; 2.28)$	0.33

By analysing in Figure 4.10 and in Figure 4.11 the overall importance histograms of the various features at different redshifts, we find that:

- the gas mass $M_{\rm gas}$ is the most important feature at all redshifts, and its importance increases for increasing redshift;
- the stellar mass M_* and the black hole mass $M_{\rm BH}$ are ranked as the second and the third most relevant features out to $z = 2$, but they are less important at $z = 3$;

Tab. 4.6: Same as Table 4.1, but for the $z = 3$ snapshot.

Snapshot $z = 3$

Feature f	(min f; max f)	$\bar{f}$
$\log(M_{\rm DM}/{\rm M}_\odot)$	$(10.92; 13.09)$	11.30
$\log(M_*/{\rm M}_\odot)$	$(8.01; 11.60)$	9.27
$\log(M_{\rm gas}/{\rm M}_\odot)$	$(9.83; 12.15)$	10.41
$\log(M_{\rm BH}/{\rm M}_\odot)$	$(6.08; 9.33)$	6.49
$\log(Z_*/Z_\odot)$	$(-1.15; 0.49)$	-0.26
$\log(Z_{\rm gas}/Z_\odot)$	$(-1.41; 0.60)$	-0.23
$\log(\dot{M}_{\rm BH}/{\rm M}_\odot\,{\rm yr}^{-1})$	$(-5.70; 0.71)$	-2.69
$\log({\rm SFR}/{\rm M}_\odot\,{\rm yr}^{-1})$	$(-0.65; 2.76)$	0.53

- the SFR is found to rise in ranking back in time, as expected by looking at the trend of the SFR density that peaks at $z \approx 2$ (*Madau plot; e.g.;* Madau et al., 1996), and it is even the second most important feature at $z = 3$;

- although the terms in some pairwise interactions change as a function of redshift, at all redshifts these interactions are not significant in making the final prediction of the DM mass.

Another interesting aspect to look at is the comparison among the 1D shape functions of the same feature at different redshifts. The easiest way to do it consists in rescaling to the same mean value of $M_{\rm DM}$ in each plot. In Figure 4.12 and in Figure 4.13 the shape functions of the 7 features at the five redshifts analysed in this section, opportunely rescaled to the mean value $M_{\rm DM} = 10^{11.4}\,{\rm M}_\odot$ of the training sample at $z = 0$, are illustrated.

The main aspects from this comparison can be summarised as follows:

- while the shape of the gas mass profile remains almost the same, only widening the ranges towards lower redshifts, the hump-like structure in the stellar mass profile previously described as well as the similar structure in the black hole mass profile tend to fade from $z = 0$ to $z = 3$;

- as expected, both the black hole accretion rate and the star formation rate are found to increase going from $z = 0$ to $z = 3$, because they play a major role in the early Universe (see Madau & Dickinson, 2014);

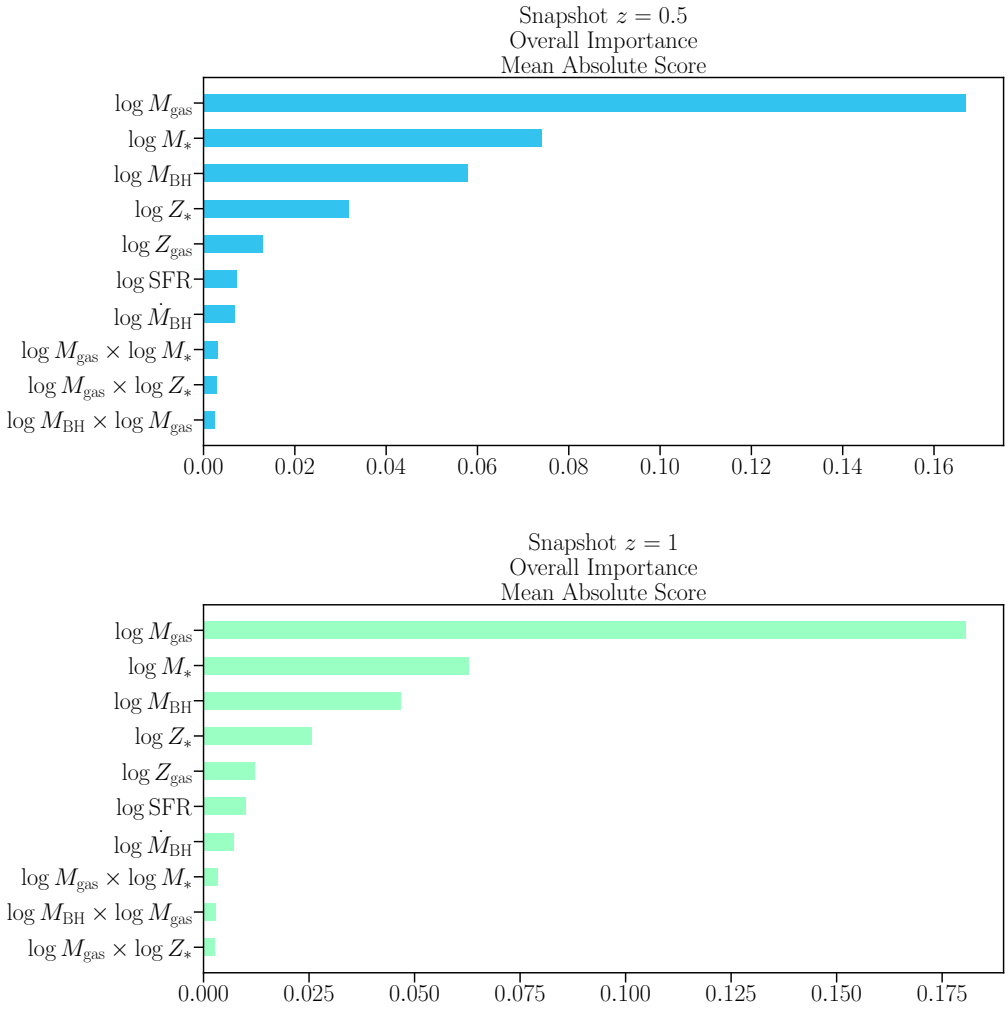

Fig. 4.10: Same as Figure 4.4, but for the training samples at the $z = 0.5$ (upper panel) and $z = 1$ (lower panel) snapshots.

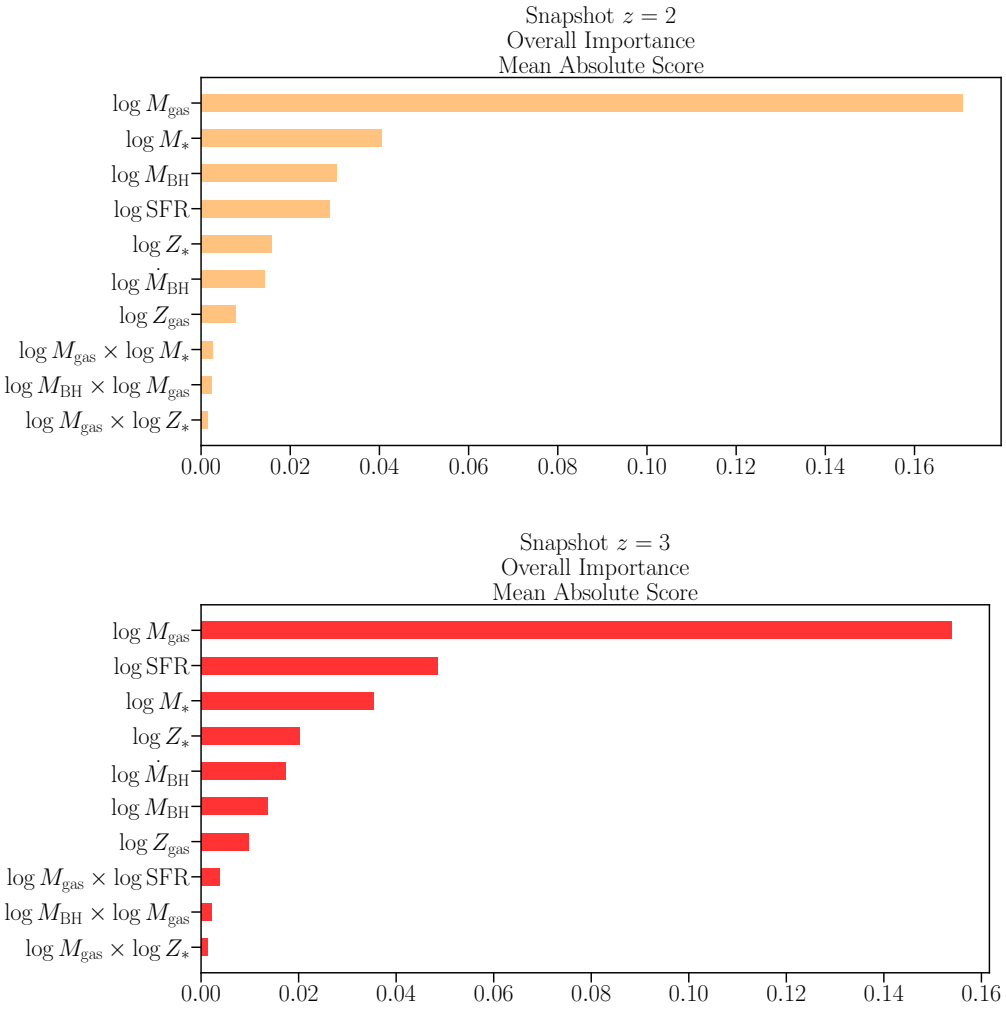

Fig. 4.11: Same as Figure 4.4, but for the training samples at the $z = 2$ (upper panel) and $z = 3$ (lower panel) snapshots.

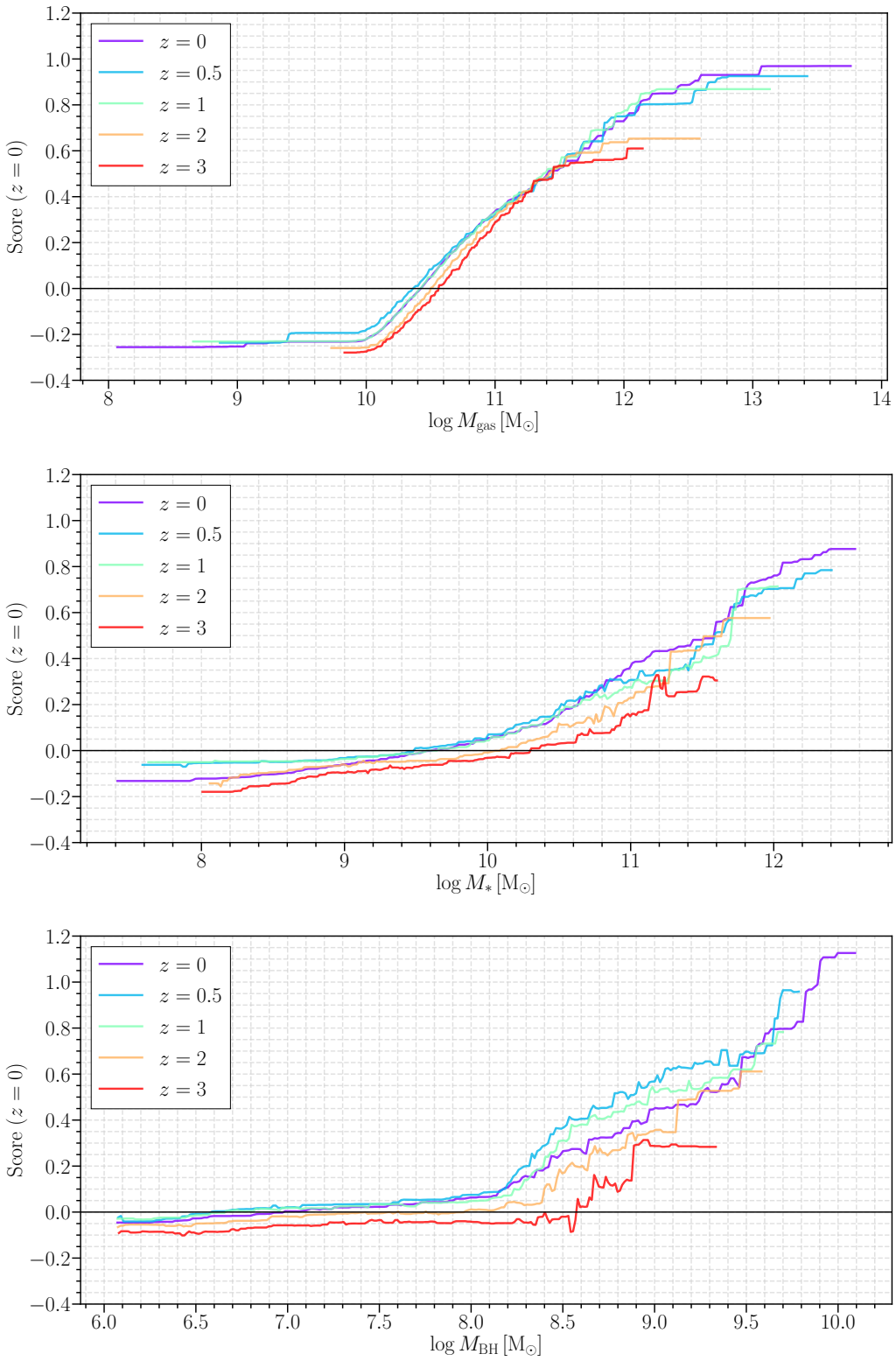

Fig. 4.12: Same as Figure 4.5, but for (from top to bottom) the gas mass, the stellar mass and the black hole mass of the training samples at at $z = 0$, $z = 0.5$, $z = 1$, $z = 2$ and $z = 3$.

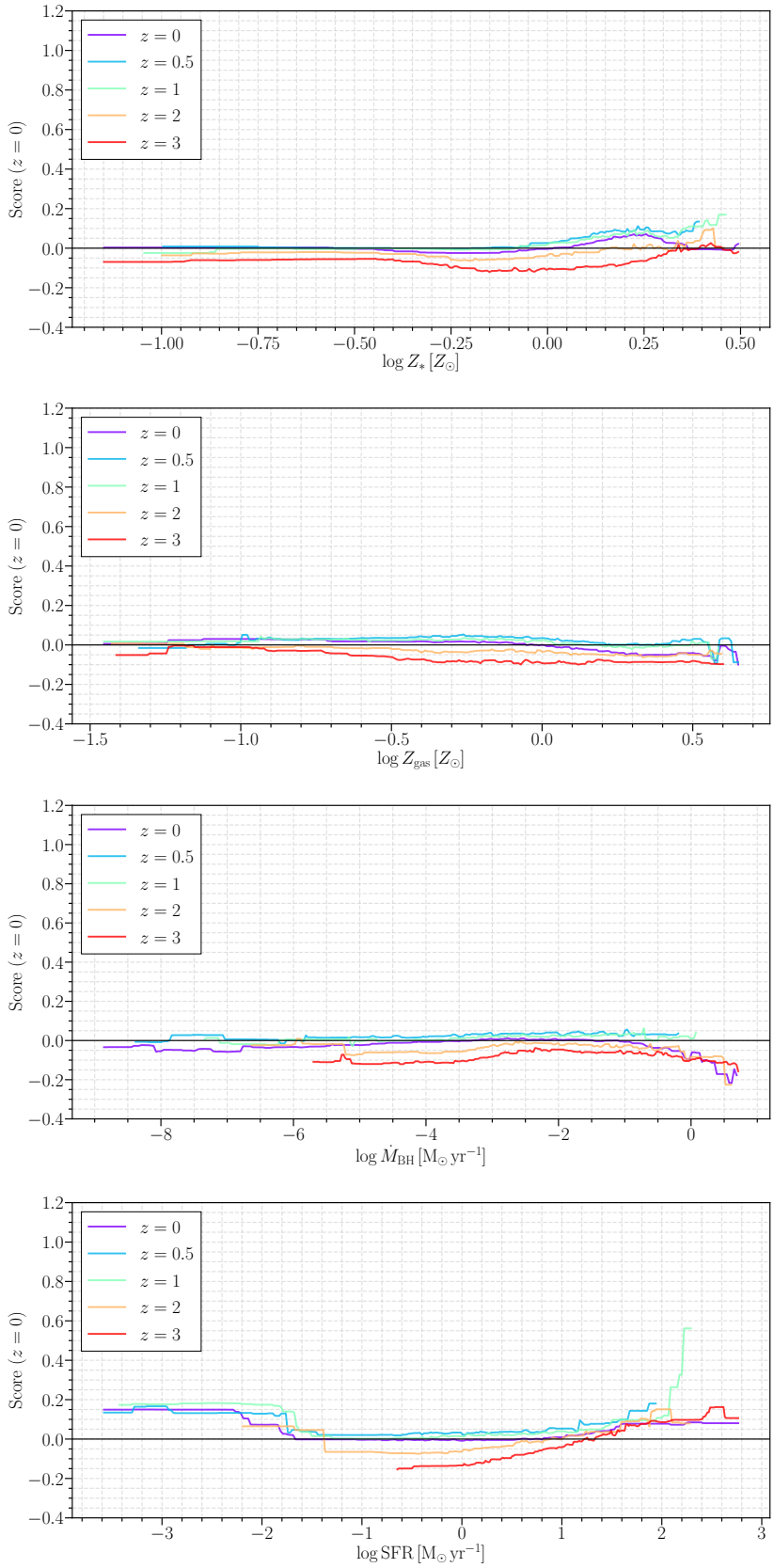

Fig. 4.13: Same as Figure 4.5, but for (from top to bottom) the stellar metallicity, the gas metallicity, the black hole accretion rate and the star formation rate of the training samples at $z = 0$, $z = 0.5$, $z = 1$, $z = 2$ and $z = 3$.

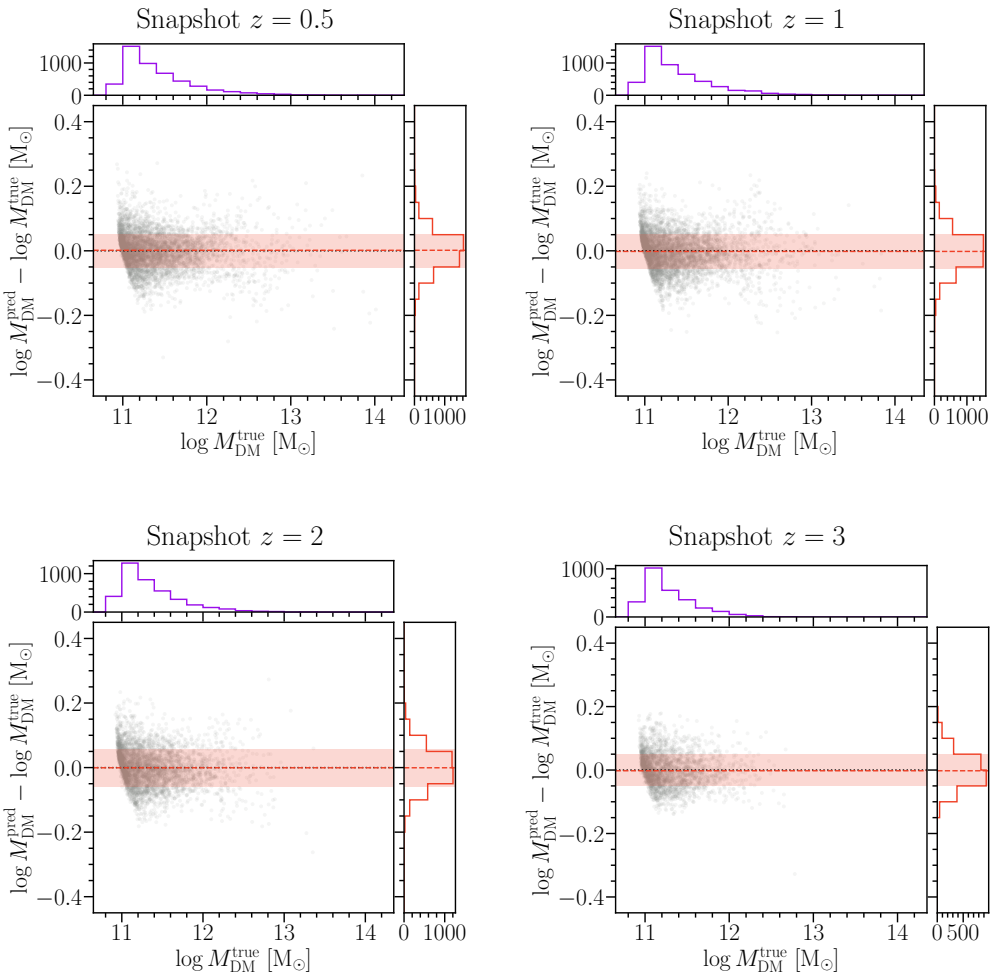

Fig. 4.14: Same as Figure 4.9, but for the $z = 0.5$ (upper left panel), $z = 1$ (upper right panel), $z = 2$ (lower left panel) and $z = 3$ (lower right panel) snapshots for the test samples.

- the rising role of the star formation rate at higher redshift in inferring the DM mass is reflected on the shape functions, that become steeper from $z = 0$ to $z = 3$, while the black hole accretion rate tends to remain almost flat.

Finally, the predictions made upon the four training samples can be applied to their test samples at the corresponding redshifts. Similarly to what found at $z = 0$, EBM predicts values of the DM mass with a scatter of $\lesssim \pm 0.06$ in the four redshifts. The comparison between $M_{\rm DM}^{\rm true}$ and $M_{\rm DM}^{\rm pred}$ for the $z = 0.5$, $z = 1$, $z = 2$ and $z = 3$ test samples are displayed in Figure 4.14.

4.4 Conclusion & Future perspectives

In this Chapter, we presented the preliminary results of a still ongoing project whose main scope is to infer the DM halo mass of simulated galaxies in the IllustrisTNG simulation making use of other physical properties, in order to possibly derive a functional form able to link the halo mass to other observables in real galaxies. In light of this challenge, we have been relying on the state-of-the-art Explainable Boosting Machine algorithm, recently developed by Microsoft Research. This new method has a very high accuracy and intelligibility and exploits some machine learning techniques like boosting or bagging in the field of the generalised additive models with pairwise interactions, GA^{2}M.

As a first analysis, we selected from the $z = 0$ snapshot of the IllustrisTNG100 simulation subhalos with $M_{\rm tot} > 10^{11}\,{\rm M}_\odot$, meaning by $M_{\rm tot}$ the sum of the masses of all particles and cells of all components in each subhalo, and we used 7 galactic properties. This sample has been split into a training sample and a test sample, with a ratio of 70:30. Although each property used plays a role in inferring $M_{\rm DM}$, the gas mass, the stellar mass and the black hole masses give the most important contributions to the final inference. Moreover, we extended our study to higher redshifts, considering also subhalos in the same range of total mass at $z = 0.5$, $z = 1$, $z = 2$ and $z = 3$, in order to test the reliability of the method in tracing the back-in-time evolution of these features. The high intelligibility that characterises the EBM method allows also to shed light on peculiarities in the properties used to infer the DM mass, as found for instance in the stellar mass and black hole mass profiles.

These are just some preliminary results, but this method is proving to be very promising, finding, at this stage, a scatter of $\lesssim \pm 0.06\,{\rm dex}$ between the actual value of $M_{\rm DM}$ from the simulation and the value predicted by the model at all redshifts. Furthermore, this scatter is found to decrease ($\simeq 0.04\,{\rm dex}$) in systems with $M_{\rm DM} \gtrsim 10^{12}\,{\rm M}_\odot$, i.e. DM halos hosting galaxies that are mostly ETGs with stellar masses $M_* \gtrsim 10^{10.5}\,{\rm M}_\odot$, as those analysed in Chapter 3.

In the next future, we plan to extend the analysis to other features of subhalos, such as kinematic properties or chemical abundances, making also use of data from IllustrisTNG300, so as to increase the statistics of objects, with the aim of obtaining a functional form that would allow to derive the DM halo mass in observed galaxies.

5 Conclusions & Future Perspectives

> *One, remember to look up at the stars and not down at your feet. Two, never give up work. Work gives you meaning and purpose and life is empty without it. Three, if you are lucky enough to find love, remember it is there and don't throw it away.*
>
> **— Stephen Hawking**

This Ph.D. thesis is mainly devoted to study the formation and evolution of early-type galaxies (ETGs) as the result of a complex merging history. In the first part of this thesis, I have studied the evolution of the stellar mass–velocity dispersion relation of massive ETGs, that I investigated by exploiting a Bayesian hierarchical approach, which results are presented in Chapter 2. In Chapter 3, I illustrated the results of a project aimed at studying the radial distributions of stellar properties, such as age, metallicity and velocity dispersion, comparing observed ETGs drawn from the MaNGA survey and simulated galaxies from the IllustrisTNG simulation suite. The main goal of this work is to explain the above-mentioned radial profiles in observed ETGs in terms of a combination of in-situ and ex-situ stellar populations, information that is directly accessible in simulations. The results presented in Chapter 3 have been obtained in collaboration with Prof. Alexie Leauthaud and her research group at the University of California Santa Cruz (UCSC). Finally, in Chapter 4, I presented the preliminary results of a project aimed at inferring the dark matter halo mass in simulated galaxies from IllustrisTNG exploiting a machine learning algorithm. This project is still ongoing and its final goal is to derive a functional form able to predict the mass of dark matter of real galaxies in the Universe. The results illustrated in Chapter 4 have been obtained during a visiting period at the UCSC, in collaboration with Prof. Alexie Leauthaud and her research group, which has been possible thanks to the Marie Skłodkowska-Curie grant received in 2019 to carry out a project on the scientific area of data analysis and machine learning.

In the following, I summarise the results presented in this thesis and I illustrate future extensions of these projects.

The cosmic evolution of the stellar mass–velocity dispersion relation of early-type galaxies

As we have seen in section 2.1, from the late 70's, we know that ETGs obey scaling relations concerning luminosity, size and stellar kinematic properties. The first empirical scaling relations to be discovered were the *Faber-Jackson relation* (Faber & Jackson, 1976) and the *Kormendy relation* (Kormendy, 1977) that link the luminosity to the stellar velocity dispersion and to the size of a galaxy, respectively. Soon thereafter, both the Faber-Jackson and Kormendy relations were discovered to be projections of a plane in a three-dimensional space, the so-called *Fundamental Plane* (Djorgovski & Davis, 1987; Dressler et al., 1987). Since then, with the improvement of technologies and the increasing of statistics in the newest surveys, systematic studies about scaling relations at different redshifts have been conducted. For instance, since it is found that at higher redshift galaxies are more compact than those in the present-day Universe, it is interesting to study the evolution of the stellar mass–size relation (e.g., Ferguson et al., 2004; van der Wel et al., 2014; Damjanov et al., 2019). Analogously, many studies show that, on average, the stellar velocity dispersion of ETGs evolves with redshift as well: in particular, for given stellar mass, the lower the redshift, the lower the velocity dispersion (e.g., van de Sande et al., 2013; Belli et al., 2014a; Gargiulo et al., 2016; Belli et al., 2017; Tanaka et al., 2019).

In this context, in Chapter 2 we presented a study focused on the evolution of the stellar mass–velocity dispersion relation of ETGs. Specifically, we developed a Bayesian hierarchical approach (described in section 2.3) to study the evolution of the $M_*-\sigma_\mathrm{e}$ relation in massive ($M_* \gtrsim 3\times10^{10}\,\mathrm{M}_\odot$) ETGs in the redshift range $0 \lesssim z \lesssim 2.5$. The first subsample we analysed is our *fiducial sample* and consists of galaxies in the redshift range $0 \lesssim z \lesssim 1.2$ drawn from the SDSS (e.g., Alam et al., 2015) and the LEGA-C (van der Wel et al., 2016) surveys. We selected ETGs, we derived stellar masses in a homogeneous way and then we corrected the velocity dispersions to an aperture of one effective radius. The second subsample taken into account is our *high-redshift sample* ($0.8 \lesssim z \lesssim 2.5$) that is composed by galaxies taken from four previous works in the literature (van de Sande et al., 2013; Belli et al., 2014a; Gargiulo et al., 2016; Belli et al., 2017), for which we simply require ETGs with stellar masses and velocity dispersions having the same definitions used for the fiducial sample. As shown in section 2.4, based on the fiducial sample, we

find out that at $z \lesssim 1.2$ the $M_*-\sigma_\mathrm{e}$ relation evolves in normalisation according to $\sigma_0 \propto M_*^\beta (1+z)^\zeta$ with $\beta \simeq 0.18$ and $\zeta \simeq 0.4$. When the slope β is allowed to evolve, it increases as $\beta(z) \simeq 0.16 + 0.26 \log(1+z)$: this model describes the evolution as well as a constant-slope model, according to the analysis of the Bayesian evidence of each model. The analysis of the *extended sample* (fiducial sample + high-redshift sample), over the wider redshift range $0 \lesssim z \lesssim 2.5$, shows results similar to those of the fiducial sample, with a slope $\beta \simeq 0.18$, but with a slightly stronger dependence of the normalisation on redshift ($\zeta \simeq 0.5$). When the slope is allowed to evolve, it varies more weakly ($\mathrm{d}\beta/\mathrm{d}\log(1+z) \simeq 0.18$) than for the fiducial sample. The intrinsic scatter of the relation is consistent with being constant $\simeq 0.08\,\mathrm{dex}$ in σ_e at fixed M_*. The results of the work presented in Chapter 2 are illustrated in Cannarozzo, Sonnenfeld, & Nipoti (2020a).

In addition to this work, we analysed the impact of adopting different selection criteria for ETGs, showing that, for instance, at least as far as a selection based on the UVJ colour–colour diagram is concerned, the results of Cannarozzo, Sonnenfeld, & Nipoti (2020a) are not biased. This analysis, described in Appendix 2.D, was taken from Cannarozzo et al. (2020b).

The results obtained in this project corroborate previous findings about the evolution of the $M_*-\sigma_\mathrm{e}$ relation of ETGs through cosmic time. The theoretical interpretation of this evolution is not straightforward. Indeed, we know that the stellar mass of individual galaxies varies with time, increasing as a consequence of mergers and star formation activity, but also decreasing because of mass return by ageing stellar populations. However, the merger-driven evolution should play the most important role, causing, on average, an increment of the stellar mass of ETGs. In the future, we plan to implement high-resolution binary simulations and analyse merger trees of galaxies in cosmological simulations to understand how individual ETGs move on the $M_*-\sigma_\mathrm{e}$ plane. Our current results indicate that, on average, the stellar velocity dispersion of individual massive ($M_* \gtrsim 3 \times 10^{11}\,\mathrm{M}_\odot$) ETGs at $z \approx 1$ must decrease while they evolve from $z \approx 1$ to $z \approx 0$.

The role of in-situ and ex-situ star formation in early-type galaxies: MaNGA versus IllustrisTNG

The merger-driven evolution of ETGs involves also aspects relating the stellar populations and their mixing. The spatial distribution of stellar populations, their metallicity, chemical abundances as well as age and other physical properties in a

galaxy contain all the information on the evolutionary processes occurred across cosmic time. In this context, I have been carrying out a project, presented in Chapter 3, aimed at interpreting the observed radial distributions of some stellar properties in massive ($M_* \gtrsim 3 \times 10^{10}\,\mathrm{M}_\odot$) ETGs from the MaNGA survey (Bundy et al., 2015; Yan et al., 2016a) in terms of a combination of two stellar components: stars formed *in situ*, i.e. within the main galaxy progenitor, and stars formed *ex situ*, i.e. in other galaxies, then accreted via mergers. To do that, we make use of ETGs taken from the IllustrisTNG simulation suite (Marinacci et al., 2018; Naiman et al., 2018; Nelson et al., 2018; Pillepich et al., 2018a; Springel et al., 2018). Concerning MaNGA data, in order to reduce the effects of systematic biases caused by different assumptions and priors, as well as diverse fitting methods (Conroy, 2013b), we rely on estimates derived by using two full spectral fitting codes: FIREFLY (Maraston & Strömbäck, 2011; Comparat et al., 2017; Goddard et al., 2017a; Wilkinson et al., 2017; Maraston et al., 2020) and PROSPECTOR (Leja et al., 2017; Johnson et al., 2019). In addition, we include estimates for velocity dispersion obtained using PPXF (Cappellari & Emsellem, 2004; Cappellari, 2017). To derive the radial profiles for MaNGA galaxies, we used the same approach as Oyarzún et al. (2019). To make a comparison with simulated galaxies, we took into account ETGs drawn from the $z = 0.1$ snapshot of IllustrisTNG100, and, for obtaining the radial profiles, we applied the method described in Huang et al. (2018) and also applied in Ardila et al. (2021).

As described in section 3.2, for both MaNGA and IllustrisTNG samples, we applied a selection of galaxies based on colours, such that ETGs are those galaxies with $(g-r) > 0.6$ (see Nelson et al., 2018), constituting our *Red galaxy sample*. In addition, we analysed the effects of another selection based on the star formation rate–stellar mass plane, so that ETGs are those galaxies characterised by star formation rates below $1\,\mathrm{dex}$ from the star-forming main sequence (as in one of the selection methods described in Donnari et al. 2019), forming our *Quiescent galaxy sample*. Among the many issues to be considered when comparing real with simulated galaxies, the different definitions of stellar masses have to be taken into account. For simulated ETGs, we explored the impact of these differences, considering the projected stellar mass within two half-mass radii (R_{2hmr}) or within a radius of 30 kpc. Concerning MaNGA ETGs, we considered stellar masses derived from diverse works in literature. In particular, we made use of stellar masses obtained from the Sérsic+Exponential fits accounting (or not) for the effects of the dust extinction (the SerExp Dusty and Dust-free model masses) from Meert et al. (2015), mass measurements listed in the original NSA catalogue derived from Petrosian and Sérsic fits, and, last but not least, the masses obtained by summing the stellar masses included in the concentric annuli

derived by FIREFLY and PROSPECTOR for building the profiles. In this work, we also analysed the pros and cons of selecting ETGs in stellar mass bins or in number-density-based stellar mass bins, for the latter case by comparing the cumulative stellar mass function of IllustrisTNG100 with those computed for the SerExp Dusty and Dust-free stellar masses by Bernardi et al. (2017). The stellar properties we compared in this projects are the stellar mass surface density, metallicity, age and velocity dispersion.

In section 3.4, we described in detail the comparison between the observed and simulated Red galaxy samples, assuming for the former the SerExp Dusty stellar mass (and showing the same analysis for the SerExp Dust-free stellar mass in Appendix 3.A), and for the latter the mass within $R_{\rm 2hmr}$. The analysis extended to the other cases (presented in Appendix 3.C) showed consistent results with those summarised in the following. Our analysis revealed a remarkable agreement between the stellar mass surface density profiles of MaNGA and IllustrisTNG ETGs. In particular, focusing on IllustrisTNG profiles, we do find that for galaxies with $M_* \lesssim 10^{11}\,{\rm M}_\odot$, the inner regions are dominated by the in-situ stellar populations out to $\approx 20\,{\rm kpc}$, while above $M_* \approx 10^{11}\,{\rm M}_\odot$ the ex-situ stellar component becomes dominant at all radii, corroborating previous results in the literature (see Pillepich et al. 2018a; Tacchella et al. 2019). This result, in addition to the similar shapes of the radial profiles of the stellar mass surface density found for the in-situ and ex-situ stellar populations and the detailed analysis of the merger history, suggests that the high-mass tail of galaxies that we observe in the present-day Universe may be the result of a stellar mass assembly history mainly marked by major mergers that tend to homogenise the stellar populations of progenitor galaxies in the merger remnant. Moreover, we found that IllustrisTNG profiles reproduce quite well also the observed radial distributions for stellar metallicity, age and velocity dispersion. Finally, we analysed separately the role of central and satellite galaxies for both IllustrisTNG and MaNGA ETGs, finding that there are not relevant differences in all the profiles between the two galaxy populations, with the only exception of the velocity dispersion profiles of massive systems, for which central simulated ETGs tend to have higher velocity dispersions than the observed counterpart. The results of this work will be presented soon in Cannarozzo, Leauthaud, Oyarzún, Huang, Diemer, Bundy, Nipoti, Sonnenfeld, & Rodriguez-Gomez (a, in prep.).

A future extension of this project will be the analysis of radial distributions of chemical abundances in both observed and simulated ETGs. Furthermore, the reconstruction of the merger trees of simulated galaxies in IllustrisTNG will allow us to study how stellar population profiles vary across cosmic time as a consequence of a merger-driven evolution.

Inferring the Dark Matter halo mass in galaxies from other observables with Machine Learning

In the context of the galaxy-halo connection, it is widely known that the dark matter (DM) halos show correlations with other physical properties of their host galaxies. The most commonly used relation between galaxies and their host DM halos is the so-called *stellar-to-halo-mass relation* (SHMR, e.g., Kravtsov et al., 2004; Moster et al., 2010; Leauthaud et al., 2011; Tinker et al., 2017; Wechsler & Tinker, 2018; Behroozi et al., 2019). Moreover, we know that there are several other empirical relations between galaxy properties. For instance, stellar mass in galaxies exhibits further correlations, such as the $M_* - M_{\rm BH}$ relation (e.g., Magorrian et al., 1998; Reines & Volonteri, 2015), or the relations involving the stellar and gas metallicities (e.g., Tremonti et al., 2004; Gallazzi et al., 2005; Gallazzi et al., 2006; Mannucci et al., 2010; Mingozzi et al., 2020). Therefore, given the complexity of the problem and the high number of galaxy properties that might be related to the DM halo in a galaxy, the study of the galaxy-halo connection can be approached relying on machine learning techniques to shed light on this intricate network of relations among several galactic properties.

In light of this challenge, I have started a project whose aim is to infer the DM halo mass in the IllustrisTNG simulations making use of other physical properties. Specifically, we have been relying on the state-of-the-art Explainable Boosting Machine (EBM) algorithm (Caruana et al., 2015; Nori et al., 2019), recently developed by Microsoft Research. This new method has a very high accuracy and intelligibility and exploits some machine learning techniques like boosting or bagging in the field of the generalised additive models with pairwise interactions (GA^{2}M, e.g., Lou, Caruana, Gehrke, & Hooker 2013). In Chapter 4, we presented the preliminary results of an analysis performed on central galaxies taken from the $z = 0$ snapshot of the IllustrisTNG100 simulation, selecting objects with $M_{\rm tot} > 10^{11}\,{\rm M}_\odot$, meaning by $M_{\rm tot}$ the sum of the masses of all particles and cells of all components in each subhalo. We trained a model on a sample of around 10,000 central subhalos, taking into account seven galaxy properties for each subhalo: the gas mass, the stellar mass, the black hole mass, the gas and stellar metallicities, the star formation rate and the black hole accretion rate. Albeit each property gives its contribution to derive $M_{\rm DM}$, the gas mass, the stellar mass and the black hole mass play the most significant roles to the overall inference. The high intelligibility characterising EBM allows also to shed light on peculiarities in the properties used to derive the DM mass. For example, in the stellar mass shape function shown in Figure 4.5, in correspondence of $M_* \approx 10^{11}\,{\rm M}_\odot$, a hump-like structure is observed. A possible interpretation for

the presence of this feature is the rising dominant role of ex-situ stellar component in massive galaxies, as found in Chapter 3.

The results described in Chapter 4 are still preliminary, but we find that the EBM method is very promising for our scope. Indeed, at this stage, the predictions made by the model applied to a test sample of ≈ 4500 halos are such that a scatter of at most $0.06\,\mathrm{dex}$ is found between the actual value of M_{DM} from the simulation and the value derived by the model. Furthermore, similar results are obtained when the same analysis is performed on central subhalos taken from different snapshots ($z = 0.5,\ 1,\ 2,\ 3$). The strength characterising EBM, in this context, is also the high capability of revealing the rising role that some properties like the star formation rate have going towards high redshifts.

In the immediate future, we are going to extend our study to other features of subhalos, making use of data from IllustrisTNG300 as well, so as to improve the statistics of objects. Overall, our main goal for this project will be to derive a functional form to be possibly used on real galaxies to provide an estimate of their DM halos exploiting all the available data for these objects. This work will be presented in Cannarozzo, Leauthaud, Sonnenfeld, Nipoti, et al. (b, in prep.).

This Ph.D. thesis confirmed and extended previous findings about ETGs, their evolution across cosmic time through mergers, as well as the existing connection between galaxies and their DM halos. The results presented in this manuscript were obtained relying on state-of-the-art methods of statistics, data analysis and machine learning, which are applicable to several studies. The project presented in Chapter 2 represents the first systematic work in literature that looks at the evolution of the $M_{*}-\sigma_{\mathrm{e}}$ relation for massive ETGs. The novel Bayesian hierarchical approach exploited (and also used in a simpler implementation in Chapter 3) is suitable to analyse the evolution of other scaling relations in ETGs, such as the size–mass relation or the Fundamental Plane. This thesis underlined also the crucial importance of making as consistent as possible comparisons between observations and simulations. The evolution of scaling relations and stellar properties in galaxies can be approached also by reconstructing the evolutionary path of individual progenitor galaxies, which would give a fundamental piece of information that is not directly accessible from observations. Therefore, from a galaxy-evolution point of view, the exploitation and/or the implementation of cosmological simulations able to model the physical processes occurring into galaxies across cosmic time can be a way to answer open questions about galaxy formation and evolution models. On the other hand, the

implementation of high-resolution hydrodynamic N-body simulations can help us to study more in detail the merger history of galaxies to understand the role of each progenitor, and the role that the gas component, supermassive black holes and other elements may have in the production of galaxy remnants. Finally, in this thesis, the project presented in Chapter 4 confirms the importance that machine learning techniques have been acquiring during the last years, both in handling the conspicuous huge amount of data from the present-day and upcoming surveys, as well as in facing very intricate and complex astrophysical and cosmological questions.

Bibliography

Eddington, A. S. (Mar. 1913). “On a formula for correcting statistics for the effects of a known error of observation”. In: *Monthly Notices of the RAS* 73, pp. 359–360 (cit. on p. 46).

Hubble, E. P. (Dec. 1926). “Extragalactic nebulae.” In: *Astrophysical Journal* 64, pp. 321–369 (cit. on p. 1).

– (1936). *Realm of the Nebulae* (cit. on p. 1).

de Vaucouleurs, Gerard (Jan. 1948). “Recherches sur les Nebuleuses Extragalactiques”. In: *Annales d’Astrophysique* 11, p. 247 (cit. on p. 7).

Salpeter, E. E. (Jan. 1955). “The Luminosity Function and Stellar Evolution.” In: *Astrophysical Journal* 121, p. 161 (cit. on pp. 5, 84).

Jeffreys, H. (1961). *Theory of Probability*. Third. Oxford, England: Oxford (cit. on p. 52).

McClure, Robert D. & Sidney van den Bergh (Dec. 1968). “UB V Observations of Field Galaxies”. In: *Astronomical Journal* 73, p. 1008 (cit. on p. 10).

Sérsic, J. L. (1968). *Atlas de galaxias australes* (cit. on pp. 7, 33).

Tinsley, Beatrice M. (Feb. 1968). “Evolution of the Stars and Gas in Galaxies”. In: *Astrophysical Journal* 151, p. 547 (cit. on p. 11).

Faber, S. M. (Sept. 1972). “Quadratic programming applied to the problem of galaxy population synthesis.” In: *Astronomy and Astrophysics* 20, p. 361 (cit. on p. 5).

Sandage, Allan (Aug. 1972). “Absolute Magnitudes of E and so Galaxies in the Virgo and Coma Clusters as a Function of U - B Color”. In: *Astrophysical Journal* 176, p. 21 (cit. on p. 10).

Searle, Leonard & Wallace L. W. Sargent (Apr. 1972). “Inferences from the Composition of Two Dwarf Blue Galaxies”. In: *Astrophysical Journal* 173, p. 25 (cit. on p. 11).

Faber, S. M. (Feb. 1973). “Variations in Spectral-Energy Distributions and Absorption-Line Strengths among Elliptical Galaxies”. In: *Astrophysical Journal* 179, pp. 731–754 (cit. on p. 5).

Larson, Richard B. (Mar. 1974). “Dynamical models for the formation and evolution of spherical galaxies”. In: *Monthly Notices of the RAS* 166, pp. 585–616 (cit. on p. 85).

Tinsley, B. M. (Sept. 1974). “Constraints on models for chemical evolution in the solar neighborhood.” In: *Astrophysical Journal* 192, pp. 629–641 (cit. on p. 11).

Faber, S. M. & R. E. Jackson (Mar. 1976). “Velocity dispersions and mass-to-light ratios for elliptical galaxies”. In: *Astrophysical Journal* 204, pp. 668–683 (cit. on pp. 15, 27, 84, 172).

Kormendy, J. (Dec. 1977). “Brightness distributions in compact and normal galaxies. II - Structure parameters of the spheroidal component”. In: *Astrophysical Journal* 218, pp. 333–346 (cit. on pp. 16, 27, 84, 172).

Rees, M. J. & J. P. Ostriker (June 1977). “Cooling, dynamics and fragmentation of massive gas clouds: clues to the masses and radii of galaxies and clusters.” In: *Monthly Notices of the RAS* 179, pp. 541–559 (cit. on p. 143).

Spinrad, Hyron (Jan. 1977). “The Ultraviolet Spectra and Color Evolution of Galaxies at Large Redshifts”. In: *Evolution of Galaxies and Stellar Populations*. Ed. by Beatrice M. Tinsley & D. Campbell Larson Richard B. Gehret, p. 301 (cit. on p. 5).

Tully, R. B. & J. R. Fisher (Feb. 1977). “Reprint of 1977A&A....54..661T. A new method of determining distance to galaxies.” In: *Astronomy and Astrophysics* 500, pp. 105–117 (cit. on p. 15).

Tinsley, B. M. (May 1978). “Evolutionary synthesis of the stellar population in elliptical galaxies. II. Late M giants and composition effects.” In: *Astrophysical Journal* 222, pp. 14–22 (cit. on p. 11).

White, S. D. M. & M. J. Rees (May 1978). “Core condensation in heavy halos: a two-stage theory for galaxy formation and clustering.” In: *Monthly Notices of the RAS* 183, pp. 341–358 (cit. on p. 143).

Wilkinson, A. & J. B. Oke (Mar. 1978). “Spectral variations in brightest cluster galaxies.” In: *Astrophysical Journal* 220, pp. 376–389 (cit. on p. 5).

Dressler, A. (Mar. 1980). “Galaxy morphology in rich clusters: implications for the formation and evolution of galaxies.” In: *Astrophysical Journal* 236, pp. 351–365 (cit. on pp. 20, 21).

Fall, S. M. & G. Efstathiou (Oct. 1980). “Formation and rotation of disc galaxies with haloes.” In: *Monthly Notices of the RAS* 193, pp. 189–206 (cit. on p. 143).

Larson, R. B., B. M. Tinsley, & C. N. Caldwell (May 1980). “The evolution of disk galaxies and the origin of S0 galaxies”. In: *Astrophysical Journal* 237, pp. 692–707 (cit. on p. 11).

O’Connell, R. W. (Mar. 1980). “Galaxy spectral synthesis. II. M 32 and the ages of galaxies.” In: *Astrophysical Journal* 236, pp. 430–440 (cit. on p. 5).

Spinrad, H. (Jan. 1980). “Spectroscopy and photometry of faint galaxies: hints at their evolution.” In: *Objects of High Redshift*. Ed. by G. O. Abell & P. J. E. Peebles. Vol. 92, pp. 39–48 (cit. on p. 5).

Bruzual A., G. (Oct. 1983). “Spectral evolution of galaxies. I. Early-type systems.” In: *Astrophysical Journal* 273, pp. 105–127 (cit. on p. 6).

Mould, J. R., J. Kristian, & G. S. Da Costa (July 1983). “Stellar populations in local group dwarf elliptical galaxies. I. NGC 147.” In: *Astrophysical Journal* 270, pp. 471–484 (cit. on p. 10).

Blumenthal, G. R., S. M. Faber, J. R. Primack, & M. J. Rees (Oct. 1984). “Formation of galaxies and large-scale structure with cold dark matter.” In: *Nature* 311, pp. 517–525 (cit. on p. 143).

Mould, J. R. (Oct. 1984). “Chemical evolution of bulges and halos.” In: *Publications of the ASP* 96, pp. 773–778 (cit. on p. 11).

Buonanno, R., C. E. Corsi, F. Fusi Pecci, E. Hardy, & R. Zinn (Nov. 1985). “Color-magnitude diagrams for the clusters and the field of the Fornaxdwarf spheroidal galaxy.” In: *Astronomy and Astrophysics* 152, pp. 65–84 (cit. on p. 10).

Renzini, Alvio & Alberto Buzzoni (1986). “Global properties of stellar populations and the spectral evolution of galaxies”. In: *Spectral evolution of galaxies*. Springer, pp. 195–235 (cit. on p. 6).

Djorgovski, S. & M. Davis (Feb. 1987). “Fundamental properties of elliptical galaxies”. In: *Astrophysical Journal* 313, pp. 59–68 (cit. on pp. 16, 27, 84, 172).

Dressler, A., D. Lynden-Bell, D. Burstein, et al. (Feb. 1987). “Spectroscopy and photometry of elliptical galaxies. I - A new distance estimator”. In: *Astrophysical Journal* 313, pp. 42–58 (cit. on pp. 16, 27, 84, 172).

Cleveland, William S. & Susan J. Devlin (1988). “Locally Weighted Regression: An Approach to Regression Analysis by Local Fitting”. In: *Journal of the American Statistical Association* 83.403, pp. 596–610. eprint: https://www.tandfonline.com/doi/pdf/10.1080/01621459.1988.10478639 (cit. on p. 45).

McCullagh, P. & J.A. Nelder (1989). *Generalized Linear Models, Second Edition*. Chapman and Hall/CRC Monographs on Statistics and Applied Probability Series. Chapman & Hall (cit. on p. 145).

Hastie, T. J. & R. J. Tibshirani (1990). *Generalized additive models*. London: Chapman & Hall, p. 335 (cit. on p. 145).

Bower, Richard G., J. R. Lucey, & Richard S. Ellis (Feb. 1992). “Precision photometry of early-type galaxies in the Coma and Virgo clusters : a test of the universality of the colour-magnitude relation - I. The data.” In: *Monthly Notices of the RAS* 254, pp. 589–600 (cit. on p. 10).

Worthey, Guy, S. M. Faber, & J. J. Gonzalez (Oct. 1992). “MG and Fe Absorption Features in Elliptical Galaxies”. In: *Astrophysical Journal* 398, p. 69 (cit. on p. 12).

Fagotto, F., A. Bressan, G. Bertelli, & C. Chiosi (1994a). “Evolutionary sequences of stellar models with new radiative opacities. III. Z=0.0004 and Z=0.05”. In: *Astronomy and Astrophysics, Supplement* 104, pp. 365–376 (cit. on p. 37).

– (1994b). “Evolutionary sequences of stellar models with new radiative opacities. IV. Z=0.004 and Z=0.008”. In: *Astronomy and Astrophysics, Supplement* 105, pp. 29–38 (cit. on p. 37).

– (1994c). “Evolutionary sequences of stellar models with new radiative opacities. IV. Z=0.004 and Z=0.008”. In: *Astronomy and Astrophysics, Supplement* 105, pp. 29–38 (cit. on p. 37).

Worthey, Guy (Nov. 1994). “Comprehensive Stellar Population Models and the Disentanglement of Age and Metallicity Effects”. In: *Astrophysical Journal, Supplement* 95, p. 107 (cit. on p. 109).

Bertin, E. & S. Arnouts (June 1996). “SExtractor: Software for source extraction.” In: *Astronomy and Astrophysics, Supplement* 117, pp. 393–404 (cit. on p. 37).

Madau, Piero, Henry C. Ferguson, Mark E. Dickinson, et al. (Dec. 1996). “High-redshift galaxies in the Hubble Deep Field: colour selection and star formation history to z$\backsim$4”. In: *Monthly Notices of the RAS* 283.4, pp. 1388–1404. arXiv: astro-ph/9607172 [astro-ph] (cit. on p. 164).

Cooper, Gregory F., Constantin F. Aliferis, Richard Ambrosino, et al. (1997). “An evaluation of machine-learning methods for predicting pneumonia mortality”. In: *Artificial Intelligence in Medicine* 9.2, pp. 107 –138 (cit. on p. 149).

Greggio, L. (Feb. 1997). “On the metallicity distribution in the nuclei of elliptical galaxies”. In: *Monthly Notices of the RAS* 285.1, pp. 151–166. arXiv: astro-ph/9609196 [astro-ph] (cit. on p. 12).

Binney, James & Michael Merrifield (1998). *Galactic Astronomy* (cit. on pp. 6, 7, 17).

Magorrian, John, Scott Tremaine, Douglas Richstone, et al. (June 1998). “The Demography of Massive Dark Objects in Galaxy Centers”. In: *Astronomical Journal* 115.6, pp. 2285–2305. arXiv: astro-ph/9708072 [astro-ph] (cit. on pp. 144, 176).

Ciotti, L. & G. Bertin (Dec. 1999). “Analytical properties of the $R^{1/m}$ law”. In: *Astronomy and Astrophysics* 352, pp. 447–451. arXiv: astro-ph/9911078 [astro-ph] (cit. on p. 8).

Jørgensen, Inger (July 1999). “E and S0 galaxies in the central part of the Coma cluster: ages, metal abundances and dark matter”. In: *Monthly Notices of the RAS* 306.3, pp. 607–636. arXiv: astro-ph/9902250 [astro-ph] (cit. on p. 12).

Trager, S. C. (Jan. 1999). “The Ages of Early-Type Galaxies: A Cautionary Tale”. In: *Photometric Redshifts and the Detection of High Redshift Galaxies*. Ed. by Ray Weymann, Lisa Storrie-Lombardi, Marcin Sawicki, & Robert Brunner. Vol. 191. Astronomical Society of the Pacific Conference Series, p. 195. arXiv: astro-ph/9906396 [astro-ph] (cit. on p. 5).

Balogh, Michael L., Julio F. Navarro, & Simon L. Morris (Sept. 2000). “The Origin of Star Formation Gradients in Rich Galaxy Clusters”. In: *Astrophysical Journal* 540.1, pp. 113–121. arXiv: astro-ph/0004078 [astro-ph] (cit. on p. 11).

Kuntschner, Harald (June 2000). “The stellar populations of early-type galaxies in the Fornax cluster”. In: *Monthly Notices of the RAS* 315.1, pp. 184–208 (cit. on p. 12).

McGaugh, S. S., J. M. Schombert, G. D. Bothun, & W. J. G. de Blok (Apr. 2000). “The Baryonic Tully-Fisher Relation”. In: *Astrophysical Journal, Letters* 533.2, pp. L99–L102. arXiv: astro-ph/0003001 [astro-ph] (cit. on pp. 144, 158).

Trager, S. C., S. M. Faber, Guy Worthey, & J. Jesús González (July 2000). “The Stellar Population Histories of Early-Type Galaxies. II. Controlling Parameters of the Stellar Populations”. In: *Astronomical Journal* 120.1, pp. 165–188. arXiv: astro-ph/0004095 [astro-ph] (cit. on p. 11).

York, Donald G., J. Adelman, Jr. Anderson John E., et al. (Sept. 2000). “The Sloan Digital Sky Survey: Technical Summary”. In: *Astronomical Journal* 120.3, pp. 1579–1587. arXiv: astro-ph/0006396 [astro-ph] (cit. on pp. 8, 87, 142).

Bacon, R., Y. Copin, G. Monnet, et al. (Sept. 2001). “The SAURON project - I. The panoramic integral-field spectrograph”. In: *Monthly Notices of the RAS* 326.1, pp. 23–35. arXiv: astro-ph/0103451 [astro-ph] (cit. on p. 85).

Kroupa, Pavel (Apr. 2001). “On the variation of the initial mass function”. In: *Monthly Notices of the RAS* 322.2, pp. 231–246. arXiv: astro-ph/0009005 [astro-ph] (cit. on pp. 84, 89).

Kuntschner, Harald, John R. Lucey, Russell J. Smith, Michael J. Hudson, & Roger L. Davies (May 2001). “On the dependence of spectroscopic indices of early-type galaxies on age, metallicity and velocity dispersion”. In: *Monthly Notices of the RAS* 323.3, pp. 615–629. arXiv: astro-ph/0011234 [astro-ph] (cit. on p. 11).

Springel, Volker, Simon D. M. White, Giuseppe Tormen, & Guinevere Kauffmann (Dec. 2001). “Populating a cluster of galaxies - I. Results at [formmu2]z=0”. In: *Monthly Notices of the RAS* 328.3, pp. 726–750. arXiv: astro-ph/0012055 [astro-ph] (cit. on p. 110).

Bertin, G., L. Ciotti, & M. Del Principe (Apr. 2002). “Weak homology of elliptical galaxies.” In: *Astronomy and Astrophysics* 386, pp. 149–168. arXiv: astro-ph/0202208 [astro-ph] (cit. on p. 71).

de Zeeuw, P. T., M. Bureau, Eric Emsellem, et al. (Jan. 2002). “The SAURON project - II. Sample and early results”. In: *Monthly Notices of the RAS* 329.3, pp. 513–530. arXiv: astro-ph/0109511 [astro-ph] (cit. on p. 85).

Proctor, R. N. & A. E. Sansom (July 2002). “A comparison of stellar populations in galaxy spheroids across a wide range of Hubble types”. In: *Monthly Notices of the RAS* 333.3, pp. 517–543. arXiv: astro-ph/0202390 [astro-ph] (cit. on p. 12).

Strauss, Michael A., David H. Weinberg, Robert H. Lupton, et al. (Sept. 2002). “Spectroscopic Target Selection in the Sloan Digital Sky Survey: The Main Galaxy Sample”. In: *Astronomical Journal* 124.3, pp. 1810–1824. arXiv: astro-ph/0206225 [astro-ph] (cit. on pp. 31, 38).

Westera, P., T. Lejeune, R. Buser, F. Cuisinier, & G. Bruzual (Jan. 2002). “A standard stellar library for evolutionary synthesis. III. Metallicity calibration”. In: *Astronomy and Astrophysics* 381, pp. 524–538. eprint: astro-ph/0110559 (cit. on p. 37).

Bruzual, G. & S. Charlot (Oct. 2003). “Stellar population synthesis at the resolution of 2003”. In: *Monthly Notices of the RAS* 344, pp. 1000–1028. eprint: astro-ph/0309134 (cit. on p. 37).

Chabrier, G. (July 2003). “Galactic Stellar and Substellar Initial Mass Function”. In: *Publications of the ASP* 115, pp. 763–795. eprint: astro-ph/0304382 (cit. on pp. 30, 84, 89, 145).

Le Fèvre, Oliver, Michel Saisse, Dario Mancini, et al. (2003). “Commissioning and performances of the VLT-VIMOS instrument”. In: *Instrument Design and Performance for Optical/Infrared Ground-based Telescopes*. Ed. by Masanori Iye & Alan F. M. Moorwood. Vol. 4841. Society of Photo-Optical Instrumentation Engineers (SPIE) Conference Series, pp. 1670–1681 (cit. on p. 31).

Nipoti, C., P. Londrillo, & L. Ciotti (June 2003). “Galaxy merging, the fundamental plane of elliptical galaxies and the M_{BH}-σ_0 relation”. In: *Monthly Notices of the RAS* 342, pp. 501–512. eprint: astro-ph/0302423 (cit. on pp. 28, 71).

Tagliaferri, Roberto, Guiseppe Longo, Stefano Andreon, et al. (2003). “Neural Networks for Photometric Redshifts Evaluation”. In: *Lecture Notes in Computer Science*. Vol. 2859, pp. 226–234 (cit. on p. 143).

Balogh, Michael L., Ivan K. Baldry, Robert Nichol, et al. (Nov. 2004). “The Bimodal Galaxy Color Distribution: Dependence on Luminosity and Environment”. In: *Astrophysical Journal, Letters* 615.2, pp. L101–L104. arXiv: astro-ph/0406266 [astro-ph] (cit. on p. 20).

Bell, Eric F., Daniel H. McIntosh, Marco Barden, et al. (Jan. 2004). “GEMS Imaging of Red-Sequence Galaxies at z$\sim$0.7: Dusty or Old?” In: *Astrophysical Journal, Letters* 600.1, pp. L11–L14. arXiv: astro-ph/0308272 [astro-ph] (cit. on p. 8).

Cappellari, M. & E. Emsellem (Feb. 2004). “Parametric Recovery of Line-of-Sight Velocity Distributions from Absorption-Line Spectra of Galaxies via Penalized Likelihood”. In: *Publications of the ASP* 116, pp. 138–147. eprint: astro-ph/0312201 (cit. on pp. 88, 89, 174).

Emsellem, Eric, Michele Cappellari, Reynier F. Peletier, et al. (Aug. 2004). “The SAURON project - III. Integral-field absorption-line kinematics of 48 elliptical and lenticular galaxies”. In: *Monthly Notices of the RAS* 352.3, pp. 721–743. arXiv: astro-ph/0404034 [astro-ph] (cit. on p. 23).

Ferguson, Henry C., Mark Dickinson, Mauro Giavalisco, et al. (2004). “The Size Evolution of High-Redshift Galaxies”. In: *Astrophysical Journal* 600.2, pp. L107–L110. arXiv: astro-ph/0309058 [astro-ph] (cit. on pp. 18, 28, 84, 172).

Jones, D. Heath, Will Saunders, Matthew Colless, et al. (Dec. 2004). “The 6dF Galaxy Survey: samples, observational techniques and the first data release”. In: *Monthly Notices of the RAS* 355.3, pp. 747–763. arXiv: astro-ph/0403501 [astro-ph] (cit. on p. 16).

Kobayashi, Chiaki (Jan. 2004). “GRAPE-SPH chemodynamical simulation of elliptical galaxies - I. Evolution of metallicity gradients”. In: *Monthly Notices of the RAS* 347.3, pp. 740–758. arXiv: astro-ph/0310160 [astro-ph] (cit. on p. 85).

Kravtsov, Andrey V., Andreas A. Berlind, Risa H. Wechsler, et al. (July 2004). “The Dark Side of the Halo Occupation Distribution”. In: *Astrophysical Journal* 609.1, pp. 35–49. arXiv: astro-ph/0308519 [astro-ph] (cit. on pp. 144, 176).

Skilling, John (2004). “Nested Sampling”. In: *AIP Conference Proceedings* 735.1, pp. 395–405. eprint: https://aip.scitation.org/doi/pdf/10.1063/1.1835238 (cit. on p. 52).

Tremonti, Christy A., Timothy M. Heckman, Guinevere Kauffmann, et al. (Oct. 2004). "The Origin of the Mass-Metallicity Relation: Insights from 53,000 Star-forming Galaxies in the Sloan Digital Sky Survey". In: *Astrophysical Journal* 613.2, pp. 898–913. arXiv: astro-ph/0405537 [astro-ph] (cit. on pp. 144, 176).

Blanton, M. R., D. J. Schlegel, M. A. Strauss, et al. (June 2005). "New York University Value-Added Galaxy Catalog: A Galaxy Catalog Based on New Public Surveys". In: *Astronomical Journal* 129, pp. 2562–2578. eprint: astro-ph/0410166 (cit. on p. 8).

Gallazzi, A., S. Charlot, J. Brinchmann, S. D. M. White, & C. A. Tremonti (Sept. 2005). "The ages and metallicities of galaxies in the local universe". In: *Monthly Notices of the RAS* 362, pp. 41–58. eprint: astro-ph/0506539 (cit. on pp. 11, 37, 144, 176).

Geller, Margaret J., Ian P. Dell'Antonio, Michael J. Kurtz, et al. (2005). "SHELS: The Hectospec Lensing Survey". In: *Astrophysical Journal* 635.2, pp. L125–L128. arXiv: astro-ph/0510351 [astro-ph] (cit. on p. 66).

Jones, D. Heath, Will Saunders, Michael Read, & Matthew Colless (Aug. 2005). "Second Data Release of the 6dF Galaxy Survey". In: *Publications of the Astron. Soc. of Australia* 22.3, pp. 277–286. arXiv: astro-ph/0505068 [astro-ph] (cit. on p. 16).

Kereš, Dušan, Neal Katz, David H. Weinberg, & Romeel Davé (Oct. 2005). "How do galaxies get their gas?" In: *Monthly Notices of the RAS* 363.1, pp. 2–28. arXiv: astro-ph/0407095 [astro-ph] (cit. on p. 11).

Thomas, Daniel, Claudia Maraston, Ralf Bender, & Claudia Mendes de Oliveira (Mar. 2005). "The Epochs of Early-Type Galaxy Formation as a Function of Environment". In: *Astrophysical Journal* 621.2, pp. 673–694. arXiv: astro-ph/0410209 [astro-ph] (cit. on pp. 11, 12, 85).

Adelman-McCarthy, Jennifer K., Marcel A. Agüeros, Sahar S. Allam, et al. (Jan. 2006). "The Fourth Data Release of the Sloan Digital Sky Survey". In: *Astrophysical Journal, Supplement* 162.1, pp. 38–48. arXiv: astro-ph/0507711 [astro-ph] (cit. on p. 113).

Boylan-Kolchin, Michael, Chung-Pei Ma, & Eliot Quataert (2006). "Red mergers and the assembly of massive elliptical galaxies: the fundamental plane and its projections". In: *Monthly Notices of the RAS* 369.3, pp. 1081–1089. arXiv: astro-ph/0601400 [astro-ph] (cit. on p. 29).

Cappellari, M., R. Bacon, M. Bureau, et al. (Mar. 2006). "The SAURON project - IV. The mass-to-light ratio, the virial mass estimator and the Fundamental Plane of elliptical and lenticular galaxies". In: *Monthly Notices of the RAS* 366, pp. 1126–1150. eprint: astro-ph/0505042 (cit. on p. 42).

Carroll, Bradley W. & Dale A. Ostlie (2006). *An introduction to modern astrophysics and cosmology* (cit. on p. 3).

Gallazzi, Anna, Stéphane Charlot, Jarle Brinchmann, & Simon D. M. White (Aug. 2006). "Ages and metallicities of early-type galaxies in the Sloan Digital Sky Survey: new insight into the physical origin of the colour-magnitude and the Mg_2-σ_V relations". In: *Monthly Notices of the RAS* 370.3, pp. 1106–1124. arXiv: astro-ph/0605300 [astro-ph] (cit. on pp. 11, 144, 176).

Gardner, Jonathan P., John C. Mather, Mark Clampin, et al. (Apr. 2006). "The James Webb Space Telescope". In: *Space Science Reviews* 123.4, pp. 485–606. arXiv: astro-ph/0606175 [astro-ph] (cit. on p. 141).

Gunn, James E., Walter A. Siegmund, Edward J. Mannery, et al. (Apr. 2006). "The 2.5 m Telescope of the Sloan Digital Sky Survey". In: *Astronomical Journal* 131.4, pp. 2332–2359. arXiv: astro-ph/0602326 [astro-ph] (cit. on p. 87).

Mandelbaum, Rachel, Uroš Seljak, Guinevere Kauffmann, Christopher M. Hirata, & Jonathan Brinkmann (May 2006). "Galaxy halo masses and satellite fractions from galaxy-galaxy lensing in the Sloan Digital Sky Survey: stellar mass, luminosity, morphology and environment dependencies". In: *Monthly Notices of the RAS* 368.2, pp. 715–731. arXiv: astro-ph/0511164 [astro-ph] (cit. on p. 144).

Robertson, Brant, Thomas J. Cox, Lars Hernquist, et al. (2006). "The Fundamental Scaling Relations of Elliptical Galaxies". In: *Astrophysical Journal* 641.1, pp. 21–40. arXiv: astro-ph/0511053 [astro-ph] (cit. on p. 29).

Sánchez-Blázquez, P., R. F. Peletier, J. Jiménez-Vicente, et al. (Sept. 2006). "Medium-resolution Isaac Newton Telescope library of empirical spectra". In: *Monthly Notices of the RAS* 371.2, pp. 703–718. arXiv: astro-ph/0607009 [astro-ph] (cit. on p. 89).

Trujillo, Ignacio, Natascha M. Förster Schreiber, Gregory Rudnick, et al. (2006). "The Size Evolution of Galaxies since z∼3: Combining SDSS, GEMS, and FIRES". In: *Astrophysical Journal* 650.1, pp. 18–41. arXiv: astro-ph/0504225 [astro-ph] (cit. on p. 18).

Blanton, Michael R. & Sam Roweis (Feb. 2007). "K-Corrections and Filter Transformations in the Ultraviolet, Optical, and Near-Infrared". In: *Astronomical Journal* 133.2, pp. 734–754. arXiv: astro-ph/0606170 [astro-ph] (cit. on p. 8).

Cappellari, Michele, Eric Emsellem, R. Bacon, et al. (Aug. 2007). "The SAURON project - X. The orbital anisotropy of elliptical and lenticular galaxies: revisiting the (V/σ, $\in$) diagram with integral-field stellar kinematics". In: *Monthly Notices of the RAS* 379.2, pp. 418–444. arXiv: astro-ph/0703533 [astro-ph] (cit. on p. 23).

Ciotti, L., B. Lanzoni, & M. Volonteri (Mar. 2007). "The Importance of Dry and Wet Merging on the Formation and Evolution of Elliptical Galaxies". In: *Astrophysical Journal* 658, pp. 65–77. eprint: astro-ph/0611328 (cit. on p. 29).

Emsellem, Eric, Michele Cappellari, Davor Krajnović, et al. (Aug. 2007). "The SAURON project - IX. A kinematic classification for early-type galaxies". In: *Monthly Notices of the RAS* 379.2, pp. 401–417. arXiv: astro-ph/0703531 [astro-ph] (cit. on p. 23).

Faber, S. M., C. N. A. Willmer, C. Wolf, et al. (Aug. 2007). "Galaxy Luminosity Functions to z∼1 from DEEP2 and COMBO-17: Implications for Red Galaxy Formation". In: *Astrophysical Journal* 665.1, pp. 265–294. arXiv: astro-ph/0506044 [astro-ph] (cit. on p. 9).

Scoville, N., H. Aussel, M. Brusa, et al. (2007). "The Cosmic Evolution Survey (COSMOS): Overview". In: *Astrophysical Journal, Supplement* 172.1, pp. 1–8. arXiv: astro-ph/0612305 [astro-ph] (cit. on p. 32).

Yang, Xiaohu, H. J. Mo, Frank C. van den Bosch, et al. (Dec. 2007). “Galaxy Groups in the SDSS DR4. I. The Catalog and Basic Properties”. In: *Astrophysical Journal* 671.1, pp. 153–170. arXiv: 0707.4640 [astro-ph] (cit. on pp. 113, 117).

Adelman-McCarthy, J. K., M. A. Agüeros, S. S. Allam, et al. (Apr. 2008). “The Sixth Data Release of the Sloan Digital Sky Survey”. In: *Astrophysical Journal, Supplement* 175, pp. 297–313. arXiv: 0707.3413 (cit. on p. 65).

Binney, James & Scott Tremaine (2008). *Galactic Dynamics: Second Edition* (cit. on p. 17).

Bolton, A. S., T. Treu, L. V. E. Koopmans, et al. (Sept. 2008). “The Sloan Lens ACS Survey. VII. Elliptical Galaxy Scaling Laws from Direct Observational Mass Measurements”. In: *Astrophysical Journal* 684, pp. 248–259. arXiv: 0805.1932 (cit. on p. 65).

Feroz, F. & M. P. Hobson (Feb. 2008). “Multimodal nested sampling: an efficient and robust alternative to Markov Chain Monte Carlo methods for astronomical data analyses”. In: *Monthly Notices of the RAS* 384, pp. 449–463. arXiv: 0704.3704 (cit. on p. 52).

Gallazzi, Anna, Jarle Brinchmann, Stéphane Charlot, & Simon D. M. White (Feb. 2008). “A census of metals and baryons in stars in the local Universe”. In: *Monthly Notices of the RAS* 383.4, pp. 1439–1458. arXiv: 0708.0533 [astro-ph] (cit. on p. 11).

Huertas-Company, M., D. Rouan, L. Tasca, G. Soucail, & O. Le Fèvre (Feb. 2008). “A robust morphological classification of high-redshift galaxies using support vector machines on seeing limited images. I. Method description”. In: *Astronomy and Astrophysics* 478.3, pp. 971–980. arXiv: 0709.1359 [astro-ph] (cit. on p. 143).

Padmanabhan, Nikhil, David J. Schlegel, Douglas P. Finkbeiner, et al. (Feb. 2008). “An Improved Photometric Calibration of the Sloan Digital Sky Survey Imaging Data”. In: *Astrophysical Journal* 674.2, pp. 1217–1233. arXiv: astro-ph/0703454 [astro-ph] (cit. on p. 8).

van der Wel, A., B. P. Holden, A. W. Zirm, et al. (Nov. 2008). “Recent Structural Evolution of Early-Type Galaxies: Size Growth from z = 1 to z = 0”. In: *Astrophysical Journal* 688, pp. 48–58. arXiv: 0808.0077 (cit. on p. 18).

Abazajian, K. N., J. K. Adelman-McCarthy, M. A. Agüeros, et al. (June 2009). “The Seventh Data Release of the Sloan Digital Sky Survey”. In: *Astrophysical Journal, Supplement* 182, pp. 543–558. arXiv: 0812.0649 (cit. on p. 8).

Auger, M. W., T. Treu, A. S. Bolton, et al. (Nov. 2009). “The Sloan Lens ACS Survey. IX. Colors, Lensing, and Stellar Masses of Early-Type Galaxies”. In: *Astrophysical Journal* 705, pp. 1099–1115. arXiv: 0911.2471 (cit. on pp. 37, 65).

Brammer, G. B., K. E. Whitaker, P. G. van Dokkum, et al. (Nov. 2009). “The Dead Sequence: A Clear Bimodality in Galaxy Colors from z = 0 to z = 2.5”. In: *Astrophysical Journal, Letters* 706.1, pp. L173–L177. arXiv: 0910.2227 [astro-ph.CO] (cit. on p. 8).

Cenarro, A. Javier & Ignacio Trujillo (May 2009). “Mild Velocity Dispersion Evolution of Spheroid-Like Massive Galaxies Since z $\sim$2”. In: *Astrophysical Journal, Letters* 696.1, pp. L43–L47. arXiv: 0902.4893 [astro-ph.CO] (cit. on p. 18).

Conroy, Charlie, James E. Gunn, & Martin White (July 2009). “The Propagation of Uncertainties in Stellar Population Synthesis Modeling. I. The Relevance of Uncertain Aspects of Stellar Evolution and the Initial Mass Function to the Derived Physical Properties of Galaxies”. In: *Astrophysical Journal* 699.1, pp. 486–506. arXiv: 0809.4261 [astro-ph] (cit. on p. 89).

Dewdney, P. E., P. J. Hall, R. T. Schilizzi, & T. J. L. W. Lazio (Aug. 2009). “The Square Kilometre Array”. In: *IEEE Proceedings* 97.8, pp. 1482–1496 (cit. on p. 141).

Feroz, F., M. P. Hobson, & M. Bridges (Oct. 2009). “MULTINEST: an efficient and robust Bayesian inference tool for cosmology and particle physics”. In: *Monthly Notices of the RAS* 398, pp. 1601–1614. arXiv: 0809.3437 (cit. on p. 52).

Hyde, Joseph B. & Mariangela Bernardi (2009a). “Curvature in the scaling relations of early-type galaxies”. In: *Monthly Notices of the RAS* 394.4, pp. 1978–1990. arXiv: 0810.4922 [astro-ph] (cit. on pp. 28, 65–69).

– (2009b). “The luminosity and stellar mass Fundamental Plane of early-type galaxies”. In: *Monthly Notices of the RAS* 396.2, pp. 1171–1185. arXiv: 0810.4924 [astro-ph] (cit. on pp. 15, 27).

Jones, D. Heath, Mike A. Read, Will Saunders, et al. (Oct. 2009). “The 6dF Galaxy Survey: final redshift release (DR3) and southern large-scale structures”. In: *Monthly Notices of the RAS* 399.2, pp. 683–698. arXiv: 0903.5451 [astro-ph.CO] (cit. on p. 16).

Lilly, Simon J., Vincent Le Brun, Christian Maier, et al. (Oct. 2009). “The zCOSMOS 10k-Bright Spectroscopic Sample”. In: *Astrophysical Journal, Supplement* 184.2, pp. 218–229 (cit. on p. 14).

More, Surhud, Frank C. van den Bosch, Marcello Cacciato, et al. (Jan. 2009). “Satellite kinematics - II. The halo mass-luminosity relation of central galaxies in SDSS”. In: *Monthly Notices of the RAS* 392.2, pp. 801–816. arXiv: 0807.4532 [astro-ph] (cit. on p. 144).

Naab, T., P. H. Johansson, & J. P. Ostriker (July 2009). “Minor Mergers and the Size Evolution of Elliptical Galaxies”. In: *Astrophysical Journal, Letters* 699, pp. L178–L182. arXiv: 0903.1636 [astro-ph.CO] (cit. on pp. 23, 28, 29, 84, 104).

Nipoti, C., T. Treu, M. W. Auger, & A. S. Bolton (Nov. 2009a). “Can Dry Merging Explain the Size Evolution of Early-Type Galaxies?” In: *Astrophysical Journal, Letters* 706, pp. L86–L90. arXiv: 0910.2731 (cit. on p. 28).

Nipoti, C., T. Treu, & A. S. Bolton (Oct. 2009b). “Dry Mergers and the Formation of Early-Type Galaxies: Constraints from Lensing and Dynamics”. In: *Astrophysical Journal* 703, pp. 1531–1544. arXiv: 0908.1621 (cit. on p. 29).

Wootten, Alwyn & A. Richard Thompson (Aug. 2009). “The Atacama Large Millimeter/-Submillimeter Array”. In: *IEEE Proceedings* 97.8, pp. 1463–1471. arXiv: 0904.3739 [astro-ph.IM] (cit. on p. 141).

Auger, M. W., T. Treu, A. S. Bolton, et al. (2010). “The Sloan Lens ACS Survey. X. Stellar, Dynamical, and Total Mass Correlations of Massive Early-type Galaxies”. In: *Astrophysical Journal* 724.1, pp. 511–525. arXiv: 1007.2880 [astro-ph.CO] (cit. on pp. 27, 50, 65–69).

Conroy, Charlie & James E. Gunn (Apr. 2010). "The Propagation of Uncertainties in Stellar Population Synthesis Modeling. III. Model Calibration, Comparison, and Evaluation". In: *Astrophysical Journal* 712.2, pp. 833–857. arXiv: 0911.3151 [astro-ph.CO] (cit. on p. 89).

Goodman, Jonathan & Jonathan Weare (2010). "Ensemble samplers with affine invariance". In: *Communications in Applied Mathematics and Computational Science* 5.1, pp. 65–80 (cit. on pp. 50, 102).

Kaiser, Nick, William Burgett, Ken Chambers, et al. (July 2010). "The Pan-STARRS wide-field optical/NIR imaging survey". In: *Ground-based and Airborne Telescopes III*. Ed. by Larry M. Stepp, Roberto Gilmozzi, & Helen J. Hall. Vol. 7733. Society of Photo-Optical Instrumentation Engineers (SPIE) Conference Series, 77330E (cit. on p. 142).

Kuntschner, Harald, Eric Emsellem, Roland Bacon, et al. (Oct. 2010). "The SAURON project - XVII. Stellar population analysis of the absorption line strength maps of 48 early-type galaxies". In: *Monthly Notices of the RAS* 408.1, pp. 97–132. arXiv: 1006.1574 [astro-ph.GA] (cit. on p. 85).

Mannucci, F., G. Cresci, R. Maiolino, A. Marconi, & A. Gnerucci (Nov. 2010). "A fundamental relation between mass, star formation rate and metallicity in local and high-redshift galaxies". In: *Monthly Notices of the RAS* 408.4, pp. 2115–2127. arXiv: 1005.0006 [astro-ph.CO] (cit. on pp. 144, 176).

Moster, Benjamin P., Rachel S. Somerville, Christian Maulbetsch, et al. (Feb. 2010). "Constraints on the Relationship between Stellar Mass and Halo Mass at Low and High Redshift". In: *Astrophysical Journal* 710.2, pp. 903–923. arXiv: 0903.4682 [astro-ph.CO] (cit. on pp. 144, 176).

Nair, Preethi B. & Roberto G. Abraham (Feb. 2010). "A Catalog of Detailed Visual Morphological Classifications for 14,034 Galaxies in the Sloan Digital Sky Survey". In: *Astrophysical Journal, Supplement* 186.2, pp. 427–456. arXiv: 1001.2401 [astro-ph.CO] (cit. on pp. 96, 97).

Oser, Ludwig, Jeremiah P. Ostriker, Thorsten Naab, Peter H. Johansson, & Andreas Burkert (Dec. 2010). "The Two Phases of Galaxy Formation". In: *Astrophysical Journal* 725.2, pp. 2312–2323. arXiv: 1010.1381 [astro-ph.CO] (cit. on pp. 23, 24, 84, 91, 104).

Pipino, Antonio, Annibale D'Ercole, Cristina Chiappini, & Francesca Matteucci (Sept. 2010). "Abundance gradient slopes versus mass in spheroids: predictions by monolithic models". In: *Monthly Notices of the RAS* 407.2, pp. 1347–1359. arXiv: 1005.2154 [astro-ph.CO] (cit. on p. 85).

Pozzetti, L., M. Bolzonella, E. Zucca, et al. (Nov. 2010). "zCOSMOS - 10k-bright spectroscopic sample. The bimodality in the galaxy stellar mass function: exploring its evolution with redshift". In: *Astronomy and Astrophysics* 523, A13, A13. arXiv: 0907.5416 [astro-ph.CO] (cit. on p. 9).

Spolaor, Max, Chiaki Kobayashi, Duncan A. Forbes, Warrick J. Couch, & George K. T. Hau (Oct. 2010). "Early-type galaxies at large galactocentric radii - II. Metallicity gradients and the [Z/H]-mass, [α/Fe]-mass relations". In: *Monthly Notices of the RAS* 408.1, pp. 272–292. arXiv: 1006.1698 [astro-ph.CO] (cit. on p. 13).

Springel, V. (Jan. 2010). “E pur si muove: Galilean-invariant cosmological hydrodynamical simulations on a moving mesh”. In: *Monthly Notices of the RAS* 401, pp. 791–851. arXiv: 0901.4107 (cit. on p. 90).

Thomas, Daniel, Claudia Maraston, Kevin Schawinski, Marc Sarzi, & Joseph Silk (June 2010). “Environment and self-regulation in galaxy formation”. In: *Monthly Notices of the RAS* 404.4, pp. 1775–1789. arXiv: 0912.0259 [astro-ph.CO] (cit. on pp. 11, 12).

Treu, Tommaso, Matthew W. Auger, Léon V. E. Koopmans, et al. (Feb. 2010). “The Initial Mass Function of Early-Type Galaxies”. In: *Astrophysical Journal* 709.2, pp. 1195–1202. arXiv: 0911.3392 [astro-ph.CO] (cit. on p. 84).

Vazdekis, A., P. Sánchez-Blázquez, J. Falcón-Barroso, et al. (June 2010). “Evolutionary stellar population synthesis with MILES - I. The base models and a new line index system”. In: *Monthly Notices of the RAS* 404.4, pp. 1639–1671. arXiv: 1004.4439 [astro-ph.CO] (cit. on p. 89).

Bernardi, Mariangela, Nathan Roche, Francesco Shankar, & Ravi K. Sheth (Mar. 2011a). “Curvature in the colour-magnitude relation but not in colour-σ: major dry mergers at $M_* > 2 \times 10^{11}$ $M_\odot$?” In: *Monthly Notices of the RAS* 412.1, pp. 684–704. arXiv: 1005.3770 [astro-ph.CO] (cit. on pp. 28, 117).

– (Mar. 2011b). “Evidence of major dry mergers at $M_* > 2 \times 10^{11}$ $M_\odot$ from curvature in early-type galaxy scaling relations?” In: *Monthly Notices of the RAS* 412.1, pp. L6–L10. arXiv: 1011.1501 [astro-ph.CO] (cit. on p. 28).

Blanton, Michael R., Eyal Kazin, Demitri Muna, Benjamin A. Weaver, & Adrian Price-Whelan (July 2011). “Improved Background Subtraction for the Sloan Digital Sky Survey Images”. In: *Astronomical Journal* 142.1, 31, p. 31. arXiv: 1105.1960 [astro-ph.IM] (cit. on p. 88).

Cappellari, Michele, Eric Emsellem, Davor Krajnović, et al. (May 2011). “The ATLAS^{3D} project - I. A volume-limited sample of 260 nearby early-type galaxies: science goals and selection criteria”. In: *Monthly Notices of the RAS* 413.2, pp. 813–836. arXiv: 1012.1551 [astro-ph.CO] (cit. on p. 85).

Eisenstein, Daniel J., David H. Weinberg, Eric Agol, et al. (2011). “SDSS-III: Massive Spectroscopic Surveys of the Distant Universe, the Milky Way, and Extra-Solar Planetary Systems”. In: *Astronomical Journal* 142.3, 72, p. 72. arXiv: 1101.1529 [astro-ph.IM] (cit. on p. 30).

Laureijs, R., J. Amiaux, S. Arduini, et al. (Oct. 2011). “Euclid Definition Study Report”. In: *arXiv e-prints*, arXiv:1110.3193, arXiv:1110.3193. arXiv: 1110.3193 [astro-ph.CO] (cit. on p. 141).

Leauthaud, Alexie, Jeremy Tinker, Peter S. Behroozi, Michael T. Busha, & Risa H. Wechsler (Sept. 2011). “A Theoretical Framework for Combining Techniques that Probe the Link Between Galaxies and Dark Matter”. In: *Astrophysical Journal* 738.1, 45, p. 45. arXiv: 1103.2077 [astro-ph.CO] (cit. on pp. 144, 176).

Lintott, Chris, Kevin Schawinski, Steven Bamford, et al. (Jan. 2011). “Galaxy Zoo 1: data release of morphological classifications for nearly 900 000 galaxies”. In: *Monthly Notices of the RAS* 410.1, pp. 166–178. arXiv: 1007.3265 [astro-ph.GA] (cit. on p. 117).

Maraston, C. & G. Strömbäck (Dec. 2011). “Stellar population models at high spectral resolution”. In: *Monthly Notices of the RAS* 418.4, pp. 2785–2811. arXiv: 1109.0543 [astro-ph.CO] (cit. on pp. 88, 89, 174).

Richards, Joseph W., Dan L. Starr, Nathaniel R. Butler, et al. (May 2011). “On Machine-learned Classification of Variable Stars with Sparse and Noisy Time-series Data”. In: *Astrophysical Journal* 733.1, 10, p. 10. arXiv: 1101.1959 [astro-ph.IM] (cit. on p. 143).

Simard, L., J. Trevor Mendel, D. R. Patton, S. L. Ellison, & A. W. McConnachie (Nov. 2011). “VizieR Online Data Catalog: Bulge+disk decompositions of SDSS galaxies (Simard+, 2011)”. In: *VizieR Online Data Catalog*, J/ApJS/196/11, J/ApJS/196/11 (cit. on pp. 74, 75).

van de Sande, Jesse, Mariska Kriek, Marijn Franx, et al. (July 2011). “The Stellar Velocity Dispersion of a Compact Massive Galaxy at z = 1.80 Using X-Shooter: Confirmation of the Evolution in the Mass-Size and Mass-Dispersion Relations”. In: *Astrophysical Journal, Letters* 736.1, L9, p. L9. arXiv: 1104.3860 [astro-ph.CO] (cit. on p. 18).

Wuyts, Stijn, Natascha M. Förster Schreiber, Dieter Lutz, et al. (Sept. 2011). “On Star Formation Rates and Star Formation Histories of Galaxies Out to z $\sim$3”. In: *Astrophysical Journal* 738.1, 106, p. 106. arXiv: 1106.5502 [astro-ph.CO] (cit. on p. 8).

Cheung, Edmond, S. M. Faber, David C. Koo, et al. (Dec. 2012). “The Dependence of Quenching upon the Inner Structure of Galaxies at 0.5 <= z < 0.8 in the DEEP2/AEGIS Survey”. In: *Astrophysical Journal* 760.2, 131, p. 131. arXiv: 1210.4173 [astro-ph.GA] (cit. on p. 8).

Cimatti, A., C. Nipoti, & P. Cassata (May 2012). “Fast evolving size of early-type galaxies at >z > 2 and the role of dissipationless (dry) merging”. In: *Monthly Notices of the RAS* 422, pp. L62–L66. arXiv: 1202.5403 (cit. on pp. 18, 29, 70).

Croom, Scott M., Jon S. Lawrence, Joss Bland-Hawthorn, et al. (Mar. 2012). “The Sydney-AAO Multi-object Integral field spectrograph”. In: *Monthly Notices of the RAS* 421.1, pp. 872–893. arXiv: 1112.3367 [astro-ph.CO] (cit. on p. 85).

Dressler, Alan, David Spergel, Matt Mountain, et al. (Oct. 2012). “Exploring the NRO Opportunity for a Hubble-sized Wide-field Near-IR Space Telescope – NEW WFIRST”. In: *arXiv e-prints*, arXiv:1210.7809, arXiv:1210.7809. arXiv: 1210.7809 [astro-ph.IM] (cit. on p. 141).

Green, J., P. Schechter, C. Baltay, et al. (Aug. 2012). “Wide-Field InfraRed Survey Telescope (WFIRST) Final Report”. In: *arXiv e-prints*, arXiv:1208.4012, arXiv:1208.4012. arXiv: 1208.4012 [astro-ph.IM] (cit. on p. 141).

Lackner, C. N., R. Cen, J. P. Ostriker, & M. R. Joung (Sept. 2012). “Building galaxies by accretion and in situ star formation”. In: *Monthly Notices of the RAS* 425.1, pp. 641–656. arXiv: 1206.0295 [astro-ph.CO] (cit. on p. 91).

López-Sanjuan, C., O. Le Fèvre, O. Ilbert, et al. (2012). “The dominant role of mergers in the size evolution of massive early-type galaxies since z $\sim$1”. In: *Astronomy and Astrophysics* 548, A7, A7. arXiv: 1202.4674 [astro-ph.CO] (cit. on p. 73).

Lou, Yin, Rich Caruana, & Johannes Gehrke (2012). “Intelligible models for classification and regression”. In: *Proceedings of the 18th ACM SIGKDD international conference on Knowledge discovery and data mining*. ACM, pp. 150–158 (cit. on p. 151).

Magoulas, Christina, Christopher M. Springob, Matthew Colless, et al. (Nov. 2012). “The 6dF Galaxy Survey: the near-infrared Fundamental Plane of early-type galaxies”. In: *Monthly Notices of the RAS* 427.1, pp. 245–273. arXiv: 1206.0385 [astro-ph.CO] (cit. on p. 17).

Nipoti, C., T. Treu, A. Leauthaud, et al. (May 2012). “Size and velocity-dispersion evolution of early-type galaxies in a Λ cold dark matter universe”. In: *Monthly Notices of the RAS* 422, pp. 1714–1731. arXiv: 1202.0971 (cit. on pp. 28, 29).

Oser, Ludwig, Thorsten Naab, Jeremiah P. Ostriker, & Peter H. Johansson (Jan. 2012). “The Cosmological Size and Velocity Dispersion Evolution of Massive Early-type Galaxies”. In: *Astrophysical Journal* 744.1, 63, p. 63. arXiv: 1106.5490 [astro-ph.CO] (cit. on pp. 18, 19).

Bezanson, R., P. van Dokkum, J. van de Sande, M. Franx, & M. Kriek (Feb. 2013a). “Massive and Newly Dead: Discovery of a Significant Population of Galaxies with High-velocity Dispersions and Strong Balmer Lines at z ˜ 1.5 from Deep Keck Spectra and HST/WFC3 Imaging”. In: *Astrophysical Journal, Letters* 764, L8, p. L8. arXiv: 1210.7236 (cit. on p. 71).

Bezanson, R., P. G. van Dokkum, J. van de Sande, et al. (Dec. 2013b). “Tight Correlations between Massive Galaxy Structural Properties and Dynamics: The Mass Fundamental Plane was in Place by z ˜ 2”. In: *Astrophysical Journal, Letters* 779, L21, p. L21. arXiv: 1309.6638 (cit. on p. 28).

Cappellari, Michele, Richard M. McDermid, Katherine Alatalo, et al. (2013). “The ATLAS^{3D} project - XX. Mass-size and mass-σ distributions of early-type galaxies: bulge fraction drives kinematics, mass-to-light ratio, molecular gas fraction and stellar initial mass function”. In: *Monthly Notices of the RAS* 432.3, pp. 1862–1893. arXiv: 1208.3523 [astro-ph.CO] (cit. on p. 45).

Conroy, Charlie (Aug. 2013a). “Modeling the Panchromatic Spectral Energy Distributions of Galaxies”. In: *Annual Review of Astron and Astrophys* 51.1, pp. 393–455. arXiv: 1301.7095 [astro-ph.CO] (cit. on p. 65).

– (Aug. 2013b). “Modeling the Panchromatic Spectral Energy Distributions of Galaxies”. In: *Annual Review of Astron and Astrophys* 51.1, pp. 393–455. arXiv: 1301.7095 [astro-ph.CO] (cit. on pp. 88, 119, 174).

Foreman-Mackey, D., D. W. Hogg, D. Lang, & J. Goodman (Mar. 2013). “emcee: The MCMC Hammer”. In: *Publications of the ASP* 125, p. 306. arXiv: 1202.3665 [astro-ph.IM] (cit. on pp. 50, 102).

Hilz, Michael, Thorsten Naab, & J. P. Ostriker (2013). “How do minor mergers promote inside-out growth of ellipticals, transforming the size, density profile and dark matter fraction?” In: *Monthly Notices of the RAS* 429.4, pp. 2924–2933. arXiv: 1206.5004 [astro-ph.GA] (cit. on pp. 23, 28, 71, 84, 104).

Lou, Yin, Rich Caruana, Johannes Gehrke, & Giles Hooker (2013). "Accurate Intelligible Models with Pairwise Interactions". In: *Proceedings of the 19th ACM SIGKDD International Conference on Knowledge Discovery and Data Mining*. KDD '13. Chicago, Illinois, USA: Association for Computing Machinery, 623–631 (cit. on pp. 147, 151, 176).

Moresco, M., L. Pozzetti, A. Cimatti, et al. (Oct. 2013). "Spot the difference. Impact of different selection criteria on observed properties of passive galaxies in zCOSMOS-20k sample". In: *Astronomy and Astrophysics* 558, A61, A61. arXiv: 1305.1308 [astro-ph.CO] (cit. on pp. 14, 61).

Muzzin, A., D. Marchesini, M. Stefanon, et al. (Nov. 2013a). "The Evolution of the Stellar Mass Functions of Star-forming and Quiescent Galaxies to z = 4 from the COSMOS/Ultra-VISTA Survey". In: *Astrophysical Journal* 777, 18, p. 18. arXiv: 1303.4409 (cit. on pp. 31, 39, 62, 81, 82).

Muzzin, Adam, Danilo Marchesini, Mauro Stefanon, et al. (May 2013b). "A Public K_s - selected Catalog in the COSMOS/ULTRAVISTA Field: Photometry, Photometric Redshifts, and Stellar Population Parameters". In: *Astrophysical Journal, Supplement* 206.1, 8, p. 8. arXiv: 1303.4410 [astro-ph.CO] (cit. on p. 81).

Oogi, Taira & Asao Habe (2013). "Dry minor mergers and size evolution of high-z compact massive early-type galaxies". In: *Monthly Notices of the RAS* 428.1, pp. 641–657 (cit. on p. 28).

Smee, Stephen A., James E. Gunn, Alan Uomoto, et al. (Aug. 2013). "The Multi-object, Fiber-fed Spectrographs for the Sloan Digital Sky Survey and the Baryon Oscillation Spectroscopic Survey". In: *Astronomical Journal* 146.2, 32, p. 32. arXiv: 1208.2233 [astro-ph.IM] (cit. on p. 88).

van de Sande, J., M. Kriek, M. Franx, et al. (July 2013). "Stellar Kinematics of z ˜ 2 Galaxies and the Inside-out Growth of Quiescent Galaxies". In: *Astrophysical Journal* 771, 85, p. 85. arXiv: 1211.3424 (cit. on pp. 28, 43, 71, 84, 172).

Willett, Kyle W., Chris J. Lintott, Steven P. Bamford, et al. (Nov. 2013). "Galaxy Zoo 2: detailed morphological classifications for 304 122 galaxies from the Sloan Digital Sky Survey". In: *Monthly Notices of the RAS* 435.4, pp. 2835–2860. arXiv: 1308.3496 [astro-ph.CO] (cit. on pp. 96, 97, 117).

Wojtak, Radosław & Gary A. Mamon (Jan. 2013). "Physical properties underlying observed kinematics of satellite galaxies". In: *Monthly Notices of the RAS* 428.3, pp. 2407–2417. arXiv: 1207.1647 [astro-ph.CO] (cit. on p. 144).

Belli, S., A. B. Newman, & R. S. Ellis (Mar. 2014a). "Velocity Dispersions and Dynamical Masses for a Large Sample of Quiescent Galaxies at z > 1: Improved Measures of the Growth in Mass and Size". In: *Astrophysical Journal* 783, 117, p. 117. arXiv: 1311.3317 (cit. on pp. 28, 43, 66–69, 71, 81, 84, 172).

Belli, Sirio, Andrew B. Newman, Richard S. Ellis, & Nick P. Konidaris (2014b). "MOSFIRE Absorption Line Spectroscopy of z > 2 Quiescent Galaxies: Probing a Period of Rapid Size Growth". In: *Astrophysical Journal* 788, L29, p. L29. arXiv: 1404.4872 [astro-ph.GA] (cit. on p. 61).

Buchner, J., A. Georgakakis, K. Nandra, et al. (2014). “X-ray spectral modelling of the AGN obscuring region in the CDFS: Bayesian model selection and catalogue”. In: *Astronomy and Astrophysics* 564, A125, A125. arXiv: 1402.0004 [astro-ph.HE] (cit. on p. 52).

Conroy, Charlie, Genevieve J. Graves, & Pieter G. van Dokkum (Jan. 2014). “Early-type Galaxy Archeology: Ages, Abundance Ratios, and Effective Temperatures from Full-spectrum Fitting”. In: *Astrophysical Journal* 780.1, 33, p. 33. arXiv: 1303.6629 [astro-ph.CO] (cit. on p. 11).

Genel, S., M. Vogelsberger, V. Springel, et al. (Nov. 2014). “Introducing the Illustris project: the evolution of galaxy populations across cosmic time”. In: *Monthly Notices of the RAS* 445, pp. 175–200. arXiv: 1405.3749 (cit. on pp. 84, 90).

Ma, Chung-Pei, Jenny E. Greene, Nicholas McConnell, et al. (Nov. 2014). “The MASSIVE Survey. I. A Volume-limited Integral-field Spectroscopic Study of the Most Massive Early-type Galaxies within 108 Mpc”. In: *Astrophysical Journal* 795.2, 158, p. 158. arXiv: 1407.1054 [astro-ph.GA] (cit. on p. 85).

Madau, Piero & Mark Dickinson (Aug. 2014). “Cosmic Star-Formation History”. In: *Annual Review of Astron and Astrophys* 52, pp. 415–486. arXiv: 1403.0007 [astro-ph.CO] (cit. on p. 164).

McIntosh, Daniel H., Cory Wagner, Andrew Cooper, et al. (July 2014). “A new population of recently quenched elliptical galaxies in the SDSS”. In: *Monthly Notices of the RAS* 442.1, pp. 533–557. arXiv: 1308.0054 [astro-ph.GA] (cit. on p. 8).

Mendel, J. T., L. Simard, M. Palmer, S. L. Ellison, & D. R. Patton (Jan. 2014). “A Catalog of Bulge, Disk, and Total Stellar Mass Estimates for the Sloan Digital Sky Survey”. In: *Astrophysical Journal, Supplement* 210, 3, p. 3. arXiv: 1310.8304 (cit. on pp. 38, 94, 100).

Pillepich, Annalisa, Mark Vogelsberger, Alis Deason, et al. (Oct. 2014). “Halo mass and assembly history exposed in the faint outskirts: the stellar and dark matter haloes of Illustris galaxies”. In: *Monthly Notices of the RAS* 444.1, pp. 237–249. arXiv: 1406.1174 [astro-ph.GA] (cit. on p. 92).

Posti, L., C. Nipoti, M. Stiavelli, & L. Ciotti (May 2014). “The imprint of dark matter haloes on the size and velocity dispersion evolution of early-type galaxies”. In: *Monthly Notices of the RAS* 440, pp. 610–623. arXiv: 1310.2255 (cit. on pp. 28, 29).

Schawinski, Kevin, C. Megan Urry, Brooke D. Simmons, et al. (May 2014). “The green valley is a red herring: Galaxy Zoo reveals two evolutionary pathways towards quenching of star formation in early- and late-type galaxies”. In: *Monthly Notices of the RAS* 440.1, pp. 889–907. arXiv: 1402.4814 [astro-ph.GA] (cit. on pp. 8, 9).

van der Wel, A., M. Franx, P. G. van Dokkum, et al. (2014). “3D-HST+CANDELS: The Evolution of the Galaxy Size-Mass Distribution since z = 3”. In: *Astrophysical Journal* 788.1, 28, p. 28. arXiv: 1404.2844 [astro-ph.GA] (cit. on pp. 18, 29, 70, 84, 172).

Vogelsberger, M., S. Genel, V. Springel, et al. (Oct. 2014a). “Introducing the Illustris Project: simulating the coevolution of dark and visible matter in the Universe”. In: *Monthly Notices of the RAS* 444, pp. 1518–1547. arXiv: 1405.2921 (cit. on pp. 84, 90).

Vogelsberger, M., S. Genel, V. Springel, et al. (May 2014b). “Properties of galaxies reproduced by a hydrodynamic simulation”. In: *Nature* 509, pp. 177–182. arXiv: 1405.1418 (cit. on pp. 84, 90).

Alam, Shadab, Franco D. Albareti, Carlos Allende Prieto, et al. (2015). “The Eleventh and Twelfth Data Releases of the Sloan Digital Sky Survey: Final Data from SDSS-III”. In: *Astrophysical Journal, Supplement* 219.1, 12, p. 12. arXiv: 1501.00963 [astro-ph.IM] (cit. on pp. 31, 92, 172).

Bezanson, R., M. Franx, & P. G. van Dokkum (Feb. 2015). “One Plane for All: Massive Star-forming and Quiescent Galaxies Lie on the Same Mass Fundamental Plane at z ˜ 0 and z ˜ 0.7”. In: *Astrophysical Journal* 799, 148, p. 148. arXiv: 1410.5818 (cit. on p. 28).

Bryant, J. J., M. S. Owers, A. S. G. Robotham, et al. (Mar. 2015). “The SAMI Galaxy Survey: instrument specification and target selection”. In: *Monthly Notices of the RAS* 447.3, pp. 2857–2879. arXiv: 1407.7335 [astro-ph.GA] (cit. on p. 85).

Bundy, Kevin, Matthew A. Bershady, David R. Law, et al. (Jan. 2015). “Overview of the SDSS-IV MaNGA Survey: Mapping nearby Galaxies at Apache Point Observatory”. In: *Astrophysical Journal* 798.1, 7, p. 7. arXiv: 1412.1482 [astro-ph.GA] (cit. on pp. 13, 85, 87, 174).

Caruana, Rich, Yin Lou, Johannes Gehrke, et al. (2015). “Intelligible models for healthcare: Predicting pneumonia risk and hospital 30-day readmission”. In: *Proceedings of the 21th ACM SIGKDD International Conference on Knowledge Discovery and Data Mining*. ACM, pp. 1721–1730 (cit. on pp. 149, 151, 176).

Contreras, S., C. M. Baugh, P. Norberg, & N. Padilla (Sept. 2015). “The galaxy-dark matter halo connection: which galaxy properties are correlated with the host halo mass?” In: *Monthly Notices of the RAS* 452.2, pp. 1861–1876. arXiv: 1502.06614 [astro-ph.GA] (cit. on p. 159).

Drory, N., N. MacDonald, M. A. Bershady, et al. (Feb. 2015). “The MaNGA Integral Field Unit Fiber Feed System for the Sloan 2.5 m Telescope”. In: *Astronomical Journal* 149.2, 77, p. 77. arXiv: 1412.1535 [astro-ph.IM] (cit. on p. 88).

Gargiulo, A., P. Saracco, M. Longhetti, et al. (Jan. 2015). “Lower mass normalization of the stellar initial mass function for dense massive early-type galaxies at z ˜ 1.4”. In: *Astronomy and Astrophysics* 573, A110, A110. arXiv: 1410.5229 (cit. on p. 43).

González Delgado, R. M., R. García-Benito, E. Pérez, et al. (Sept. 2015). “The CALIFA survey across the Hubble sequence. Spatially resolved stellar population properties in galaxies”. In: *Astronomy and Astrophysics* 581, A103, A103. arXiv: 1506.04157 [astro-ph.GA] (cit. on p. 11).

Greene, Jenny E., Ryan Janish, Chung-Pei Ma, et al. (July 2015). “The MASSIVE Survey. II. Stellar Population Trends Out to Large Radius in Massive Early-type Galaxies”. In: *Astrophysical Journal* 807.1, 11, p. 11. arXiv: 1504.02483 [astro-ph.GA] (cit. on p. 86).

Hirschmann, Michaela, Thorsten Naab, Jeremiah P. Ostriker, et al. (May 2015). “The stellar accretion origin of stellar population gradients in massive galaxies at large radii”. In: *Monthly Notices of the RAS* 449.1, pp. 528–550. arXiv: 1410.2244 [astro-ph.GA] (cit. on p. 85).

Law, David R., Renbin Yan, Matthew A. Bershady, et al. (July 2015). “Observing Strategy for the SDSS-IV/MaNGA IFU Galaxy Survey”. In: *Astronomical Journal* 150.1, 19, p. 19. arXiv: 1505.04285 [astro-ph.IM] (cit. on p. 88).

Mason, C. A., T. Treu, K. B. Schmidt, et al. (May 2015). “Correcting the z $\sim$ 8 Galaxy Luminosity Function for Gravitational Lensing Magnification Bias”. In: *Astrophysical Journal* 805, 79, p. 79. arXiv: 1502.03795 (cit. on pp. 66–70).

Meert, A., V. Vikram, & M. Bernardi (Feb. 2015). “A catalogue of 2D photometric decompositions in the SDSS-DR7 spectroscopic main galaxy sample: preferred models and systematics”. In: *Monthly Notices of the RAS* 446, pp. 3943–3974. arXiv: 1406.4179 (cit. on pp. 74, 94, 100, 121, 127, 174).

Peng, Y., R. Maiolino, & R. Cochrane (May 2015). “Strangulation as the primary mechanism for shutting down star formation in galaxies”. In: *Nature* 521.7551, pp. 192–195. arXiv: 1505.03143 [astro-ph.GA] (cit. on p. 11).

Reines, Amy E. & Marta Volonteri (Nov. 2015). “Relations between Central Black Hole Mass and Total Galaxy Stellar Mass in the Local Universe”. In: *Astrophysical Journal* 813.2, 82, p. 82. arXiv: 1508.06274 [astro-ph.GA] (cit. on pp. 144, 176).

Rodriguez-Gomez, Vicente, Shy Genel, Mark Vogelsberger, et al. (May 2015). “The merger rate of galaxies in the Illustris simulation: a comparison with observations and semi-empirical models”. In: *Monthly Notices of the RAS* 449.1, pp. 49–64. arXiv: 1502.01339 [astro-ph.GA] (cit. on pp. 92, 108).

Sijacki, D., M. Vogelsberger, S. Genel, et al. (Sept. 2015). “The Illustris simulation: the evolving population of black holes across cosmic time”. In: *Monthly Notices of the RAS* 452, pp. 575–596. arXiv: 1408.6842 (cit. on pp. 84, 90).

Somerville, Rachel S. & Romeel Davé (2015). “Physical Models of Galaxy Formation in a Cosmological Framework”. In: *Annual Review of Astron and Astrophys* 53, pp. 51–113. arXiv: 1412.2712 [astro-ph.GA] (cit. on p. 27).

Spergel, D., N. Gehrels, C. Baltay, et al. (Mar. 2015). “Wide-Field InfrarRed Survey Telescope-Astrophysics Focused Telescope Assets WFIRST-AFTA 2015 Report”. In: *arXiv e-prints*, arXiv:1503.03757, arXiv:1503.03757. arXiv: 1503.03757 [astro-ph.IM] (cit. on p. 141).

Cappellari, Michele (Sept. 2016). “Structure and Kinematics of Early-Type Galaxies from Integral Field Spectroscopy”. In: *Annual Review of Astron and Astrophys* 54, pp. 597–665. arXiv: 1602.04267 [astro-ph.GA] (cit. on pp. 13, 23, 117).

Choi, Jieun, Aaron Dotter, Charlie Conroy, et al. (June 2016). “Mesa Isochrones and Stellar Tracks (MIST). I. Solar-scaled Models”. In: *Astrophysical Journal* 823.2, 102, p. 102. arXiv: 1604.08592 [astro-ph.SR] (cit. on p. 89).

Cook, B. A., C. Conroy, A. Pillepich, V. Rodriguez-Gomez, & L. Hernquist (Dec. 2016). “The Information Content of Stellar Halos: Stellar Population Gradients and Accretion Histories in Early-type Illustris Galaxies”. In: *Astrophysical Journal* 833.2, 158, p. 158. arXiv: 1610.00014 [astro-ph.GA] (cit. on p. 85).

Dotter, Aaron (Jan. 2016). “MESA Isochrones and Stellar Tracks (MIST) 0: Methods for the Construction of Stellar Isochrones”. In: *Astrophysical Journal, Supplement* 222.1, 8, p. 8. arXiv: 1601.05144 [astro-ph.SR] (cit. on p. 89).

Gaia Collaboration, T. Prusti, J. H. J. de Bruijne, et al. (Nov. 2016). “The Gaia mission”. In: *Astronomy and Astrophysics* 595, A1, A1. arXiv: 1609.04153 [astro-ph.IM] (cit. on p. 142).

Gargiulo, A., P. Saracco, S. Tamburri, I. Lonoce, & F. Ciocca (2016). “Ultramassive dense early-type galaxies: Velocity dispersions and number density evolution since z = 1.6”. In: *Astronomy and Astrophysics* 592, A132, A132. arXiv: 1605.03014 [astro-ph.GA] (cit. on pp. 28, 84, 172).

Law, David R., Brian Cherinka, Renbin Yan, et al. (Oct. 2016). “The Data Reduction Pipeline for the SDSS-IV MaNGA IFU Galaxy Survey”. In: *Astronomical Journal* 152.4, 83, p. 83. arXiv: 1607.08619 [astro-ph.IM] (cit. on p. 88).

Mandelbaum, Rachel, Wenting Wang, Ying Zu, et al. (Apr. 2016). “Strong bimodality in the host halo mass of central galaxies from galaxy-galaxy lensing”. In: *Monthly Notices of the RAS* 457.3, pp. 3200–3218. arXiv: 1509.06762 [astro-ph.GA] (cit. on p. 144).

Planck Collaboration, P. A. R. Ade, N. Aghanim, et al. (Sept. 2016). “Planck 2015 results. XIII. Cosmological parameters”. In: *Astronomy and Astrophysics* 594, A13, A13. arXiv: 1502.01589 [astro-ph.CO] (cit. on pp. 87, 91, 145).

Rodriguez-Gomez, Vicente, Annalisa Pillepich, Laura V. Sales, et al. (May 2016). “The stellar mass assembly of galaxies in the Illustris simulation: growth by mergers and the spatial distribution of accreted stars”. In: *Monthly Notices of the RAS* 458.3, pp. 2371–2390. arXiv: 1511.08804 [astro-ph.GA] (cit. on pp. 84, 91, 92, 108).

Sánchez, S. F., R. García-Benito, S. Zibetti, et al. (Oct. 2016). “CALIFA, the Calar Alto Legacy Integral Field Area survey. IV. Third public data release”. In: *Astronomy and Astrophysics* 594, A36, A36. arXiv: 1604.02289 [astro-ph.GA] (cit. on p. 85).

van der Wel, A., K. Noeske, R. Bezanson, et al. (Apr. 2016). “The VLT LEGA-C Spectroscopic Survey: The Physics of Galaxies at a Lookback Time of 7 Gyr”. In: *Astrophysical Journal, Supplement* 223, 29, p. 29. arXiv: 1603.05479 (cit. on pp. 30, 172).

Yan, Renbin, Kevin Bundy, David R. Law, et al. (Dec. 2016a). “SDSS-IV MaNGA IFS Galaxy Survey—Survey Design, Execution, and Initial Data Quality”. In: *Astronomical Journal* 152.6, 197, p. 197. arXiv: 1607.08613 [astro-ph.GA] (cit. on pp. 87, 174).

Yan, Renbin, Christy Tremonti, Matthew A. Bershady, et al. (Jan. 2016b). “SDSS-IV/MaNGA: Spectrophotometric Calibration Technique”. In: *Astronomical Journal* 151.1, 8, p. 8. arXiv: 1511.01496 [astro-ph.IM] (cit. on p. 88).

Zahid, H. J., M. J. Geller, D. G. Fabricant, & H. S. Hwang (Dec. 2016a). “The Scaling of Stellar Mass and Central Stellar Velocity Dispersion for Quiescent Galaxies at z<0.7”. In: *Astrophysical Journal* 832, 203, p. 203. arXiv: 1607.04275 (cit. on pp. 27, 66–69).

Zahid, H. Jabran, Ivana Damjanov, Margaret J. Geller, Ho Seong Hwang, & Daniel G. Fabricant (2016b). “The Stellar Mass Fundamental Plane and Compact Quiescent Galaxies at z < 0.6”. In: *Astrophysical Journal* 821.2, 101, p. 101. arXiv: 1510.04703 [astro-ph.GA] (cit. on pp. 28, 71).

Belli, S., A. B. Newman, & R. S. Ellis (Jan. 2017). “MOSFIRE Spectroscopy of Quiescent Galaxies at $1.5 < z < 2.5$. I. Evolution of Structural and Dynamical Properties”. In: *Astrophysical Journal* 834, 18, p. 18. arXiv: 1608.00608 (cit. on pp. 28, 43, 61, 84, 172).

Bernardi, M., A. Meert, R. K. Sheth, et al. (May 2017). “The high mass end of the stellar mass function: Dependence on stellar population models and agreement between fits to the light profile”. In: *Monthly Notices of the RAS* 467.2, pp. 2217–2233. arXiv: 1604.01036 [astro-ph.GA] (cit. on pp. 100, 175).

Blanton, Michael R., Matthew A. Bershady, Bela Abolfathi, et al. (July 2017). “Sloan Digital Sky Survey IV: Mapping the Milky Way, Nearby Galaxies, and the Distant Universe”. In: *Astronomical Journal* 154.1, 28, p. 28. arXiv: 1703.00052 [astro-ph.GA] (cit. on p. 87).

Cappellari, Michele (Apr. 2017). “Improving the full spectrum fitting method: accurate convolution with Gauss-Hermite functions”. In: *Monthly Notices of the RAS* 466.1, pp. 798–811. arXiv: 1607.08538 [astro-ph.GA] (cit. on pp. 88, 89, 174).

Comparat, Johan, Claudia Maraston, Daniel Goddard, et al. (Nov. 2017). “Stellar population properties for 2 million galaxies from SDSS DR14 and DEEP2 DR4 from full spectral fitting”. In: *arXiv e-prints*, arXiv:1711.06575, arXiv:1711.06575. arXiv: 1711.06575 [astro-ph.GA] (cit. on pp. 88, 174).

Frigo, M. & M. Balcells (2017). “Dynamical masses and non-homology of massive elliptical galaxies grown by dry mergers”. In: *Monthly Notices of the RAS* 469.2, pp. 2184–2201. arXiv: 1611.01662 [astro-ph.GA] (cit. on pp. 28, 71).

Goddard, D., D. Thomas, C. Maraston, et al. (Apr. 2017a). “SDSS-IV MaNGA: Spatially resolved star formation histories in galaxies as a function of galaxy mass and type”. In: *Monthly Notices of the RAS* 466.4, pp. 4731–4758. arXiv: 1612.01546 [astro-ph.GA] (cit. on pp. 88, 174).

Goddard, D., D. Thomas, C. Maraston, et al. (Feb. 2017b). “SDSS-IV MaNGA: stellar population gradients as a function of galaxy environment”. In: *Monthly Notices of the RAS* 465.1, pp. 688–700. arXiv: 1612.01545 [astro-ph.GA] (cit. on pp. 86, 89).

Guo, Hong, Cheng Li, Zheng Zheng, et al. (Sept. 2017). “Constraining the H I-Halo Mass Relation from Galaxy Clustering”. In: *Astrophysical Journal* 846.1, 61, p. 61. arXiv: 1707.01999 [astro-ph.GA] (cit. on pp. 144, 159).

Leja, J., B. D. Johnson, C. Conroy, P. G. van Dokkum, & N. Byler (2017). “Deriving Physical Properties from Broadband Photometry with Prospector: Description of the Model and a Demonstration of its Accuracy Using 129 Galaxies in the Local Universe”. In: *Astrophysical Journal* 837, p. 170. eprint: 1609.09073 (cit. on pp. 88, 174).

Naab, Thorsten & Jeremiah P. Ostriker (2017). “Theoretical Challenges in Galaxy Formation”. In: *Annual Review of Astron and Astrophys* 55.1, pp. 59–109. arXiv: 1612.06891 [astro-ph.GA] (cit. on p. 27).

Taylor, Philip & Chiaki Kobayashi (Nov. 2017). “The metallicity and elemental abundance gradients of simulated galaxies and their environmental dependence”. In: *Monthly Notices of the RAS* 471.4, pp. 3856–3870. arXiv: 1707.06488 [astro-ph.GA] (cit. on p. 85).

Tinker, Jeremy L., Joel R. Brownstein, Hong Guo, et al. (Apr. 2017). “The Correlation between Halo Mass and Stellar Mass for the Most Massive Galaxies in the Universe”. In: *Astrophysical Journal* 839.2, 121, p. 121. arXiv: 1607.04678 [astro-ph.GA] (cit. on pp. 144, 176).

Weinberger, Rainer, Volker Springel, Lars Hernquist, et al. (Mar. 2017). “Simulating galaxy formation with black hole driven thermal and kinetic feedback”. In: *Monthly Notices of the RAS* 465.3, pp. 3291–3308. arXiv: 1607.03486 [astro-ph.GA] (cit. on p. 90).

Wilkinson, David M., Claudia Maraston, Daniel Goddard, Daniel Thomas, & Taniya Parikh (Dec. 2017). “FIREFLY (Fitting IteRativEly For Likelihood analYsis): a full spectral fitting code”. In: *Monthly Notices of the RAS* 472.4, pp. 4297–4326. arXiv: 1711.00865 [astro-ph.GA] (cit. on pp. 88, 89, 174).

Zahid, H. Jabran & Margaret J. Geller (May 2017). “Velocity Dispersion, Size, Sérsic Index, and D $_n$4000: The Scaling of Stellar Mass with Dynamical Mass for Quiescent Galaxies”. In: *Astrophysical Journal* 841.1, 32, p. 32. arXiv: 1701.01350 [astro-ph.GA] (cit. on p. 43).

Zahid, H. Jabran, Rolf-Peter Kudritzki, Charlie Conroy, Brett Andrews, & I. Ting Ho (Sept. 2017). “Stellar Absorption Line Analysis of Local Star-forming Galaxies: The Relation between Stellar Mass, Metallicity, Dust Attenuation, and Star Formation Rate”. In: *Astrophysical Journal* 847.1, 18, p. 18. arXiv: 1708.07107 [astro-ph.GA] (cit. on p. 11).

Zheng, Zheng, Huiyuan Wang, Junqiang Ge, et al. (Mar. 2017). “SDSS-IV MaNGA: environmental dependence of stellar age and metallicity gradients in nearby galaxies”. In: *Monthly Notices of the RAS* 465.4, pp. 4572–4588. arXiv: 1612.01523 [astro-ph.GA] (cit. on p. 86).

Abbott, T. M. C., F. B. Abdalla, A. Alarcon, et al. (Aug. 2018). “Dark Energy Survey year 1 results: Cosmological constraints from galaxy clustering and weak lensing”. In: *Physical Review D* 98.4, 043526, p. 043526. arXiv: 1708.01530 [astro-ph.CO] (cit. on p. 142).

Agarwal, Shankar, Romeel Davé, & Bruce A. Bassett (Aug. 2018). “Painting galaxies into dark matter haloes using machine learning”. In: *Monthly Notices of the RAS* 478.3, pp. 3410–3422. arXiv: 1712.03255 [astro-ph.GA] (cit. on p. 143).

Aihara, H., R. Armstrong, S. Bickerton, et al. (Jan. 2018). “First data release of the Hyper Suprime-Cam Subaru Strategic Program”. In: *Publications of the ASJ* 70, S8, S8. arXiv: 1702.08449 [astro-ph.IM] (cit. on pp. 30, 37, 94).

Bernardi, M., R. K. Sheth, H. Dominguez-Sanchez, et al. (June 2018). “M_*/L gradients driven by IMF variation: large impact on dynamical stellar mass estimates”. In: *Monthly Notices of the RAS* 477.2, pp. 2560–2571. arXiv: 1712.05414 [astro-ph.GA] (cit. on p. 65).

Damjanov, Ivana, H. Jabran Zahid, Margaret J. Geller, Daniel G. Fabricant, & Ho Seong Hwang (Feb. 2018). “hCOSMOS: A Dense Spectroscopic Survey of r $\leq$ 21.3 Galaxies in the COSMOS field”. In: *Astrophysical Journal, Supplement* 234.2, 21, p. 21. arXiv: 1710.01733 [astro-ph.GA] (cit. on pp. 66–69).

Domínguez Sánchez, H., M. Huertas-Company, M. Bernardi, D. Tuccillo, & J. L. Fischer (May 2018). “Improving galaxy morphologies for SDSS with Deep Learning”. In: *Monthly Notices of the RAS* 476.3, pp. 3661–3676. arXiv: 1711.05744 [astro-ph.GA] (cit. on p. 31).

Huang, Song, Alexie Leauthaud, Jenny E. Greene, et al. (Apr. 2018). “Individual stellar haloes of massive galaxies measured to 100 kpc at 0.3 < z < 0.5 using Hyper Suprime-Cam”. In: *Monthly Notices of the RAS* 475.3, pp. 3348–3368. arXiv: 1707.01904 [astro-ph.GA] (cit. on pp. 33, 99, 174).

Kravtsov, A. V., A. A. Vikhlinin, & A. V. Meshcheryakov (Jan. 2018). “Stellar Mass—Halo Mass Relation and Star Formation Efficiency in High-Mass Halos”. In: *Astronomy Letters* 44.1, pp. 8–34. arXiv: 1401.7329 [astro-ph.CO] (cit. on p. 144).

Li, Hongyu, Shude Mao, Michele Cappellari, et al. (May 2018). “SDSS-IV MaNGA: global stellar population and gradients for about 2000 early-type and spiral galaxies on the mass-size plane”. In: *Monthly Notices of the RAS* 476.2, pp. 1765–1775. arXiv: 1802.01819 [astro-ph.GA] (cit. on pp. 13, 65, 85, 86).

Lovell, Mark R., Annalisa Pillepich, Shy Genel, et al. (Dec. 2018). “The fraction of dark matter within galaxies from the IllustrisTNG simulations”. In: *Monthly Notices of the RAS* 481.2, pp. 1950–1975. arXiv: 1801.10170 [astro-ph.GA] (cit. on p. 116).

Marinacci, Federico, Mark Vogelsberger, Rüdiger Pakmor, et al. (Nov. 2018). “First results from the IllustrisTNG simulations: radio haloes and magnetic fields”. In: *Monthly Notices of the RAS* 480.4, pp. 5113–5139. arXiv: 1707.03396 [astro-ph.CO] (cit. on pp. 90, 174).

Miyazaki, Satoshi, Yutaka Komiyama, Satoshi Kawanomoto, et al. (2018). “Hyper Suprime-Cam: System design and verification of image quality”. In: *Publications of the ASJ* 70, S1, S1 (cit. on pp. 30, 94).

Naiman, Jill P., Annalisa Pillepich, Volker Springel, et al. (June 2018). “First results from the IllustrisTNG simulations: a tale of two elements - chemical evolution of magnesium and europium”. In: *Monthly Notices of the RAS* 477.1, pp. 1206–1224. arXiv: 1707.03401 [astro-ph.GA] (cit. on pp. 90, 174).

Nelson, Dylan, Annalisa Pillepich, Volker Springel, et al. (Mar. 2018). “First results from the IllustrisTNG simulations: the galaxy colour bimodality”. In: *Monthly Notices of the RAS* 475.1, pp. 624–647. arXiv: 1707.03395 [astro-ph.GA] (cit. on pp. 90, 92, 93, 174).

Obreja, Aura, Andrea V. Macciò, Benjamin Moster, et al. (July 2018). “Introducing galactic structure finder: the multiple stellar kinematic structures of a simulated Milky Way mass galaxy”. In: *Monthly Notices of the RAS* 477.4, pp. 4915–4930. arXiv: 1804.05576 [astro-ph.GA] (cit. on p. 143).

Parikh, Taniya, Daniel Thomas, Claudia Maraston, et al. (July 2018). “SDSS-IV MaNGA: the spatially resolved stellar initial mass function in ∼400 early-type galaxies”. In: *Monthly Notices of the RAS* 477.3, pp. 3954–3982. arXiv: 1803.08515 [astro-ph.GA] (cit. on p. 117).

Pillepich, Annalisa, Dylan Nelson, Lars Hernquist, et al. (Mar. 2018a). “First results from the IllustrisTNG simulations: the stellar mass content of groups and clusters of galaxies”. In: *Monthly Notices of the RAS* 475.1, pp. 648–675. arXiv: 1707.03406 [astro-ph.GA] (cit. on pp. 90–92, 104, 119, 159, 174, 175).

Pillepich, Annalisa, Volker Springel, Dylan Nelson, et al. (Jan. 2018b). “Simulating galaxy formation with the IllustrisTNG model”. In: *Monthly Notices of the RAS* 473.3, pp. 4077–4106. arXiv: 1703.02970 [astro-ph.GA] (cit. on p. 90).

Sonnenfeld, Alessandro, Alexie Leauthaud, Matthew W. Auger, et al. (Nov. 2018). “Evidence for radial variations in the stellar mass-to-light ratio of massive galaxies from weak and strong lensing”. In: *Monthly Notices of the RAS* 481.1, pp. 164–184. arXiv: 1801.01883 [astro-ph.GA] (cit. on p. 65).

Springel, Volker, Rüdiger Pakmor, Annalisa Pillepich, et al. (Mar. 2018). “First results from the IllustrisTNG simulations: matter and galaxy clustering”. In: *Monthly Notices of the RAS* 475.1, pp. 676–698. arXiv: 1707.03397 [astro-ph.GA] (cit. on pp. 90, 174).

Straatman, C. M. S., A. van der Wel, R. Bezanson, et al. (Dec. 2018). “The Large Early Galaxy Astrophysics Census (LEGA-C) Data Release 2: Dynamical and Stellar Population Properties of $z \lesssim 1$ Galaxies in the COSMOS Field”. In: *Astrophysical Journal, Supplement* 239, 27, p. 27. arXiv: 1809.08236 (cit. on pp. 31, 39, 47).

Sullivan, David, Ilian T. Iliev, & Keri L. Dixon (Jan. 2018). “Using artificial neural networks to constrain the halo baryon fraction during reionization”. In: *Monthly Notices of the RAS* 473.1, pp. 38–58. arXiv: 1707.01427 [astro-ph.GA] (cit. on p. 143).

Tan, Sarah, Rich Caruana, Giles Hooker, & Yin Lou (2018). “Distill-and-compare: auditing black-box models using transparent model distillation”. In: *Proceedings of the 2018 AAAI/ACM Conference on AI, Ethics, and Society*. ACM, pp. 303–310 (cit. on p. 151).

Troxel, M. A., N. MacCrann, J. Zuntz, et al. (Aug. 2018). “Dark Energy Survey Year 1 results: Cosmological constraints from cosmic shear”. In: *Physical Review D* 98.4, 043528, p. 043528. arXiv: 1708.01538 [astro-ph.CO] (cit. on p. 142).

Wechsler, Risa H. & Jeremy L. Tinker (Sept. 2018). “The Connection Between Galaxies and Their Dark Matter Halos”. In: *Annual Review of Astron and Astrophys* 56, pp. 435–487. arXiv: 1804.03097 [astro-ph.GA] (cit. on pp. 144, 158, 176).

Zhang, Hong-Xin, Thomas H. Puzia, Eric W. Peng, et al. (May 2018). “Stellar Population Properties of Ultracompact Dwarfs in M87: A Mass-Metallicity Correlation Connecting Low-metallicity Globular Clusters and Compact Ellipticals”. In: *Astrophysical Journal* 858.1, 37, p. 37. arXiv: 1803.07577 [astro-ph.GA] (cit. on p. 11).

Aguado, D. S., Romina Ahumada, Andrés Almeida, et al. (Feb. 2019). “The Fifteenth Data Release of the Sloan Digital Sky Surveys: First Release of MaNGA-derived Quantities, Data Visualization Tools, and Stellar Library”. In: *Astrophysical Journal, Supplement* 240.2, 23, p. 23. arXiv: 1812.02759 [astro-ph.IM] (cit. on p. 88).

Aihara, Hiroaki, Yusra AlSayyad, Makoto Ando, et al. (Dec. 2019). “Second data release of the Hyper Suprime-Cam Subaru Strategic Program”. In: *Publications of the ASJ* 71.6, 114, p. 114. arXiv: 1905.12221 [astro-ph.IM] (cit. on p. 37).

Baron, Dalya (Apr. 2019). “Machine Learning in Astronomy: a practical overview”. In: *arXiv e-prints*, arXiv:1904.07248, arXiv:1904.07248. arXiv: 1904.07248 [astro-ph.IM] (cit. on p. 143).

Behroozi, Peter, Risa H. Wechsler, Andrew P. Hearin, & Charlie Conroy (Sept. 2019). “UNIVERSEMACHINE: The correlation between galaxy growth and dark matter halo assembly from z = 0-10”. In: *Monthly Notices of the RAS* 488.3, pp. 3143–3194. arXiv: 1806.07893 [astro-ph.GA] (cit. on pp. 144, 176).

Bernardi, M., H. Domínguez Sánchez, J. R. Brownstein, N. Drory, & R. K. Sheth (Nov. 2019). “Galaxy properties as revealed by MaNGA - II. Differences in stellar populations of slow and fast rotator ellipticals and dependence on environment”. In: *Monthly Notices of the RAS* 489.4, pp. 5633–5652. arXiv: 1904.11996 [astro-ph.GA] (cit. on p. 117).

Carrasco-Davis, Rodrigo, Guillermo Cabrera-Vives, Francisco Förster, et al. (Oct. 2019). “Deep Learning for Image Sequence Classification of Astronomical Events”. In: *Publications of the ASP* 131.1004, p. 108006. arXiv: 1807.03869 [astro-ph.IM] (cit. on p. 143).

Chattopadhyay, Tanuka, Didier Fraix-Burnet, & Saptarshi Mondal (Oct. 2019). “Unsupervised Classification of Galaxies. I. Independent Component Analysis Feature Selection”. In: *Publications of the ASP* 131.1004, p. 108010. arXiv: 1802.02856 [astro-ph.CO] (cit. on p. 143).

Cimatti, Andrea, Filippo Fraternali, & Carlo Nipoti (2019). *Introduction to galaxy formation and evolution. From primordial gas to present-day galaxies*. Cambridge University Press (cit. on pp. 4, 6, 10, 17, 23, 70, 81).

Damjanov, Ivana, H. Jabran Zahid, Margaret J. Geller, et al. (2019). “Quiescent Galaxy Size and Spectroscopic Evolution: Combining HSC Imaging and Hectospec Spectroscopy”. In: *Astrophysical Journal* 872.1, 91, p. 91. arXiv: 1809.10705 [astro-ph.GA] (cit. on pp. 18, 28, 84, 172).

Decroos, Tom & J. Davis (2019). “Interpretable Prediction of Goals in Soccer”. In: (cit. on p. 151).

Domínguez Sánchez, H., M. Bernardi, J. R. Brownstein, N. Drory, & R. K. Sheth (Nov. 2019). “Galaxy properties as revealed by MaNGA - I. Constraints on IMF and M_*/L gradients in ellipticals”. In: *Monthly Notices of the RAS* 489.4, pp. 5612–5632. arXiv: 1904.11992 [astro-ph.GA] (cit. on p. 65).

Donnari, Martina, Annalisa Pillepich, Dylan Nelson, et al. (June 2019). “The star formation activity of IllustrisTNG galaxies: main sequence, UVJ diagram, quenched fractions, and systematics”. In: *Monthly Notices of the RAS* 485.4, pp. 4817–4840. arXiv: 1812.07584 [astro-ph.GA] (cit. on pp. 94, 127, 174).

Fischer, J. L., H. Domínguez Sánchez, & M. Bernardi (Feb. 2019). “SDSS-IV MaNGA PyMorph Photometric and Deep Learning Morphological Catalogues and implications for bulge properties and stellar angular momentum”. In: *Monthly Notices of the RAS* 483.2, pp. 2057–2077. arXiv: 1811.02580 [astro-ph.GA] (cit. on pp. 96, 121).

Greene, Jenny E., Melanie Veale, Chung-Pei Ma, et al. (Mar. 2019). "The MASSIVE Survey. XII. Connecting Stellar Populations of Early-type Galaxies to Kinematics and Environment". In: *Astrophysical Journal* 874.1, 66, p. 66. arXiv: 1901.01271 [astro-ph.GA] (cit. on p. 86).

Ivezić, Željko, Steven M. Kahn, J. Anthony Tyson, et al. (Mar. 2019). "LSST: From Science Drivers to Reference Design and Anticipated Data Products". In: *Astrophysical Journal* 873.2, 111, p. 111. arXiv: 0805.2366 [astro-ph] (cit. on p. 141).

Johnson, Benjamin D., Joel L. Leja, Charlie Conroy, & Joshua S. Speagle (May 2019). *Prospector: Stellar population inference from spectra and SEDs*. ascl: 1905.025 (cit. on pp. 88, 174).

Lange, Johannes U., Frank C. van den Bosch, Andrew R. Zentner, Kuan Wang, & Antonio S. Villarreal (Aug. 2019). "Updated results on the galaxy-halo connection from satellite kinematics in SDSS". In: *Monthly Notices of the RAS* 487.3, pp. 3112–3129. arXiv: 1811.03596 [astro-ph.CO] (cit. on p. 144).

Leja, Joel, Adam C. Carnall, Benjamin D. Johnson, Charlie Conroy, & Joshua S. Speagle (May 2019). "How to Measure Galaxy Star Formation Histories. II. Nonparametric Models". In: *Astrophysical Journal* 876.1, 3, p. 3. arXiv: 1811.03637 [astro-ph.GA] (cit. on p. 89).

Lengerich, Benjamin, Sarah Tan, Chun-Hao Chang, Giles Hooker, & Rich Caruana (2019). "Purifying Interaction Effects with the Functional ANOVA: An Efficient Algorithm for Recovering Identifiable Additive Models". In: *arXiv preprint arXiv:1911.04974* (cit. on p. 151).

Luken, Kieran J., Ray P. Norris, & Laurence A. F. Park (Oct. 2019). "Preliminary Results of Using k-Nearest Neighbors Regression to Estimate the Redshift of Radio-selected Data Sets". In: *Publications of the ASP* 131.1004, p. 108003. arXiv: 1810.10714 [astro-ph.GA] (cit. on p. 143).

Maiolino, R. & F. Mannucci (Feb. 2019). "De re metallica: the cosmic chemical evolution of galaxies". In: *Astronomy and Astrophysics Reviews* 27.1, 3, p. 3. arXiv: 1811.09642 [astro-ph.GA] (cit. on p. 11).

Nelson, Dylan, Annalisa Pillepich, Volker Springel, et al. (Dec. 2019). "First results from the TNG50 simulation: galactic outflows driven by supernovae and black hole feedback". In: *Monthly Notices of the RAS* 490.3, pp. 3234–3261. arXiv: 1902.05554 [astro-ph.GA] (cit. on p. 91).

Nori, Harsha, Samuel Jenkins, Paul Koch, & Rich Caruana (Sept. 2019). "InterpretML: A Unified Framework for Machine Learning Interpretability". In: *arXiv e-prints*, arXiv:1909.09223, arXiv:1909.09223. arXiv: 1909.09223 [cs.LG] (cit. on pp. 147, 151, 176).

Norris, Ray P., M. Salvato, G. Longo, et al. (Oct. 2019). "A Comparison of Photometric Redshift Techniques for Large Radio Surveys". In: *Publications of the ASP* 131.1004, p. 108004. arXiv: 1902.05188 [astro-ph.IM] (cit. on p. 143).

Obreja, Aura, Aaron A. Dutton, Andrea V. Macciò, et al. (Aug. 2019). "NIHAO XVI: the properties and evolution of kinematically selected discs, bulges, and stellar haloes". In: *Monthly Notices of the RAS* 487.3, pp. 4424–4456. arXiv: 1804.06635 [astro-ph.GA] (cit. on p. 143).

Oyarzún, Grecco A., Kevin Bundy, Kyle B. Westfall, et al. (Aug. 2019). “Signatures of Stellar Accretion in MaNGA Early-type Galaxies”. In: *Astrophysical Journal* 880.2, 111, p. 111. arXiv: 1906.05298 [astro-ph.GA] (cit. on pp. 86, 90, 98, 174).

Parikh, Taniya, Daniel Thomas, Claudia Maraston, et al. (Mar. 2019). “SDSS-IV MaNGA: local and global chemical abundance patterns in early-type galaxies”. In: *Monthly Notices of the RAS* 483.3, pp. 3420–3436. arXiv: 1812.02753 [astro-ph.GA] (cit. on p. 117).

Pérez-Carrasco, M., G. Cabrera-Vives, M. Martinez-Marin, et al. (Oct. 2019). “Multiband Galaxy Morphologies for CLASH: A Convolutional Neural Network Transferred from CANDELS”. In: *Publications of the ASP* 131.1004, p. 108002. arXiv: 1810.07857 [astro-ph.IM] (cit. on p. 143).

Pillepich, Annalisa, Dylan Nelson, Volker Springel, et al. (Dec. 2019). “First results from the TNG50 simulation: the evolution of stellar and gaseous discs across cosmic time”. In: *Monthly Notices of the RAS* 490.3, pp. 3196–3233. arXiv: 1902.05553 [astro-ph.GA] (cit. on p. 91).

Salvato, Mara, Olivier Ilbert, & Ben Hoyle (June 2019). “The many flavours of photometric redshifts”. In: *Nature Astronomy* 3, pp. 212–222. arXiv: 1805.12574 [astro-ph.GA] (cit. on p. 143).

Sonnenfeld, A., W. Wang, & N. Bahcall (Feb. 2019). “Hyper Suprime-Cam view of the CMASS galaxy sample. Halo mass as a function of stellar mass, size, and Sérsic index”. In: *Astronomy and Astrophysics* 622, A30, A30. arXiv: 1811.04934 (cit. on pp. 38, 62, 94).

Tacchella, Sandro, Benedikt Diemer, Lars Hernquist, et al. (Aug. 2019). “Morphology and star formation in IllustrisTNG: the build-up of spheroids and discs”. In: *Monthly Notices of the RAS* 487.4, pp. 5416–5440. arXiv: 1904.12860 [astro-ph.GA] (cit. on pp. 92, 93, 104, 119, 159, 175).

Tanaka, Masayuki, Francesco Valentino, Sune Toft, et al. (2019). “Stellar Velocity Dispersion of a Massive Quenching Galaxy at z=4.01”. In: *arXiv e-prints*, arXiv:1909.10721, arXiv:1909.10721. arXiv: 1909.10721 [astro-ph.GA] (cit. on pp. 28, 84, 172).

van de Sande, Jesse, Claudia D. P. Lagos, Charlotte Welker, et al. (Mar. 2019). “The SAMI Galaxy Survey: comparing 3D spectroscopic observations with galaxies from cosmological hydrodynamical simulations”. In: *Monthly Notices of the RAS* 484.1, pp. 869–891. arXiv: 1810.10542 [astro-ph.GA] (cit. on p. 119).

Westfall, Kyle B., Michele Cappellari, Matthew A. Bershady, et al. (Dec. 2019). “The Data Analysis Pipeline for the SDSS-IV MaNGA IFU Galaxy Survey: Overview”. In: *Astronomical Journal* 158.6, 231, p. 231. arXiv: 1901.00856 [astro-ph.GA] (cit. on p. 88).

Zhang, Xuezhou, Sarah Tan, Paul Koch, et al. (2019). “Axiomatic Interpretability for Multiclass Additive Models”. In: *Proceedings of the 25th ACM SIGKDD International Conference on Knowledge Discovery & Data Mining*. ACM, pp. 226–234 (cit. on p. 151).

Agarwal, Rishabh, Nicholas Frosst, Xuezhou Zhang, Rich Caruana, & Geoffrey E. Hinton (Apr. 2020). “Neural Additive Models: Interpretable Machine Learning with Neural Nets”. In: *arXiv e-prints*, arXiv:2004.13912, arXiv:2004.13912. arXiv: 2004.13912 [cs.LG] (cit. on p. 151).

Cannarozzo, Carlo, Alessandro Sonnenfeld, & Carlo Nipoti (Aug. 2020a). "The cosmic evolution of the stellar mass-velocity dispersion relation of early-type galaxies". In: *Monthly Notices of the RAS* 498.1, pp. 1101–1120. arXiv: 1910.06987 [astro-ph.GA] (cit. on pp. 27, 84, 173).

Cannarozzo, Carlo, Carlo Nipoti, Alessandro Sonnenfeld, et al. (June 2020b). "The merger-driven evolution of massive early-type galaxies". In: *arXiv e-prints*, arXiv:2006.05427, arXiv:2006.05427. arXiv: 2006.05427 [astro-ph.GA] (cit. on pp. 27, 62, 173).

Chang, Chun-Hao, Sarah Tan, Ben Lengerich, Anna Goldenberg, & Rich Caruana (2020). "How Interpretable and Trustworthy are GAMs?" In: *arXiv preprint arXiv:2006.06466* (cit. on p. 151).

Darshana Abeyrathna, K., Ole-Christoffer Granmo, & Morten Goodwin (May 2020). "Extending the Tsetlin Machine With Integer-Weighted Clauses for Increased Interpretability". In: *arXiv e-prints*, arXiv:2005.05131, arXiv:2005.05131. arXiv: 2005.05131 [cs.AI] (cit. on p. 151).

Domínguez Sánchez, H., M. Bernardi, F. Nikakhtar, B. Margalef-Bentabol, & R. K. Sheth (July 2020). "Galaxy properties as revealed by MaNGA - III. Kinematic profiles and stellar population gradients in S0s". In: *Monthly Notices of the RAS* 495.3, pp. 2894–2908. arXiv: 2005.07693 [astro-ph.GA] (cit. on pp. 96, 97, 117).

Girelli, G., L. Pozzetti, M. Bolzonella, et al. (Feb. 2020). "The stellar-to-halo mass relation over the past 12 Gyr. I. Standard ΛCDM model". In: *Astronomy and Astrophysics* 634, A135, A135. arXiv: 2001.02230 [astro-ph.CO] (cit. on p. 144).

Kaur, Harmanpreet, Harsha Nori, Samuel Jenkins, et al. (2020). "Interpreting Interpretability: Understanding Data Scientists' Use of Interpretability Tools for Machine Learning". In: *Proceedings of the 2020 CHI Conference on Human Factors in Computing Systems*, pp. 1–14 (cit. on p. 151).

Maraston, C., L. Hill, D. Thomas, et al. (June 2020). "Stellar population models based on the SDSS-IV MaStar library of stellar spectra - I. Intermediate-age/old models". In: *Monthly Notices of the RAS* 496.3, pp. 2962–2997. arXiv: 1911.05748 [astro-ph.SR] (cit. on pp. 88, 174).

Mingozzi, M., F. Belfiore, G. Cresci, et al. (Apr. 2020). "SDSS IV MaNGA: Metallicity and ionisation parameter in local star-forming galaxies from Bayesian fitting to photoionisation models". In: *Astronomy and Astrophysics* 636, A42, A42. arXiv: 2002.05744 [astro-ph.GA] (cit. on pp. 144, 176).

Moster, Benjamin P., Thorsten Naab, Magnus Lindström, & Joseph A. O'Leary (May 2020). "GalaxyNet: Connecting galaxies and dark matter haloes with deep neural networks and reinforcement learning in large volumes". In: *arXiv e-prints*, arXiv:2005.12276, arXiv:2005.12276. arXiv: 2005.12276 [astro-ph.GA] (cit. on p. 143).

Nipoti, Carlo, Carlo Cannarozzo, Francesco Calura, Alessandro Sonnenfeld, & Tommaso Treu (Sept. 2020). "Stellar velocity dispersion and initial mass function gradients in dissipationless galaxy mergers". In: *Monthly Notices of the RAS* 499.1, pp. 559–572. arXiv: 2009.05583 [astro-ph.GA] (cit. on p. 84).

Pulsoni, C., O. Gerhard, M. Arnaboldi, et al. (Sept. 2020). "The stellar halos of ETGs in the IllustrisTNG simulations: The photometric and kinematic diversity of galaxies at large radii". In: *Astronomy and Astrophysics* 641, A60, A60. arXiv: 2004.13042 [astro-ph.GA] (cit. on p. 117).

Santucci, Giulia, Sarah Brough, Nicholas Scott, et al. (June 2020). "The SAMI Galaxy Survey: Stellar Population Gradients of Central Galaxies". In: *Astrophysical Journal* 896.1, 75, p. 75. arXiv: 2005.00541 [astro-ph.GA] (cit. on p. 86).

Speagle, Joshua S. (Apr. 2020). "DYNESTY: a dynamic nested sampling package for estimating Bayesian posteriors and evidences". In: *Monthly Notices of the RAS* 493.3, pp. 3132–3158. arXiv: 1904.02180 [astro-ph.IM] (cit. on p. 89).

Walmsley, Mike, Lewis Smith, Chris Lintott, et al. (Jan. 2020). "Galaxy Zoo: probabilistic morphology through Bayesian CNNs and active learning". In: *Monthly Notices of the RAS* 491.2, pp. 1554–1574. arXiv: 1905.07424 [astro-ph.GA] (cit. on p. 151).

Wang, Caroline, Bin Han, Bhrij Patel, Feroze Mohideen, & Cynthia Rudin (May 2020a). "In Pursuit of Interpretable, Fair and Accurate Machine Learning for Criminal Recidivism Prediction". In: *arXiv e-prints*, arXiv:2005.04176, arXiv:2005.04176. arXiv: 2005.04176 [stat.ML] (cit. on p. 151).

Wang, H., Z. Huang, D. Zhang, et al. (2020b). "Integrating Co-Clustering and Interpretable Machine Learning for the Prediction of Intravenous Immunoglobulin Resistance in Kawasaki Disease". In: *IEEE Access* 8, pp. 97064–97071 (cit. on p. 151).

Yang, Zebin, Aijun Zhang, & Agus Sudjianto (Mar. 2020). "GAMI-Net: An Explainable Neural Network based on Generalized Additive Models with Structured Interactions". In: *arXiv e-prints*, arXiv:2003.07132, arXiv:2003.07132. arXiv: 2003.07132 [stat.ML] (cit. on p. 151).

Zhou, Jiandong, Gary Tse, Sharen Lee, et al. (2020). "Identifying main and interaction effects of risk factors to predict intensive care admission in patients hospitalized with COVID-19: a retrospective cohort study in Hong Kong". In: *medRxiv*. eprint: https://www.medrxiv.org/content/early/2020/07/02/2020.06.30.20143651.full.pdf (cit. on p. 151).

Ardila, Felipe, Song Huang, Alexie Leauthaud, et al. (Jan. 2021). "Stellar and weak lensing profiles of massive galaxies in the Hyper-Suprime Cam survey and in hydrodynamic simulations". In: *Monthly Notices of the RAS* 500.1, pp. 432–447. arXiv: 2010.00123 [astro-ph.GA] (cit. on pp. 95, 99, 174).

Cannarozzo, Carlo, Alexie Leauthaud, Grecco Oyarzún, et al. (a, in prep.). "The role of in-situ and ex-situ stellar populations in early-type galaxies: MaNGA versus IllustrisTNG" (cit. on pp. 83, 175).

Cannarozzo, Carlo, Alexie Leauthaud, Alessandro Sonnenfeld, Carlo Nipoti, & al. (b, in prep.). "Inferring the Dark Matter halo mass in galaxies from other observables with Machine Learning" (cit. on pp. 141, 177).

List of Figures

1.1 The Hubble tuning-fork sequence diagram. This plot is taken from https://www.spacetelescope.org/images/heic9902o/. 2

1.2 Examples of oblate (top panels) and prolate (bottom panels) spheroids. Top panels: oblate spheroid with $a = b > c$. If $c/a = 0.6$, the apparent shape for observer A corresponds to an E4 galaxy ($\beta/\alpha = 0.6$), while for observer B corresponds to an E0 galaxy ($\beta/\alpha = 1$). Bottom panels: prolate spheroid with $a > b = c$. If $b/a = 0.6$, the apparent shape for observer A corresponds to an E0 galaxy, while for observer B corresponds to an E4 galaxy. This plot is an adapted version of two original plots taken from Carroll & Ostlie (2006). 3

1.3 The bolometric luminosity of the different types of stars as a function of time for a solar metallicity population SSP with a Salpeter initial mass function. The types of stars shown are *main sequence* (MS), *horizontal branch* (HB), *subgiant branch* (SGB), *red giant branch* (RGB), *asymptotic giant branch* (AGB), and *post asymptotic giant branch* (P-AGB) stars. The upper x-axis indicates the corresponding main sequence turnoff (TO) mass. This plot is taken from Renzini & Buzzoni (1986, in *Spectral Evolution of Galaxies*, eds. C. Chiosi & A. Renzini, Reidel Publishing). . 6

1.4 The reddening-corrected $u - r$ colour–mass diagrams for the whole galaxy sample (top-left panel), and for the ETGs (top-right panel) and LTGs (bottom-right panel), respectively of the SDSS DR7. The two green lines in the three plots delimit the green valley. This plot is taken from Schawinski et al. (2014). 9

1.5 Stellar mass–metallicity relation (left panel) and stellar mass–age relation (right panel) for $z \simeq 0.05$ SDSS quiescent (red curves) and star forming (blue curves) galaxies. These plots are adapted from Peng, Maiolino, & Cochrane (2015). 11

1.6 The $\mathrm{age}{-}\sigma$ (top panel), $[Z/\mathrm{H}]\,{-}\sigma$ (middle panel), and $[\alpha/\mathrm{Fe}]\,{-}\sigma$ (bottom panel) relations are shown. Open red dots and black squares represent central values and mean stellar values of stellar population parameters of the sample considered by Spolaor et al. (2010). The red and black lines are the weighted least-squares linear fits. This plot is taken from Spolaor et al. (2010). 13

1.7 The Fundamental Plane of galaxies from the 6dFGS. Blue and black dots trace galaxies above and below the best-fitting plane, respectively. This plot is taken from Magoulas et al. (2012). 17

1.8 The stellar mass–size relation in six redshift bins for ETGs (red dots) and LTGs (blue dots) from the 3D-HST+CANDELS composite-sample. This plot is taken from van der Wel et al. (2014). 18

1.9 The central projected velocity dispersion as a function of redshift for observed and simulated galaxies with $M_* \approx 10^{11}\,\mathrm{M}_\odot$ from Oser et al. (2012). Solid symbols trace star-forming galaxies, while empty symbols represent quiescent galaxies. The black curves show the result of a power-law fit for all (dashed curve) and the quiescent (solid curve) galaxies, respectively. Adapted from Oser et al. (2012). 19

1.10 The morphology–density relation for more than 6000 galaxies in 55 clusters. The fraction of galaxies as a function of the projected galaxy density ρ_{proj} (or the 3D density ρ) is shown for ellipticals E (open dots), lenticulars S0 (filled dots), and spiral + irregular (crosses). This plot is taken from Dressler (1980). 21

1.11 The average stellar mass contents for the in-situ and ex-situ stellar populations (normalised to the total stellar mass at $z = 0$) as a function of redshift for massive ETGs (with virial masses of $12.7 \lesssim \log(M_{200}/\mathrm{M}_\odot) \lesssim 13.4$) in a cosmological hydrodynamical simulation. This is an adapted version of a plot taken from Oser et al. (2010). . . . 24

2.1 Equivalent width of Hβ, $\mathrm{EW}(\mathrm{H}\beta)$, as a function of equivalent width of [O II], $\mathrm{EW}([\mathrm{O\,II}])$, for galaxies drawn from the original catalogues of SDSS (circles) and LEGA-C (squares). For LEGA-C galaxies, we show only objects with signal-to-noise ratio > 10. The black dashed line represents a linear fit to the data. Galaxies in the shaded region of the diagram ($\mathrm{EW}([\mathrm{O\,II}]) < -5\,$Å) are excluded from our sample of ETGs. . 32

2.2 A succesful case of Sérsic model in the g, r, i, z and y filters (from the top to the bottom) for one galaxy (HSC ID #42648136191078699) of the fiducial sample. Left panels show the original images of the galaxy in the five filters, while right panels illustrate the corresponding models. 34

2.3 Same as Figure 2.2, but for one galaxy (HSC ID #41214944259116180) of the fiducial sample for which the Sérsic fit is unsuccessful. 35

2.4 Colour-composite HSC images of a set of SDSS main sample ETGs that passed our selection in EW([O II]) and our visual inspection. 36

2.5 Colour-composite HSC images of a set of SDSS main sample galaxies that passed our selection in EW([O II]), but were rejected in our visual inspection step, due to the presence of disks and/or spiral arms. 36

2.6 Stellar mass as a function of SDSS $r-$band Petrosian magnitude, for SDSS main sample ETGs in three narrow redshift bins (upper pannel). Horizontal dashed lines mark, in each redshift bin, the stellar mass above which an ETG drawn from the SDSS main sample has more than 99% probability of entering our sample. Distribution in the ratio between stellar mass and observed-frame $r-$band Petrosian luminosity of the galaxies in the three redshift bins shown in the upper panel (lower panel). The 99-th percentile of each distribution is marked by a vertical dashed line. This value, multiplied by the Petrosian luminosity corresponding to the limiting $r-$band magnitude of the SDSS main sample, $r_{\rm P} = 17.77$, gives the 99% completeness limit shown in the upper panel. 40

2.7 Stellar mass as a function of redshift for SDSS (upper panel) and LEGA-C (lower panel) galaxies. The solid curves represent the empirical 99% mass-completeness limits. The horizontal dashed lines represent the absolute lower stellar mass limit $10^{10.5}\,{\rm M}_{\odot}$, while the vertical dashed lines are the lowest ($z = 0.05$) and highest ($z = 0.20$) redshift limits imposed in the SDSS galaxy selection. In the upper panel, grey dots represent all the 2127 SDSS main sample galaxies morphologically selected and with ${\rm EW([O\,II])} \geq -5\,$Å, while black dots are the 413 objects above the mass-completeness limit, with $\log(M_*/{\rm M}_{\odot}) > 10.5$ in the redshift range $0.05 < z < 0.2$. In the lower panel, grey dots are the 492 LEGA-C galaxies selected in morphology, EW([O II]) and K_s-band magnitude, while the black dots represent the final LEGA-C sample of 178 ETGs above the mass-completeness limit. 41

2.8 Distributions of the subsamples and samples of ETGs in redshift (upper panel) and stellar mass (lower panel). From the top to the bottom, the SDSS subsample, the LEGA-C subsample, the high-redshift sample (vdS13+B14+G15+B17 subsamples), the fiducial sample (SDSS+LEGA-C subsamples) and the extended sample (fiducial sample+high-resdhift sample) distributions are shown. 44

2.9 Redshift distribution of the extended sample on the $M_*-\sigma_e$ plane. In the left panel each galaxy is colour-coded as a function of its redshift, while in the right panel the redshift distribution is smoothed by means of the two-dimensional Locally Weighted Regression (LOESS, Cleveland & Devlin, 1988) using the Python implementation of Cappellari et al. (2013, available at `https://www-astro.physics.ox.ac.uk/~mxc/software/`). 45

2.10 Posterior probability distributions of the hyper-parameters for model $\mathcal{M}^{\rm SDSS}$ (see Tables 2.4 and 2.5). In the 1D distributions (upper panel of each column) the vertical solid lines and colours delimit the 68, 95 and 99.7-th quantile based posterior credible interval. In the 2D distributions (all the other panels) the contours enclose the 68, 95 and 99.7 percent posterior credible regions. The dashed lines indicate the median values of the hyper-parameters. 56

2.11 Same as Figure 2.10, but for models $\mathcal{M}^{fid}_{\rm const,NES}$ (pink contours) and $\mathcal{M}^{ext}_{\rm const,NES}$ (azure contours; see Tables 2.4 and 2.5). 57

2.12 Same as Figure 2.10, but for models $\mathcal{M}^{fid}_{\rm evo,NES}$ (green contours) and $\mathcal{M}^{ext}_{\rm evo,NES}$ (orange contours; see Tables 2.4 and 2.5). 58

2.13 Median central stellar velocity dispersion σ_e at $M_* = 10^{11}\,{\rm M}_\odot$ (upper panel) and slope β of the M_*–σ_e relation (lower panel) as functions of redshift for models $\mathcal{M}^{fid}_{\rm const,NES}$ (pink dashed curve), $\mathcal{M}^{fid}_{\rm evo,NES}$ (green dotted curves), $\mathcal{M}^{ext}_{\rm const,NES}$ (azure dashed curve) and $\mathcal{M}^{ext}_{\rm evo,NES}$ (orange dotted curves). In the lower panel the curves for models $\mathcal{M}^{fid}_{\rm const,NES}$ and $\mathcal{M}^{ext}_{\rm const,NES}$ are identical, and are represented by the grey solid line. The curves are obtained by computing, at given x, the median value of y (where x and y are the quantities in abscissa and ordinate, respectively) among all the values sampled by the posterior distribution obtained with the MCMC; similarly, the shaded bands, which we will refer to as 1σ uncertainty bands, are defined by computing the 16% and the 84% of the distribution of y, at given x, for the same sampling. . . 63

2.14 Central stellar velocity dispersion as a function of stellar mass. In the left panels the curves represent the median relations of the fiducial-sample models $\mathcal{M}^{fid}_{\rm const,NES}$ (upper panel) and $\mathcal{M}^{fid}_{\rm evo,NES}$ (lower panel), at $z = 0$, $z = 0.5$ and $z = 1$. In the right panels the curves represent the median relations of the extended-sample models $\mathcal{M}^{ext}_{\rm const,NES}$ (upper panel) and $\mathcal{M}^{ext}_{\rm evo,NES}$ (lower panel), at $z = 0$, $z = 0.5$, $z = 1$, $z = 1.5$ and $z = 2$. The bands indicate the 1σ uncertainty ranges. The median relations and the 1σ bands are computed as described in the caption of Figure 2.13. The grey error bars represent the redshift-independent intrinsic scatter. The dots indicate the positions in these diagrams of the ETGs of the fiducial (left panels) and extended (right panels) samples. 64

2.15 Comparison between the median M_*–$\sigma_{\rm e}$ relations of our models $\mathcal{M}_{\rm const,NES}$ (dashed curves) and $\mathcal{M}_{\rm evo,NES}$ (dotted curves), and fits from the literature (solid curves) at $z = 0.2$ (upper left panel), $z = 0.35$ (upper right panel), $z = 1.23$ (lower left panel) and $z = 2$ (lower right panel). Upper left panel: the red and blue solid curves are the linear fits of Auger et al. (2010), including and not including the intrinsic scatter, respectively, while the gold and light green solid curves are the linear and the quadratic fits of Hyde & Bernardi (2009a), respectively. The thin dash-dotted curve is the median relation of model $\mathcal{M}^{fid}_{\rm evo,NS}$, in which we assume zero intrinsic scatter (see text). Upper right panel: the azure curve is the linear fit for the hCOS20.6 galaxies ($0.2 < z < 0.5$) by Damjanov et al. (2018), the brown curve is the linear fit of Zahid et al. (2016a) for the SHELS sample ($0.3 < z < 0.4$) and the violet curve is the fit of Mason et al. (2015) evaluated at $z = 0.35$. Lower left panel: the green curve is the linear fit of Belli et al. (2014a) and the violet curve is the fit of Mason et al. (2015) evaluated at $z = 1.23$. Lower right panel: the violet curve is the fit of Mason et al. (2015) evaluated at $z = 2$. Each curve is shown over the stellar mass range spanned by the considered data set. 68

2.16 Left panel: distribution of the ratio between our r-band stellar mass-to-light ratio ($(M_*/L_r)_{\rm CSN}$) and those obtained by M14 assuming dust-free ($(M_*/L_r)_{\rm DF}$, blue histogram) and dusty ($(M_*/L_r)_{\rm D}$, red histogram) models for the SDSS galaxies of our sample. Right panel: distribution of the ratio between our r-band luminosity ($L_{r,\rm CSN}$) and that of Simard et al. (2011) ($L_{r,\rm Simard}$) for the same galaxies as in the left panel. In both panels, the dashed lines represent the medians of the distributions, while the intervals between the 16-th and 84-th percentiles are indicated by the shaded areas. 75

2.17 Pure Sérsic fit stellar masses based on the dust-free (left panel) and dusty (right panel) models of M14 ($\log M_{*,\mathrm{DF}}$ and $\log M_{*,\mathrm{D}}$, respectively) as functions of our stellar masses ($\log M_{*,\mathrm{CSN}}$) for the SDSS galaxies of our sample. The distributions are represented as two-dimensional histograms: the darkest the colour of the pixel the highest the number of galaxies. In each panel, the solid line represents the 1:1 relation, while the dashed line is the linear fit to the data. 75

2.18 Same as Figure 2.10, but for model $\mathcal{M}^{\mathrm{mock}}$ (dark grey contours). The thick orange solid lines indicate the input values of the hyper-parameters μ_0^{mock}, β_0^{mock} and ψ_0^{mock}. 80

2.19 UVJ colour-colour diagram for the LEGA-C sample of 178 ETGs (red dots). The broken line separates quiescent (upper-left region) and star-forming galaxies (lower-right region) as in Muzzin et al. (2013a). 82

2.20 Posterior probability distributions of the hyper-parameters for the M_*–σ_{e} models $\mathcal{M}^{fid}_{\mathrm{const,NES}}$ (purple contours) and $\mathcal{M}^{fid,UVJ}_{\mathrm{const,NES}}$ (blue contours). In the 1D distributions (top panel of each column) the vertical solid lines and colours delimit the 68, 95 and 99.7-th quantile based posterior credible interval. In the 2D distributions (all the other panels) the contours enclose the 68, 95 and 99.7 percent posterior credible regions. The lines indicate the median values of the hyper-parameters. 82

3.1 Distributions of simulated $(g-r)$ colours at different mass bins in IllustrisTNG100-1 (blue curve) compared with SDSS (black curve) and Illustris-1 (red curve) estimates. This plot is taken from Nelson et al. (2018). 93

3.2 Comparison between the 2D stellar mass within $2R_{\mathrm{hm}}$ ($M_*^{\mathrm{2hmr,2D}}$, x-axis) and the 3D stellar mass within $2r_{\mathrm{hm}}$ ($M_*^{\mathrm{2hmr,3D}}$, y-axis) for the IllustrisTNG starting sample of ≈ 3000 subhalos with $\log(M_*^{\mathrm{tot,3D}}/\mathrm{M}_\odot) \geq 10.5$. 95

3.3 Red galaxy samples with with $(g-r) > 0.6$. Left panel: the scatter distribution indicates the MaNGA sample assuming the SerExp Dusty masses (orange dots). The 2D histogram indicates the IllustrisTNG colour-selected sample, assuming the 2hmr mass. Right panel: 1D histograms of the mass distributions for the MaNGA (orange histogram) and the IllustrisTNG (grey histogram) estimates. 97

3.4 Distributions of the $\mathrm{T\text{-}Type}$ (left panel) and P_{S0} (right panel) morphological parameters for our MaNGA Red Galaxy sample. A value of $\mathrm{T\text{-}Type} \leq 0$ identifies an ETG, i.e. a system with a E/S0 morphology, otherwise the source is a LTG. The parameter P_{S0} gives the probability for each galaxy of being a S0 lenticular galaxy (with $P_{\mathrm{S0}} > 0.5$) rather than a pure elliptical (with $P_{\mathrm{S0}} < 0.5$). In both panels, the black dashed lines divide the plots between ETGs and LTGs, and between pure ellipticals and lenticulars, respectively. 98

3.5 Cumulative stellar mass functions for the IllustrisTNG (red solid curve) and the MaNGA samples for the SerExp Dusty (black dotted curve) and the Dust-free (black dashed curve) stellar mass measurements. The CSMFs are compared at the same number-density-based stellar mass bins built deriving the values of number density of the MaNGA galaxy CSMFs corresponding to the stellar mass values $\log(M_*/\mathrm{M}_\odot) = 10.5, 11.0, 11.5$: from -2.50 to -3.15 (blue shaded region), from -3.15 to -4.15 (green shaded region), and below -4.15 (yellow shaded region). The vertical lines trace the stellar mass values of each galaxy sample corresponding to their number density value, following the same formalism in colours and curve styles. The grey shaded regions correspond to value of stellar masses and/or number densities excluded by our selection. 101

3.6 Radial profiles of (from the top to the bottom) stellar mass surface density, metallicity, age, and velocity dispersion in three bins of stellar mass for MaNGA and IllustrisTNG Red galaxies. For MaNGA ETGs we use the Dusty model masses, while for IllustrisTNG ETGs we use the 2hmr masses. The green, yellow and violet dots represent the median estimates for MaNGA ETGs from FIREFLY, PROSPECTOR and pPXF codes, respectively, in the 5 radial bins identified by the grey dashed lines. The two black curves represent the median value of each stellar property for the total stellar populations in IllustrisTNG galaxies in 20 radial bins spaced uniformly in log over the range $0-150\,\mathrm{kpc}$, both obtained from the original maps and from the maps convolved with the MaNGA PSF, respectively. The black shaded area is the region that lies in between the profiles obtained from the original and the convolved IllustrisTNG maps. The errorbars represent the 1σ uncertainties on the median for MaNGA and IllustrisTNG estimates. The hatched area (0:2.1 kpc) shows 3x the force resolution of the stellar particles in IllustrisTNG.105

3.7 Radial profiles of (from the top to the bottom) stellar mass surface density, metallicity, age, and velocity dispersion in three bins of stellar mass for IllustrisTNG Red galaxies. The black solid, red dashed and blue dotted curves (and their shaded areas) are the same as in Figure 3.6, but for the total, the in-situ, and the ex-situ stellar populations, respectively. The errorbars represent the 1σ uncertainties on the median for IllustrisTNG estimates. The hatched area (0:2.1 kpc) shows 3x the force resolution of the stellar particles in IllustrisTNG. 106

3.8 Violin plots of eight properties related to the merger history of the IllustrisTNG ETGs. First row: fractions of the in-situ (left panel) and the ex-situ (right panel) stellar components. Second row: fractions of the ex-situ stellar component due to all mergers ($0 < \mu_* < 1$, excluding stars stripped from surviving galaxies), and only due to major mergers (right panel) normalised to the total ex-situ stellar fraction. Third row: number of minor (left panel) and major (right panel) mergers. Fourth row: redshifts of the lasts minor (left panel) and major (right panel) mergers. All the distributions are shown for the three stellar mass bins as in Figure 3.6 and in Figure 3.7. For each violin plot the median value of the corresponding distribution is reported. 107

3.9 Same as Figure 3.6, but in number-density-based stellar mass bins. . . 111

3.10 Same as Figure 3.7, but in number-density-based stellar mass bins. . . 112

3.11 Top panels: radial profiles for stellar mass surface density in three bins of stellar mass for MaNGA and IllustrisTNG Red central and satellite galaxies. For MaNGA ETGs we use the Dusty model masses, while for IllustrisTNG ETGs we use the 2hmr masses. The green and yellow dots represent the median estimates for MaNGA central ETGs from FIREFLY and PROSPECTOR codes, while the azure and redbrick dots are the median values obtained for MaNGA satellites ETGs, in the 5 radial bins identified by the grey dashed lines. The errorbars represent the 1σ uncertainties for MaNGA and IllustrisTNG estimates. The black and grey curve represent the median value of each stellar property for the total stellar populations in central and satellite IllustrisTNG galaxies in 20 radial bins spaced uniformly in log over the range $0-150\,\mathrm{kpc}$, both obtained from the maps convolved with the MaNGA PSF. Bottom panels: the red dashed and blue dotted curves represent the in-situ and the ex-situ stellar components for centrals, while the pink dashed and cyan dotted curves indicate the in-situ and ex-situ stellar components for satellites. For clarity reasons, we omit the errobars for the plots in the lower panels. The hatched area (0:2.1 kpc) shows 3x the force resolution of the stellar particles in IllustrisTNG. 114

3.12 Same as in Figure 3.11, but for stellar metallicity. 115

3.13 Same as in Figure 3.11, but for stellar age. 115

3.14 Same as in Figure 3.11, but for stellar velocity dispersion. The violet and orange diamonds represent the median estimates for MaNGA central and satellite ETGs from PPXF code, respectively. 116

3.15 Same as Figure 3.3, but for the SerExp Dust-free model stellar mass for MaNGA galaxies. 122

3.16 Same as Figure 3.4, but for the SerExp Dust-free model stellar mass for MaNGA galaxies. 122

3.17 Same as Figure 3.6, but for the Dust-free model masses for MaNGA ETGs. 123

3.18 Same as Figure 3.6, but in number-density-based stellar mass bins and for the Dust-free model masses for MaNGA ETGs. 124

3.19 The $z-M_*$ scatter distributions of the Red galaxy samples of MaNGA, using the SerExp Dusty model (left panel) and the SerExp Dust-free model (right panel) masses. The black solid curves trace the fit of each distribution. In each plot the corresponding fit functional form is reported. The two stripes of dots in each panel trace the Primary sample (the lower cloud) and the Secondary sample (the upper cloud) of the MaNGA total sample. 126

3.20 Same as in Figure 3.3, but for Quiescent galaxies, i.e. galaxies with star formation rate below $1\,\mathrm{dex}$ the star-forming main sequence of galaxies, using the SerExp Dusty (top panels) and the SerExp Dust-free (bottom panels) stellar masses. 129
3.21 Radial profiles of (from the top to the bottom) stellar mass surface density, metallicity, age, and velocity dispersion in three bins of mass for MaNGA and IllustrisTNG Quiescent galaxies. For MaNGA ETGs we use the Dusty model masses, while for IllustrisTNG ETGs we use the 2hmr masses. The green, yellow and violet dots represent the median estimates for MaNGA ETGs from FIREFLY, PROSPECTOR and pPXF codes, respectively, in the 5 radial bins identified by the grey dashed lines.The black solid, red dashed and blue dotted curves represent the median profiles of each stellar property for the total, the in-situ and the ex-situ stellar populations in IllustrisTNG galaxies in 20 radial bins spaced uniformly in log over the range $0-150\,\mathrm{kpc}$ obtained from the original maps. The black, green, yellow and violet shaded areas indicate the 68% intrinsic scatter distributions for IllustrisTNG, FIREFLY, PROSPECTOR, and pPXF profiles, respectively. The errorbars represent the 1σ uncertainties on the median for MaNGA and IllustrisTNG estimates. The hatched area (0:2.1 kpc) shows 3x the force resolution of the stellar particles in IllustrisTNG. 130
3.22 Same as Figure 3.21, but assuming the SerExp Dust-free model masses for MaNGA galaxies. 131
3.23 Same as Figure 3.20, but for Red galaxies. For MaNGA galaxies we adopt, from the top to the bottom panels, the NSA Sérsic masses (blue dots and histograms), the NSA Petrosian masses (pink dots and histograms) and the masses included into the 5 radial bins computed by FIREFLY (green dots and histograms) and PROSPECTOR (yellow dots and histograms), while for IllustrisTNG galaxies we assume the masses within an aperture of $30\,\mathrm{kpc}$ (grey 1D and 2D histograms). 132
3.24 Same as Figure 3.21, but for Red galaxies and assuming the NSA Sérsic masses for MaNGA galaxies, and the masses within $30\,\mathrm{kpc}$ for IllustrisTNG galaxies. 133
3.25 Same as Figure 3.21, but for Red galaxies and assuming the NSA Petrosian masses for MaNGA galaxies, and the masses within $30\,\mathrm{kpc}$ for IllustrisTNG galaxies. 134
3.26 Same as Figure 3.21, but for Red galaxies and assuming the masses within the 5 radial bins computed by FIREFLY and PROSPECTOR for MaNGA galaxies, and the masses within $30\,\mathrm{kpc}$ for IllustrisTNG galaxies. 135

3.27 Same as Figure 3.23, but for Quiescent galaxies. 136

3.28 Same as Figure 3.21, but assuming the NSA Sérsic masses for MaNGA galaxies, and the masses within $30\,\mathrm{kpc}$ for IllustrisTNG galaxies. 137

3.29 Same as Figure 3.21, but assuming the NSA Petrosian masses for MaNGA galaxies, and the masses within $30\,\mathrm{kpc}$ for IllustrisTNG galaxies. 138

3.30 Same as Figure 3.21, but assuming the masses within the 5 radial bins computed by FIREFLY and PROSPECTOR for MaNGA galaxies, and the masses within $30\,\mathrm{kpc}$ for IllustrisTNG galaxies. 139

4.1 The 1D age profile (left panel) and the 2D age−cancer map (right panel). The y-axis in the 1D profile and the colorbar in the 2D map represent the entire range of the POD. The green errorbars are ± 1 standard deviation of POD derived from bagging runs. The plots are adapted from Caruana et al. (2015). 149

4.2 Target variable M_{DM} as a function of the stellar mass M_* (upper left panel), the gas mass M_{gas} (upper right panel), and the black hole mass M_{BH} (lower panel) for the training sample. In each panel, the 1D red histogram on the y-right-axis represents the distribution of the target M_{DM}, while the 1D violet histogram on the x-upper-axis represents the distribution of each feature. Above each plot the Pearson correlation coefficient is reported. 153

4.3 Same as Figure 4.2, but for the stellar metallicity Z_* (upper left panel), the gas metallicity Z_{gas} (upper right panel), the black hole accretion rate $\dot{M}_{\mathrm{BH}}$ (lower left panel), and the star formation rate SFR (lower right panel). 154

4.4 Overall importance diagram of the 7 features and the 3 most relevant pairwise interactions used by EBM. The contribute of each term is additive thanks to the modularity of the GAM/GA^{2}Ms. 155

4.5 Single feature score profiles for the gas mass (top panel), stellar mass (middle panel) and for the black hole mass (bottom panel). In each panel, the y-axis indicates the score, i.e. the value in units of $\log M_{\mathrm{DM}}$ to be added to the mean of DM mass value of the training sample, $\log(M_{\mathrm{DM}}/\mathrm{M}_\odot) \simeq 11.4$. The shaded regions represent the ± 1 standard deviation of the variation of score estimated by 100 rounds of bagging. 156

4.6 Same as Figure 4.5, but (from top to bottom) for the stellar metallicity, the gas metallicity, the black hole accretion rate and the star formation rate. 157

4.7 Pairwise interaction 2D maps for the couples $\log M_{\rm gas} - \log M_{\rm BH}$ (left panel), $\log M_* - \log M_{\rm gas}$ (middle panel), and $\log Z_* - \log M_{\rm gas}$ (right panel). These maps are coloured as a function of the score with the same range of the y-axes as in the plots of Figure 4.5 and Figure 4.6. . 158
4.8 Relative importance histograms of the single features and the three most significant pairwise interactions for two subhalos of the $z = 0$ test sample. Above each plot, the true DM mass ($M_{\rm DM}^{\rm true}$) and the mass predicted by the model ($M_{\rm DM}^{\rm pred}$) are reported. 160
4.9 Difference between the predicted and the true DM masses as a function of the true DM mass for the subhalos of the test sample at $z = 0$. The dotted black line represents $M_{\rm DM}^{\rm true} = M_{\rm DM}^{\rm pred}$. The red dashed line traces the median of the distribution, while the shaded region indicates the 68-th percentile of the distribution. 161
4.10 Same as Figure 4.4, but for the training samples at the $z = 0.5$ (upper panel) and $z = 1$ (lower panel) snapshots. 165
4.11 Same as Figure 4.4, but for the training samples at the $z = 2$ (upper panel) and $z = 3$ (lower panel) snapshots. 166
4.12 Same as Figure 4.5, but for (from top to bottom) the gas mass, the stellar mass and the black hole mass of the training samples at at $z = 0$, $z = 0.5$, $z = 1$, $z = 2$ and $z = 3$. 167
4.13 Same as Figure 4.5, but for (from top to bottom) the stellar metallicity, the gas metallicity, the black hole accretion rate and the star formation rate of the training samples at $z = 0$, $z = 0.5$, $z = 1$, $z = 2$ and $z = 3$. . 168
4.14 Same as Figure 4.9, but for the $z = 0.5$ (upper left panel), $z = 1$ (upper right panel), $z = 2$ (lower left panel) and $z = 3$ (lower right panel) snapshots for the test samples. 169

List of Tables

2.1 Summary table of the selection steps adopted to build the final SDSS and LEGA-C samples. 42

2.2 Properties of the subsamples of ETGs used to build our fiducial (SDSS and LEGA-C) and high-redshift (vdS13, B14, G15 and B17) samples. Column 1: subsample name. Column 2: redshift range. Column 3: stellar mass range in logarithm. Column 4: number of galaxies. 43

2.3 Jeffreys' scale (Jeffreys, 1961), giving the strength of evidence in the comparison of two models having Bayes factor $\mathcal{B}$ (equation 2.29). . . . 52

2.4 Hyper-parameters used in the models. Column 1: name of the model. Column 2: name of the hyper-parameter. Column 3: description of the hyper-parameter. Column 4: uniform priors used in the models ("low" and "up" indicate, respectively, the lower and upper bounds). For those hyper-parameters showing two ranges for prior assumptions, the first refers to the fiducial sample and the second to the extended sample. $M_*^{\rm piv}$ and $z^{\rm piv}$ are the median values of stellar mass and redshift of the SDSS ETGs (subsection 2.3.2). 53

2.5 Inferred median and 68% posterior credible intervals of the hyper-parameters of the models. 55

2.6 Logarithm of the Bayesian evidence, $\ln \mathcal{Z}$, and logarithm of the Bayes factor, $\ln \mathcal{B}$, of the models. The values of $\mathcal{B}$ are relative to the Bayesian evidence of model $\mathcal{M}^{fid}_{\rm const,NES}$ for the fiducial sample and of model $\mathcal{M}^{ext}_{\rm const,NES}$ for the extended sample, i.e. the models with the highest evidences for given sample. 59

2.7 Values of the parameters of Equation 2.34, according to the fits of the literature works that we compared with our model. $\gamma = 0$ in all cases, but in the case of the quadratic fit of Hyde & Bernardi (2009a), for which $\gamma = -0.044$. 67

3.1 List of priors used for our PROSPECTOR runs. Column 1: parameter. Column 2: prior. 90

3.2 Summary table of the MaNGA and IllustrisTNG samples. Column 1: sample. Column 2: stellar mass range in logarithm. Column 3: mean value. Column 4: median value. Stellar masses are in units of $M_\odot$. . . 96
3.3 Values of stellar mass corresponding to each number density value for the three CMFs. Column 1: number density in logarithm. Column 2: stellar mass in logarithm for the MaNGA Dusty/Dust free model samples. Column 3: stellar mass in logarithm for the IllustrisTNG sample. 102
3.4 Hyper-parameters used to compute MaNGA profiles. Column 1: stellar property. Column 2: Prior on the mean (low; up). Column 3: Prior on the intrinsic scatter (low; up). 103

4.1 Variables of the training sample. Column 1: Variable. Column 2: range of values in logarithm. Column 3: mean value. 152
4.2 Number of subhalos in the training and test samples at snapshots $z = 0$, $z = 0.5$, $z = 1$, $z = 2$, $z = 3$. Column 1: redshift of the snapshot. Columns 2: number of subhalos in the training sample. Columns 3: number of subhalos in the test sample. 162
4.3 Same as Table 4.1, but for the $z = 0.5$ snapshot. 162
4.4 Same as Table 4.1, but for the $z = 1$ snapshot. 163
4.5 Same as Table 4.1, but for the $z = 2$ snapshot. 163
4.6 Same as Table 4.1, but for the $z = 3$ snapshot. 164